博士論文

Development of a New Type of Geocell as Tensile Reinforcement for GRS RWs

（補強土擁壁の引張り補強材としての活用に向けた新型ジオセルの開発）

韩 鑫晔

Xinye HAN

A thesis submitted in partial fulfillment
of the requirements for the degree of

Doctor of Philosophy

Department of Civil Engineering
University of Tokyo
Tokyo, Japan

September, 2014

ABSTRACT

In the last two decades, in Japan, more than 150 km of geosynthetic-reinforced soil retaining walls (GRS RWs) with a stage-constructed full-height rigid (FHR) facing have been constructed for railways, highways and other infrastructures. This is due mainly to their greater seismic resistance compared to conventional type of RWs. To achieve a high seismic stability of GRS RWs, high tensile resistance of the reinforcement layer at the back of the facing wall is crucial. Geogrid is commonly used as planar tensile reinforcement of the backfill of RWs, embankments and other earth-structures. However, GRS RWs with geogrid reinforcement may encounter the following potential problems: In Japan, geogrid reinforcement requires the use of high-quality backfill materials (i.e. well-compacted sandy soils) to ensure good interlocking of soil particles within the aperture of the geogrid. Nevertheless, in reality, locally abundant and economic soil materials, which may be poorly-graded or include large particles, are often used as the backfill materials. This results in a decrease in its deformability, since the bond stress along the interface between the geogrid and the backfill becomes lower than the shear strength of the backfill to a larger extent with an increase in the backfill soil particle size; What's more, for other GRS structures such as a GRS integral bridge, due to the presence of heavy girder structure, large earthquake-induced inertial force may be activated, which requires the reinforcement to provide a higher pullout resistance. In order to alleviate these problems and improve the overall seismic performance of GRS structures, traditional type geocells (i.e. diamond-shaped geocells) have been firstly introduced and tested. However, their performance was found to be not adequate in the case of very severe earthquakes. Therefore, in this thesis, a new type of geocell, namely square-shaped geocell, was developed. Essentially, it consists of square-shaped cells constituted of a series of straight longitudinal members with transversal walls at separated locations.

In this study, the tensile strength of the newly-developed square-shaped geocell was evaluated by pullout tests comparing to the traditional diamond-shaped geocell and commercial geogrids embedded in gravelly soils with different particle size (i.e. Gravel No. 1, D_{50}=3.2 mm, Gravel No. 3, D_{50}=7.5 mm and Gravel No. 5, D_{50}=14.2 mm). It was found that the square-shaped geocell shows a less pronounced progressive deformation, higher pullout peak

resistance and higher pre-peak stiffness than diamond-shaped geocell when using as backfill soils Gravel No.1 and Gravel No.3. This can be attributed to the effect of the in-plane geometry of the new geocell. In fact, the presence of straight longitudinal members in the square-shaped geocell reduces the progressive deformation of the cells compared with diamond-shaped geocell when subjected to a pullout force, which enhances the pre-peak stiffness and the pullout peak resistance of the geocell. In addition, comparison between square-shaped geocell and commercial geogrids revealed that the peak and the residual pullout resistances of the square-shaped geocell increase and become higher than those of the commercial geogrids with an increase in backfill soil particle size from Gravel No.1 to Gravel No.3. Such a behavior confirms the advantageous use of the square-shaped geocell over the commercial geogrid due to more efficient confinement of larger soil particles in the cells resulting in a larger anchorage capacity of the cells.

The combined effects of geocell height and particle size of backfill soil on the interface mechanism between the geocell and the adjacent backfill soil was also investigated. In general, it was observed that the pullout resistance increases with an increase in the transversal member height of the square-shaped geocell. However, there exists an upper limit of the pullout resistance that is reached when the height of the transversal member exceeds certain values and such threshold increases with an increase in the backfill particle size. A conceptualized pullout interaction mechanism was proposed based on the pullout test results. The pullout resistance is equal to the smaller value between: (i) the shear resistance within the shear bands along the upper and bottom faces of a geocell, which is independent of the height of the geocell members; and (ii) the anchorage resistance induced by passive pressure developing inside the cells, which increases with an increase in the height of the geocell members. Therefore, as the height of the geocell increases, the total pullout resistance approaches to the anchorage resistance and increases with an increase in the height of the geocell. However, when the geocell height reaches a certain limit value, the pullout resistance is given by the shear resistance and, thus, it does not increase with a further increase in the height of geocell. Both shear resistance and anchorage resistance, and therefore the pullout resistance, increase with an increase in backfill particle size.

In addition, the effect of spacing between transversal members on pullout resistance was investigated. It was found that when the pullout resistance of the geocell is determined by the shear resistance within the shear bands along the upper and bottom faces of the geocell, the spacing between transversal members has little influence on the pullout resistance, which

means that reducing the number of transversal members is possible for cost effectiveness.

Although the pre-peak pullout stiffness of the geocell model (made of softer material, with scale factor of 1/10) was found to be lower than that of the commercial geogrid (made of stiffer material), this drawback could be minimized by preloading, which reduces the slackness of the transversal members. The pre-peak stiffness may increase not only by good initial test setting-up, but also by using stiffer longitudinal and transversal members to reduce the progressive development of tensile forces in the pullout direction of the geocell.

The seismic performance of GRS RW using square-shaped geocell (geocell-RS RW) backfilled with sand was evaluated comparing to traditional non-reinforced T-shape RW and geogrid-RS RW (with geogrid^{M} reinforcements having relative larger aperture size) by shaking table model tests. In addition, shaking table model tests on non-reinforced T-shape RW, geogrid-RS RW (with geogrid^{M} reinforcements having relative larger aperture size and geogrid^{C} reinforcements having relative smaller aperture size) and geocell-RS RW backfilled with gravel were also conducted to check if geocell-RS RW has or does not have a higher seismic stability than geogrid-RS RW in the backfill with larger particles. The seismic performance of geocell-RS RW was found as follows:

1) Based on the evaluation of residual overturning angle and sliding displacement of the wall, geocell-RS RW shows more ductile behavior than geogrid-RS RW and non-reinforced T-shape RW when backfilled with sand. This trend becomes more pronounced when backfilled with gravel under higher base acceleration.

2) From the analysis of settlements of the backfill soil, geocell-RS RW shows better performance than geogrid-RS RW and non-reinforced T-shape RW by restricting settlements under higher base acceleration.

3) From the evaluation of response accelerations of the wall and the backfill soil, in the case of sand backfill, the response amplification of geocell-RW is similar with geogrid-RS RW. While in the case of gravel backfill, geocell-RS RW shows a smaller amplification response than geogrid-RS RW under higher base acceleration. This suggests that geocell-RS RW has a higher seismic stability than geogrid-RS RW under higher base acceleration (i.e. from 468 gal to 844 gal) especially if embedded in gravels having larger particles.

4) The threshold acceleration was defined as the amplitude of the base acceleration in the active state when the residual lateral displacement of the facing wall at the position of the top of the wall reaches 5% of the total wall height. Based on this concept, it was found that at the threshold state the threshold acceleration of geocell-RS RW is higher than that of geogrid-

RS RW in both backfill of sand and gravel, indicating that geocell-RS RW exhibits a higher seismic stability than geogrid-RS RW. It was also noted that, as the backfill soil changes from sand to gravel, the threshold acceleration of geocell-RS RW almost keeps steady, while the threshold acceleration of geogrid-RS RW decreases, indicating a decrease in seismic stability of geogrid-RS RW.

5) The dynamic behavior of geocell-RS RW was analyzed as a damped single-degree-of-freedom system. It was found that when backfilled with sand, although geogrid-RS RW and geocell-RS RW may show some unstable dynamic behavior, both clearly exhibits higher dynamic strength, dynamic ductility and damping capacity at failure than non-reinforced T-shape RW. Alternatively, when backfilled with gravel, geocell-RS RW clearly shows higher dynamic strength, dynamic ductility and damping capacity at failure than geogrid-RS RW.

The analysis of shaking table model tests of geocell-RS RW and geogrid-RS RW demonstrated that the geocell has an substantial benefit to confine larger soil particles comparing to geogrid, which induces a higher anchorage resistance and/or higher shear resistance at the top and bottom interfaces between geocell and the adjacent backfill than geogrid, therefore increasing the seismic performance of GRS RW, especially in the case of very severe earthquakes.

ACKNOWLEDGEMENT

I am so grateful to so many people who give me the chance to conduct research in The University of Tokyo.

First and foremost I would like to express my deepest gratitude to my supervisor, Associate Professor Takashi Kiyota, Institute of Industrial Science, The University of Tokyo. In academic field, without your kind-hearted guidance, constructive criticisms, and amazing patience, I cannot complete this research. I also want to thank you for your immense kindness and help in my daily life. You are not only a very young and cool supervisor, but also a handsome and warm-hearted friend. I will remember that you always introduce Japanese culture and ask me to enjoy Japanese life. Joining the BBQ party in your house, joining ski trips, and joining summer trips, etc. will be precious memory in my future life.

Besides, I am deeply grateful to the PH.D thesis committee members, Emeritus Professor Fumio Tatsuoka (The University of Tokyo), Professor Junichi Koseki (Institute of Industrial Science, The University of Tokyo), Professor Ikuo Towhata and Associate Professor Taro Uchimura (Geotechnical Engineering Laboratory, The University of Tokyo), Dr. Kenji Watanabe (Railway Technical Research Institute, Japan) for their valuable comments, criticisms, suggestions for my research. I also feel that I am fortunate to meet many good professors who have a really wide range of knowledge from The University of Tokyo: Emeritus Professor Kazuo Konagai, Professor Kimiro Meguro, Professor Reiko Kuwano, etc.

I am extremely obliged to Dr. Hiroyuki Kyokawa, who taught me how to perform the numerical simulation and gave me a lot of valuable suggestions for my research, and also I am deeply indebted to Dr. Gabriele Chiaro, who helped me to improve the whole thesis, the PowerPoint slides, the presentations and relax me whenever I was in a difficult time. I am equally thankful to Dr. Rama Mohan Pokhrel and Dr. Yasuyo Hosono for your support in my research life in Kiyota Laboratory, The University of Tokyo.

My special appreciation goes to Mr. Toshihiko Katagiri, Kiyota Laboratory, The University of Tokyo, for his highly cooperative kind supports in assembling shaking table model tests. In

addition, I am so grateful to Mr. Michiyuki Harata from TOKYO PRINTING INK MFG. CO., LTD. providing experimental materials and chances for the field investigation. I would not have been able to complete all my experiments without their helps.

I am also grateful to Miss Hiroko Takasaki, the secretary of Kiyota laboratory for her friendly support in handling many aspects during the course of my study.

I would like to express my gratitude to all the members of Kiyota laboratory that I have met during these three years. Especially thanks due to my tutor Mr. Suyama for helping me a lot in administrative aspects during my first step of life in Japan. My sincere appreciation is forwarded to international students in Kiyota laboratory: Miss Jina Lee, Miss Mary Roxanne Agilpay, Mr. Chieh-Yu WU. Chatting with you within a wide range of topics was the most pleasure time during my three years, and I learnt a lot from you. Thanks to the members of "geocell" research group: Mr. Tomoharu Mera, Mr. Yudai Otsuka, Mr. Hirotoshi Miyamoto. Thanks to other members: Mr. Yohei Koike, Mr. Kenta Uemura, Mr. Itsuro Arai, Miss Yuki Umehara. I also express my sincere gratitude to all members not list above. I wish all the wishes for the bright life for them. All the people in Kiyota laboratory contributed to an extremely nice laboratory atmosphere, which make me comfortable and enjoyable during three years' study.

I would like to thank my host family in Japan, the Kubota family and his wife who considered me as part of their family and supported me morally, and my friends from Japan, China, UK, Hong Kong, etc. who were and are a great source of strength.

I sincerely acknowledge the China Scholarship Council, for providing the financial assistance for my three year's study in Japan.

Last but not least, I would like to express my deepest gratitude to all my family members for their never-ending support and encouragement during my whole course of study. This thesis and my future achievements are all dedicated to them with genuine appreciation and respect.

Tokyo in September 2014

TABLE OF CONTENTS

CHAPTER 3: TESTING APPARATUSES, MATERIALS AND PROCEDURES

CHAPTER 4: EVALUATION ON THE PULLOUT CHARACTERISTICS OF NEWLY-DEVELOPED GEOCELL

CHAPTER 5: SEISMIC PERFORMANCE OF GRS RWS WITH NEWLY-DEVELOPED GEOCELL

CHAPTER 6: CONCLUSIONS AND RECOMMENDATIONS

CHAPTER 7: APPENDIXES

LIST OF TABLES

CHAPTER 2

CHAPTER 3

CHAPTER 4

CHAPTER 5

LIST OF FIGURES

CHAPTER 1

CHAPTER 2

CHAPTER 3

CHAPTER 4

CHAPTER 5

CHAPTER 7

1 INTRODUCTION

1.1 Background

Worldwide, geosynthetic-Reinforced Soil (GRS) structures have been widely used for embankments, retaining walls, bridge abutments etc. GRS structures have merits such as simple construction, lower cost and are environmentally-friendly compared to conventional concrete structures. Koerner et al. (1998) reported that the cost of GRS retaining walls (GRS RWs) was typically less than half that of conventional gravity-type retaining walls. In addition, a large number of GRS structures were constructed in seismically-active areas and exhibited high seismic resistance during past major earthquakes. For example, as shown Fig. 1.1, the high performance of a reinforced soil structure in Yamamoto town (Miyagi prefecture, Japan) during the 2011 off the Pacific Coast of Tohoku Earthquake (henceforward simply referred to 2011 Tohoku Earthquake) confirmed the high seismic stability of GRS compared to unreinforced soil structure.

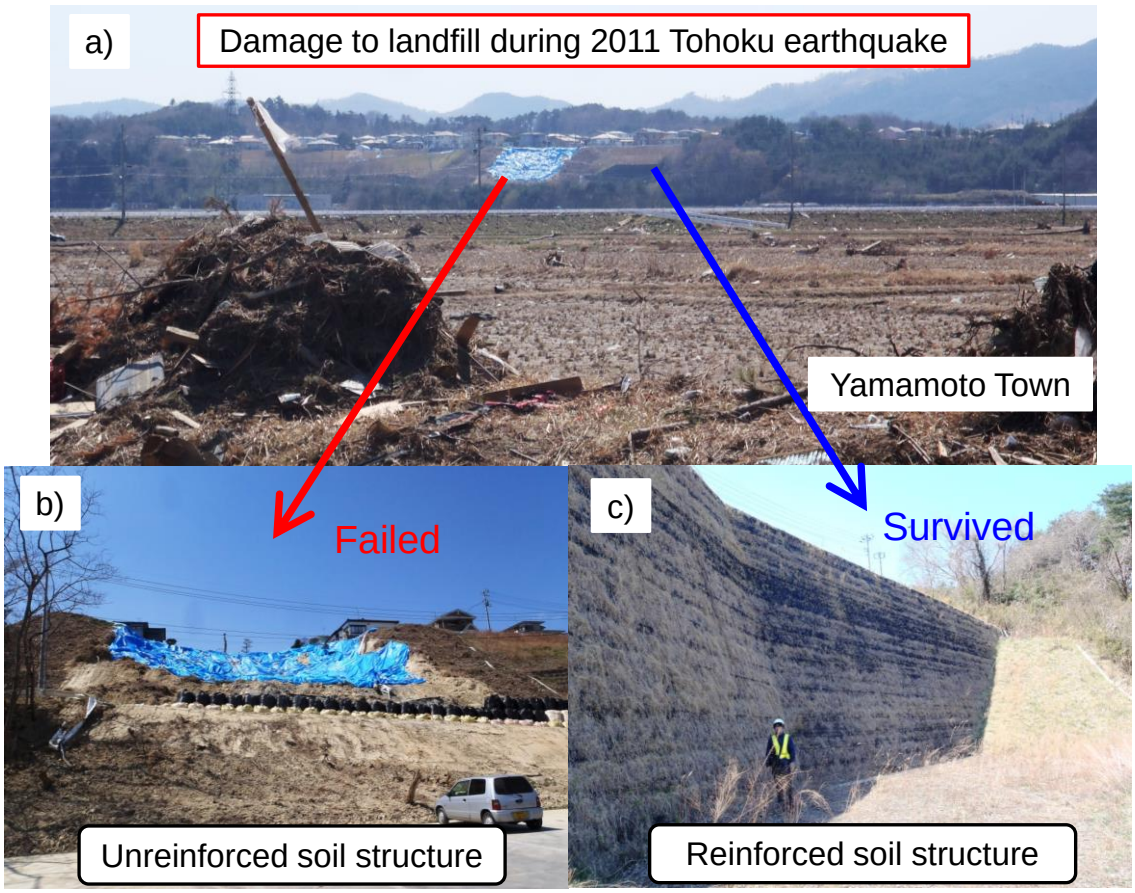

Fig. 1.1 a) Damage to landfill during the 2011 Tohoku Earthquake in Yamamoto Town, Japan; b) a collapsed unreinforced soil structure; c) survived reinforced soil structure (by the courtesy of Kiyota Laboratory, Institute Industrial of science, The University of Tokyo)

1.1.1 A brief introduction to GRS RWs with a FHR facing

In Japan, GRS RW with a stage-constructed full-height rigid (FHR) facing was developed in the late 1990's and is now the standard RW construction technology for railways including bullet train lines, replacing traditional type RWs (i.e. gravity type and cantilever reinforced concrete RWs) (Tatsuoka et al., 1997a, 2007, 2012, 2013). Up to 2013, this new type of GRS RW has been constructed in more than 980 sites and the total wall length is around 150 km (Tatsuoka et al., 2014). So far, due to its high seismic resistance, no problematic case (i.e. damage or failure) has been reported during past major earthquakes, such as the 1995 Kobe earthquake and the 2011 Tohoku Earthquake, while a large number of traditional type RWs fully collapsed during these severe earthquakes and other strong ones.

Tatsuoka et al. (1997a, 2007, 2012, 2013, and 2014) provides the details of construction procedures and the basic characteristics of GRS RW with a FHR facing. The staged construction method (Fig. 1.2, Tatsuoka et al., 2009) consists of the following steps:

1) A small foundation for FHR facing is constructed;

2) The GRS RW is constructed with gravel-filled gabions placed at the shoulder of each soil layer;

3) A thin and lightly steel-reinforced concrete facing (FHR facing) is cast-in-place adjacent to the wrapped-around wall face, (only after major deformation of the backfill soil and subsoil is completed), which provides a good connection between the FHR facing and reinforcement layers;

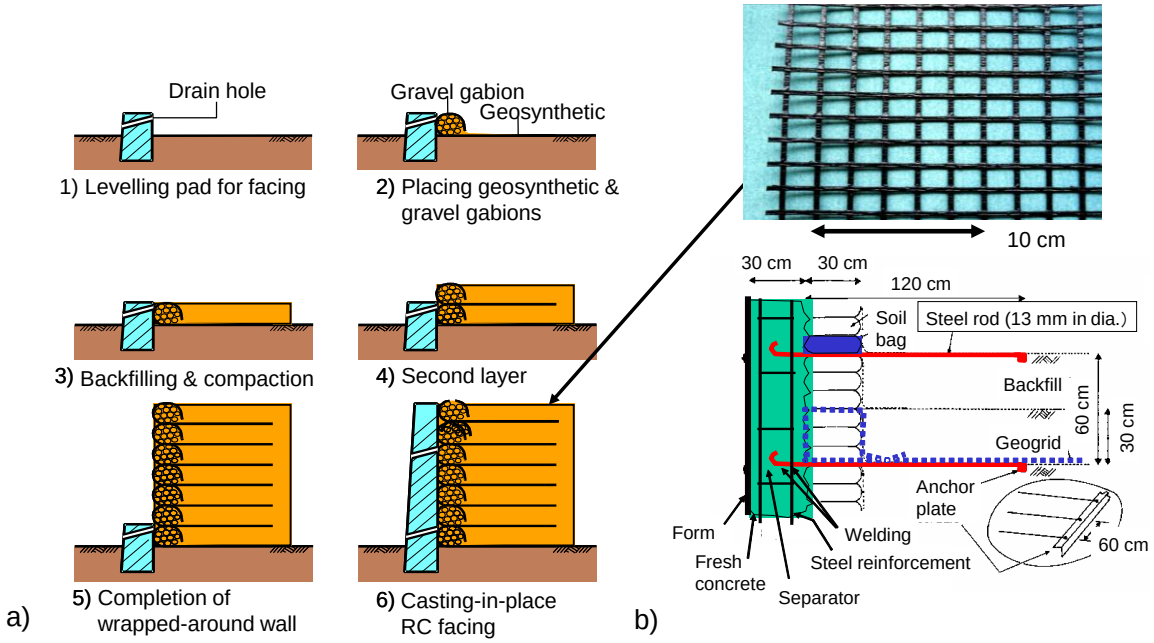

Fig. 1.2 Staged construction of a GRS RW: a) Construction procedures; b) Details of connection between the facing and the reinforced backfill (adopted from Tatsuoka et al., 2009).

Basic characteristics of GRS RW with a FHR facing (Tatsuoka et. al., 2007) are summarized hereafter:

FHR facing

The FHR facing works as a continuous beam and the reinforcement layers act as a small span to support this continuous beam at regular intervals (i.e. 30 cm) (Fig. 1.3b), which results in a small overturning moment and lateral thrust force acting on the facing base. There is no need for pile foundations in usual cases. While traditional type RW basically work as a cantilever structure (Fig. 1.3a), they often require pile foundations, since large overturning moment and lateral thrust force may concentrate at the toe of the wall. Moreover, the FHR facing effectively prevents local failure in the reinforced backfill zone and in the facing itself (i.e. structural collapse of the discrete panel facing).

Connection between FHR facing and reinforcement layers

Firm connection between the FHR facing and reinforcement layers ensures that relatively large earth pressures can be activated at the back of the FHR facing, resulting in high confining pressures in the backfill associated with high tensile stress in the reinforcements, therefore, high stiffness and strength of the backfill.

Geosynthetic reinforcements

Geogrid reinforcement is used for cohesionless soils to ensure good interlocking, and a composite of non-woven and woven geotextiles is used for cohesive soil to provide better drainage and tensile resistance of the backfill. Furthermore, relatively short reinforcements are required for the stability of GRS RW with FHR facing compared with metal strip reinforcement for RWs with discrete panel facing, since planar reinforcement has a relatively short anchorage length to activate the tensile rupture strength.

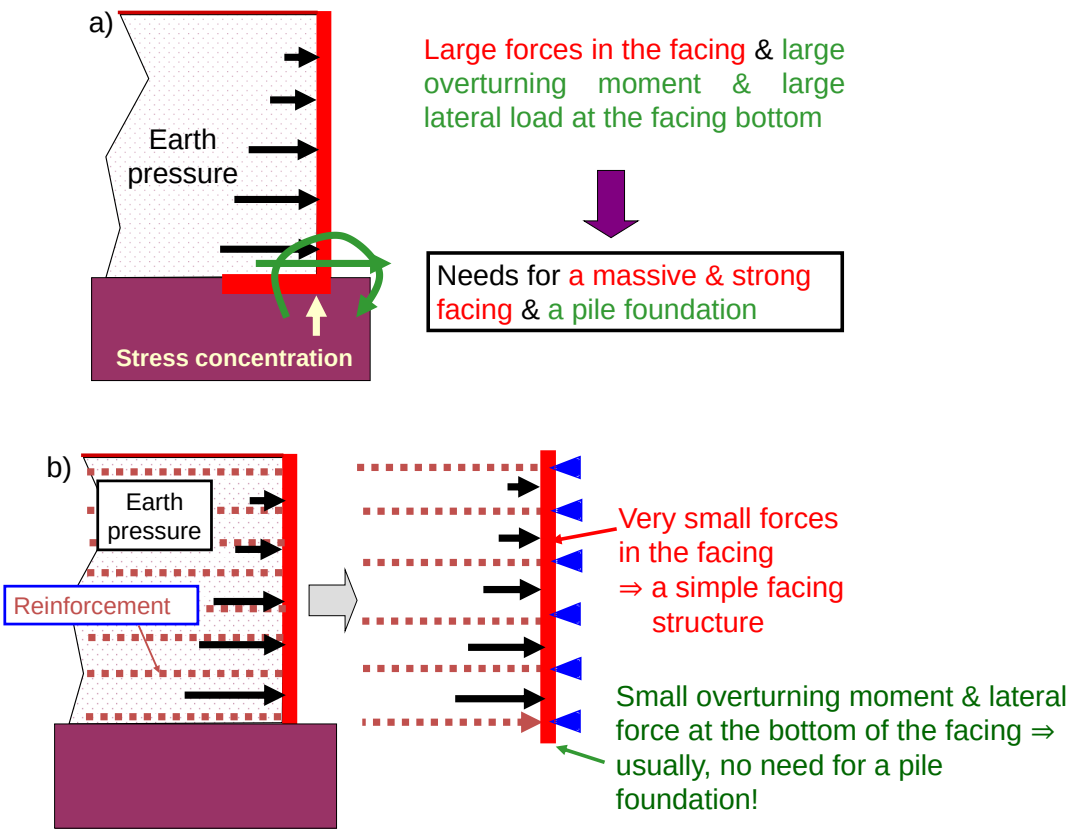

Fig. 1.3 a) Traditional type RW as a cantilever structure; b) GRS RW with a FHR facing as a continuous beam supported at many points with a small span (adopted from Tatsuoka et al., 2007).

1.1.2 Seismic performance of GRS RWs with a FHR facing: Case history and laboratory testing

Due to the excellent features, high seismic performance of GRS RW with a FHR facing has been demonstrated by both field case history and physical model tests.

Tatsuoka et al. (1995, 1996, 1997b) reported that a large number of conventional type RWs, such as gravity-type RW, leaning-type RW and cantilever-type RW were seriously damaged, while GRS RWs with a FHR facing performed very well during the severe 1995 Kobe Earthquakes (Mw = 7.3). Sandri (1997) conducted a review on geogrid-reinforced segmental RWs in the Los Angeles area immediately after the 1994 Northridge Earthquake (Mw = 6.7), revealing the excellent performance of geogrid-reinforced segmental RWs compared to the collapsed cantilever RWs. However, Ling et al. (2001) and Huang (2000) conducted a post-earthquake survey around the central Taiwan region after the 1999 Chi-chi Earthquake (Mw = 7.3), and found that several GRS RWs (i.e. geogrid-reinforced segmental RWs) were damaged. Such damage was primarily associated with the deformation of the segmental blocks via sliding, toppling and bulging, which confirmed the importance of good connection between the facing wall and the reinforcements (i.e. using a FHR facing).

Shaking table model tests have been often used to qualitatively and quantitatively evaluate the seismic performance of reinforced soil structures. Matsuo et al. (1998) presented the results of a series of shaking table model tests on GRS RWs models. The influential factors on the seismic behavior or failure mechanisms of GRS RWs, such as the geogrid reinforcement length, wall height, wall facing type, wall slope and the input acceleration waveform were examined. It was found that the horizontal displacement at the top of a wall with a rigid facing was larger than the corresponding displacement of a wall with segmental facing. This was an unexpected result, which is possibly due to the difference in mass between the rigid facing and segmental facing. Koseki et al. (1998) carried out shaking table and tilt table tests on small-scale models of a GRS RWs with a FHR facing and conventional type (gravity-type, leaning type, and cantilever-type), showing that the major failure mode of both conventional-type RWs and GRS RWs was overturning. In addition, for GRS RWs, the reinforced backfill experienced simple shear deformation, which can be included in displacement calculation for GRS RWs. Koseki et al. (1998) also pointed out that the effects of post-peak reduction of the shear resistance along the failure should also be considered in the design of RWs. Watanabe et al. (2003) conducted a series of shaking table model tests on conventional type (cantilever

type, gravity-type, leaning-type) RWs and GRS RWs with a FHR facing. It was found that GRS RWs with a FHR facing showed more ductile behavior than other types of RWs. Different failure mechanisms on different types of RWs were observed: when the conventional type RWs started to tilt, the subsoil reaction force at the toe of wall suddenly decreased due to the loss of bearing capacity, while the tensile force in the reinforcement of GRS RWs was mobilized effectively to resist overturning. It was also suggested that using longer reinforcement at the wall crest can improve the seismic performance of the structure. Nakajima et al. (2008) investigated the effects of material properties (i.e. pullout resistances, rupture strength and tensile rigidities) of reinforcements on the seismic performance of reinforced soil retaining walls, showing that larger pullout resistance mobilized at relatively small pullout displacements range would work effectively to reduce the tilting angle of the wall facing. Later, based on a series of shaking table model tests on GRS RWs with a FHR facing, Nakajima et al. (2010) also found that the effects of 1) subsoil and backfill deformation, 2) failure plane formation in backfill, and 3) pullout resistance by reinforcements on the seismic performance of GRS RWs with a FHR facing were significant. Accordingly, Nakajima et al. (2010) developed a simplified procedure to evaluate the residual displacements of the GRS RWs with a FHR facing by considering the aspects mentioned above.

1.1.3 Other applications on GRS RWs with a FHR facing

Based on the technology, other applications of GRS RWs with a FHR facing have been reviewed by Koseki (2006, 2011).

Further combination with other types of reinforcements

Kato et al. (2002) and Nakajima et al. (2007) proposed a GRS RWs with a FHR facing constructed on the slope enhanced by installing soil nails below the base of the facing. Nakajima et al. (2006) improved the seismic stability of GRS RWs with a FHR facing by installing a sheet pile connected to the foot of the facing.

Further improvement of the backfill soil properties

Aoki et al. (2003) proposed a new type of bridge abutment using cement-treated gravel backfill for GRS RWs with a FHR facing to improve its seismic resistance, and it has been constructed for the new bullet train in Kyushu Island (Aoki et al. 2005).

GRS integral bridge

Recently, based on the technology of GRS RWs with a FHR facing, a new type of bridge called GRS integral bridge (Fig. 1.4, Tatsuoka et al., 2009, 2012, 2013 and 2014) was developed to alleviate the problems of traditional type bridges, integral bridges and GRS RW bridges. It was constructed by a continuous girder integrated to a pair of abutments without using bearings, and the backfill reinforced with geosynthetic reinforcements firmly connected to the back facings of the abutments. This is a combination of the integral bridge and the GRS-RW bridge technologies, taking advantage of their excellent features while alleviating their drawbacks. The detailed characteristics of the GRS integral bridge has been introduced by Tatsuoka et al. (2009). Based on model test results, Tatsuoka et al. (2009) summarized the load and resistance components for the facing rotation relative to the backfill for GRS integral bridges, as shown in Fig. 1.5. Two major resisting components against the large earthquake-induced inertial force resulting from the heavy superstructure (i.e. girder) were found: (1) the passive pressure in the upper part of the backfill; and (2) the tensile force of the reinforcement at the lower part of the facing. The factor (1) can be enhanced by the cement-treatment method, while factor (2) is the minimum value among the connection strength, the tensile rupture of the reinforcement and the pullout resistance of the reinforcement.

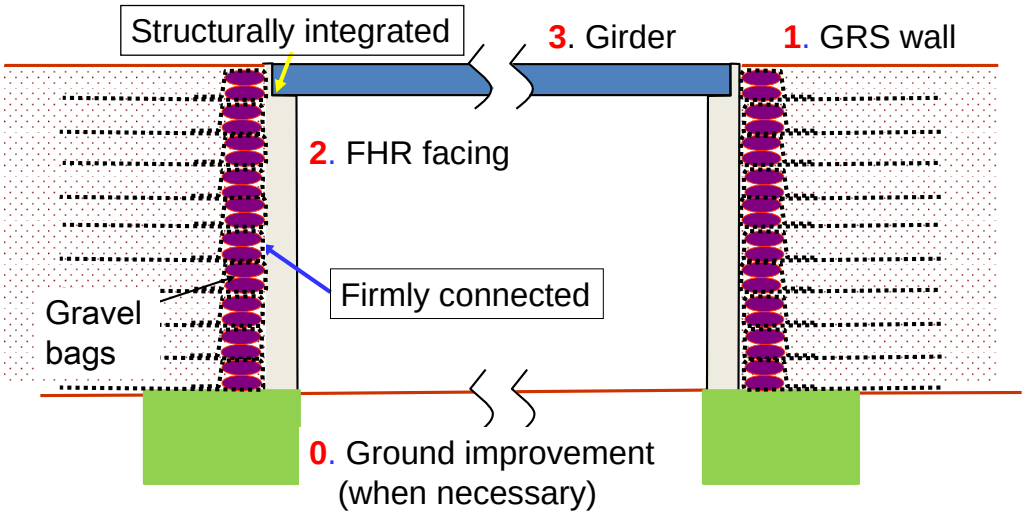

Fig. 1.4 Schematic diagram of GRS integral bridge (adopted from Tatsuoka et al., 2009).

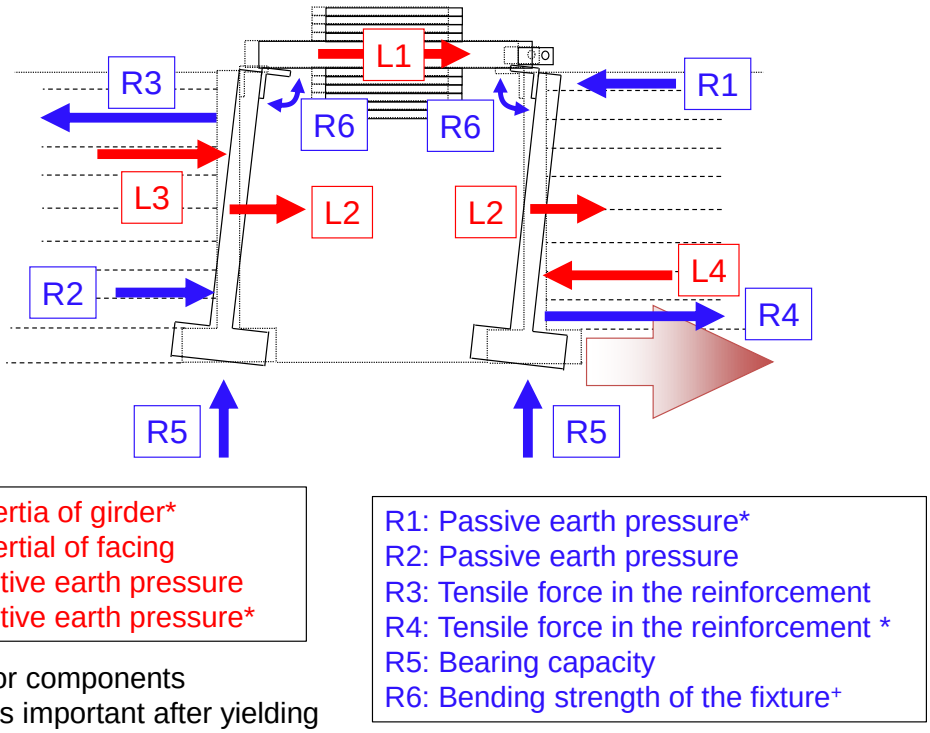

Fig. 1.5 Load and resistance components for GRS integral bridge (adopted from Tatsuoka et al., 2009).

1.2 Research objectives and scope of study

Based on the literature review on GRS RWs with a FHR facing previously described, it is clear that the seismic performance of GRS RWs with a FHR facing can be improved by the following two aspects: 1) soil reinforcement methods, e.g. further combination with large diameter nails (Kato et al., 2002 and Nakajima et al., 2007) or sheet pile (Nakajima et al., 2006); and 2) soil improvement methods, such as cement-treatment of the reinforced backfill. This research aims at the first method- soil reinforcement technique.

As well-known, to achieve a high seismic stability of GRS RWs or GRS integral bridges, high tensile resistance of the reinforcement layers at the back of facing wall is very crucial. Geogrids, as shown in Fig. 1.2, are commonly used as planar reinforcement to tensile-reinforce the backfill of RWs. However, GRS RWs with geogrids may encounter the following potential problems:

1) In Japan, geogrid reinforcement requires the use of high-quality backfill soil (i.e. well-compacted sandy soils) to ensure good interlocking of soil particles within the aperture of the geogrid. Although some low-quality soils can be improved by the cement-treatment method, usually locally available and economic soils, which may also be poorly-graded or include larger particles, are inevitably used as backfill. This may result in a decrease in its deformability, since the bond stress along the interface between the geogrid and the backfill becomes lower than the shear strength of the backfill to a larger extent with an increase in the backfill soil particle size.
2) For other GRS structures such as GRS integral bridges (Figs. 1.4 and 5), due to heavy girder structures, a larger earthquake-induced inertial force would be activated, requiring the reinforcement to provide a higher pullout resistance.

In order to minimize these problems and improve the overall seismic performance of GRS RWs or GRS integral bridges, the following objectives were identified in this thesis:

1) Develop a tensile reinforcement that can confine large soil particles and provide large pullout resistance;
2) Evaluate the tensile function of this newly-developed reinforcement compared with traditional-type reinforcements (i.e. geogrids) based on laboratory pullout tests;

3) Investigate the pullout interaction mechanisms between the newly-developed reinforcement and the adjacent soil, considering the effects of backfill soil particle size
4) Propose a practical construction method for the application of this newly-developed reinforcement in GRS RWs
5) Evaluate the seismic performance of GRS RWs with the newly-developed reinforcement by shaking table model tests

1.3 Organization of the thesis

This thesis is composed of the following chapters:

In Chapter 1, the background of the proposed research is described and relevant previous studies are critically reviewed. The objectives of this study and the outline of this thesis are defined.

In Chapter 2, the newly-developed reinforcement called square-shaped geocell is described. Differences between the newly-developed square-shaped geocell and traditional type reinforcements (i.e. diamond-shaped geocell and ordinary commercial geogrid) are presented. Typical practical application of traditional type reinforcements and related research are also reviewed from previous literatures.

Chapter 3 describes in detail the methodology adopted in this thesis, with specific reference to the laboratory pullout tests and shaking table model tests. In particular, Section 3.2 introduces the pullout apparatus (newly-developed in Kiyota Laboratory, Institute of Industrial Science (IIS), the University of Tokyo), the pullout testing procedure and testing materials. Section 3.3 describes the shaking table facility (IIS, University of Tokyo), the employed model wall (i.e. model wall facing), reinforcements and clamps, backfill and foundation materials. The instrumentation (e.g. accelerometers, displacement transducers, earth pressure gauges etc.) used to measure the dynamic model wall response and seismic loading method is also described. Details of the construction procedures of the wall models are finally presented.

In Chapter 4, evaluation of the tensile characteristics of the newly-developed square-shaped geocell is conducted by laboratory pullout tests. Section 4.2 compares the pullout behavior of square-shaped geocell and that of traditional diamond-shaped geocell. On the other hand, Section 4.3 compares the pullout behavior of square-shaped geocell with that of ordinary commercial geogrid. Based on these test results, the basic pullout mechanisms among square-shaped geocell, diamond-shaped geocell and geogrid are identified. In Section 4.4, the drawbacks of square-shaped geocell are discussed and corresponding improvement measures are suggested for construction work. In Sections 4.5 and 4.6, possible combined effects of geocell height and particle size of backfill soil on interface mechanisms between the geocell and adjacent backfill soil are also investigated. A conceptualized pullout interaction mechanism is proposed based on the test results. Other influential factors, such as the spacing

between transversal members of square-shaped geocell reinforcement, on the pullout resistance of square-shaped geocell are also investigated.

In Chapter 5, evaluation of the seismic performances of geocell-RS RWs, geogrid-RS RWs and conventional type RWs backfilled with sand or gravel is carried out by shaking table model tests. Section 5.2 presents typical test results for each case study and the corresponding deformation modes obtained through image analysis. The seismic performance of each wall model is investigated in Section 5.3 based on the evaluation of the residual deformation of the wall, the settlement of the backfill soil, the acceleration response of the wall and backfill soil, and the critical acceleration. In Section 5.4, a simplified analysis of the dynamic stability of various types of wall models is conducted under the framework of a single-degree-of-freedom.

Chapter 6 is dedicated to the major conclusions of this research and recommendations for future research.

1.4 References

1. Aoki, H., Watanabe, K., Tateyama, M. and Yonezawa,T. (2003). "Shaking table tests on earthquake resistant bridge abutment", Proc. of 12th Asian Regional Conf. on Soil Mechanics and Geotechnical Engineering, 1, 267-270.
2. Aoki, H., Yonezawa,T., Tateyama, M. Shinoda, M. and Watanabe, K. (2005). "Development of a seismic abutment with geogrid-reinforced cement-treated backfills", Proc. of 16th International Conf. on Soil Mechanics and Geotechnical Engineering, 3, 1315-1318.
3. Huang, C.C. (2000). "Investigations of the damaged soil retaining structures during the Chi-Chi earthquake", Journal of the Chinese Institute of Engineers, 23(4), 417-428.
4. Kato, N., Huang, C.C., Tateyama, M., Watanabe, K., Koseki, J. and Tatsuoka, F. (2002). Seismic stability of several types of retaining walls on sand slope, Proc. of 7th International Conference on Geosynthetics, Nice, 1, 237-240.
5. Koener, R.M. (1998). "Designing with Geosynthetics", 4th Edn., Prentice-Hall, Englewood Cliffs, NJ.
6. Koseki, J., Munaf, Y., Tatsuoka, F., Tateyama, M., Kojima, K. and Sato, T. (1998). "Shaking and tilt table tests of geosynthetic-reinforced soil and conventional-type retaining walls", Geosynthetics International, Vol. 5, Nos. 1-2, pp. 73-96.
7. Koseki, J., Bathurst, R.J., Güler, E., Kuwano, J., and Maugeri, M. (2006). "Seismic stability of reinforced soil walls", Proc. of the 8th International Conference on Geosynthetics, Yokohama, Japan, 51-77.
8. Koseki, J. (2011). "Use of geosynthetics to improve seismic performance of earth structures", Proc. of the 15th African Regional Conference on Soil Mechanics and Geotechnical Engineering, Athens, Greece, 1, 40-60.
9. Ling, H. I., Leshchinsky, D., and Chou, N. N. S. (2001). "Post-earthquake investigation on several geosynthetic-reinforced soil retaining walls and slopes during the ji-ji earthquake of Taiwan." Soil Dynamics and Earthquake Engineering, 21(4), 297-313.
10. Matsuo, O. Tsutsumi, T., Yokoyama, K. and Saito, Y. (1998). "Shaking table tests and analyses of geosythetic-reinforced soil retaining walls", Geosynthetics International, 5(1&2), 97-126.
11. Nakajima, S., Koseki, J., Watanabe, K., Tateyama, M. and Kato, N. (2006). "Shaking table model tests on geogrid reinforced soil retaining wall with embedded sheet pile", Proc.of 8th International Conference on Geosynthetics, Yokohama, 4, 1507-1510.
12. Nakajima, S. Koseki, J. Tateyama, M. and Watanabe, K. (2007). "Shaking table model tests on retaining walls reinforced with soil nailings", New Horizons in Earth Reinforcement, Taylor and Francis, 707-712.
13. Nakajima, S., Hong, K., Mulmi, S., Koseki, J., Watanabe, K. and Tateyama, M. (2008). "Study on seismic performance of geogrid reinforced soil retaining walls and deformation characteristics of backfill soil", Proc. of the 4th Asian Regional Conference on Geosynthetics, Shanghai, China, 211-216.
14. Nakajima, S., Koseki, J., Watanabe, K., and Tateyama, M. (2010). "Simplified procedure to evaluate earthquake-induced residual displacement of geosynthetic reinforced soil retaining walls", Soils and Foundations, 50(6), 659-678.

15. Sandri, D. (1997). "Performance summary of reinforced soil structures in the Greater Los Angeles area after the Northridge earthquake", Geotextiles and Geomembranes, 15(4-6), 235-253.
16. Tatsuoka, F., Tateyama, M., Koseki, J. and Uchimura, T. (1995). "Geotextile-reinforced soil retaining wall and their seismic bahaviour", Proc. of 10th Asian Regional Conf. on Soil Mechanics and Foundation Engineering, Beijing, 2, 26-49.
17. Tatsuoka, F., Tateyama M. and Koseki, J. (1996). "Performance of soil retaining walls for railway embankments", Soils and Foundations, Special Issue of Soils and Foundations on Geotechnical Aspects of the January 17 1995 Hyogoken-Nambu Earthquake, 311-324.
18. Tatsuoka, F., Tateyama, M, Uchimura, T. and Koseki, J. (1997a). "Geosynthetic-reinforced soil retaining walls as important permanent structures". Mercer Lecture, Geosynthetic International, Vol.4, No.2, pp.81-136.
19. Tatsuoka, F., Koseki, J. and Tateyama, M. (1997b). "Performance of reinforced soil structures during the 1995 Hyogoken-Nanbu Earthquake", Earth Reinforcement, Balkema, 2, 973-1008.
20. Tatsuoka, F., Tateyama, M., Mohri, Y. and Matsushima, K. (2007). "Remedial treatment of soil structures using geosynthetic-reinforcing technology". Geotextiles and Geomembranes, 25 (4 & 5): 204-220.
21. Tatsuoka, F., Hirakawa, D., Nojiri, M., Aizawa, H., Nishikiori, H., Soma, R., Tateyama, M. and Watanabe, K. (2009). "A new type of integral bridge comprising geosynthetic-reinforced soil walls", Geosynthetics International, 16(4), 301-326.
22. Tatsuoka, F., Tateyama, M., Koseki, J. (2012). "GRS structures recently developed and constructed for railways and roads in japan", Proc. of 2nd International Conference on Transportation Geotechnics (ICTG), Hokkaido, Japan, pp 63-85.
23. Tatsuoka, F., Tateyama, M., Koda, M., and Koseki, J. (2013). "Seismic design, construction and performance of geosynthetic-reinforced soil retaining walls and bridge abutments for railways in japan", Geo-Congress 2013: pp. 1143-1157.
24. Tatsuoka, F., Tateyama, M., Koda, M., Watanabe, K., Koseki, J., Aoki, H., and Yonezawa, T. (2014). "Design, construction and performance of GRS structures for railways in Japan", Proc. of 10th International Conference on Geosynthetics, Berlin.
25. Watanabe, K., Munaf, Y., Koseki, J., Tateyama, M. and Kojima, K. (2003). "Behaviors of several types of model retaining walls subjected to irregular excitation", Soils and Foundations, 43(5), 13-27.

2 DEVELOPMENT OF A NEW TYPE OF GEOCELL

2.1 Introduction

Geocell, as a three-dimensional soil confinement system, has the ability to confine large soil particles. Thus, it has more attractive features than other planar reinforcement (i.e. geotextiles and geogrids). Common type geocells (named diamond-shaped geocells in this thesis) have a diamond in-plane shape and are usually used as a base reinforcement to support roads, embankments, and lighthouses.

In this chapter, aiming at the objectives stated in Chapter 1 (i.e. the development of a tensile reinforcement for GRS RWs which can confine large soil particles and provide large pullout resistance), a new type of geocell, namely square-shaped geocell, was developed as an effective tensile reinforcement for GRS RWs. Detailed description of this newly-developed geocell as well as discussion of its potential advantages as tensile-reinforcement for RWs, compared to diamond-shaped geocell and traditional-type tensile reinforcement (i.e. geogrid) for GRS RWs are given in Section 2.2. In Section 2.3, the tensile function of the geogrid by pullout tests is firstly discussed. The current state-of-the-art interaction mechanisms between geogrid and soil are addressed. Secondly, a detailed description of traditional type geocell (i.e. diamond-shaped geocell) and its applications as a base reinforcement are presented. Related research regarding traditional type geocell are critically reviewed. Lastly, other types of soil tensile-reinforcements for the RWs are also introduced.

2.2 Description of a newly-developed geocell: square-shaped geocell

Figure 2.1 shows a typical configuration of the newly-developed square-shaped geocell. For the sake of comparison, traditional-type diamond-shaped geocell is shown in Fig. 2.2.

The square-shaped geocell is constituted of straight longitudinal members with transversal walls at separated locations, forming square confinement cells. For the prototype used in the laboratory testing, both longitudinal and transversal wall members were made of polypropylene (PP) or High-Density-Polyethylene (HDPE) in strips approximately 250 mm wide and 1.2 mm thick. The transversal wall members are welded at separate locations towards the longitudinal members along their 250 mm width. The size of each cell is 600 mm in the longitudinal direction and 500 mm in the transversal direction. Then they are filled with sand or gravel and compacted using a vibratory hand-operated plate compactor. It is important to remark that, in real projects, the size of each cell and the height of square-shaped geocell should be carefully determined based on available local backfill materials, the design specifications, loading conditions, etc.

The square-shaped geocell used as a tensile reinforcement for GRS RWs may have the following advantages:

- Compared to diamond-shaped geocell, the longitudinal members of the square-shaped geocell are straight to enhance high pullout pre-peak stiffness, allowing a low modulus materials for the manufacturing purpose.
- Compared to planar reinforcements such as geogrids:

(1) The three-dimensional structure of the geocell allows the confinement of soil with larger particles, which makes possible the use of locally available and economic large-particle soils.

(2) The increased height of transversal wall members can produce higher pullout bearing resistance rather than the resistance relying only on the friction or interlocking between soil and planar reinforcements, which can further improve the seismic stability of GRS RW.

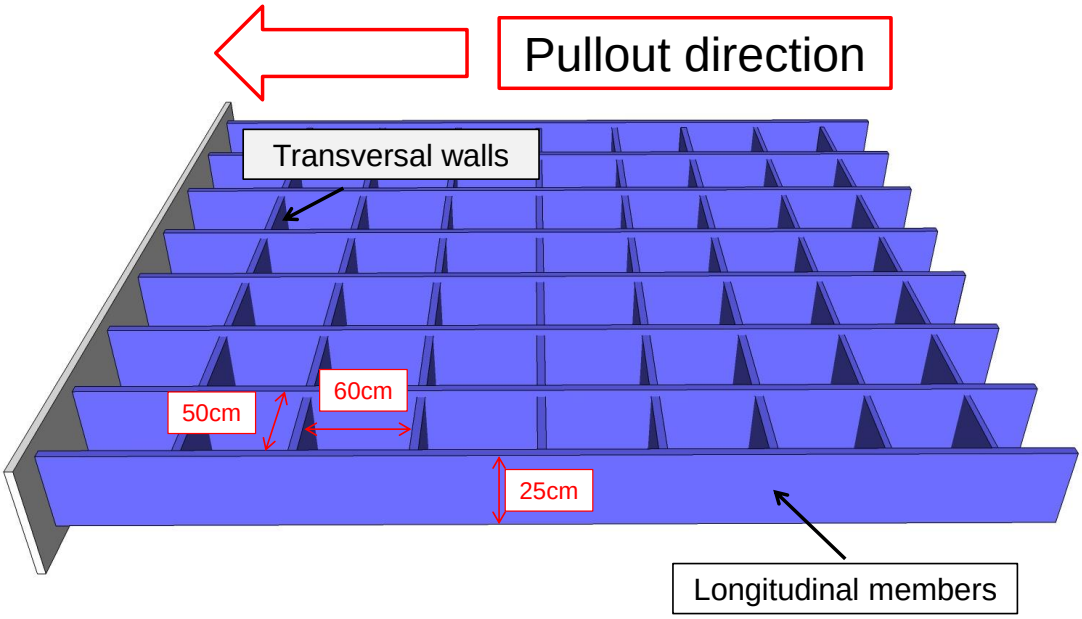

Fig. 2.1 Typical configuration of newly-developed square-shaped geocell

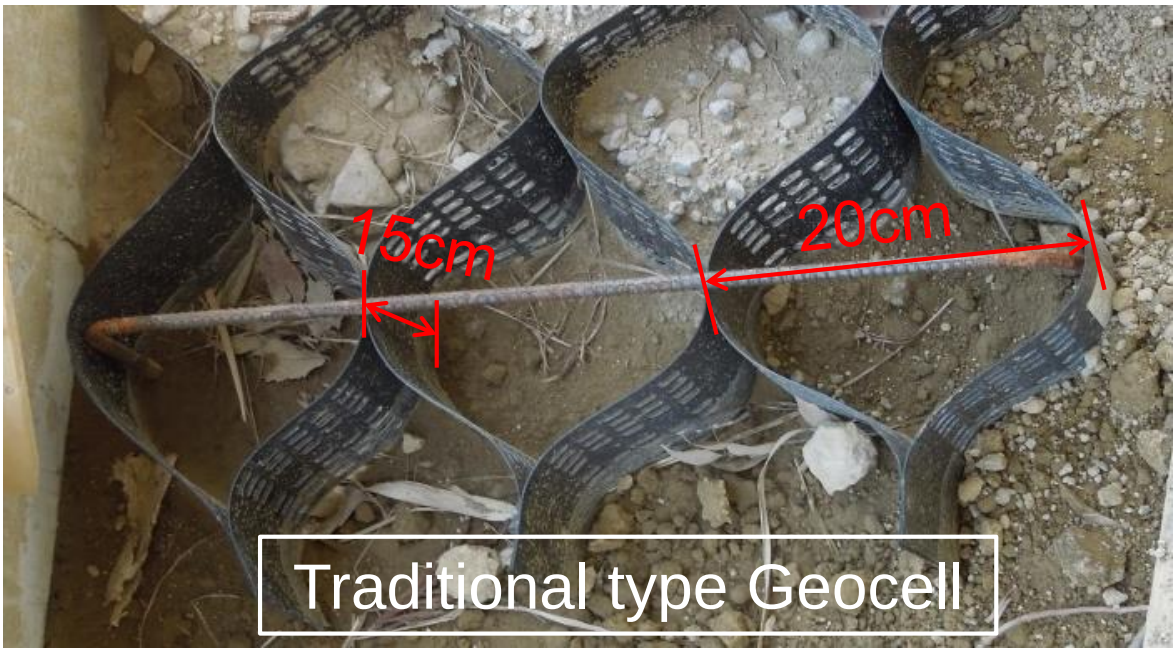

Fig. 2.2 Traditional diamond-shaped geocell

2.3 Traditional type reinforcements

2.3.1 Geogrid reinforcements

Geogrids have been widely used as base reinforcement to provide confinement and increase the bearing capacity of earth-structures. For comparison purposes, the application of geogrids as tensile reinforcement for retaining walls is of great interest in this current research and, thus, is reviewed hereafter.

Experimental studies

Tatsuoka et al. (2007) pointed out that, as planar reinforcements, when geogrids are used to tensile-reinforce the backfill of RWs, cohesionless soil is often required to ensure good interlocking between soil particles and geogrid, therefore high pullout resistance. Pullout tests are relevant for the study of the tensile performance of geogrid reinforcement and the interaction mechanisms between geogrid reinforcement and soils.

Nishikiori et al. (2007 and 2008) conducted a series of pullout tests using different types of phosphor-bronze grids and other different types of commercial geogrids backfilled with Toyoura sand with relative density of 90% under surcharge of 1 kPa and 30kPa, respectively. Fig. 2.3 and Table 2.1 summarize the tests results and test cases, from which the general conclusions can be derived: the pullout resistance increases with an increase in: 1) the covering ratio and surface roughness of the longitudinal members of the grid; and 2) the thickness of transversal members of the grid. The peak resistance by the surface friction (factor 1) tends to be mobilized earlier than the passive pressure resistance (factor 2).

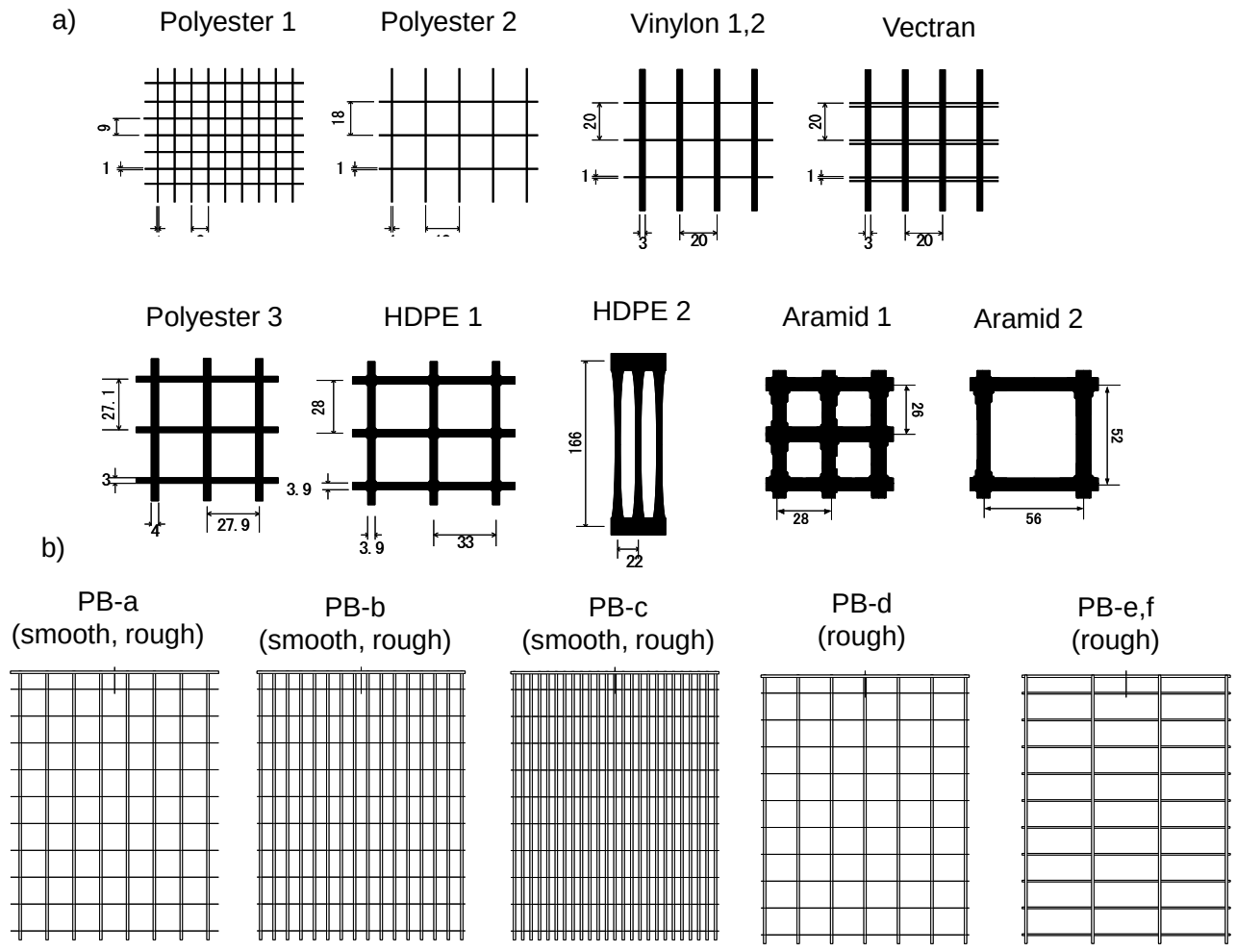

Fig. 2.3 a) Polymer geosynthetics and b) phosphor-bronze grids (adopted from Nishikiori et al., 2007 and 2008).

Table 2.1 Pullout resistances of different reinforcements (adopted from Nishikiori et al., 2007 and 2008).

Reinforcement	Covering ratio	Thickness	Transversal members	Longitudinal members			φ_{dst} from direct shear test [deg.]	Pullout strength T [kN/m] for normal stress of	
	CR[%]	t[mm]	Strand number	Strand number	Ruperture tensile strength in air at a rate of 1%/sec, T [kN/m]	Stiffness at ε= 1% E_1[kN/m]		3.35kPa	32.35kPa
Polyester 1	20.3	1	47	27	43.3	477	30	2.4	10
Polyester 2	10.6	1	25	14	21.7	239	30	2.3	8 (break)
Vinylon 1	23.3	1	24	15	85.8	1348	29.9	2.6	12.5
Vinylon 2	19.5	1	24	15	52.5	102	29.9	2.7	14
Vectran	25.1	1	26	15	91.5	471	-	3	12
HDPE1	25.9	5	16	10	35	1264	21.1	2.6	14.5
HDPE2	28.3	3	4	13	50	673	21.2	2.3	8
Poylester 3	25.8	1.5	20	10	48.7	356	30	2.9	14
Aramid 1	47.9	4.4	18	10	56	1350	16.7	2.7	15.5
Aramid 2	24	4.4	9	5	28	675	16.7	3	14.5
PB-a smooth	10.6	0.5	15	8	10.6	2016	26.6	1.25	5.5
PB-a' rough	10.6	0.5	15	8	10.6	2016	35	1.4	-
PB-a rough	10.6	1.1	15	8	10.6	2016	35	2.25	10
PB-b smooth	19.5	0.5	15	16	24.3	4176	26.6	1.6	6.5
PB-b rough	19.5	1.1	15	16	24.3	4176	35	2.9	15
PB-c smooth	29.6	0.5	15	25	36	6480	26.6	1.6	7.5
PB-c rough	29.6	1.1	15	25	36.3	6480	35	3.2	-
PB-d rough	11.1	1.6	15	7	8.7	1656	35	2.25	9 (break)
PB-e rough	11	2.7	15	4	4.7	792	35	3.25	-
PB-f rough	11	1.7	15	4	4.7	792	35	2.3	5(break)

Minažek et al. (2013) reviewed the soil-reinforcement interaction by pullout tests and confirmed the conclusions derived by Giroud (2009), indicating that the soil-geogrid interaction mechanism can be summarized based on the following two aspects: 1) increased soil stiffness due to interlocking of the soil particles in the aperture of the geogrid; and 2) pullout resistance induced by the friction and passive resistance of the transversal members. The grid strain was required to achieve any kind of interaction. It was stressed that the soil particle interlocking in geogrid apertures can contribute to the geogrid pullout resistance.

Lopes et al. (1999) also found that the use of backfill consisting of particles having a size appropriate to be interlocked with the aperture of geogrid increases the pullout stiffness of the geogrid as well as the pullout resistance. The effect of particle size relative to the thickness of grid transversal members was investigated by Palmeira et al. (1989) and Palmeira (2008). Their results showed that the normalized bearing strength would be independent of soil particles for a ratio between member thickness and soil particle size over 12. In addition, the interference between transversal grid members was also investigated. They found that, when the ratio between the spacing of transversal members and member thickness was over 40, negligible or no interference occurred. Other aspects such as the shape and bending stiffness of transversal members were investigated by Brown et al. (2007). It was shown that a low

bending stiffness would induce a progressive mobilization of bearing resistance, therefore a low pullout resistance.

DEM simulation

The discrete element method (DEM) is a powerful tool to gain a micromechanical understanding of the interaction mechanism between geogrid and soil, and thus, optimizing geogrid-soil structure performance. Chen et al. (2014) evaluated the interlocking behavior of geogrid-reinforced railway ballasts by pullout tests and DEM simulations. The DEM simulation results provided good prediction of the pullout resistance. Interestingly, the effect of particle shape on the pullout resistance was also examined, showing that an 8-ball tetrahedral clump has more angularity and roughness and, thus, it seems to be more representative of the real ballasts. Using a DEM approach, McDowell et al. (2006) also modelled the interaction between ballast and geogrid by simulating pullout tests. They investigated the effect of the ratio between geogrid aperture size and soil particle size on the pullout resistance, which showed that the optimum ratio of 1.4 gave a higher peak pullout resistance mobilized at the smallest displacements. Tutumluer et al. (2012) carried out DEM simulations of direct shear tests on both unreinforced and geogrid-reinforced aggregates. The effects of aperture shape and size of geogrid on mechanical interlocking were investigated, suggesting that an appropriate geogrid aperture size and shape relative to aggregate size and shape, grading, and density, as well as the properties of the geogrid members can increase the stiffness around the geogrid reinforcements.

2.3.2 Geocell reinforcements

Traditional type geocell

A definition of geocell is provided by the International Geosynthetics Society (IGS) as follows:

"*Geocells are relatively thick, three-dimensional networks constructed from strips of polymeric sheet. The strips are joined together to form interconnected cells that are infilled with soil and sometimes concrete. In some cases 0.5 m to 1 m wide strips of polyolefin geogrids have been linked together with vertical polymeric rods used to form deep geocell layers called geomattresses.*"

A typical commercial geocell product, so-called diamond-shaped geocell, is shown in Fig. 2.2. The geocell is typically made of HDPE 250 mm wide and 1.2 mm thick strips. These strips are usually welded along their 250 mm strips at around 700 mm intervals. Each cell can be expanded to a diamond shape, approximately 500 mm in size, and filled with sand or gravel and compacted using a vibratory hand-operated plate compactor.

As a three-dimensional soil confinement system, traditional diamond-shaped geocell, can confine soil particles effectively in the cells, enhancing soil shear strength and increasing the bearing capacity. They have been widely applied in construction roads over soft soils, soil stabilization for embankments, and protection against erosion in steep slopes. Fig. 2.4 shows typical practical engineering applications of geocell systems to construct a reservoir and to stabilize the soil nearby bridge abutments. In recent years, geocells have been used also as the facing of retaining wall structures and steep slopes, as shown in Fig. 2.5.

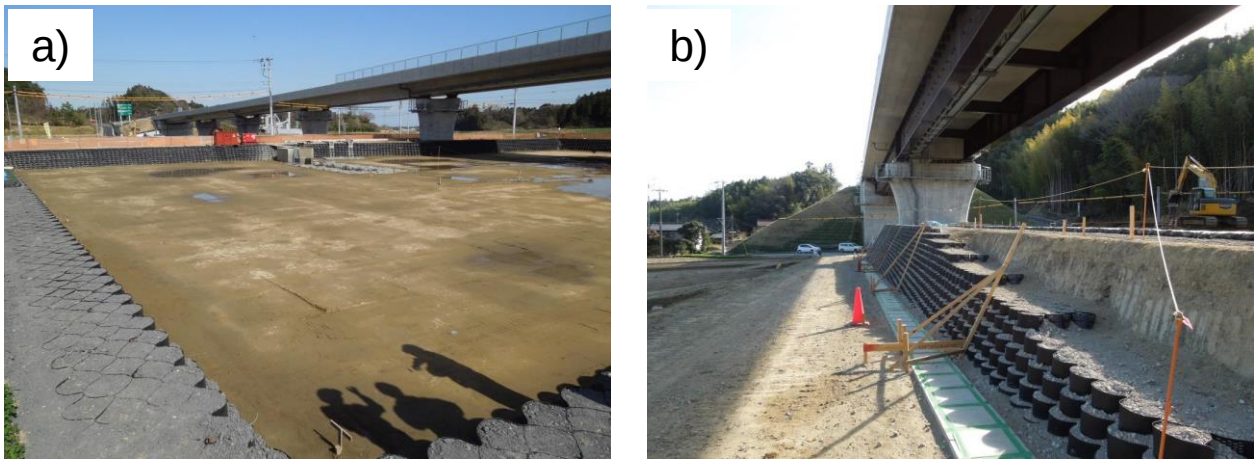

Fig. 2.4 a) Construction of reservoir using geocell systems; b) Stabilization of soils nearby bridge abutments

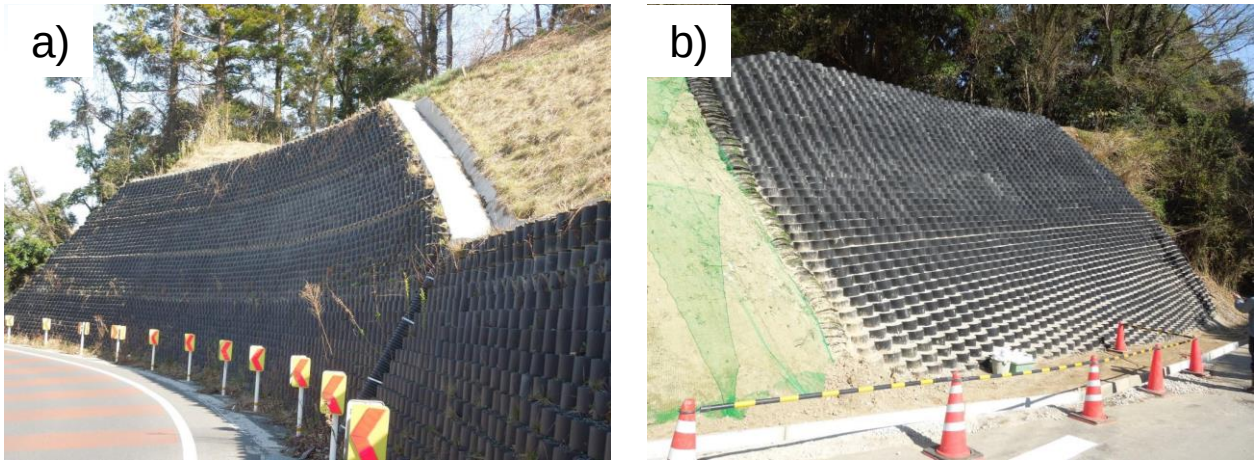

Fig. 2.5 a) Retaining wall and b) a steep slope constructed by using geocell facing

Previous research on traditional type geocell

Many studies were carried out on traditional type geocell reinforcements (i.e. diamond-shaped geocell) mainly to check their performance as base reinforcements subjected to vertical loads for roads, embankments and lighthouses. Yuu et al. (2008) reviewed the current research on the geocell-reinforced base course over weak subgrade, showing that geocells can provide exceptional soil confinement and enhance the performance of the base course on weak subgrade. Bathurst et al. (1993), Rajagopal et al. (1999) and Mengelt et al. (2006) conducted triaxial compression tests to investigate the confinement effect of a single geocell or multiple geocells. Many laboratory model tests were conducted on geocell reinforcement compared with other types of reinforcement. Mhaiskar et al. (1994) conducted model tests on geocells and a planar reinforced base. They found that a geocell-reinforced sand layer performed better than the planar reinforced sand layer and the unreinforced sand layer under cyclic loading. Dash (2004) carried out model tests on strip footings supported by sand beds reinforced with geocells, planar and randomly distributed mesh elements. The improvement performance of geocells, in terms of increase in bearing capacity and reduction in surface heave and settlements, is superior to that of the other type of reinforcements. Leshchinsky et al. (2013) conducted a series of embankment model tests and numerical simulations, and a parametric study showed that the use of geocells provides a composite mattress effect that distributes subgrade stress more uniformly than the case without reinforcement, increasing bearing capacity and reducing settlement.

Laboratory model tests were also conducted to investigate other factors influencing the performance of geocell-reinforced bases, such as geometric structure and dimension, properties of geocell material and properties of infilled soil, loading methods etc. Dash et al. (2001a and 2001b) discussed the geometric factors affecting the performance of geocell-reinforced base and found that optimum values of the geocell height/width ratio and the loading area width/geocell width ratio exist. Mhaiskar et al. (1994) concluded that the geocell-reinforced base has better performance when the geocell material has a higher modulus. Dash et al. (2001b, 2010) also showed that the bearing capacity of geocell-reinforced base increases as the density of infill soil increases. Pokharel et al. (2010) investigated the behavior of single geocell-reinforced bases under static loading, showing that a geocell placed in a circular shape has a higher bearing capacity than that placed in an elliptical shape and a higher elastic modulus of geocell material results in a higher stiffness and bearing capacity of the reinforced base. Based on model tests on geocell-reinforced sand foundation, Dash (2012) suggested that

geocell made of geogrids of higher strength, relatively smaller size aperture opening and ribs of orthogonal orientation gives better performance.

The engineering application of geocells to retaining walls is relatively new due to the lack of related studies. As far as the authors have investigated in the literature, there exists very limited research on the evaluation of tensile function of geocell. Ling et al. (2009) investigated the seismic performance of several soil retaining walls having a geocell facing using shaking table model tests. The results show that walls having a geocell facing are flexible and show much better seismic performance than rigid walls. In addition, the wall with geocells acting as reinforcement layers exhibits better performance than that reinforced by geogrids. Kiyota et al. (2009) and Kuroda (2012) firstly conducted a serious of pullout tests using diamond-shaped geocell models and commercial geogrids to investigate whether or not the geocells can be used as tensile reinforcements. It was found that, although the diamond-shaped geocell model shows higher pullout resistance, the pre-peak stiffness is lower than the geogrids due to progressive large deformation of diamond-shaped cells.

2.3.3 Other types of reinforcements

Other soil reinforcements were also developed as tensile-reinforcement for retaining walls. In Thailand, inextensible reinforcements, such as ribbed steel strip and steel grid reinforcements were widely used to stabilize retaining walls and/or steep slopes (Bergado et al., 1996). Horpibulsuk et al. (2010) have introduced a new cost-effective reinforcement called "bearing reinforcement", which is composed of longitudinal members and transversal members (bearing members). The longitudinal members are made of a deformed steel bar, which shows high pullout friction resistance, and the transversal members are a set of equal angles, which provides high pullout bearing resistance. The newly-developed "bearing reinforcement" has an advantage to provide high pullout bearing resistance by transversal members, while only a few transversal members are needed in the resistant zone. As a result, bearing reinforcement is cost-effective compared with steel grid reinforcement. Influential factors on the pullout resistance, such as spacing between transversal members, leg length and particle size of backfill soil, were investigated (Horpibulsuk et al., 2010 and Suksiripattanapong et al., 2013).

Khedkar et al. (2009) has proposed a three-dimensional cellular reinforcement in which longitudinal members are connected perpendicularly to transversal members of the same height. Pullout tests using sand have shown that cellular reinforcement performs better than planar reinforcements. In addition, the ultimate pullout force increases with an increase in the height of reinforcement up to a height of 30 mm. With further increase in the height of members, ultimate pullout force slightly decreases. In addition, the optimum ratio of spacing between transversal members and the height of members is 3.3. Moreover, Racana et al. (2003) investigated the effect of geometry on the pullout resistance of geocells and suggested that corrugated geometry forming a network of geocells is preferred as reinforcement to provide larger pullout resistance. Zhang et al. (2006) also suggested that three-dimensional reinforcement has better performance than planar reinforcements based on triaxial tests.

2.4 Summary

A new type of (square-shaped) geocell

A new type of geocell, named square-shaped geocell, which is capable of confining large soil particles, has been developed aimed at providing better tensile-reinforcement to the backfill of GRS RWs. .

Geogrid as tensile reinforcement

The pullout resistance of geogrid is essential for the seismic stability of GRS RWs. Based on a comprehensive literature review of the pullout behavior of geogrid reinforcements, the pullout interaction mechanism between geogrid and soil could be summarized. As shown in Fig. 2.6, the pullout resistance of geogrid is controlled by:

1) Friction between soil particles and geogrid members;
2) Friction between soil particles interlocked in the grid aperture and adjacent soil particles;
3) Passive soil resistance induced by grid transversal members;
4) The interlocking of soil particles in the aperture of the geogrid has an important influence on the pullout resistance of geogrid reinforcement. An appropriate geogrid aperture size and shape relative to soil particle size and shape, grading, and density, as well as the properties of the geogrid members would induce better interlocking resulting in an increase in the pullout resistance of the geogrid.

Diamond-shaped geocell as base reinforcement

The traditional type geocell, named diamond-shaped geocell is described. From the review of the engineering application and current state-of-practice, diamond-shaped geocell is often used as base reinforcement subjected to vertical loads. As shown in Fig. 2.7, since its 3-D structure can provide an excellent soil confinement, the soil strength and the bearing capacity can be vastly improved. As far as the authors have investigated in the literature, there exists very limited practical application of diamond-shaped geocell and comprehensive research on its tensile performance is lacking.

Other types of tensile reinforcements

In order to increase the pullout resistance of reinforcements, several new types of tensile reinforcement have been developed by different researchers, such as “bearing reinforcement” (Horpibulsuk et al., 2010) and “cellular reinforcement” (Khedkar et al., 2009). It is suggested

that reinforcement with ribbed members or a 3-D structure can provide larger pullout resistance compared to planar reinforcements.

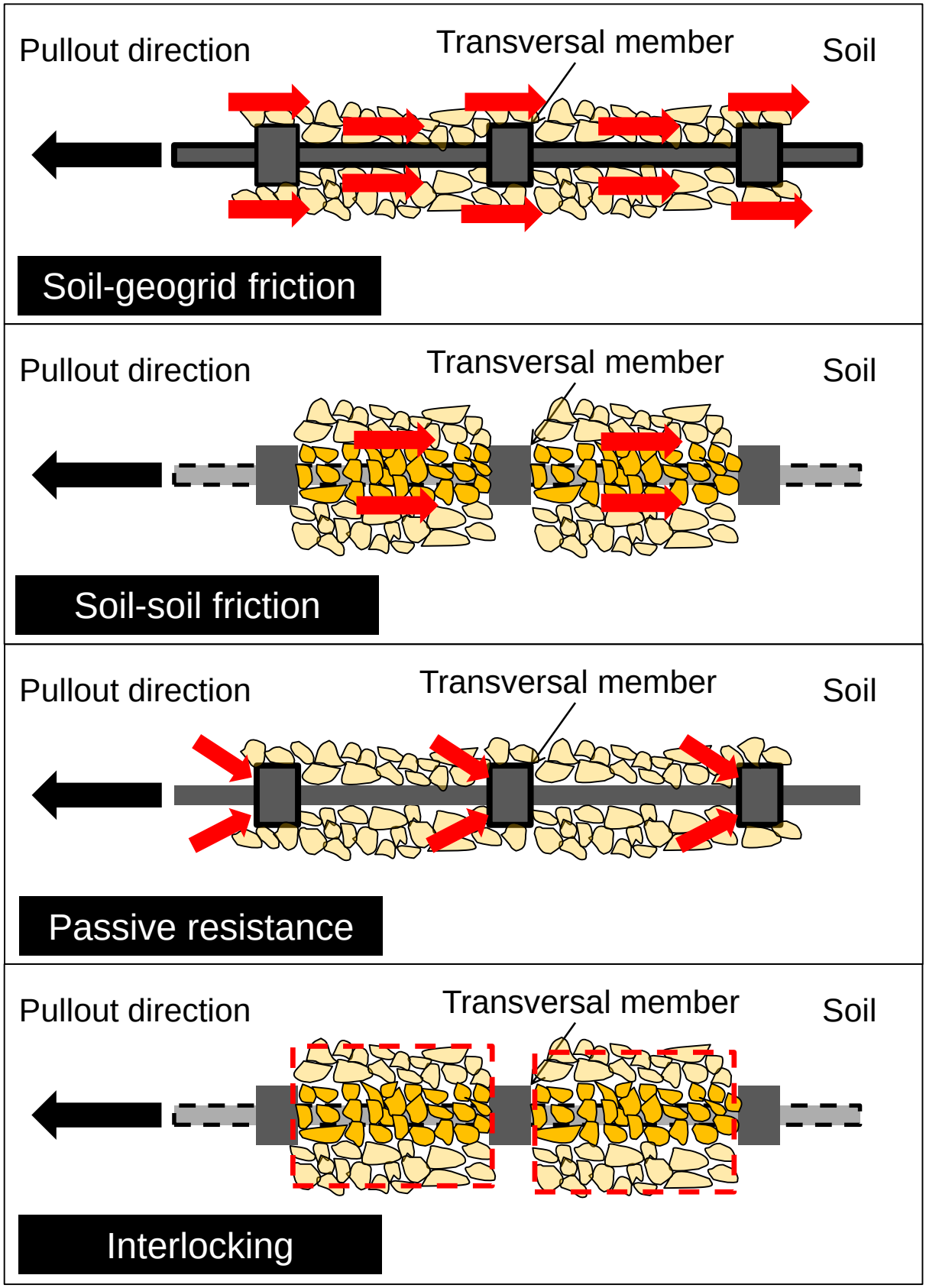

Fig. 2.6 Pullout mechanism of geogrid

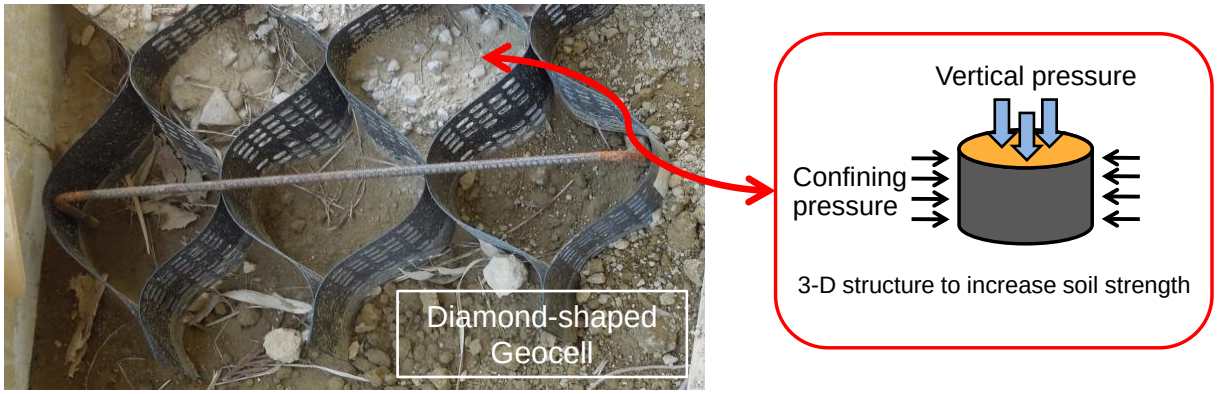

Fig. 2.7 Mechanism of stabilization of soil with geocells

2.5 References

1. Bathurst, R.J. and Karpurapu, R. (1993). "Large scale triaxial compression testing of geocell reinforced granular soils", Geotechnical Testing Journal, 16(3), 296-303.
2. Bergado, D.T., Chai, J.C. and Miura, N. (1996). "Predication of pullout resistance and pullout force-displacement relationship for inextensible grid reinforcements", Soils and Foundations, 36(4), 11-22.
3. Brown, S.F., Kwan, J. and Thom, N.H. (2007). "Identifying the key parameters that influence geogrid reinforcement of railway ballast", Geotextiles and Geomembranes, 25(6), 326–335.
4. Chen, C., McDowell, G.R. and Thom, N.H. (2014). "Investigating geogrid-reinforced ballast: experimental pull-out tests and discrete element modelling", Soils and Foundations, 54(1), 1-11.
5. Dash, S.K., Krishnaswamy, N.R. and Rajagopal, K. (2001a). "Bearing capacity of strip footings supported on geocell reinforced sand", Geotextiles and Geomembranes, 19(4), 235-256.
6. Dash, S.K., Rajagopal, K. and Krishnaswamy, N.R. (2001b). "Strip footing on geocell reinforced sand beds with additional planar reinforcement", Geotextiles and Geomembranes, 19(8), 529-538.
7. Dash, S.K., Rajagopal, K. and Krishnaswamy, N.R. (2004). "Performance of different geosynthetic reinforcement materials in sand foundations", Geosynthetics International, 11(1), 35-42.
8. Dash, S.K. (2010). "Influence of Relative Density of Soil on Performance of Geocell-Reinforced Sand Foundations", Journal of Materials in Civil Engineering, 22(5), 533-538,
9. Dash, S.K. (2012). "Effect of geocell type on load-carrying mechanisms of geocell-reinforced sand foundations", International Journal of Geomechechanics, 12(5), 537-548.
10. Giroud, J.P. (2009). "An assessment of the use of geogrids in unpaved roads and unpaved areas", Proceedings of the 2009 Geogrid Jubilee Symposium, Institution of Civil Engineers, London.
11. Horpibulsuk, S. and Niramitkornburee, A. (2010). "Pullout resistance of bearing reinforcement embedded in sand", Soils and Foundations, 50(2), 215-226.
12. Khedkar, M.S. and Mandal, J.N. (2009). "Pullout behaviour of cellular reinforcements", Geotextiles and Geomembranes, 27(4), 262-271.
13. Kiyota, T., Soma, R., Munoz, H., Kuroda, T., Ohta, J., Harata, M. and Tatsuoka, F. (2009). "Pullout behaviour of geocell placed as reinforcement in backfill", Geosynthetics Engineering Journal 24(0), 75-82. (In Japanese).
14. Kuroda, T. (2012). "Evaluation of static and seismic stability of bridges with reinforced backfill and integrated structural (new type and rehabilitated type bridges) by model tests", Master Thesis, Department of Civil Engineering, Tokyo University of Science. (In Japanese).
15. Leshchinsky, B. and Ling, H. (2013). "Effects of geocell confinement on strength and deformation behavior of gravel", Journal of Geotechnical and Geoenvironmental Engineering, 139(2), 340-352.
16. Ling, H.I., Leshchinsky, D., Wang, J.P., Mohri, Y. and Rosen, A. (2009). "Seismic response of geocell retaining walls: experimental studies", ASCE Journal of Geotechnical and Geoenvironmental Engineering, 135, 515-524.

17. Lopes, M.L. and Lopes, M.L. (1999). "Soil-geosynthetic interaction-influence of soil particle size and geosynthetic structure", Geosynthetics International, 6(4), 261-282.
18. McDowell, G.R., Harireche, O., Konietzky, H., Brown, S.F. and Thom, N.H. (2006). "Discrete element modelling of geogrid-reinforced aggregates", Proceedings of the Institute of Civil Engineers-Geotechnical Engineering, 159(1), 35-48.
19. Mengelt, M., Edil, T.B. and Benson, H.H. (2006). "Resilient modulus and plastic deformation of soil confined in a geocell", Geosynthetics International, 13(5), 195-205.
20. Mhaiskar, S.Y. and Mandal, J.N. (1994). "Three dimensional geocell structure: performance under repetitive loads". Proceedings of the 5th International Conference on Geotextile, Geomembranes and Related products, Singapore, 155-158.
21. Minažek. K. and Mulabdić. M. (2013). "A review of soil and reinforcement interaction testing in reinforced soil by pullout test", GRAĐEVINAR 65 (3), 235-250.
22. Nishikiori, H., Aizawa, H., Soma, R., Sonda, Y., Hirakawa, D. and Tatsuoka, F. (2007). "Pull-out resistance of various types of reinforcement embedded in sand", Geosynthetics Engineering Journal 22, 97-102. (In Japanese).
23. Nishikiori, H., Soma, R., Aizawa, H., Hirakawa, D. and Tatsuoka, F. (2008). "Evaluation of various factors to pull-out resistance of various types of reinforcement embedded in sand", Geosynthetics Engineering Journal, 23, 23-30. (In Japanese).
24. Palmeira, E.M. and Milligan, G.W.E. (1989). "Scale and other factors affecting the results of pull-out tests of grid buried in sand", Geotechnique, 11(3), 511-524.
25. Palmeira, E.M. (2008). "Soil-geosynthetic interaction: modeling and analysis", Proceedings of the 4th European Geosynthetics Conference, Edinburgh, 1-30.
26. Pokharel, S.K., Han, J., Leshchinsky, D., Parsons, R.L., and Halahmi, I. (2010) "Investigation of factors influencing behavior of single geocell-reinforced bases under static loading". Geotextiles and Geomembranes, 28(6), 570-578.
27. Racana, N., Grediac, M. and Gourves, R. (2003). "Pull-out response of corrugated geotextile strips". Geotextiles and Geomembranes, 21(5), 265-288.
28. Rajagopal, K., Krishnaswamy, N.R. and Latha, G.M. (1999). "Behavior of sand confined with single and multiple geocells". Geotextiles and Geomembranes, 17(13), 171-184.
29. Suksiripattanapong, C., Horpibulsuk, S., Chinkulkijniwat, A. and Chai, J.C. (2013). "Pullout resistance of bearing reinforcement embedded in coarse-grained soils", Geotextiles and Geomembranes, 36, 44-54.
30. Tatsuoka, F., Tateyama, M., Mohri, Y. and Matsushima, K. (2007). "Remedial treatment of soil structures using geosynthetic-reinforcing technology", Geotextiles and Geomembranes, 25(4 & 5): 204-220.
31. Tutumluer, E., Huang, H., and Bian, X. (2012). "Geogrid-aggregate interlock mechanism investigated through aggregate imaging-based discrete element modeling approach", International Journal of Geomechechanics, 12(4), 391-398.
32. WWW.GEOSYNTHETICSSOCIETY.ORG
33. Yuu, J., Han, J., Rosen, A., Parsons, R.L. and Leshchinsky, D. (2008). "Technical review of geocell-reinforced base courses over weak subgrade", Geo-Americas Conference Proceedings, 1022-1030.
34. Zhang, M.X., Javad, A.A. and Min, X., (2006). "Triaxial tests of sand reinforced with 3D inclusions", Geotextiles and Geomembranes, 24(4), 201-209.

3 TESTING APPARATUSES, MATERIALS AND PROCEDURES

3.1 Introduction

The tensile function of a newly-developed square-shaped geocell placed in the soil backfill was evaluated by laboratory pullout tests, and the seismic performance of GRS RW with the newly-developed geocell was evaluated by shaking table model tests. The pullout test apparatus and shaking table test apparatus as well as the test materials and procedures are described in this chapter.

3.2 Pullout tests

3.2.1 Introduction

The pullout test on reinforcement materials has been conducted over the past thirty years, since it provides not only important strength parameters that are necessary for the design of reinforced soil structures, but also essential explanation of the interaction mechanisms of different types of soils and reinforcements (Palmeira 2008, Minažek et al., 2013). In this study, pullout tests were used to evaluate the tensile function of a newly-developed geocell compared to a traditional-type geocell and ordinary commercial geogrids embedded in the soil backfills.

3.2.2 Pullout test apparatus

The pullout apparatus used in this experimental program was newly-developed in the Institute of Industrial Science, the University of Tokyo (Fig. 3.1). It essentially consists of two parts: the soil container and the loading system, as described below.

Soil container

The rectangular steel soil container with inner dimensions of 700 mm (length) × 400 mm (width) × 500 mm (height) was used. The geocell/geogrid model was embedded in a soil specimen inside the soil container (Fig. 3.1) and pulled out under plane strain conditions. The opening of the front wall for pulling out the geocell/geogrid was changed by using steel bars. As shown in Fig. 3.2, the maximum height of the opening was100 mm. Since the size of the front opening has an influence on the pullout resistance, an appropriate opening size should be determined. In Sections 4.2, 4.3 and 4.4, the opening of the front wall was set to 46.5 mm (Figs. 3.2b and c) for the comparison of the pullout behavior of the square-shaped geocell, diamond-shaped geocell and various types of geogrids, as well as the investigation of basic pullout characteristics of the square-shaped geocell. In Section 4.5 and 4.6, the opening of the front wall was set to 100 mm (Fig. 3.2d) for the investigation of the influence of geocell height relative to the soil particle size. For the test of geogrid as a planar reinforcement, sponge tapes with height of 10 mm were pasted at the upper and bottom edges of the steel bars (Fig. 3.2b), to prevent the soils falling out during pullout tests. For the tests on the geocells (i.e. square-shaped geocell and diamond-shaped geocell), the same amount of paper (Figs. 3.2c and d) was provided at the opening of the front wall to prevent the soils from falling out during the pullout tests.

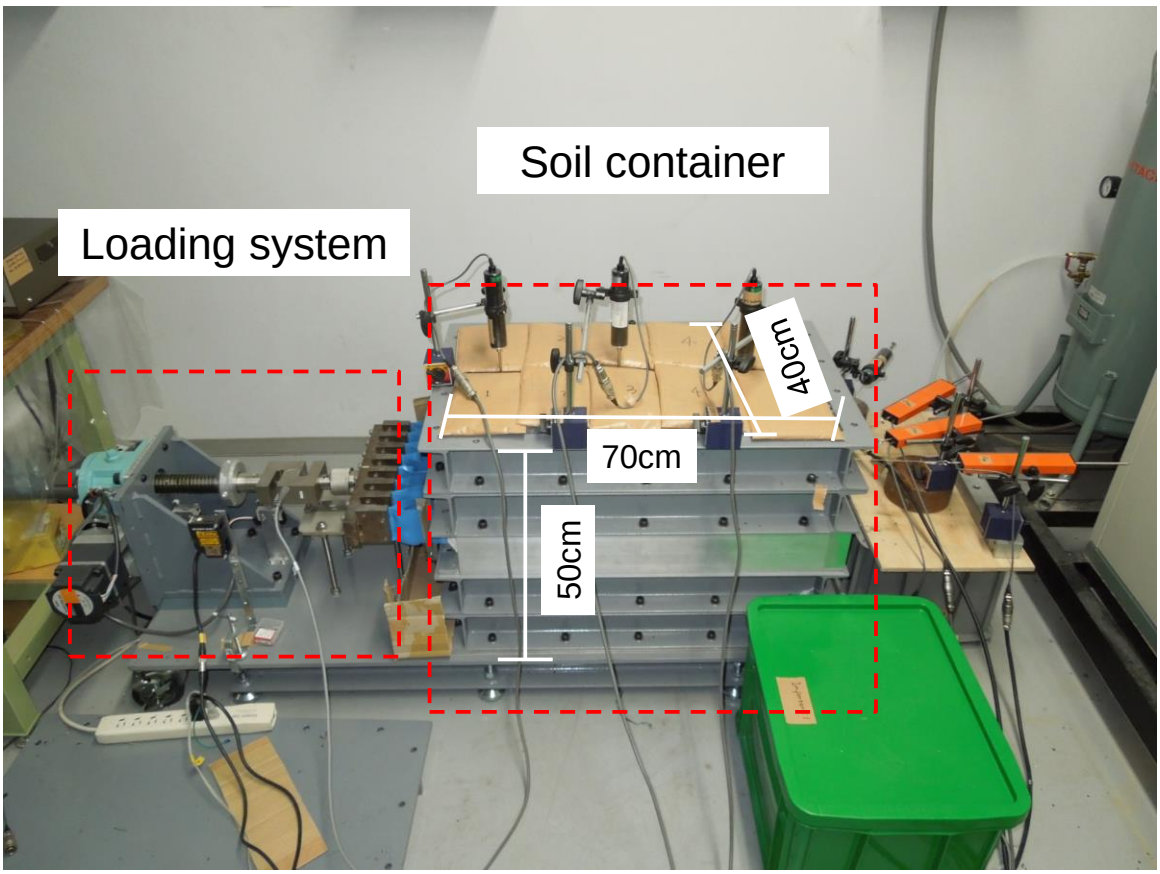

Fig. 3.1 Pullout test apparatus

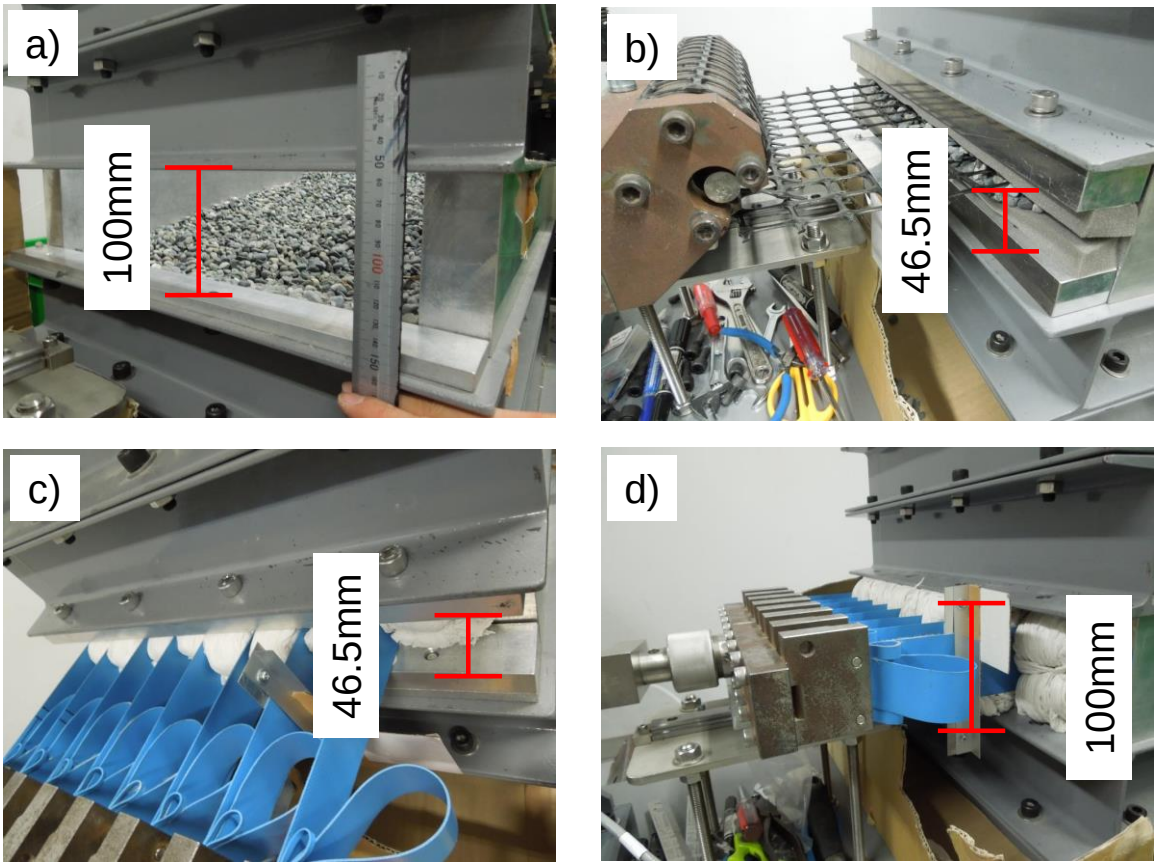

Fig. 3.2 Front opening of soil container

Loading system

The pullout loading system (Fig. 3.1, Figs. 3.3a and b) was controlled by a motor, which provides for a large pullout deformation rate range, varying from almost zero to 10 mm/min. In this study, the geocell/geogrid model was pulled out at a constant displacement rate of 2.5 mm/min. A tensile load cell (Fig. 3.3b) with a capacity of 49 kN and accuracy of 98 N was connected to the pullout loading system. A clamp was connected firmly to this load cell. As shown in Fig. 3.4, two types of clamps for geocell reinforcements (3-D reinforcements) and geogrid reinforcements (planar reinforcements), respectively, were designed to provide a perfectly rigid connection by preventing the slippage of the reinforcement during the pullout process. The data acquisition system was DATA LOGGER TDS-150 (Fig. 3.3c) manufactured by Tokyo Sokki Kenkyujo Co., Ltd with 10 channels and a sampling time of 3 seconds, which is adequate for static pullout tests.

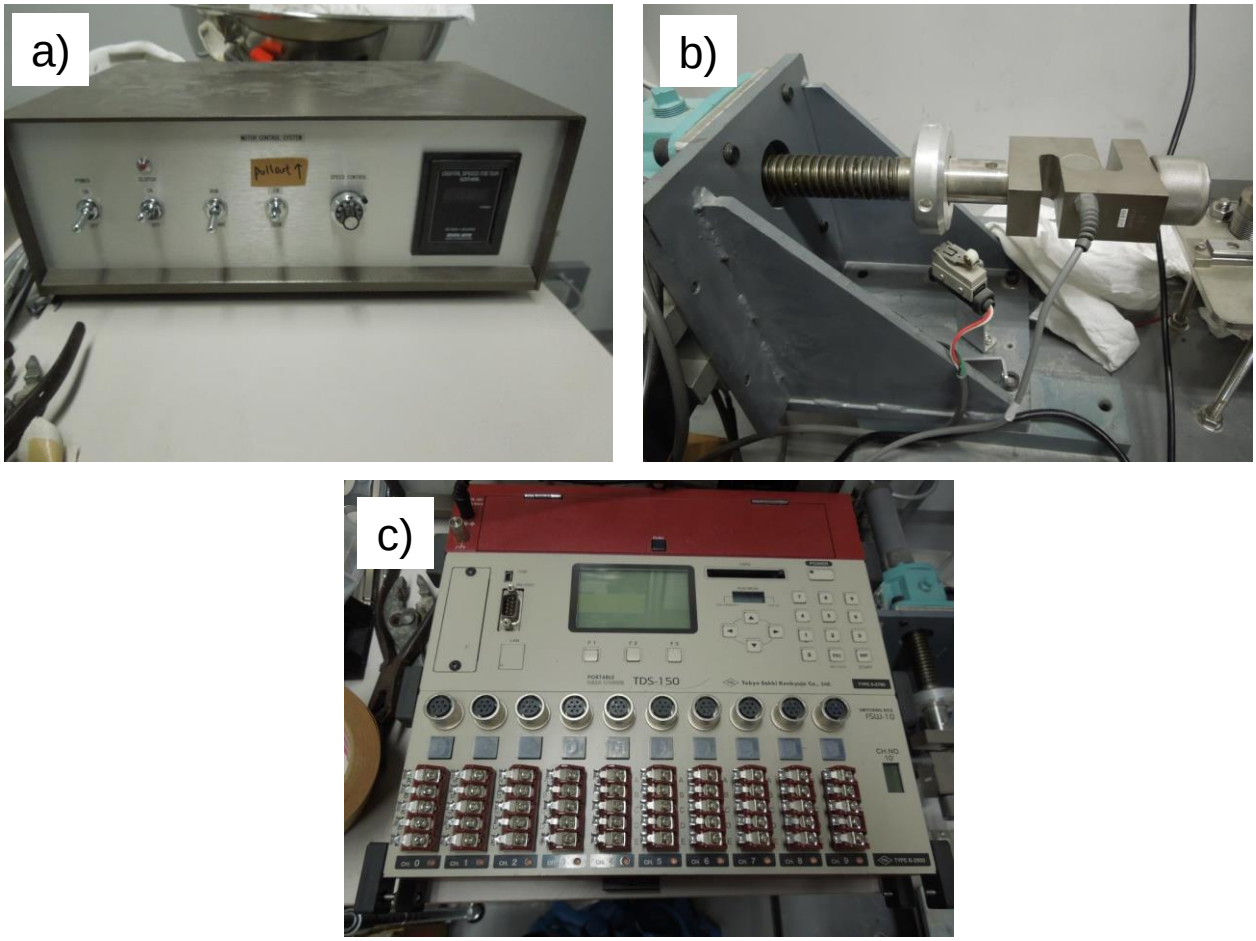

Fig. 3.3 a) Motor control system; b) a tensile load cell; c) data acquisition system.

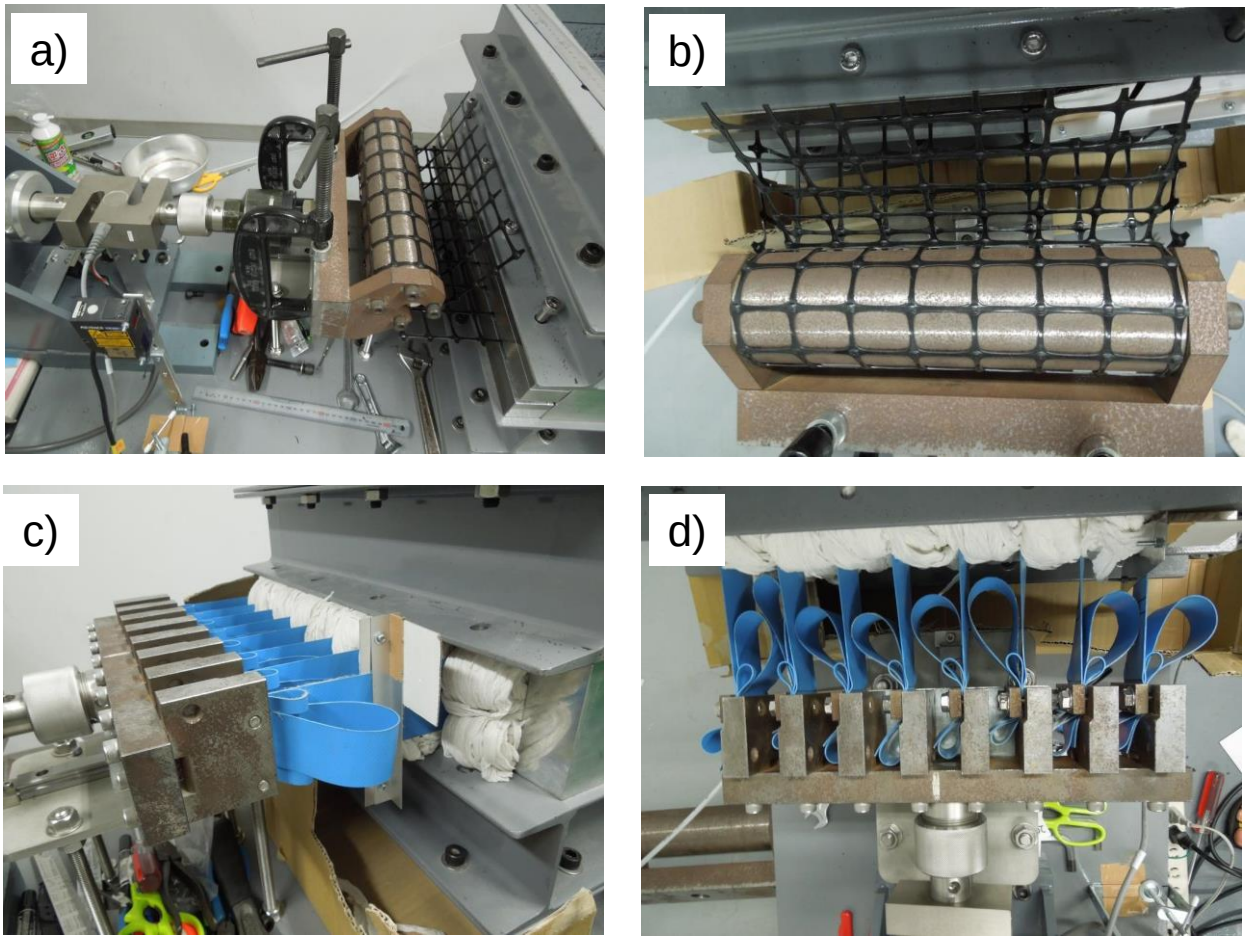

Fig. 3.4 Clamps for: a) and b) geogrid reinforcement; c) and d) geocell reinforcement.

3.2.3 Pullout test specimens: soil materials and reinforcements

Three types of poorly graded sub-rounded gravelly soils, Gravel No.1 (D_{50}=3.2 mm), Gravel No.3 (D_{50}=7.5 mm) and Gravel No.5 (D_{50}=14.2 mm), were used (Figs. 3.5 and 3.6).

Two types of geocell models were prepared: square-shaped geocell (i.e. newly-developed geocell) and diamond-shaped geocell (i.e. traditional-type geocell) by a scale factor of 1/10. As shown in Fig. 3.7a, the square-shaped geocell reinforcement is 480 mm (length) × 350 mm (width), having eight square-shaped cells in the longitudinal direction and seven square-shaped cells in the transverse direction. The height of transversal members is 25 mm and the size of each cell is 60 mm × 50 mm. The longitudinal members are 20 mm higher than the transversal members (i.e. 45 mm). As shown in Fig. 3.7b, the diamond-shaped geocell model is 480 mm (length) × 350 mm (width) × 25 mm (height), having eight diamond-shaped cells in both the longitudinal direction and transverse direction.

However, to check the influence of geocell height relative to soil particle size, several square-shaped geocells with different transversal heights were prepared. For example, square-shaped geocells with full height (H) of transverse members 12.5 mm, 25 mm, 40 mm, 60 mm and 80 mm were also prepared. Note that, the spacing between transversal members can also be changed by adding or reducing transversal members to check the influence of the spacing between transversal members. The members of the geocell are made of polyester (PET) covered with PVC for protection. The members of the geocell model used in these scaled-down model tests are weaker and softer than those (made of HDPE) used in full-scale GRS structures (Kongkitkul et al., 2007). The tensile strength of the members is 1700 N/3cm provided by TOKYO PRINTING INK MFG. CO., LTD.

For comparison, a geogrid product called Tensar SS-35 (Fig. 3.7c) with 28 mm × 33 mm square-shaped apertures and 5 mm thickness was also prepared. Tensar SS-35 is made of polypropylene (PP) with a tensile strength of 50 kN/m. Although a PP geogrid is generally stiff, this geogrid type is among the weakest and strongest among those that are usually used with full-scale GRS structures. The global dimensions of the specimen of this geogrid model are the same as those of the square-shaped geocell model.

Fig. 3.5 Backfill materials used in this study a) Gravel No.1; b) Gravel No.3; c) Gravel No.5.

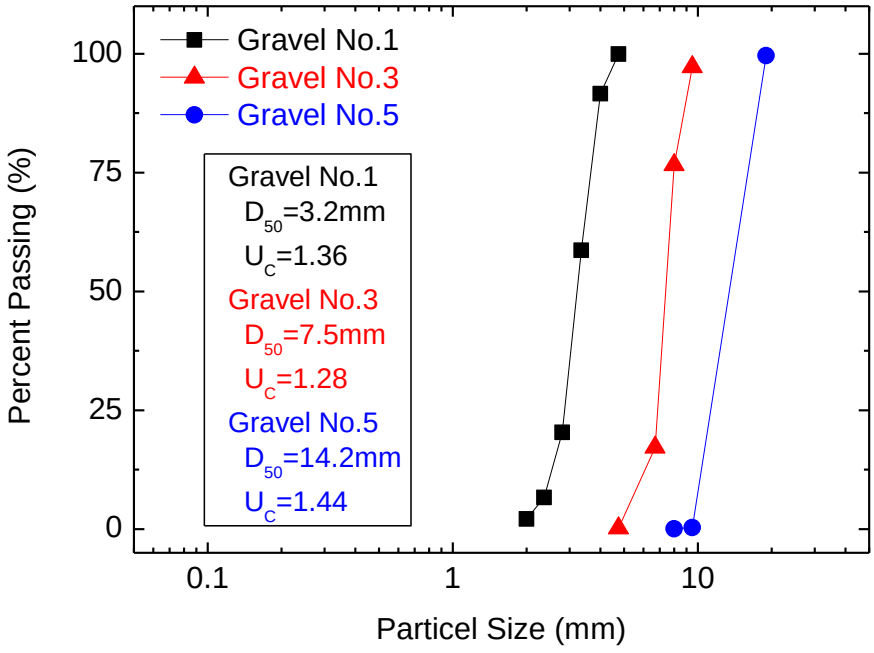

Fig. 3.6 Particle size distribution of gravels.

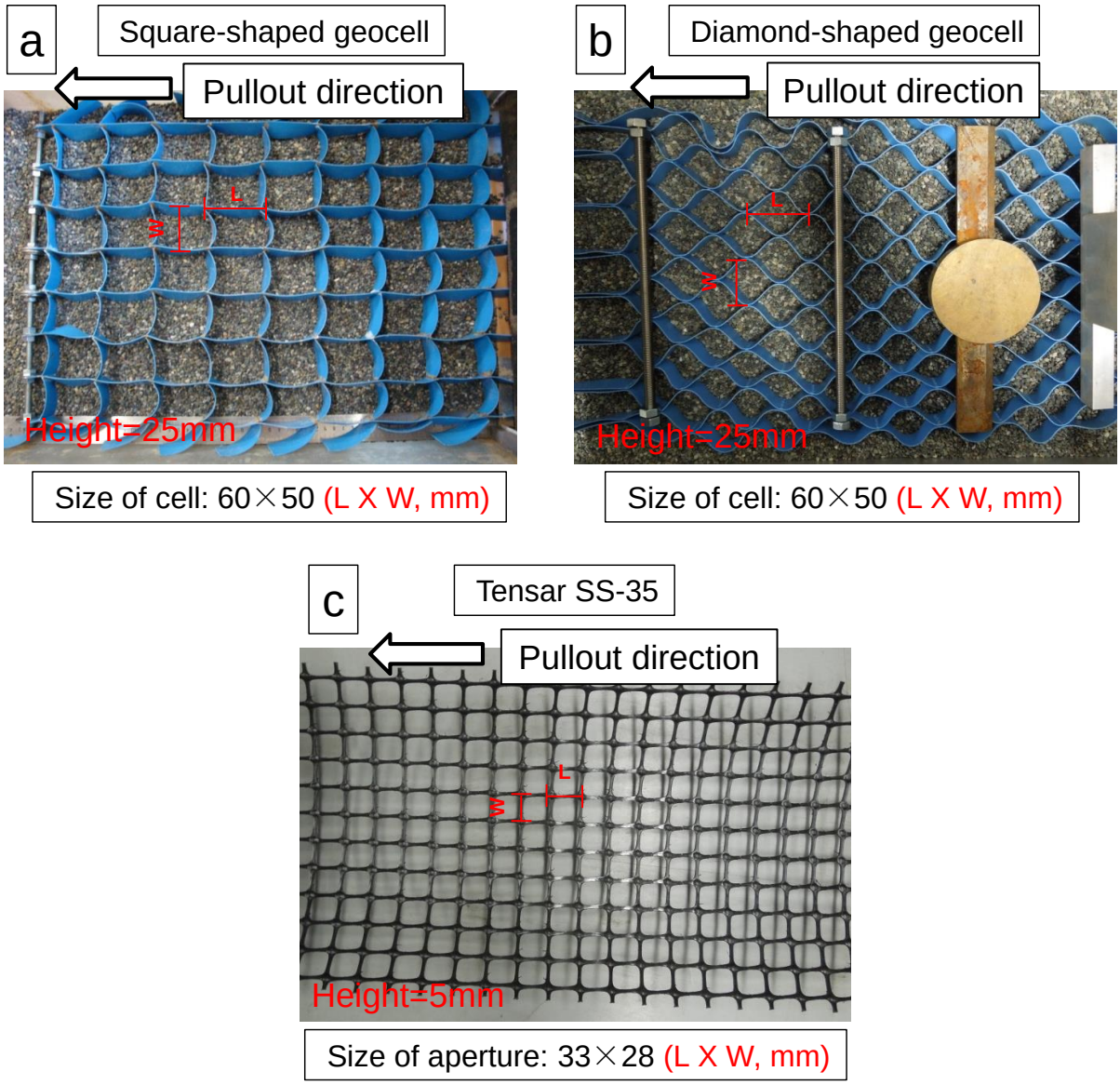

Fig. 3.7 Types of reinforcements: a) square-shaped geocell model; b) diamond-shaped geocell model; c) Tensar SS-35

3.2.4 Pullout test procedures

Backfill soil preparation

Gravel particles were poured into the soil box and compacted in 25 cm-thick sub-layers positioning a geocell/geogrid model at a prescribed level in the backfill. The degree of compaction (Standard Proctor) is 100 %.

Set up of the measurement gauges

As indicated in Fig. 3.8a, the front horizontal displacement (d_0) of the reinforcement relative to the sand box was monitored with a laser deformation transducer. As indicated in Figs. 3.8b and c, the horizontal displacements at distances of 60 mm (d_{60}), 180 mm (d_{180}), 300 mm (d_{300}), and 540 mm (d_{540}) from the face of front wall along the geocell/geogrid model were measured by several linear variable differential transformers (LVDTs). This measurement allows proper interpretation of the interface force transfer mechanism that is essential for the appropriate evaluation of the pullout resistance mechanism. To this scope, thin inextensible stainless steel wires were connected to the designated locations of the geocell/geogrid model. The wires were protected from interaction with the adjacent backfill material by being placed into stiff tubes and connected to the LVDTs mounted on the rear wall of soil box.

In addition, the vertical displacements at the backfill crest were also measured at distances of 60 mm (V_{60}), 300 mm (V_{300}), and 540 mm (V_{540}) from the face of the front wall by three LVDTs (Figs. 3.9a and b).

Set up of the surcharge

After filling soil materials and setting up the measurement gauges, leads shots were placed on the top of the backfill to provide a surcharge of 1 kPa to simulate the weight of the road base for railways or highways (Fig. 3.9c). This loading method at a flexible top boundary is preferred to measure, with as much as small restraint, vertical deformation of the backfill caused by the dilatancy of soil around the geocell/geogrid model during the pullout process.

Start the data acquisition system and motor control system

The geocell/geogrid model was pulled out at a constant displacement rate of 2.5 mm/min (i.e. 1500 rpm) using a precision jack driven by a motor. The pullout force was measured with a tensile load cell. All instrumentations were connected to an electronic data logger that can record all measurements at desired time intervals.

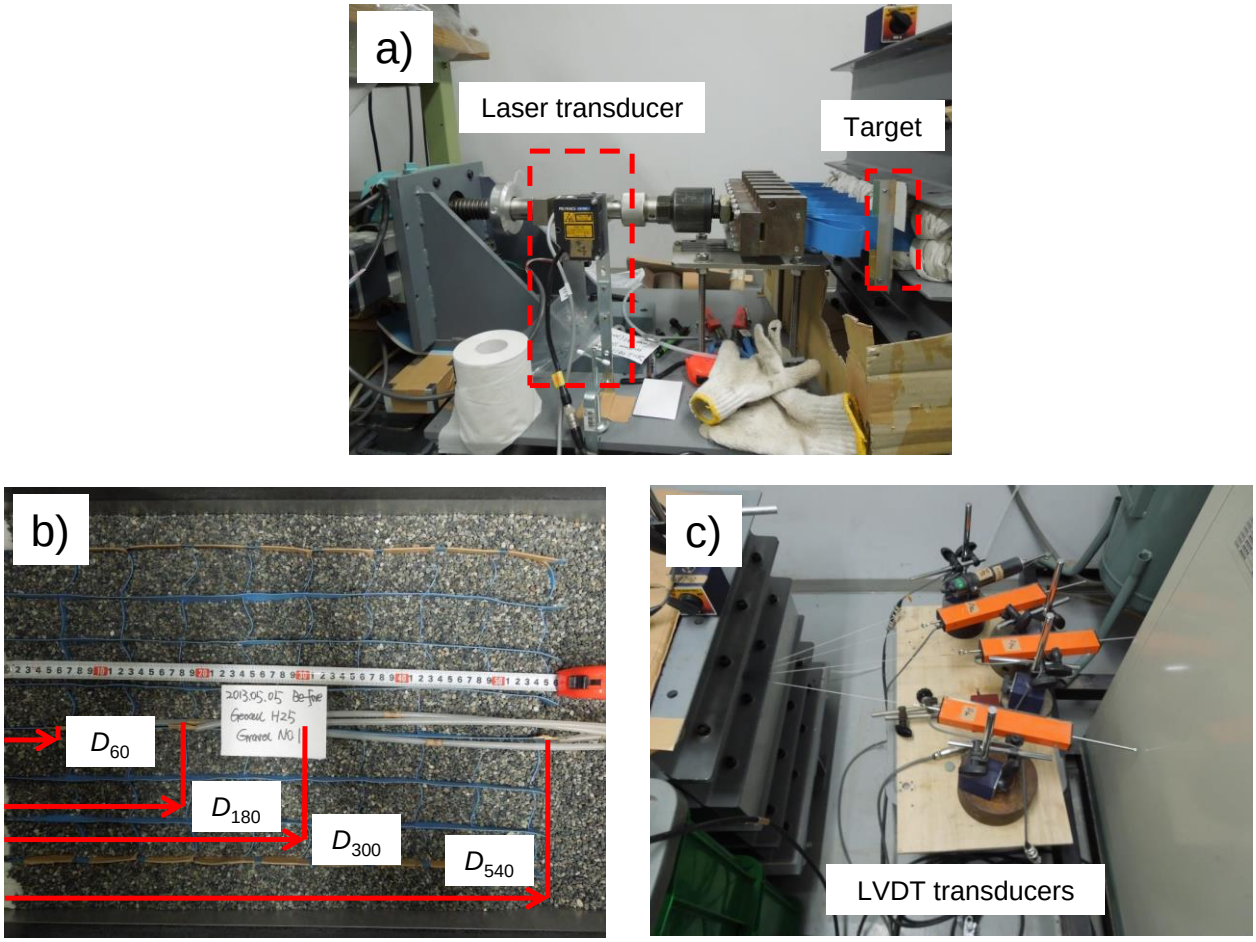

Fig. 3.8 Measurement of horizontal displacements by: a) laser transducer (d_0); b) and c) LVDT transducers (d_{60}, d_{180}, d_{300}, d_{540})

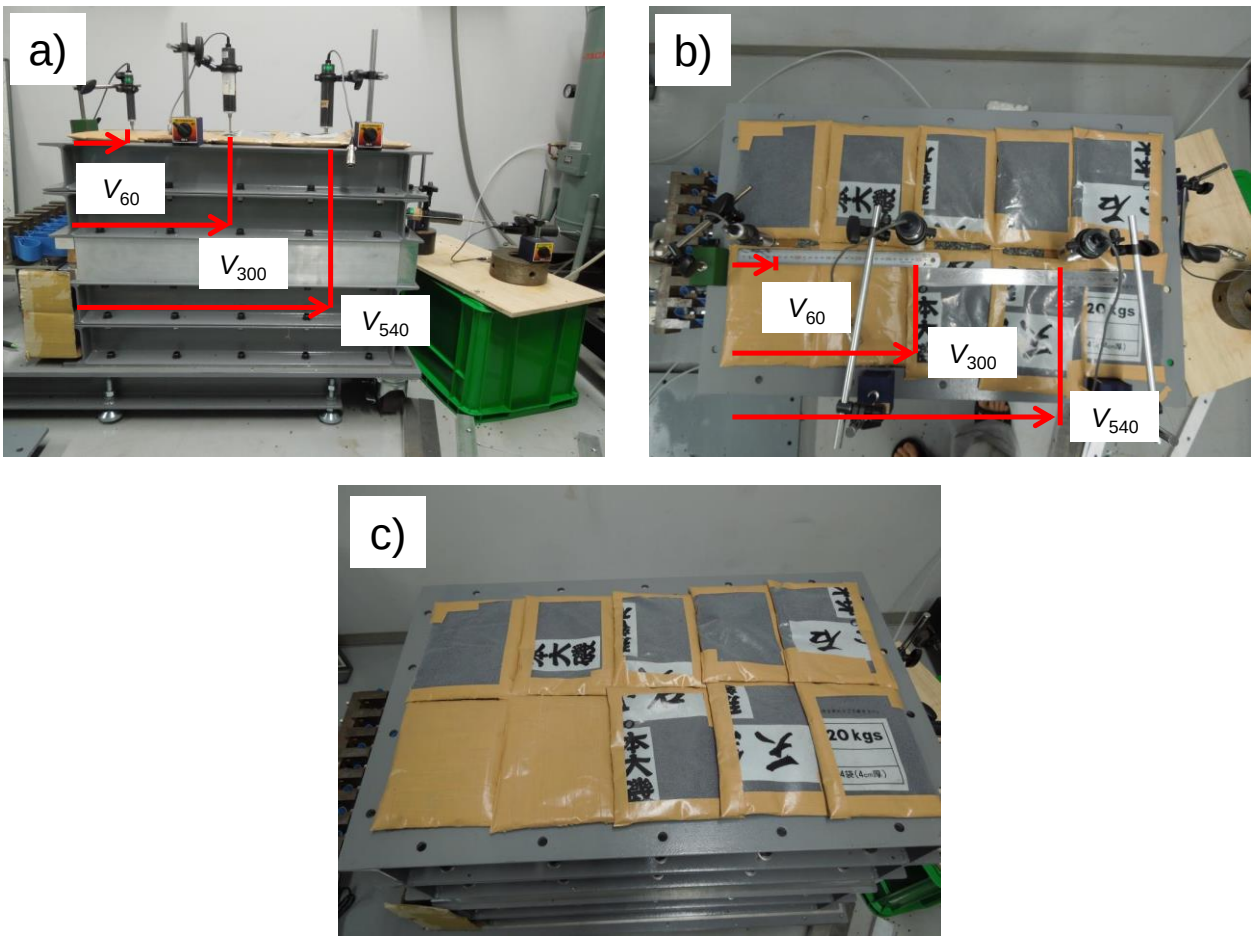

Fig. 3.9 Measurement of vertical displacements (V_{60}, V_{300}, V_{540}) from: a) side view and b) top view; c) surcharge using lead shots

3.3 Shaking table test

3.3.1 Introduction

1-g shaking table model tests have been the most common approach to qualitatively and quantitatively evaluate the seismic performance of reinforced soil structures (e.g. Matsuo et al. 1998, Bathurst et al. 2002, Koseki et al. 2006). The application of the 1-g shaking table model test provides the advantage of simulating complex systems, such as reinforced soil wall systems under controlled testing conditions and the opportunity to gain insight to the fundamental mechanism of these systems. Although the results of the model tests might be influenced by low confining pressures, boundary conditions etc., it can be used for the calibration of numerical methods, therefore predicting the response of prototype systems.

This section first describes the shaking table facility at the IIS, the University of Tokyo. In this research, three types of retaining wall models were prepared: non-reinforced traditional-type RW (i.e. T-shape RW) and GRS RWs with the reinforcement of newly-developed square-shaped geocell and geogrids. The model wall materials, such as model wall facing, reinforcements and clamps, backfill and subsoil materials are discussed considering the similitude. Similitude rules that are used to scale the prototype parameters to the reduced-scale model parameters are also presented. Additionally, a measurement technology for the purpose of image analysis is also introduced. The instrumentations used to measure the model wall response are described, which include accelerometers, displacement transducers, ordinary digital camera and a high-speed camera used to observe soil deformation through the transparent acrylic sidewall for image analysis. The seismic loading method is described afterwards. Finally, the construction procedures of wall models to simulate the construction sequence of prototype GRS RW are also presented.

3.3.2 Shaking table test facility

Shaking table specifications

The shaking table facility used in this study belongs to the Earthquake Resistant Structure Research Center (ERS) of the IIS, University of Tokyo. The shaking table was originally constructed to 6 degrees of freedom, but actually the table motion is limited only to the two horizontal degrees of freedom for stable operations. The major specifications of this shaking table facility are summarized in Table 3.1 and the shaking table is shown in Fig. 3.10.

Table 3.1 Shaking table specifications

Specification	Value
Table size	1.5 m ×1.5 m
Payload capacity	2 ton
Controlled degrees of freedom	3 (vertical and horizontal)
Translations	X, Y and Z
Frequency	DC~100Hz
Exciting force	2 tonf
Maximum acceleration (X and Y)	2.5G sin wave for 0 ton payload
	1.1G sin wave for 2 ton payload
	0.7G sin wave for 2 ton payload
Maximum displacement (X and Y)	200 mmp.p
Maximum velocity (X and Y)	1.1 m/s

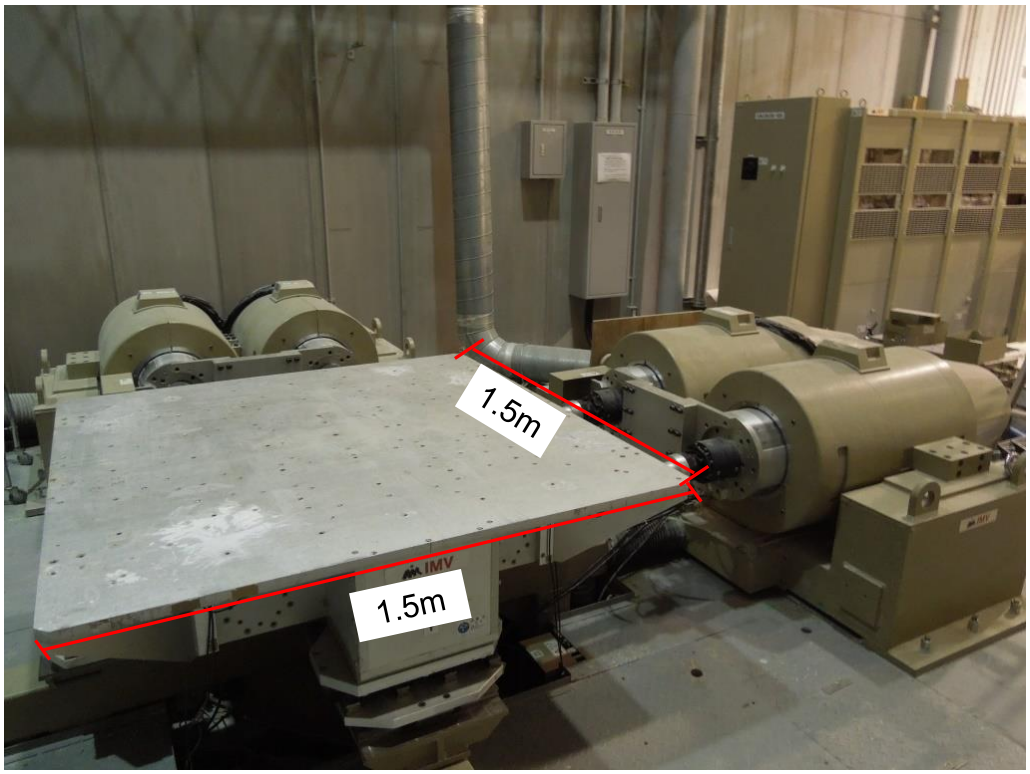

Fig. 3.10 Shaking table facility

Data acquisition system

A conventional data acquisition system used for static tests may not be adequate to handle the special loading conditions associated with dynamic tests. So a higher sampling time is required to avoid data aliasing and to capture the peak values of the dynamic wall response during shaking. The data acquisition system, EDX-200A, from Kyowa Electronic Instruments Co., Ltd. Inc. was used to capture the output data with 64 channels and a scanning rate of 100 Hz.

Soil container

A strong soil container (Fig. 3.11) with inner dimensions of 1800 mm × 400 mm in plan and 875 mm in height was used to enclose the tested retaining wall models. Both the front and back side of this container were comprised of transparent-tempered glass windows to make the deformation behavior of the model visible. The box was connected to the shaking table using ten 10 mm diameter bolts to ensure rigid body movement of the shaking table.

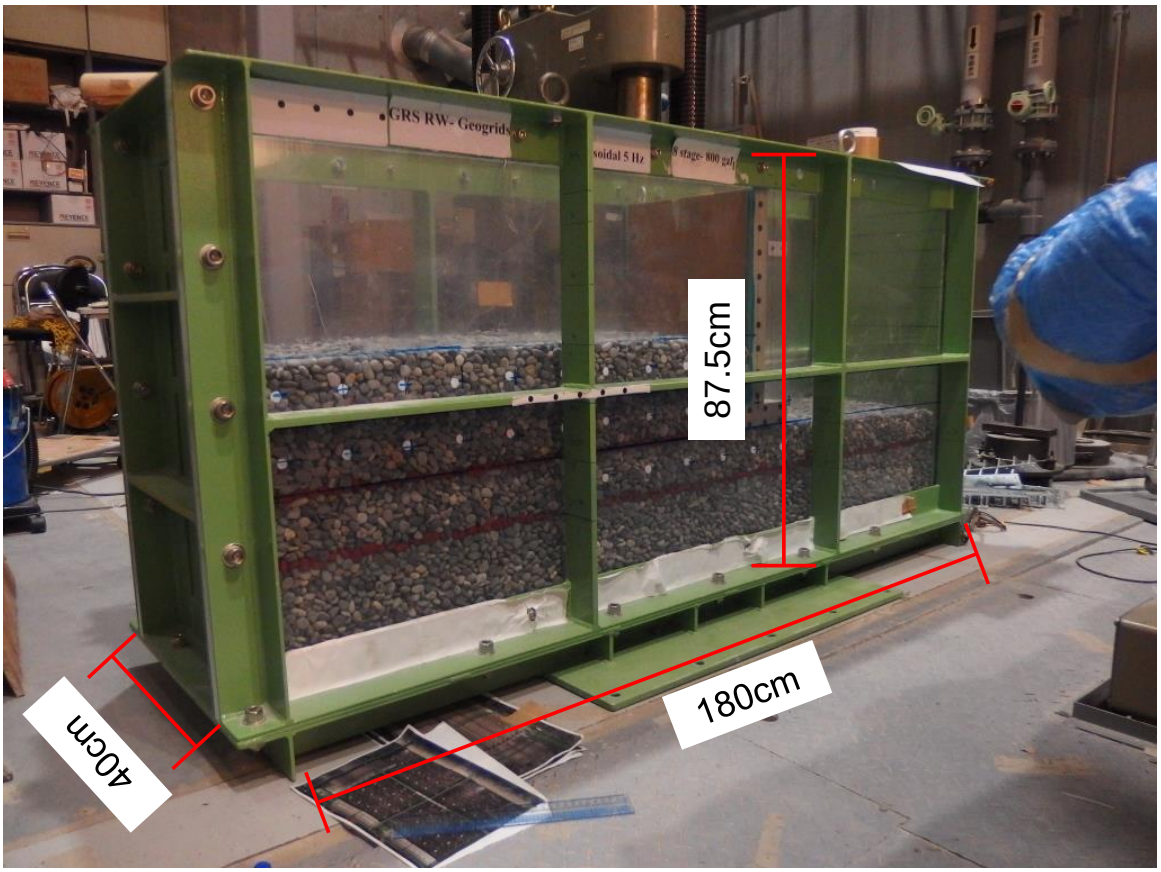

Fig. 3.11 Strong soil container

3.3.3 Model wall materials

Model wall facing

As shown in Fig. 3.12a, assuming a scale down factor of 1/10, both geocell-RS RW model and geogrid-RS RW model are constructed by a full-height rigid (FHR) facing panel (Tatsuoka. et al. 2007) having a size of 395 mm in width, 500 mm in height and 30 mm in thickness. The entire FHR facing panel weighs 16 kg, the rigidity of which is maintained during preparation and testing.

As shown in Fig. 3.12b, the T-shape RW is constructed by a FHR facing (395 mm-wide × 450 mm high × 45 mm thick) strongly connected with a spread-footing foundation (395 mm wide × 50 mm high × 200 mm thick) having a weight of 32 kg. All the wall models were made of duralumin with a similar density of concrete (ρ_d = 2.7 g/cm^3). The back face of T-shape RW and the bottom surface of the foundation directly in contact with the subsoil were made rough by being covered with a sheet of sand paper (# 150). In addition, the back faces of the FHR facings for the geogrid-reinforced RWs and geocell-reinforced RWs were also made rough by being covered with a sheet of sand paper (# 150). In order to minimize friction between the edge of the retaining wall models and the side glass wall of the soil box, a sponge tape and grease were used (Fig. 3.12b). This also prevented any leakage of sand from the gap between RW models and the soil container.

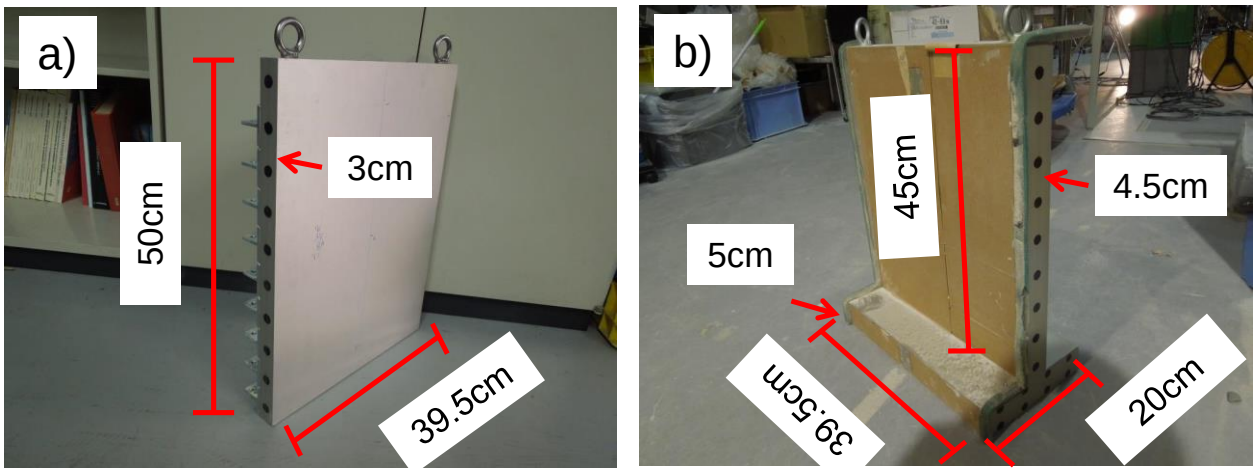

Fig. 3.12 a) A facing for GRS RW model; b) T-shape wall model

Reinforcements and clamps

For geogrid-RS RW models, two types of geogrids were prepared: Geogrid^{M} and Geogrid^{C}. Geogrid^{M} (Fig. 3.13a) was constructed by a set of regular grids comprising longitudinal members (made of thin and narrow phosphor-bronze strips, 0.2 mm thick × 3 mm wide) welded at nodes to transversal members (made of mild steel bar, 0.5 mm in diameter) at intervals of 35 mm. To effectively mobilize the friction between the reinforcement and the backfill, sand particles were glued on the surface of the strips. Strain gauges were attached to the reinforcements to measure the tensile force. The Geogrid^{M} reinforcement is 360 mm (length) × 350 mm (width) having a tensile strength of 10.6 kN/m. And Geogrid^{C} (Fig. 3.13b) is a commercial type geogrid with smaller aperture (6.3 mm × 6.3 mm) compared to Geogrid^{M}. It is made of polyester with tensile strength of 39.2 kN/m.

For geocell-RS RW models, the square-shaped geocell model reinforcements (Fig. 3.13c) were also set to 360 mm (length) × 350 mm (width), having six square cells in the longitudinal direction and seven square cells in the transverse direction. The height of the transverse member was 25 mm and the size of each cell was 60 mm × 50 mm. The geocell was made of polyester (PET) covered with PVC for protection, which is a relatively soft material that can be used in scaled-down model tests (Kongkitkul et al., 2007). The tensile strength of the members is 1700 N/3cm. Note that the geometric shape and arrangement of reinforcements in GRS RWs are determined by referring to those actual one considered scale factor of 1/10.

As shown in Fig. 3.14, two types of clamps for geogrid reinforcement and geocell reinforcement, respectively, were designed to provide a perfectly rigid reinforcement-facing wall connection by preventing the slippage of the reinforcement layers relative to the facing wall.

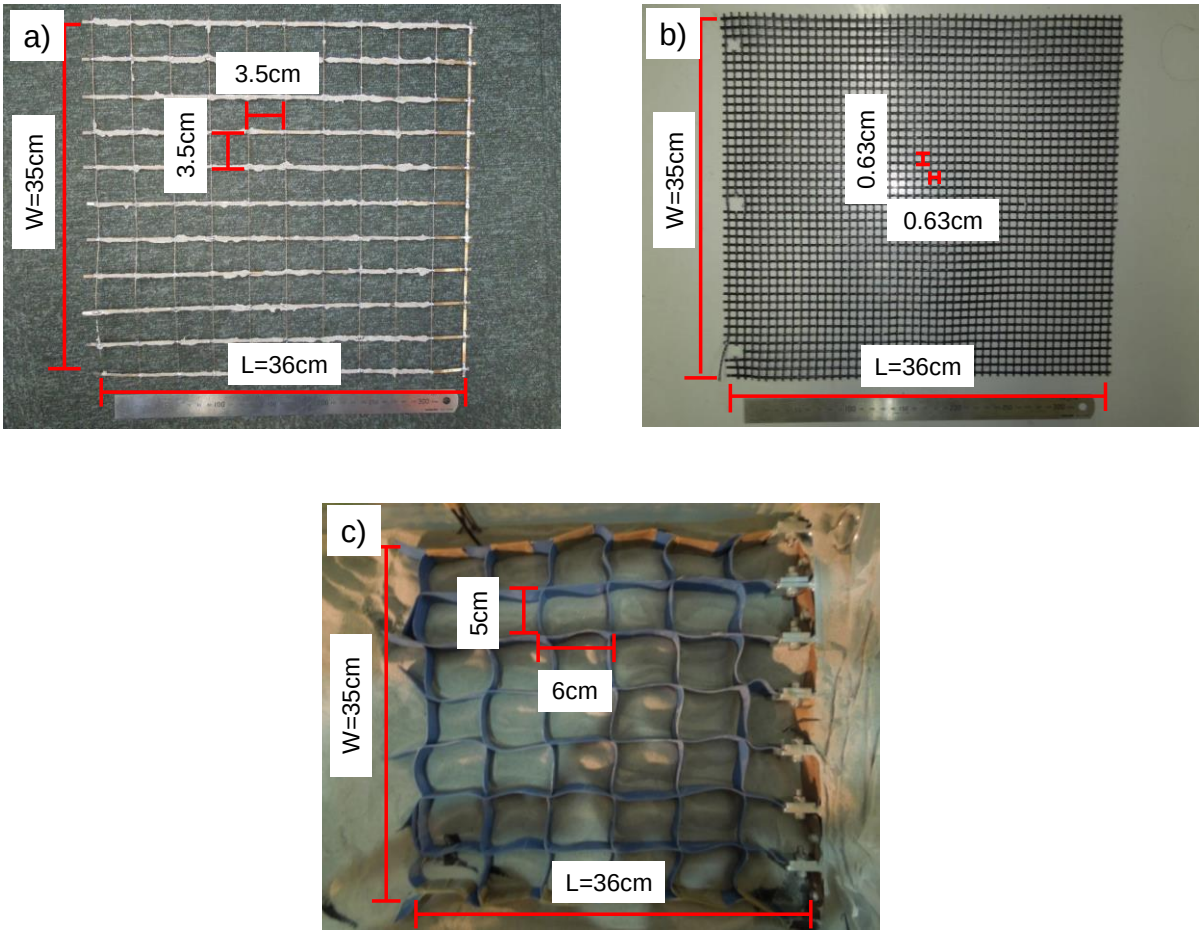

Fig. 3.13 Photos of: a) geogrid^{M}; b) geogrid^{C} and c) geocell model

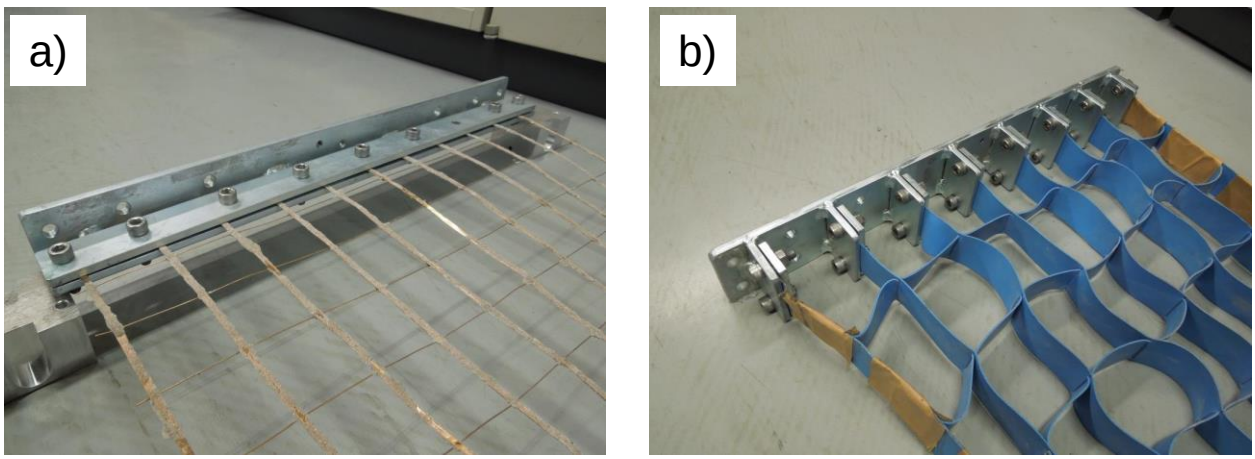

Fig. 3.14 Photos of: a) clamp for geogrid; b) clamp for geocell model

Backfill soil and subsoil

Figs. 3.15, 3.16 and 3.17 show the cross-sections of three different retaining wall models. As can be seen, the thickness of subsoil is 30 cm. In this study, two types of soil materials were used: Silica sand No.7 (D_{50}=0.25 mm, U_c=2.2) and Gravel No.5 (D_{50}=14.2 mm; U_c=1.44, Fig. 3.18).

In the case of sand, the subsoil and backfill soil were produced by air pluviating air-dried Silica No.7 sand (D_{50}=0.25mm, U_c=2.2) to obtain a relative density about 90% (ρ_d=1.5g/cm^3). The multi-sieve equipment used in this study for air pluviation method is shown in Fig. 3.19 and the influence of height of multi-sieve equipment above the surface of the ground has been checked, showing that the relative density can be reached around 90% by using passing plate with holes of 10 mm-diameter when the height is over 40 cm which is satisfied the requirement of this experiment.

In the case of gravel, the compaction degree is controlled to 100% (ρ_d=1.78 g/cm^3) by manual hand-held plate compaction method. As shown in Fig. 3.20, gravel material are placed in a number of layers with each layer compacted to a prescribed dry unit weight while its density is controlled by adjusting the height of the layer.

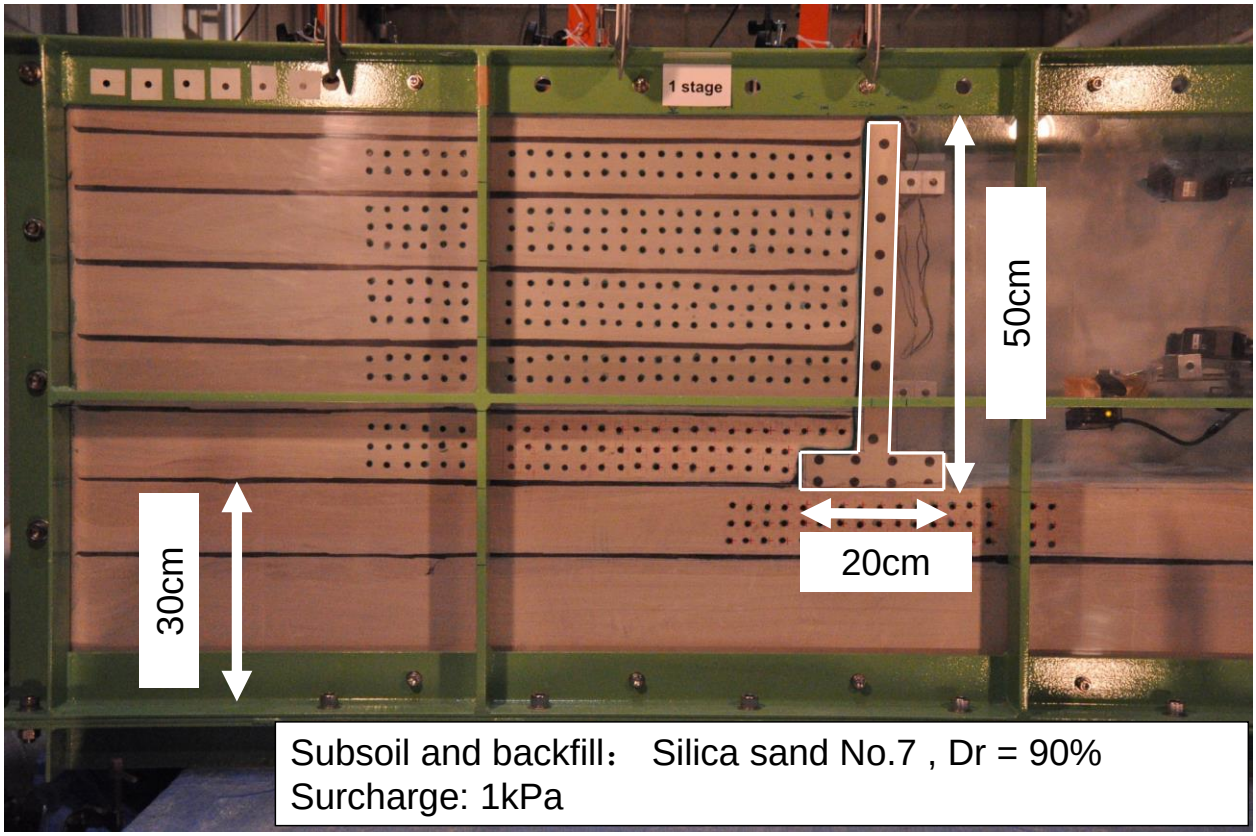

Fig. 3.15 Cross-section of T-shape RW model

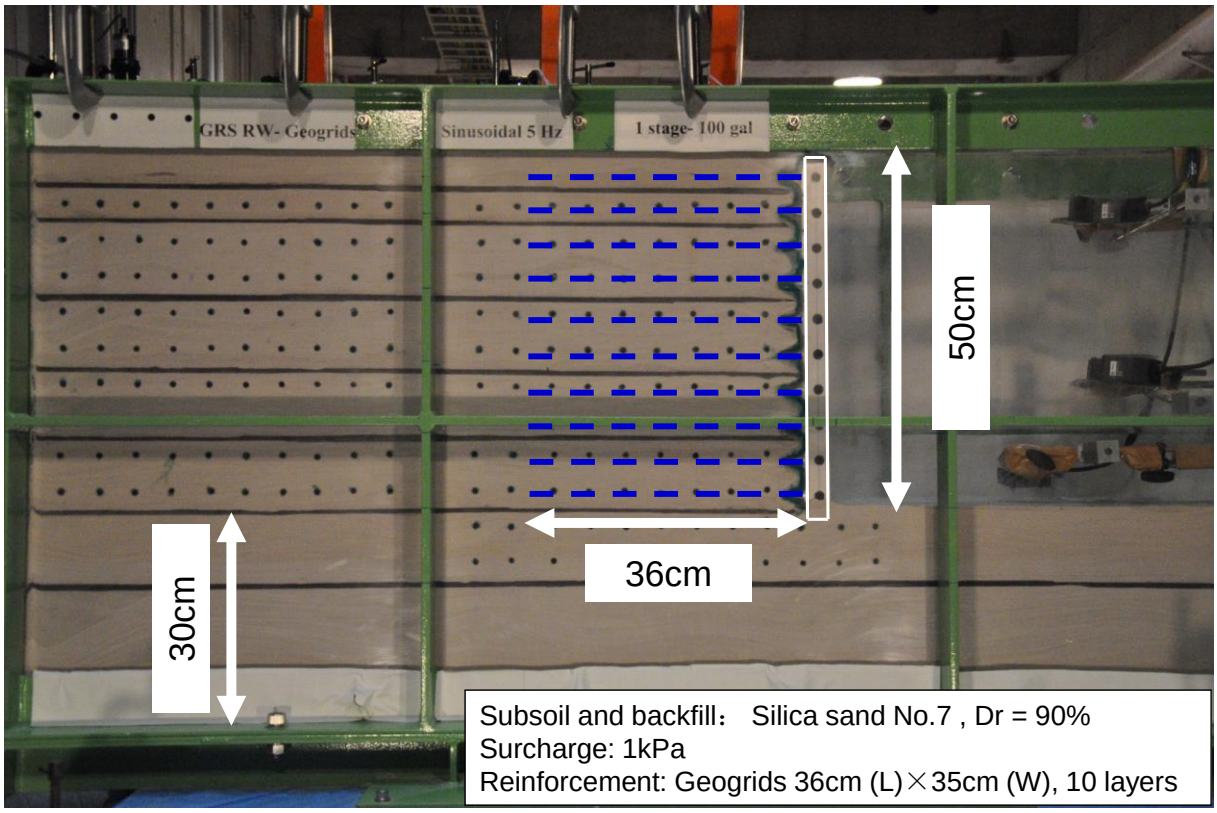

Fig. 3.16 Cross-section of geogrid-RS RW model

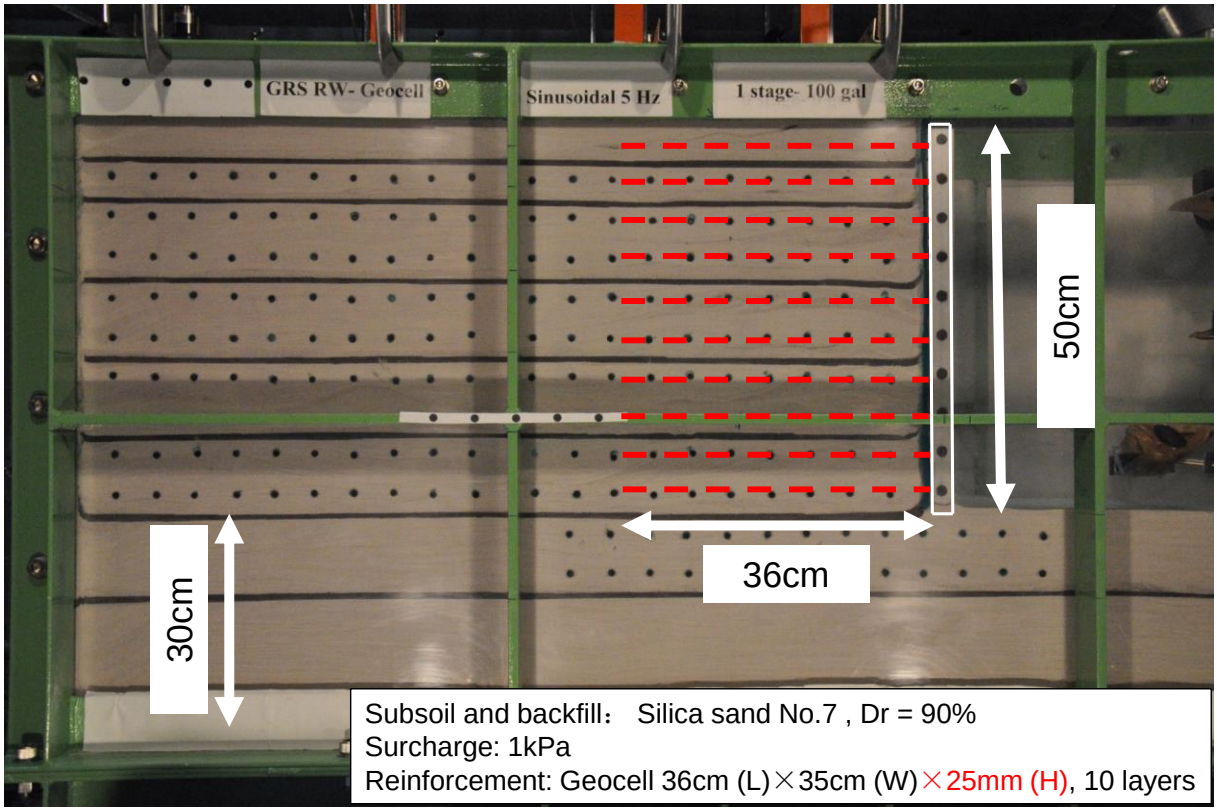

Fig. 3.17 Cross-section of geocell-RS RW model

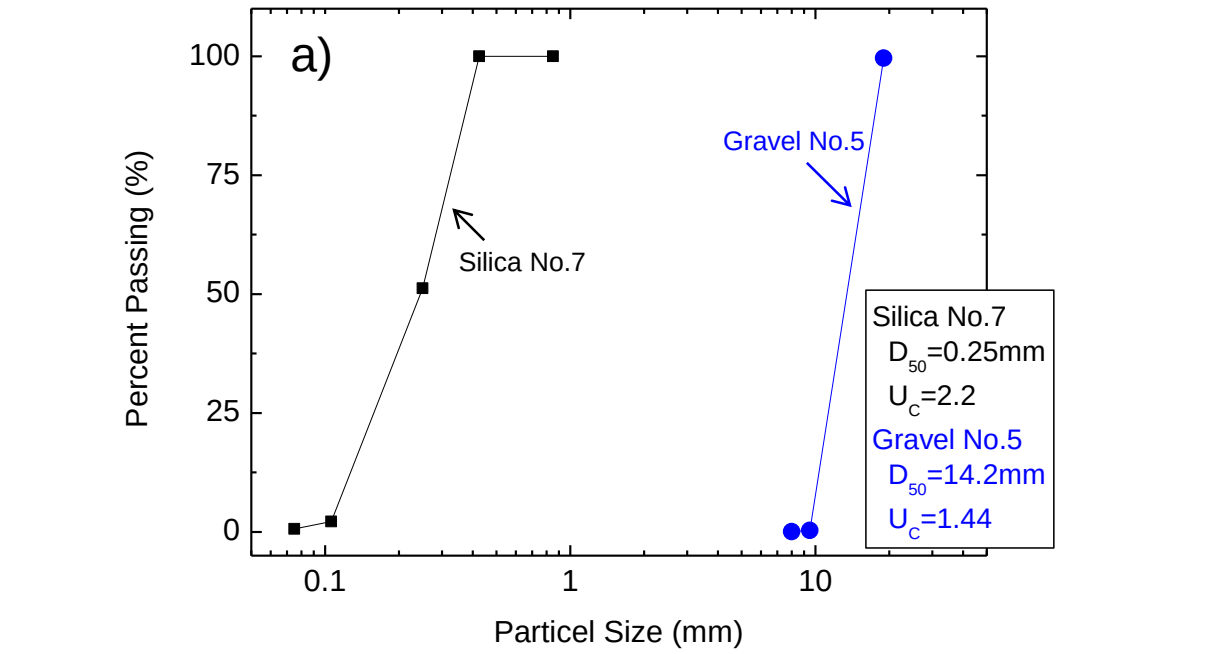

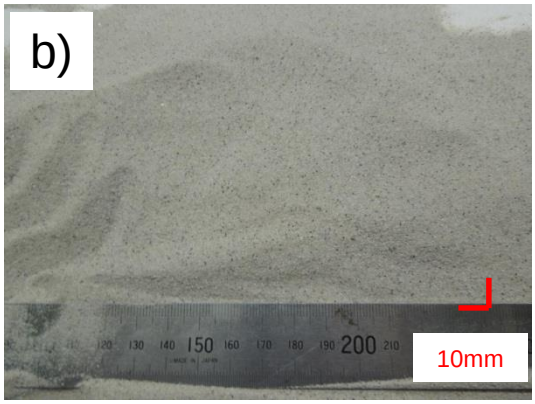

Silica No.7 (D_{50}=0.25mm)

Gravel No.5 (D_{50}=14.2mm)

Fig. 3.18 Properties of backfill soil materials: a) Particle size distributions; 2) Silica sand No.7; 3) Gravel No.5

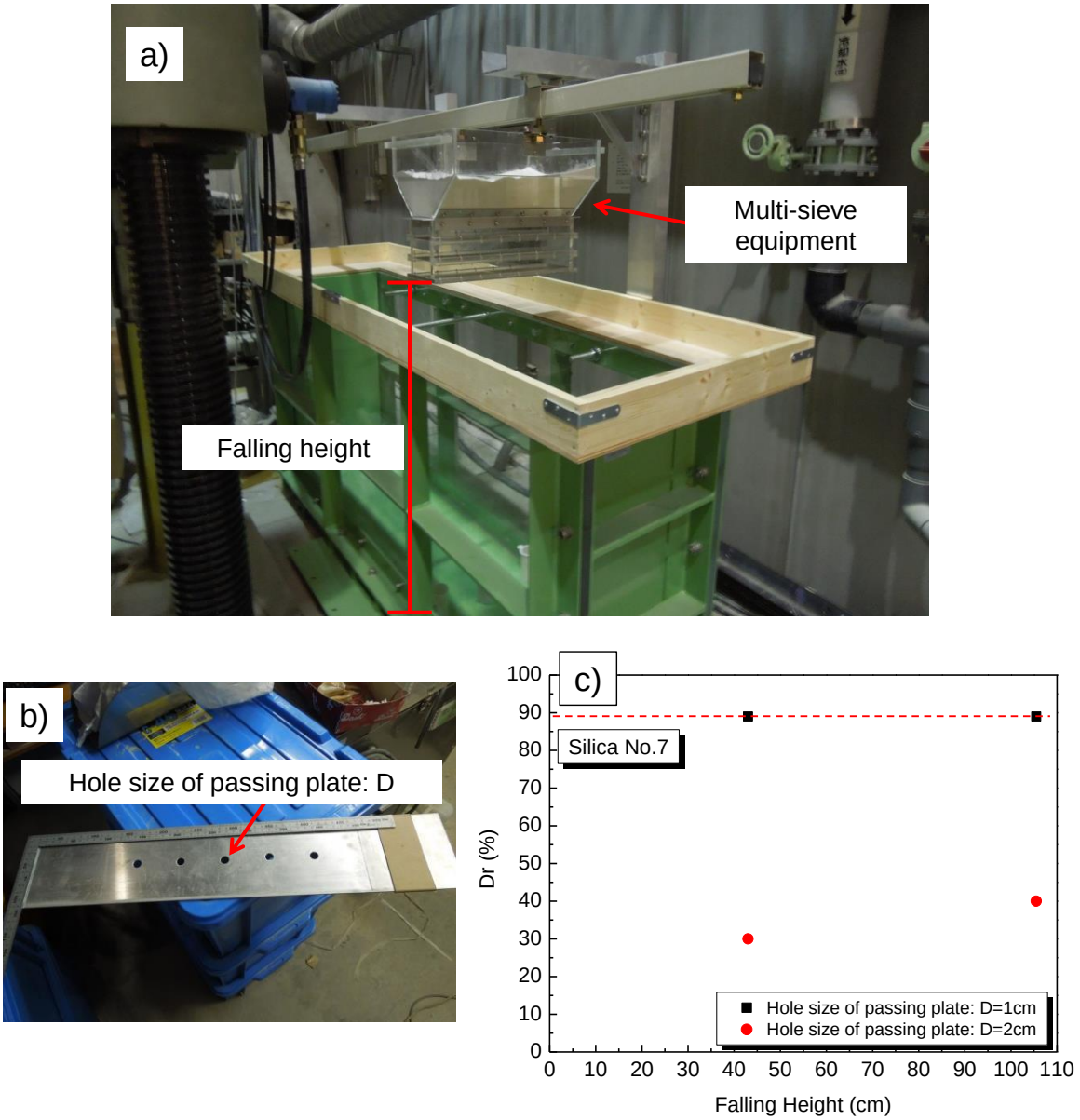

Fig. 3.19 Air pluviation method for sand: 1)multi-seive equipment; 2) passing plate; 3) influence of falling height and hole size of passing plate

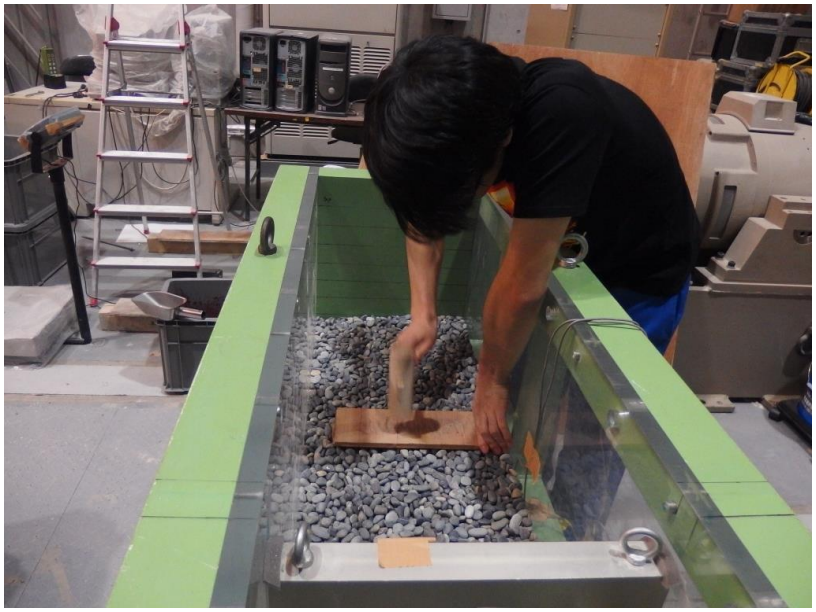

Fig. 3.20 Manual hand-held plate compaction method for gravel

Markers and horizontal layers

As shown in Fig. 3.21, to capture the deformation of the backfill throughout the shaking tests, in the case of sand, thin horizontal layers with a width of about 5 mm of black-dyed Silica sand were placed at a vertical spacing of 100 mm immediately behind the front transparent glass window of soil box. In addition, a number of rivets made of aluminum with a black circular flat edge were used as targets and set into the backfill soil adjacent to the transparent glass window at a horizontal spacing of 50 mm and a vertical spacing of 50 mm for the purpose of measuring two-dimensional deformation of the backfill. In order to ensure permanent contact between the glass and the targets, thereby following the surrounding sand movement, silicon grease is smeared between the targets and the glass.

In the case of gravel, red horizontal layers of gravel were placed at a vertical spacing of 100 mm immediately behind the front transparent glass window of soil box. White rivets having a similar size of the gravel particles were used as targets and set into the backfill gravel adjacent to the transparent glass window at a horizontal spacing of 100 mm and a vertical spacing of 100 mm.

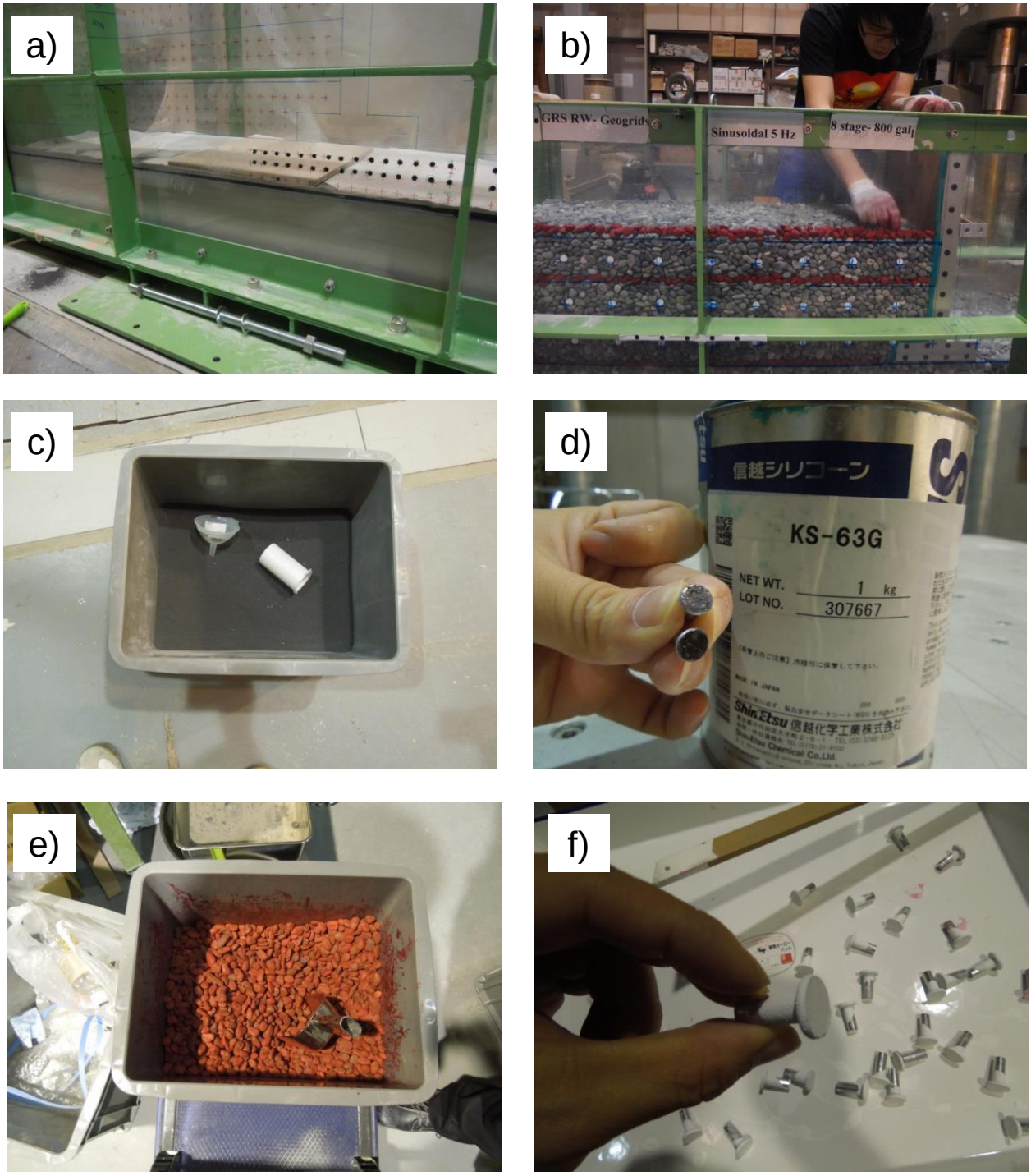

Fig. 3.21 Markers and colored horizontal layer: a) in the case of sand; b) in the case of gravel; c) black-dyed sand for horizontal layer; d) black markers and grease for sand; e) red gravel for horizontal layer; f) white markers for gravel.

Surcharge

After filling the sand, a surcharge of 1 kPa was applied by placing lead shots on the surface of the backfill to simulate the weight of the road base for railways or highways.

Similitude

In order to quantitatively predict the behavior of the prototype structure from the model response, the model should be scaled-down from the full-size structure. Several researchers (i.e. Kagawa, 1978; Iai, 1989 etc.) have developed a number of expressions to correlate the model quantities with corresponding prototype quantities, based on so-called similitude rules (Rocha, 1957). Yamaguchi et al. (1976), Helter and Gudeus (1988), Tatsuoka et al. (1989) found that not only the geometrical scale factor should be considered, but also the scale of stress. In particular, Tatsuoka et al. (1989) concluded that the results of 1-G shaking table model test would be influenced by these two phenomena, namely the pressure level and particle size effects. Despite the inherent limitations of model tests, they have been widely used to investigate the basic mechanism of the prototype structure.

Based on previous research, Table 3.2 shows typical scale factors for the primary parameters in reduced-scale shaking table model tests. In this thesis, the geometrical scale factor of λ=10 was used.

Table 3.2 Scale factors for different physical quantities in reduced-scale model shaking table tests

Physical quantities	Symbol	Scale factor (model/prototype)
Density	ρ	1
Length	l	$1/\lambda$
Stress	σ	$1/\lambda$
Strain	ε	$1/\sqrt{\lambda}$
Frequency	f	$\lambda^{3/4}$
Acceleration	g	1

3.3.4 Instrumentation and base excitation

The accelerations, deformations and earth pressure were measured using accelerometers and displacement transduces (i.e. laser sensors and LVDT sensors) and load cells, respectively. These transducers are positioned at predefined locations during the step by step construction of the retaining wall models as shown in Fig. 3.22.

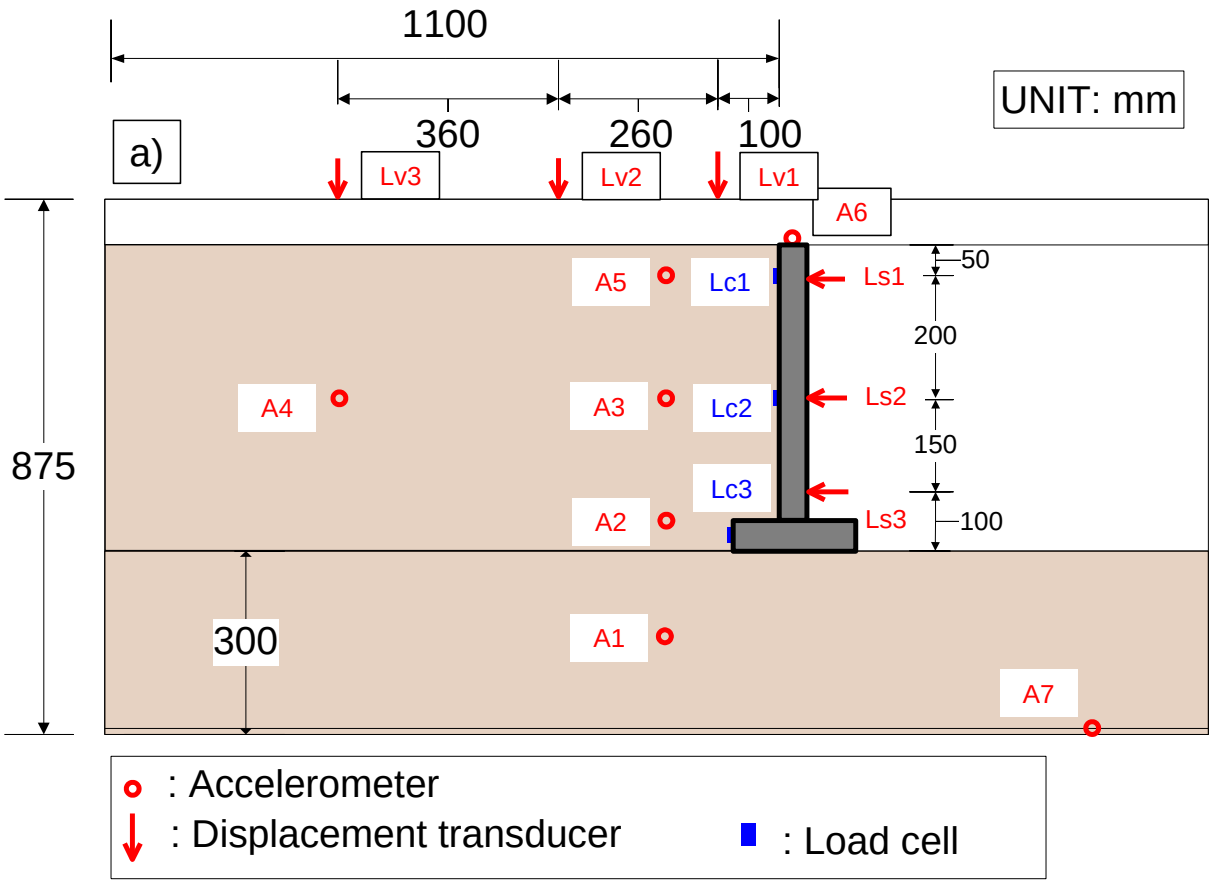

Fig. 3.22 Schematic diagram of cross-section of a) T-shape RW model

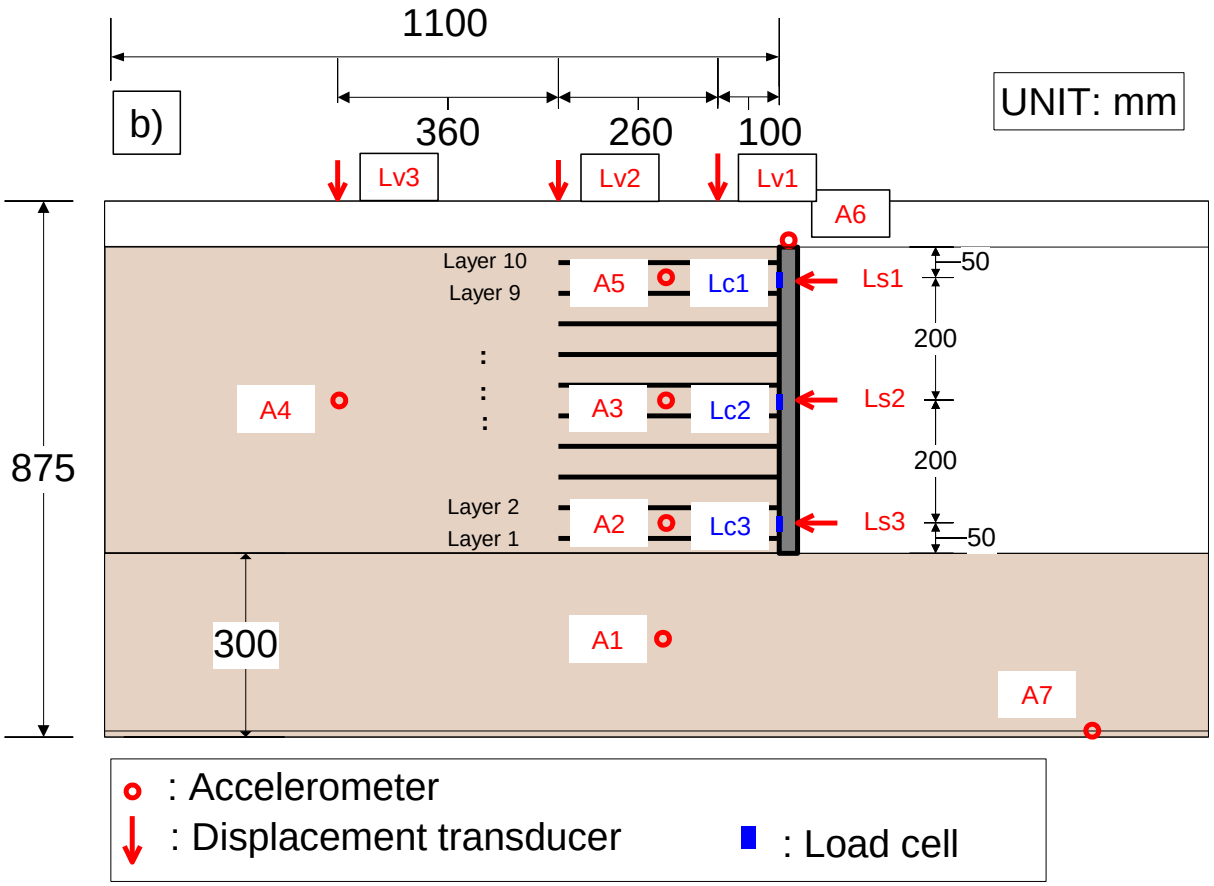

Fig. 3.22 (Continued) Schematic diagram of cross-section of b) GRS RW model

Displacement transducers

Deformations of facing wall were measured using laser sensors attached to rigid bars which were fixed firmly to the soil container. Deformation of the facing wall were measured at three points from top to bottom along the centerline of the facing wall as shown in Figs. 3.22 and 3.23. The laser transducers (Fig. 3.23b) used in this study were manufactured by Kenyence Corporation. Laser sensor LB-300 with a capacity of 100 mm was selected to measure the bottom displacement of the wall (L_S1), and laser sensor LK-G405 with a capacity of 100 mm was selected to measure the top and middle displacement of the wall (L_S2, L_S3).

The settlements of the backfill behind the wall were also measured using three vertical LVDT sensors connected to the soil container frame with stiff beams (Fig. 3.24a). The LVDT (Fig. 3.24b) were made by Tokyo Sokki Kenkyujo Co. Ltd. with a capacity of 100 mm. In addition, rigid plates were placed on the top of the backfill at predefined position as a target for the LVDT. In addition, high speed camera and digital camera were used in this study to capture the deformation of the retaining wall during shaking.

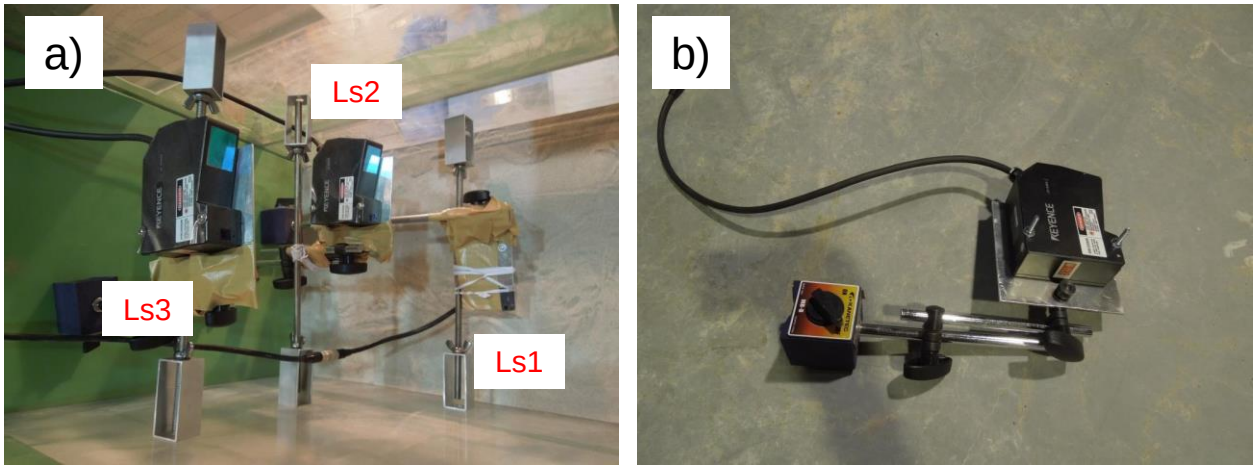

Fig. 3.23 a) Installation of laser transducers; b) laser transducer (LK-G405)

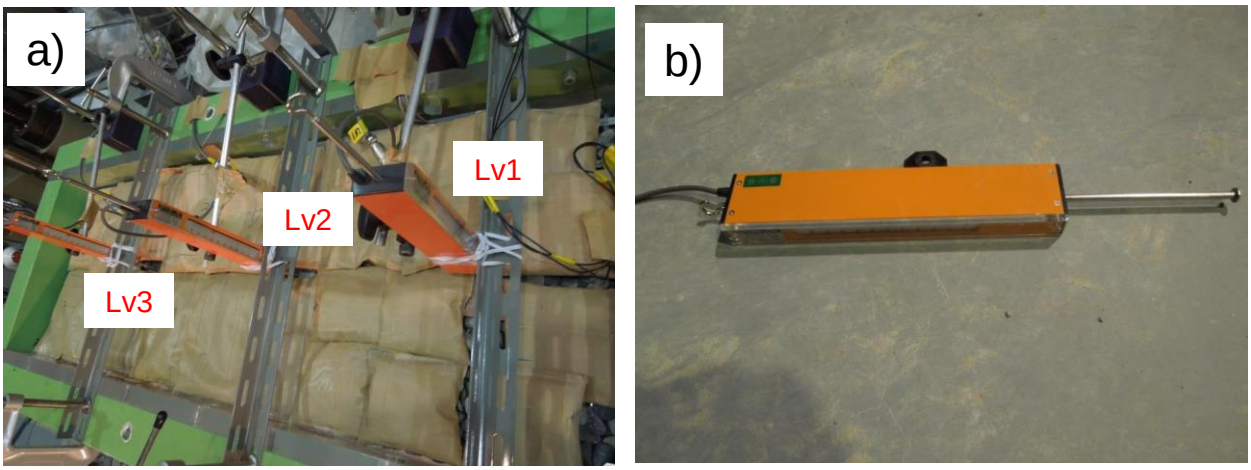

Fig. 3.24 a) Installation of LVDT; b) LVDT

Accelerometers

From Fig. 3.22, in total seven accelerometers were positioned at predefined locations. One accelerometer (A7) was attached to the container base to measure the base acceleration. Alternatively, another accelerometer (A6) was attached to the top of the wall to measure the response acceleration of the wall. The response acceleration of various reinforced backfill zones (A2, A3 and A5) were measured by three accelerometers located vertically in line 180 mm away from the wall face and along the box center-line to reduce boundary effects. Another accelerometer (A4) was positioned into the unreinforced backfill zone along the box centerline, 720 mm far from the wall facing to quantify the far-field response. The last accelerometer (A1) was embedded into the foundation subsoil. Accelerometer Model AS-2GB with a capacity of 2 g manufactured by Kyowa Electronic Instruments Co. Ltd. Inc. was selected. To avoid tilting during shaking, the accelerometers embedded into the soil deposit were attached to aluminum plates measuring nominally 50 mm × 50 mm and 3 mm thick, as shown in Fig. 3.25.

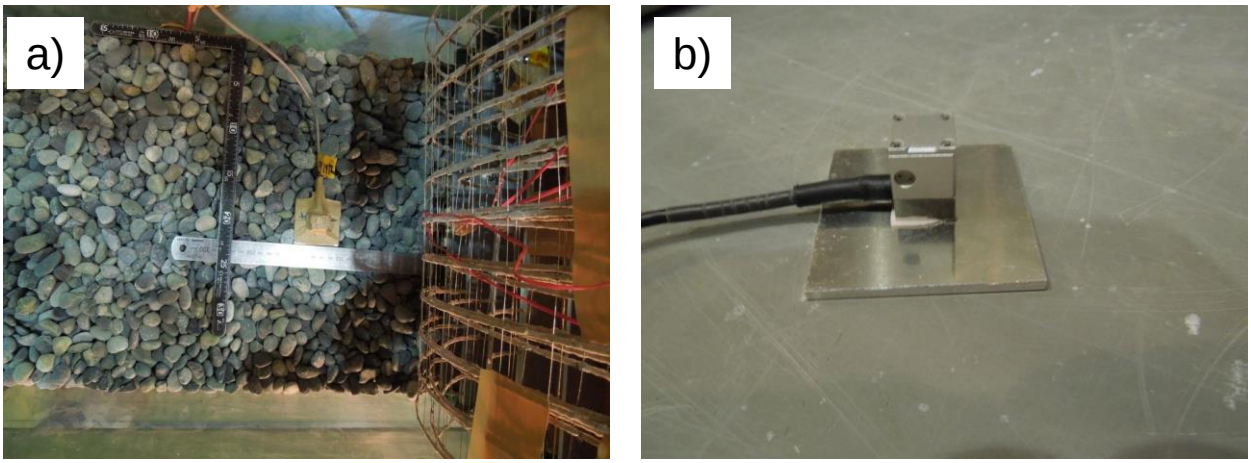

Fig. 3.25 a) Installation of accelerometer sensors; b) Accelerometer Model AS-2GB attached to an aluminum plate

Load cells

As schematically shown in Fig. 3.22, three load cells were used to measure the earth pressure at the back of the facing wall and along the centerline of the wall at three different elevations. The load cell (Fig. 3.26a) was selected as MC-2L made from TOYO SOKKI CO. Ltd. Each load cell is capable of measuring forces up to 20 N. Fig. 3.26 shows the installation of the load cell for different types of retaining wall models. Each load cell is encapsulated in a block, which is connected to the back of wall by two bolts. The size of load cell (100 mm in diameter) allows easy placement into the block with no adverse effect. A regular rigid plate is placed on the surface of the load cell by using bolts or tape to fix. In addition, two different types of blocks were designed to meet the requirement of different types of reinforcement clamps. However, it is anticipated that, although so, the test results as shown in Chapter 5 are not accurate enough, so that better load cell set up should be used in the future to provide more reliable test results.

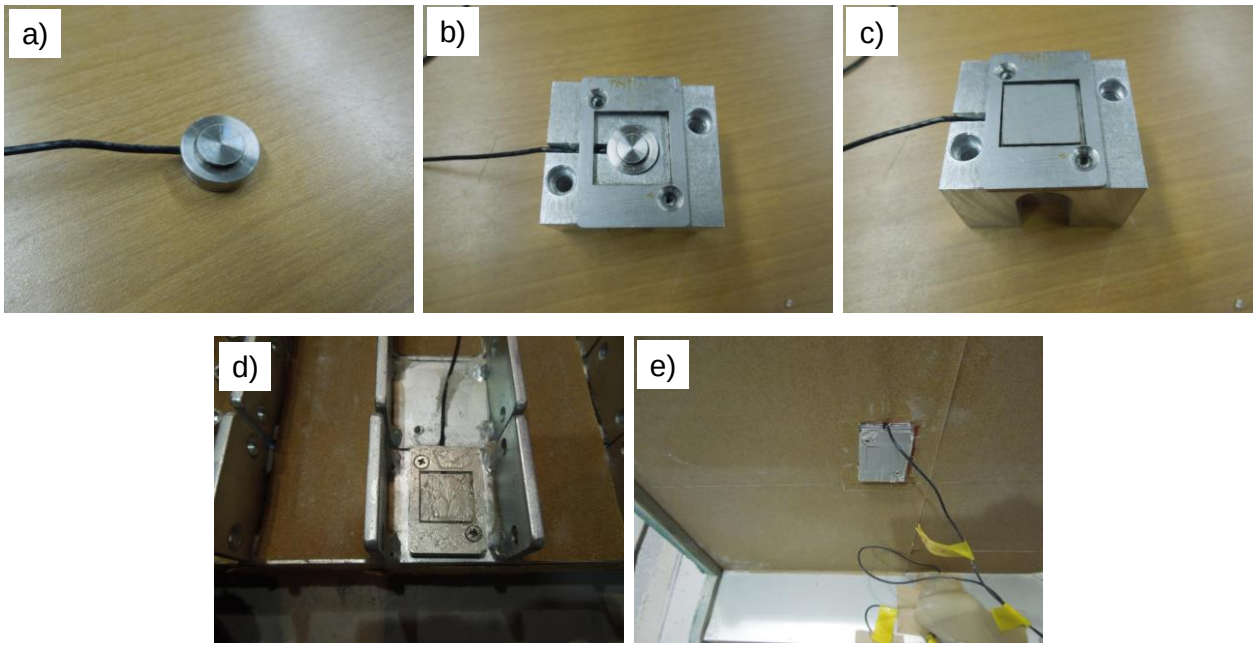

Fig. 3.26 a)-c) Installation of load cell for geogrid-RS RW; d) Installation of load cell for geocell-RS RW; e) Installation of load cell for T-shape RW

Base excitation

Considering the similitude for the model test (Table 3.2), each retaining wall model was subjected to twenty cycles per stage of harmonic sinusoidal base acceleration motion at a predominant frequency f_i=5 Hz. The acceleration amplitude was increased stage by stage with a target increment of 100 gal from 100 gal until the failure or collapse of the retaining wall model was observed (Fig. 3.27). It simulates both level of the peak ground acceleration level and predominant frequency of severe earthquakes in the full scale, in particular, the 1995 Hyogoken-Nambu Earthquake, or Kobe Earthquake with the highest peak ground acceleration of 818 gals and the predominant frequency of 1~3 Hz in a broad sense. Then the base excitation in this model tests was designed by the scale factor of 1/10 (Muñoz, 2010). In addition, such a frequency was selected to allow comparison of existing results by other shaking table model tests carried out at this frequency of excitation (Mathsuo et al. 1998, Watanabe et al. 2003).

Strain gauges

Geogrid^M is made of phosphor-bronze. As a result, strain gages (KFG) with an amplifier (DB-120T-8) manufactured by Kyowa Electronic Instruments Co. Ltd. Inc. were selected and attached to the geogrids by the two-gage method.

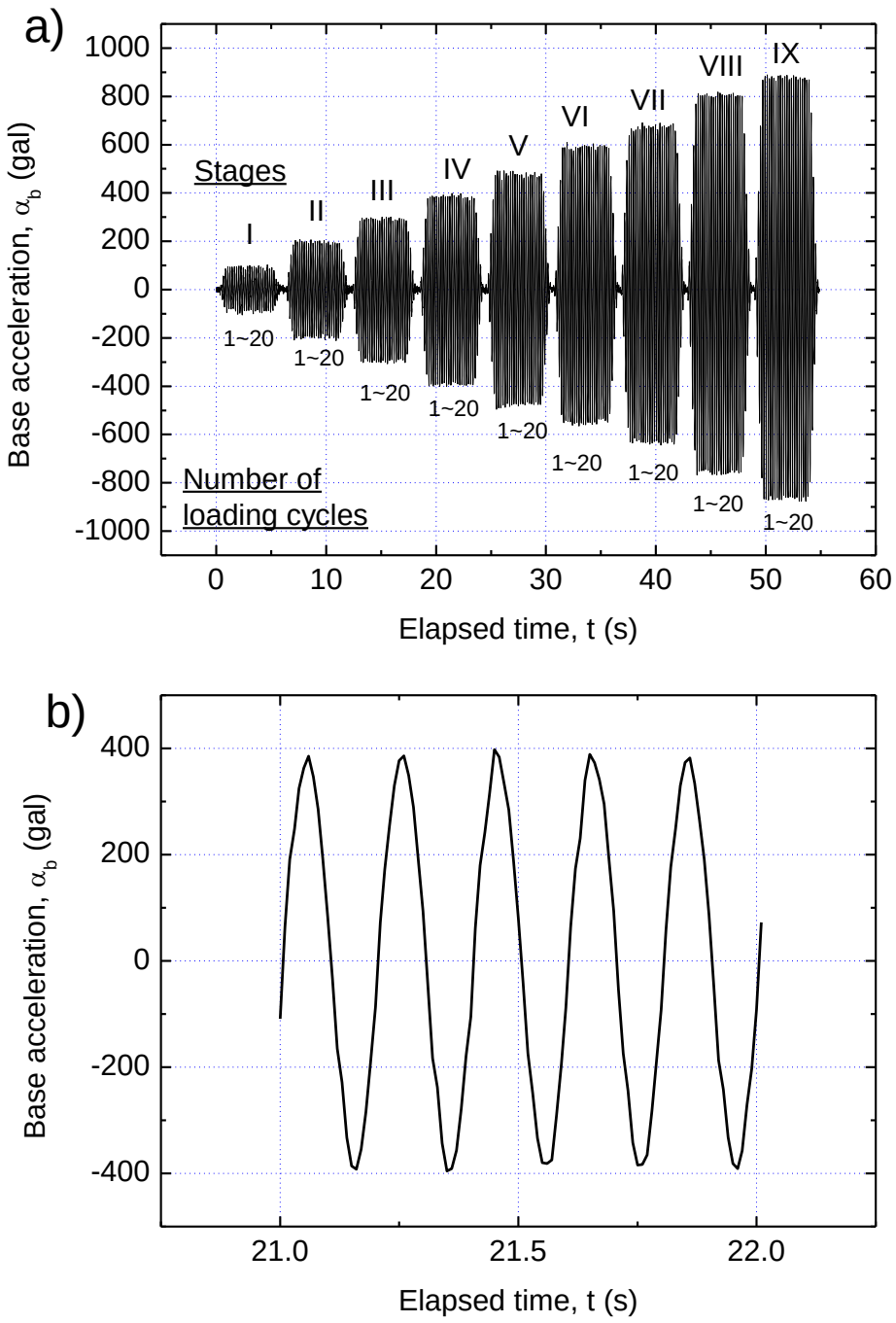

Fig. 3.27 Input base acceleration characteristics: a) Base input acceleration; b) One-second window.

3.3.5 Construction procedures of retaining wall models

The staged construction procedure for GRS RW with FHR facing and its advantage has been discussed in Chapter 1 by referring to Tatsuoka et al. (2007). In this study, the model wall was not constructed entirely following the staged manner for full-scale retaining. Rather, a similar but simplified method was introduced. The staged construction of the model wall involved the following steps:

(1) Prepare the subsoil deposit by using the air-pluviation method (for the backfill of sand, Fig. 3.19) and the manual hand-held plate compaction method (for the backfill of gravel, Fig. 3.3-20), at the same time, the thin horizontal layer and the markers are placed at specified position as described in Fig. 3.21.

(2) Fix the clamps to the back of the wall facing.

(3) Set up the wall facing on the subsoil deposit and brace the wall facing by two or three steel bars (Fig. 3.28)

(4) Connect the reinforcement to the clamps, and incorporate the horizontal thin layer and markers and place accelerometers on the specified position for one layer construction. Care should be taken not to impart any tension to the reinforcement, since this could alter the stress condition of the model prior to shaking.

(4) Prepare the backfill soil deposit layer by layer following the same as at point (1)

(5) Upon completion of compaction of all layers, the facing braces can be removed.

(6) Set up the laser sensors, LVDT sensors to the predefined locations (Figs. 3.22, 3.23 and 3.24), and link all the instrumentations to the data acquisition system, EDX-200A.

(7) Set up the digital camera, initialize the data acquisition and start the test.

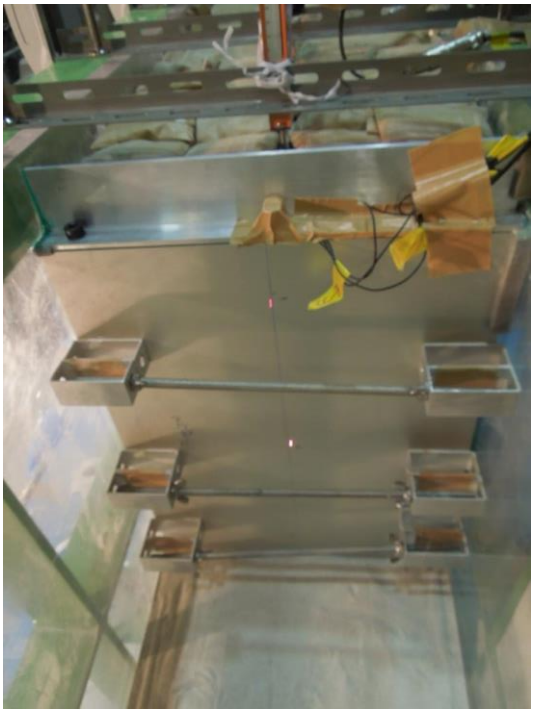

Fig. 3.28 Steel bars to support the wall facing during construction of backfill

3.4 References

1. Bathurst, R.J., Hatami, K. and Alfaro, M.C. (2002). "Geosynthetic reinforced soil walls and slopes: seismic aspects", Geosynthetics and Their Applications (S.K. Shukla Ed.), Thomas Telford, 327-392.
2. Hettler, A. and Gudehus, G. (1988). "Influence of the foundation width on the bearing capacity factor", Soils and Foundations, 28(4), 81-92.
3. Iai, S. (1989). "Similitude for shaking tests on soil structure-fluid models in 1g gravitational fields", Soils and Foundations, 29(1), 105-118.
4. Kagawa, T. (1978). "On the similitude in model vibration tests of earth structures". Proc. of Japan Society of Civil Engineers, No. 275, pp. 69-77. (In Japanese)
5. Matsuo, O. Tsutsumi, T., Yokoyama, K. and Saito, Y. (1998). "Shaking table tests and analyses of geosynthetic-reinforced soil retaining walls", Geosynthetics International, 5(1&2), 97-126.
6. Kongkitkul, W., Hirakawa, D. and Tatsuoka, F. (2007). "Viscous behaviour of geogrids; experiment and simulation", Soils and Foundations, 47(2), 265-283.
7. Koseki, J., Bathurst, R.J., Güler, E., Kuwano, J., and Maugeri, M. (2006). "Seismic stability of reinforced soil walls", Proceedings of the 8th International Conference on Geosynthetics, Yokohama, Japan, 51-77.
8. Minažek. K. and Mulabdić. M. (2013). "A review of soil and reinforcement interaction testing in reinforced soil by pullout test", GRAĐEVINAR 65 (3), 235-250.
9. Muñoz, H. (2010). "Dynamic performance of conventional type and reinforced soil bridges", Master Thesis, Department of Civil Engineering, Tokyo University of Science.
10. Palmeira, E.M. (2008). "Soil-geosynthetic interaction: modeling and analysis", Proc. of 4th European Geosynthetics Conference, Edinburgh, 1-30.
11. Rocha, M. (1957). "The possibility of solving soil mechanics problems by the use of models", Proceedings of the 4th ICMSFE, 1, 183-188.
12. Tatsuoka, F., Tani, K., Okahara, M., Morimoto, T., Tatsua, M., Takagi, M. and Mori H. (1989). "Discussion of Influence of the foundation width on the bearing capacity factor by Hettler y Gudehus (1988)", Soils and Foundations, 29(4), 146-154.
13. Tatsuoka, F., Tateyama, M., Mohri, Y. and Matsushima, K. (2007). "Remedial treatment of soil structures using geosynthetic-reinforcing technology". Geotextiles and Geomembranes, 25(4-5): 204-220.
14. Watanabe, K., Munaf, Y., Koseki, J., Tateyama, M. and Kojima, K. (2003). "Behaviors of several types of model retaining walls subjected to irregular excitation", Soils and Foundations, 43(5), 13-27.
15. Yamaguchi, H., Kimura, T. and Fuji-I, N. (1976). "On the foundation of progressive failure on the bearing capacity of shallow foundations in dense sand", Soils and Foundations, 16(4), 11-22.

4 EVALUATION ON THE PULLOUT CHARACTERISTICS OF NEWLY-DEVELOPED GEOCELL

4.1 Introduction

In this chapter, evaluation of the pullout characteristics of a newly-developed geocell (i.e. square-shaped geocell) is conducted by laboratory pullout tests. Firstly, by comparison between the newly-developed square-shaped geocell and traditional diamond-shaped geocell, different pullout behaviors and different stress-deformation mechanisms were found. Secondly, the pullout behavior of square-shaped geocell is compared with that of a commercial geogrid, which is commonly used as a tensile reinforcement for GRS RWs. This is to investigate whether or not a square-shaped geocell can be used to replace the traditional type reinforcement (i.e. geogrid) as a tensile reinforcement, especially in view of the advantage of efficiently confining large soil particles. Based on this research, the basic pullout mechanism of a square-shaped geocell was found to be different from that of geogrids, as summarized in Chapter 2 (Fig. 2.6). In addition, some drawbacks of square-shaped geocells compared with geogrids are presented and feasible improvements are proposed for the construction work.

As described in Chapter 2, reinforcements with 3-D structure have the advantage of providing high pullout bearing resistance by transversal members (Racana et al., 2003; Khedkar et al., 2009; Horpibulsuk et al., 2010; Suksiripattanapong et al., 2013). Therefore, the combined effects of geocell height and the particle size of backfill soil on interface mechanisms between the geocell and adjacent backfill soil were investigated. A conceptualized pullout interaction mechanism was proposed based on the test results. In addition, other influential factors (i.e. the spacing between transversal members) on the pullout resistance of square-shaped geocell were also investigated.

4.2 Comparison between newly-developed geocell and traditional-type geocell behaviors

Many studies have been carried out on the performance of traditional diamond-shaped geocells as base reinforcement subjected to vertical loads, showing outstanding features e.g. efficient soil confinement, increasing bearing capacity etc. However, very limited research has been conducted on the tensile function of tradition type geocells. In this section, the pullout characteristics of a newly-developed square-shaped geocell (Fig. 3.7a) and traditional-type diamond-shaped geocell (Fig. 3.7b) are evaluated by using two types of backfill materials, Gravel No.1(D_{50}=3.2 mm) and Gravel No.3 (D_{50}=7.5 mm, Figs. 3.5 and 3.6). The test cases are shown in Table 4.1.

Table 4.1 Test cases for diamond-shaped geocell and square-shaped geocell.

Test number	Reinforcement	Reinforcement height (mm)	Cell or grid size (mm)	Backfill materials[A)]	Opening height of front wall (mm)
DG1-A	Diamond-shaped geocell	25	50 × 60	Gravel No.1	46.5
DG3-A	Diamond-shaped geocell	25	50 × 60	Gravel No.3	46.5
SG1-A	Square-shaped geocell	25	50 × 60	Gravel No.1	46.5
SG3-A	Square-shaped geocell	25	50 × 60	Gravel No.3	46.5

A) Gravel No.1: D_{50} = 3.2 mm; Gravel No.3: D_{50} = 7.5 mm (Figs. 3.5 and 3.6)

4.2.1 Typical test results

Typical pullout test results on square-shaped geocell and diamond-shaped geocell embedded in Gravel No.1 and Gravel No.3 are presented in Fig. 4.1. The pullout resistance (P) versus horizontal displacement (d_{60}) of geocells is plotted in Figs. 4.1a and 4.1c, while the vertical displacement (V_{60}) of the backfill surface and horizontal displacement (d_{60}) of geocells is plotted in Figs. 4.1b and 4.1d. It is found that square-shaped geocell shows both higher peak pullout resistance and higher pre-peak stiffness than diamond-shaped geocell in both soil materials.

It is interesting to note that, for square-shaped geocell embedded in Gravel No.1, with increasing pullout horizontal displacement (d_{60}) there is a high peak pullout resistance indicating a contribution from dilatancy of soil, and then as pullout continues the resistance decreases to a residual state (Figs. 4.1a and 4.1b). The peak pullout resistance is mobilized when the tangential slope of the V_{60}-D_{60} relation becomes the maximum (Figs. 4.1a and 4.1b). This trend of behavior is essentially the same as that of unreinforced granular soils. It is likely therefore that the mobilization of peak pullout resistance in the tests with square-shaped geocell can be associated with the mobilization of the peak shear strength of the backfill zone adjacent to the geocell. However, when the shear strength in the adjacent backfill zone becomes the residual value, than the pullout resistance of geocell becomes its residual value.

Alternatively, for diamond-shaped geocell embedded in Gravel No.1, the dilatant contribution is lower than that of square-shaped geocell (Figs. 4.1b). This is can be associated with the fact that the value of the pullout resistance is lower than that of square-shaped geocell for both peak state and residual state (Figs. 4.1a).

As shown in Figs. 4.1c and 4.1d, the pullout behavior of square-shaped geocell and diamond-shaped geocell embedded in Gravel No.3 was also investigated. Similar to the case of Gravel No.1, square-shaped geocell exhibits not only higher peak pullout resistance but also higher residual pullout resistance than diamond-shaped geocell (Fig. 4.2). Moreover, as the particle size increases from D_{50}=2.3 mm (Gravel No.1) to D_{50}=7.5 mm (Gravel No.3), the peak pullout resistance increases due to an increase of dilatancy for both diamond-shaped geocell and square-shaped geocell. Differences in the mobilization pattern of pullout resistance between the square-shaped geocell and diamond-shaped geocell are due to differences in the

mobilization mechanism of strength in the backfill that are caused by different geometries of geocell (Fig. 3.7), as explained below.

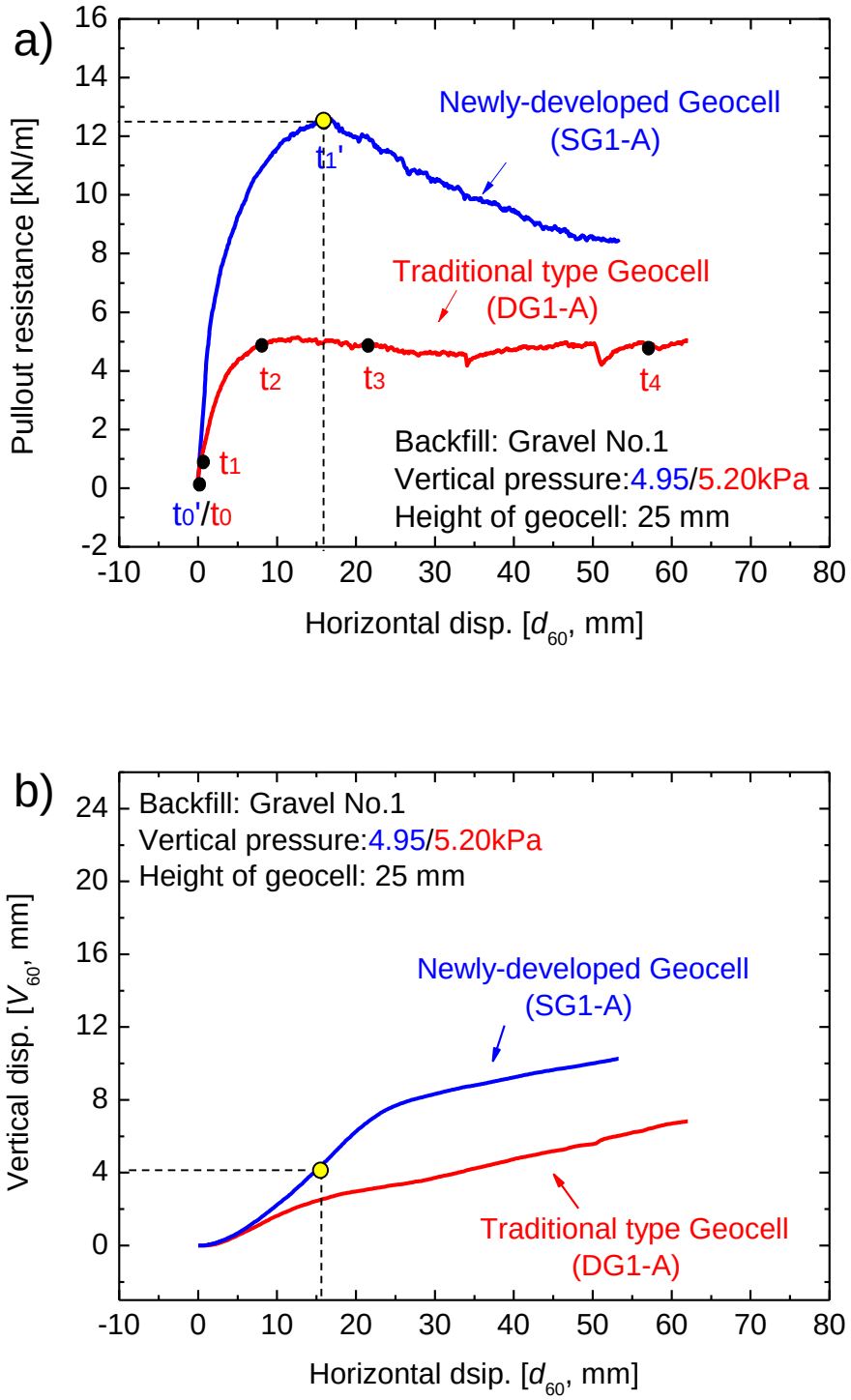

Fig. 4.1 Typical pullout behaviors of square-shaped geocell and diamond-shaped geocell: (a) and (c), pullout resistance against horizontal displacements (d_{60}); (b) and (d), relationships between vertical displacement (V_{60}) and horizontal displacement (d_{60})

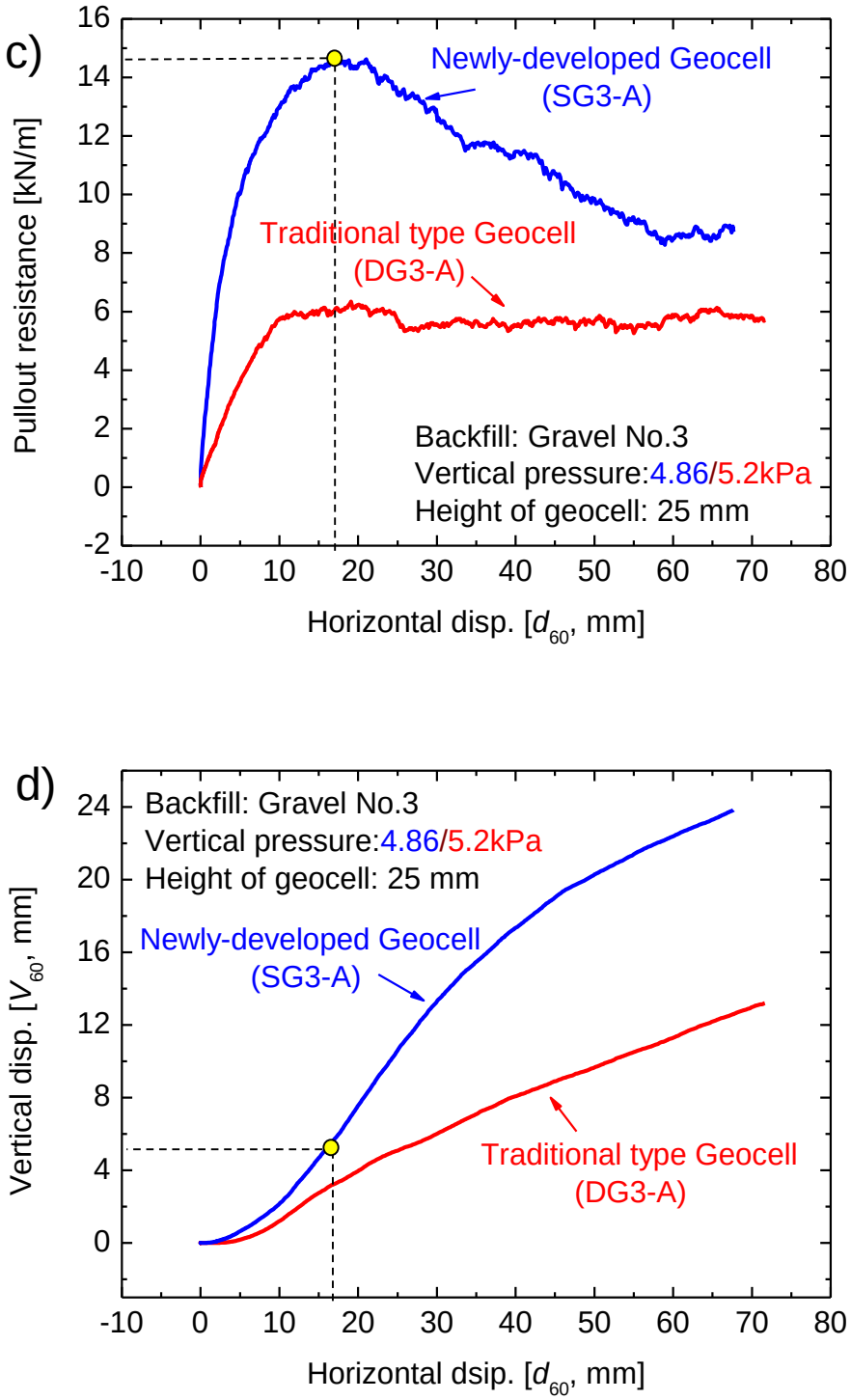

Fig. 4.1 (Continued) Typical pullout behaviors of square-shaped geocell and diamond-shaped geocell: (a) and (c), pullout resistance against horizontal displacements (d_{60}); (b) and (d), relationships between vertical displacement (V_{60}) and horizontal displacement (d_{60})

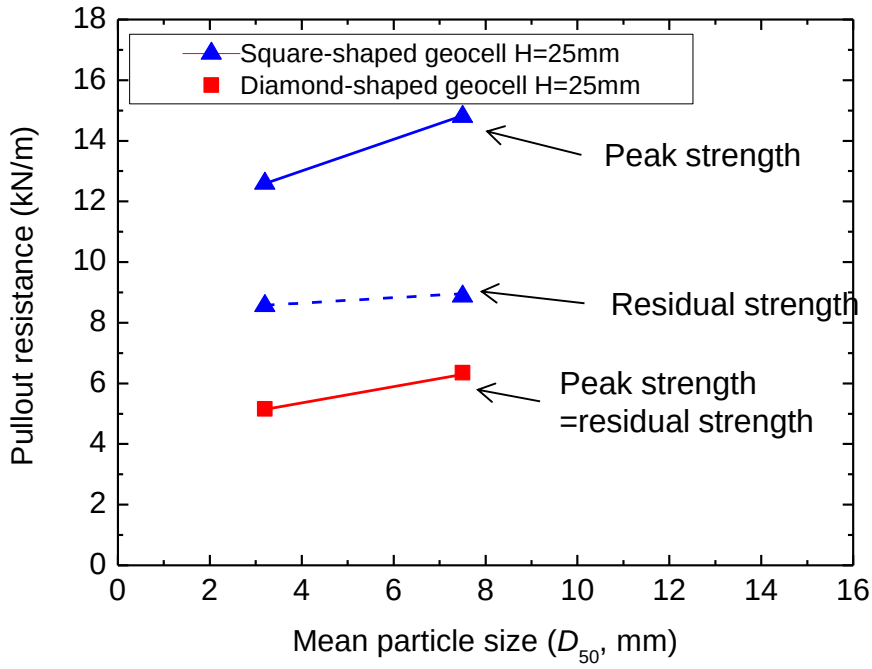

Fig. 4.2 Peak and residual pullout resistances for geocell reinforcement embedded in Gravel No.1 and Gravel No.3.

4.2.2 Stress-deformation mechanisms between square-shaped geocell and diamond-shaped geocell

The stress-deformation mechanism between square-shaped geocell and diamond-shaped geocell was analyzed from typical test results DG1-A and SG1-A shown in Fig. 4.1 for geocells embedded in the backfill of Gravel No.1. Fig. 4.3 shows the distributions of local horizontal displacement in the axial direction for both the square-shaped geocell and the diamond-shaped geocell for different applied pullout force levels. The slope of the respective curves represents the local axial strain. The following two different phases may be identified in the tests on the square-shaped geocell (Fig. 4.3a).

Phase 1: Pre-peak phase

This is the pre-peak phase until the peak pullout state is achieved at P = 12.6 kN/m. During Phase 1, the tensile force in the geocell is progressively transferred to the adjacent backfill along the geocell from the front end to the rear end. This behavior can be associated with an increase in the local tensile strain with increasing pullout force at higher rates closer to the front end. The force is transferred via shear resistance at the interface between the geocell and the adjacent backfill and passive anchorage resistance induced by the passive earth pressure developing inside the cells. In this process, the deformation of each cell has an important influence on the pre-stiffness and development of peak pullout resistance.

Phase 2: Post-peak phase

In the post-peak phase, the local displacement and distance curves at different pullout displacements become parallel to each other, which mean that the entire geocell model is pulled out without changing the tensile strain distribution. It is likely that, in this phase, the pullout resistance is controlled by the shear strength at the interface between the geocell and the adjacent backfill, which decreases from the peak to the residual at faster rates closer to the front end.

In the case of the diamond-shaped geocell (Figure 4.3b), it appears that only Phase 1 occurs. The distribution of tensile strain along the diamond-shaped geocell in Phase 1 is larger than in the test on the square-shaped geocell. This means that, due to larger deformation of the diamond-shaped geocell, the force transfer from the geocell to the adjacent backfill is more progressive than in the test on the square-shaped geocell, resulting in lower pre-peak stiffness and peak pullout resistance.

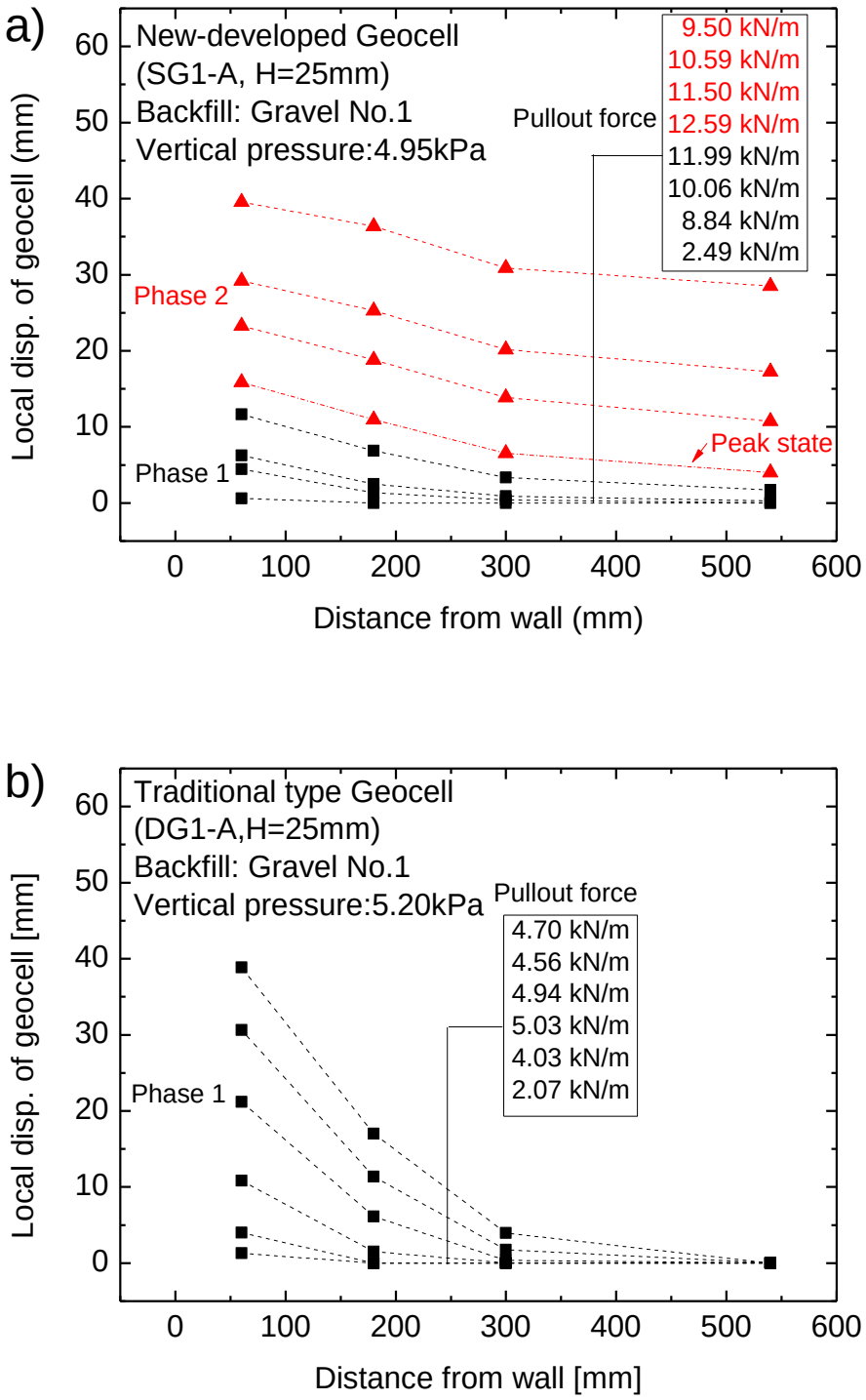

Fig. 4.3 Local horizontal displacements for different pullout force levels: a) square-shaped geocell and b) diamond-shaped geocell.

Figures 4.4 and 4.5 show the variation with time of the stress-deformation characteristics of the diamond-shaped geocell and square-shaped geocell subjected to a pullout force. The schematic diagrams of stress-deformation mechanism are also given in these figures. For the diamond-shaped geocell (Figs. 4.1a and 4.4), from t_0 (initial state) to t_1 (the first state), the first diamond cell starts to deform and provides certain pullout resistance (Figs. 4.1a and 4.4) until other cells reach the same residual resistance state of the first cell. Afterwards, from t_1 to t_2, the second and the third cells deform and provide their pullout resistances until the rest of the cells reach the same residual resistance state of them. This procedure repeats from t_2 to t_3 until all cells work in the pullout Phase 1 (Pre-peak phase). These deformation characteristics of the diamond-shaped geocell can be characterized as progressive deformation in Phase 1, which induces the force transfer from the geocell to the adjacent backfill, are more progressive than in the test on the square-shaped geocell, resulting in lower pre-peak stiffness and peak pullout resistance. However, as shown in Figs. 4.1a and 4.5, the square-shaped geocell only shows slightly progressive deformation in Phase 1 from t_0 (initial state) to t_1 (peak state). After that, all square cells work immediately providing larger peak pullout resistance and higher initial stiffness than diamond-shaped geocell.

At the end of the tests, soil was removed carefully and it was possible to observe the final deformation states of the diamond-shaped geocell and squared-shaped geocell (Fig. 4.6). In fact, the diamond-shaped geocell clearly shows shrinkage deformation characteristics (Fig. 4.6a), which indicates that the cell members gradually experienced extension from the front position close to the clamp to the end, while the square-shaped geocell displays non-shrinkage deformation characteristics (Fig. 4.6b), indicating that straight longitudinal members of square-shaped geocell reduce the progressive deformation of the cells, which induce a higher pullout resistance.

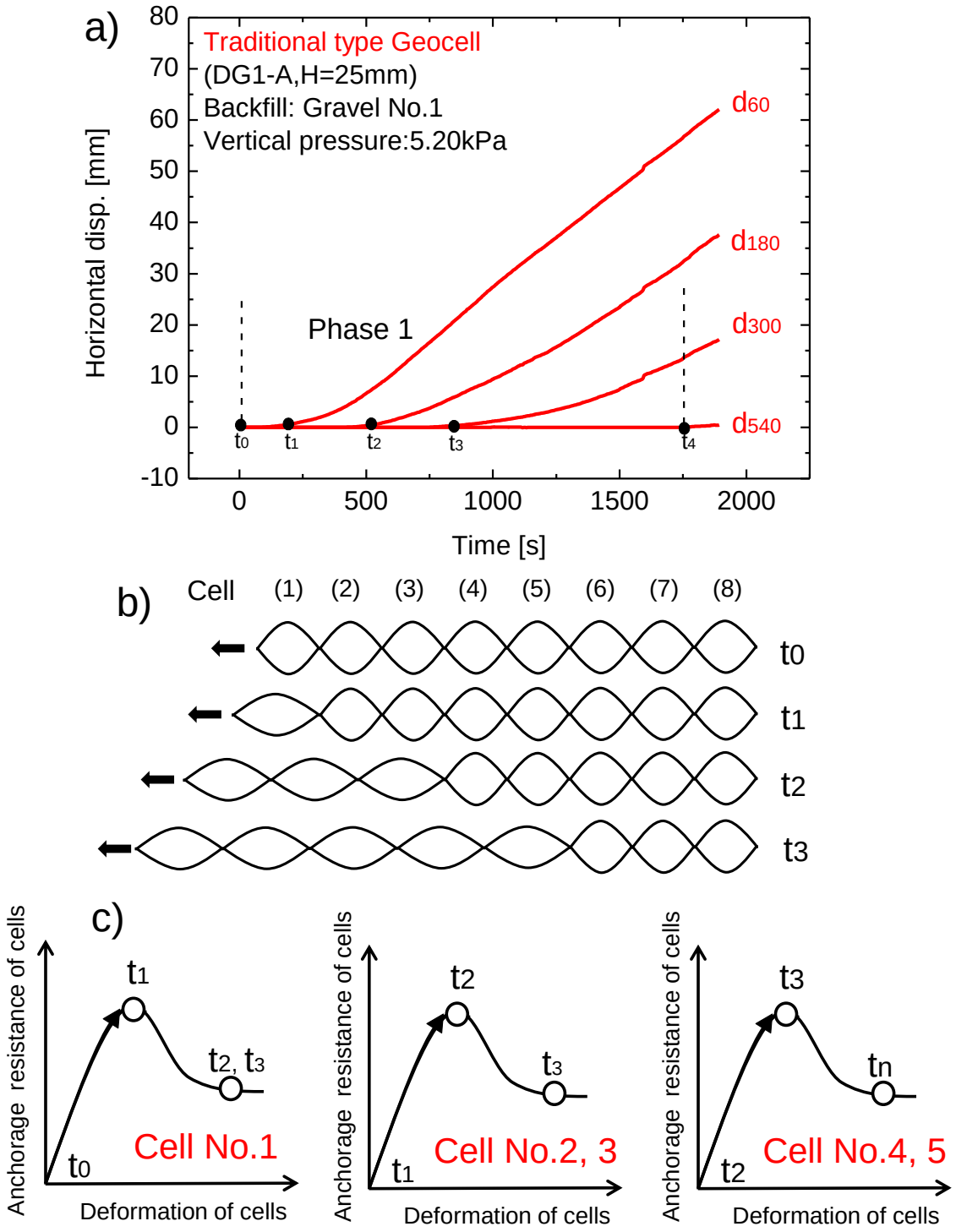

Fig. 4.4 Stress-deformation characteristics of diamond-shaped geocell: a) horizontal displacement versus elapsed time; b) schematic diagram of deformation status varying with time; c) schematic diagram of stress-deformation mechanism.

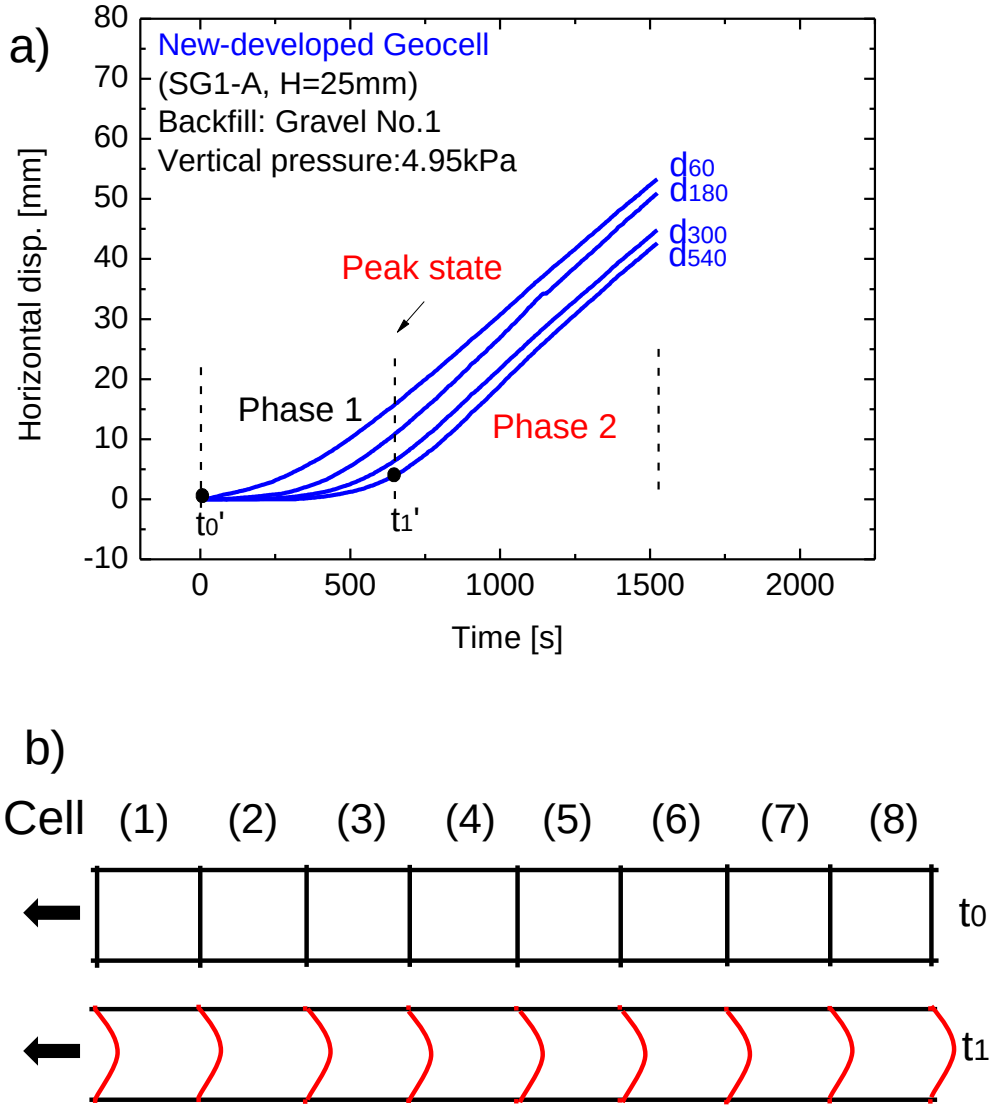

Fig. 4.5 Stress-deformation characteristics of square-shaped geocell: a) horizontal displacement versus elapsed time; b) schematic diagram of deformation status varying with time.

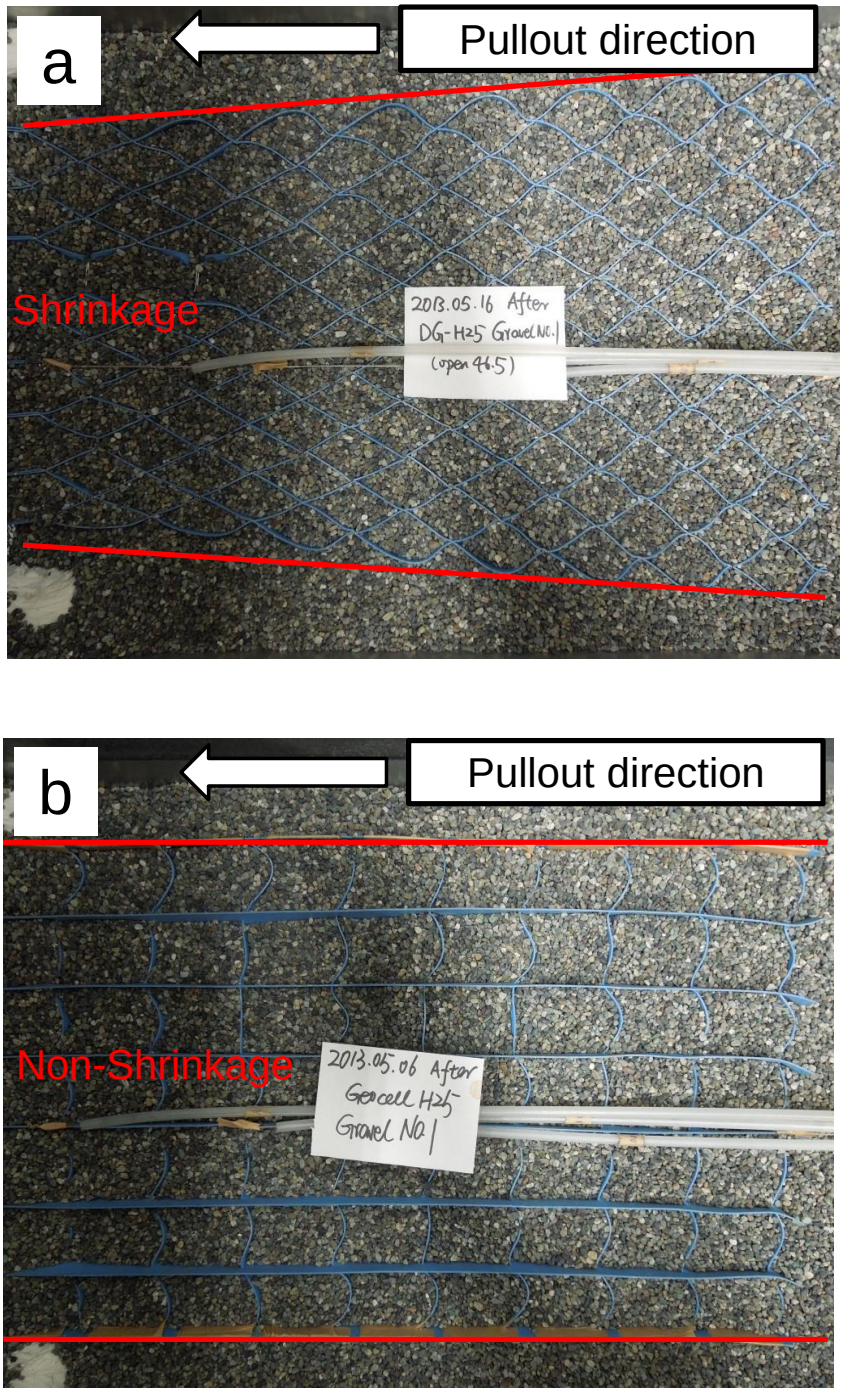

Fig. 4.6 Final deformation state for: a) diamond-shaped geocell; and b) square-shaped geocell

4.3 Comparison between newly-developed geocell and commercial geogrid behaviors

Geogrids (Fig. 3.7c) are commonly used as planar tensile-reinforcement of the backfill of RWs, embankments and other soil structures. However, the bond stress along the interface between the geogrid and the backfill becomes lower than the shear strength of the backfill to a larger extent with an increase in particle size. The newly-developed geocell as tensile reinforcement of soil retaining structures aims at alleviating this problem.

Therefore, in this section, a series of pullout tests were performed on a square-shaped geocell model shown in Fig. 3.7a and a commercial geogrid product (Tensar SS-35, Fig. 3.7c) embedded in gravelly soils having different particle sizes to examine whether or not square-shaped geocells can perform as suitable tensile reinforcement by effectively confining large soil particles. The basic properties of Tensar SS-35 and the square-shaped geocell model have been described in Chapter 3, Section 3.2.3. It should be noted that, Tensar SS-35 is made of polypropylene (PP). Although a PP geogrid is generally stiff, this geogrid type is among the weakest and softest among those that are usually used for full-scale GRS structures. On the other hand, the members of the geocell are made of polyester (PET) covered with PVC for protection. The members of the geocell model used in these scaled-down model tests are weaker and softer than the one (i.e. HDPE or PP) to be used in full-scale GRS structures (Kongkitkul et al., 2007). In addition, both particle size of the backfill soil and the cell size of square-shaped geocell were scaled down by a scale factor of 1/10, while the aperture size of the geogrid (i.e. Tensar SS-35) was not scaled down. Details of the test cases are shown in Table 4.2.

Table 4.2 Test cases for square-shaped geocell and commercial geogrid.

Test number	Reinforcement	Height of transversal member (mm)	Cell or grid size (mm)	Backfill materials[A)]	Opening height of front wall (mm)
SG1-A	Square-shaped geocell	25	50 × 60	Gravel No.1	46.5
SG1[P)]-A	Square-shaped geocell	25	50 × 60	Gravel No.1	46.5
SG3-A	Square-shaped geocell	25	50 × 60	Gravel No.3	46.5
SG3[P)]-A	Square-shaped geocell	25	50 × 60	Gravel No.3	46.5
GG1-A	Geogrid[B)]	5	33 × 28	Gravel No.1	46.5
GG3-A	Geogrid[B)]	5	33 × 28	Gravel No.3	46.5
GG5-A	Geogrid[B)]	5	33 × 28	Gravel No.5	46.5

A) Gravel No.1: D_{50}=3.2 mm; Gravel No.3: D_{50}=7.5 mm; Gravel No.5: D_{50}=14.2 mm (Figs. 3.5 and 3.6);
B) Geogrid: Tensar SS-35;
P) Preloading before test.

4.3.1 Typical test results

Typical pullout test results for the square-shaped geocell and geogrid embedded in Gravel No.1 and Gravel No.3 are presented in Fig. 4.7. The pullout resistance (P) and horizontal displacement (d_{60}) relationships are plotted in Figs. 4.7a and c, while the vertical displacement (V_{60}) at the backfill crest and horizontal displacement (d_{60}) relationships are plotted in Figs. 4.7b and 4.7d.

When embedded in Gravel No.1 (smaller particles), the square-shaped geocell shows similar peak pullout resistance to the geogrid, but noticeably lower pre-peak stiffness. When embedded in Gravel No.3 (larger particles), the square-shaped geocell exhibits markedly higher peak pullout resistance, but still lower initial stiffness than the geogrid. In both cases, the square-shaped geocell exhibits higher residual pullout resistance than the geogrid.

Interestingly, pullout resistance of the geocell larger than that of the geogrid can be associated with the dilatancy rate of the geocell, which was larger than that for the geogrid (Figs. 4.7), as observed when embedded in larger size particles of backfill (i.e. Gravel No.3) and at large horizontal displacements (d_{60}) in the post-peak state. This trend is particularly obvious in the post-peak regime approaching the residual state. The opposite trend of strength and dilatancy can be seen in the pre-peak state. That is, with the geocell embedded in Gravel No.1, before horizontal displacement (d_{60}) reaches 16 mm, the dilatancy rate in the test of the geocell is noticeably lower than that of the geogrid (Fig. 4.7b), which is associated with lower pre-peak stiffness (Fig. 4.7a). Subsequently, the dilatancy rate in the test with the geocell becomes larger and reaches the peak value, which is followed by a gradual decrease toward the residual value. From Figs. 4.7c and 4.7d, similar behavior can be seen for the geocell and the geogrid embedded in Gravel No. 3, where the peak pullout resistance is mobilized when the tangential slope of the V_{60}-D_{60} relationship becomes maximum (Figs. 4.7b and 4.7d). This behavior is essentially the same as that for unreinforced granular soils. It is likely, therefore, that the mobilization of peak pullout resistance in the tests with the geocell and geogrid is always associated with the mobilization of the peak shear strength of the backfill zone adjacent to the geocell or geogrid. So, when the shear strength in the adjacent backfill zone becomes the residual value, the pullout resistance becomes its residual value. Differences in the mobilization pattern of pullout resistance between the geocell and the geogrid are due to differences in the mobilization mechanism of strength in the backfill that are caused by

different dimensions and stiffness of the geocell and geogrid, as explained below (See Section 4.2.2 for comparison).

Hereafter, typical test results of SG1-A and GG1-A (i.e. in the backfill of Gravel No.1) are analyzed and discussed.

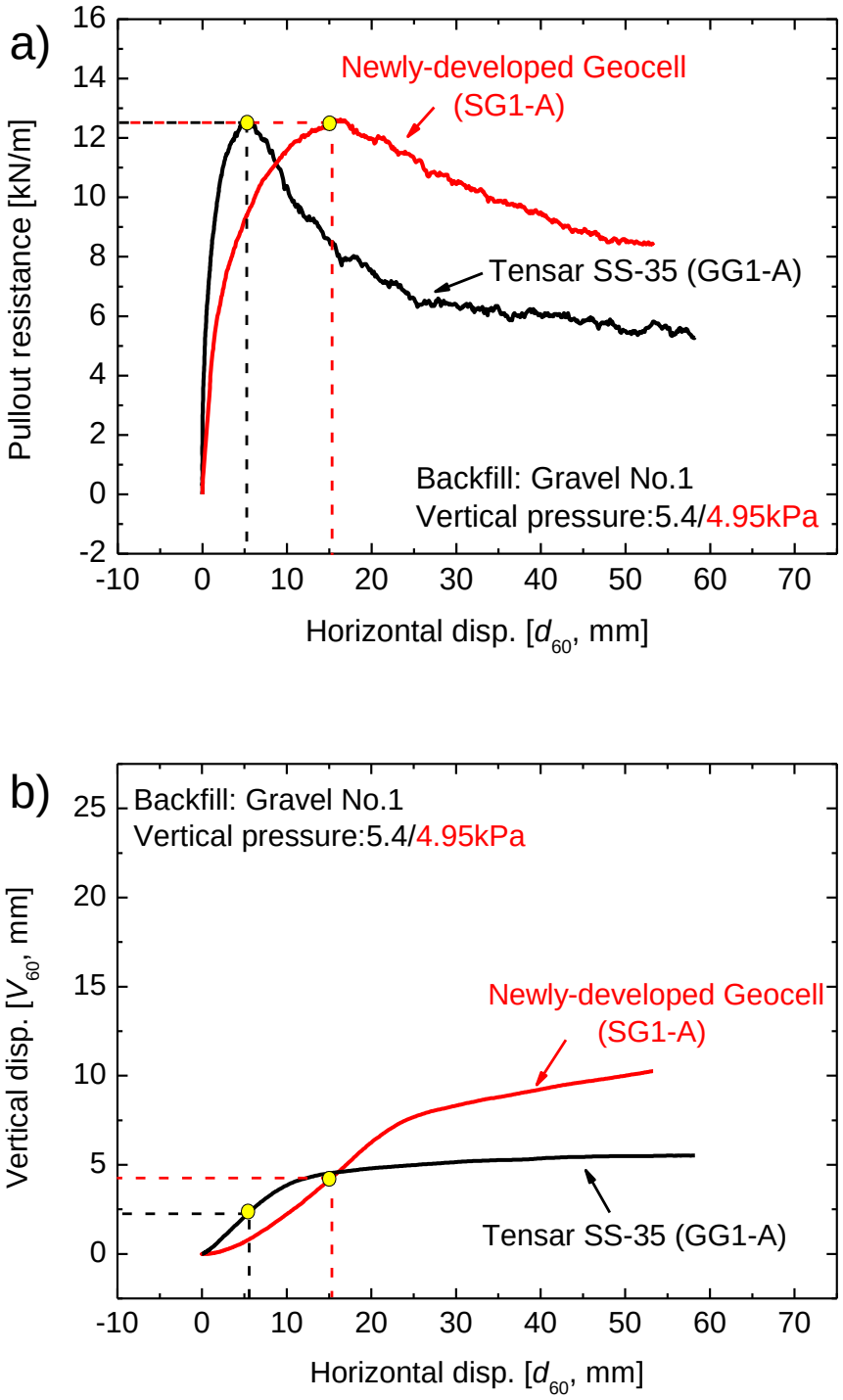

Fig. 4.7 Typical pullout behaviors of square-shaped geocell and geogrid: (a) and (c), pullout resistance against horizontal displacements (d_{60}); (b) and (d), relationships between vertical displacement (V_{60}) and horizontal displacement (d_{60})

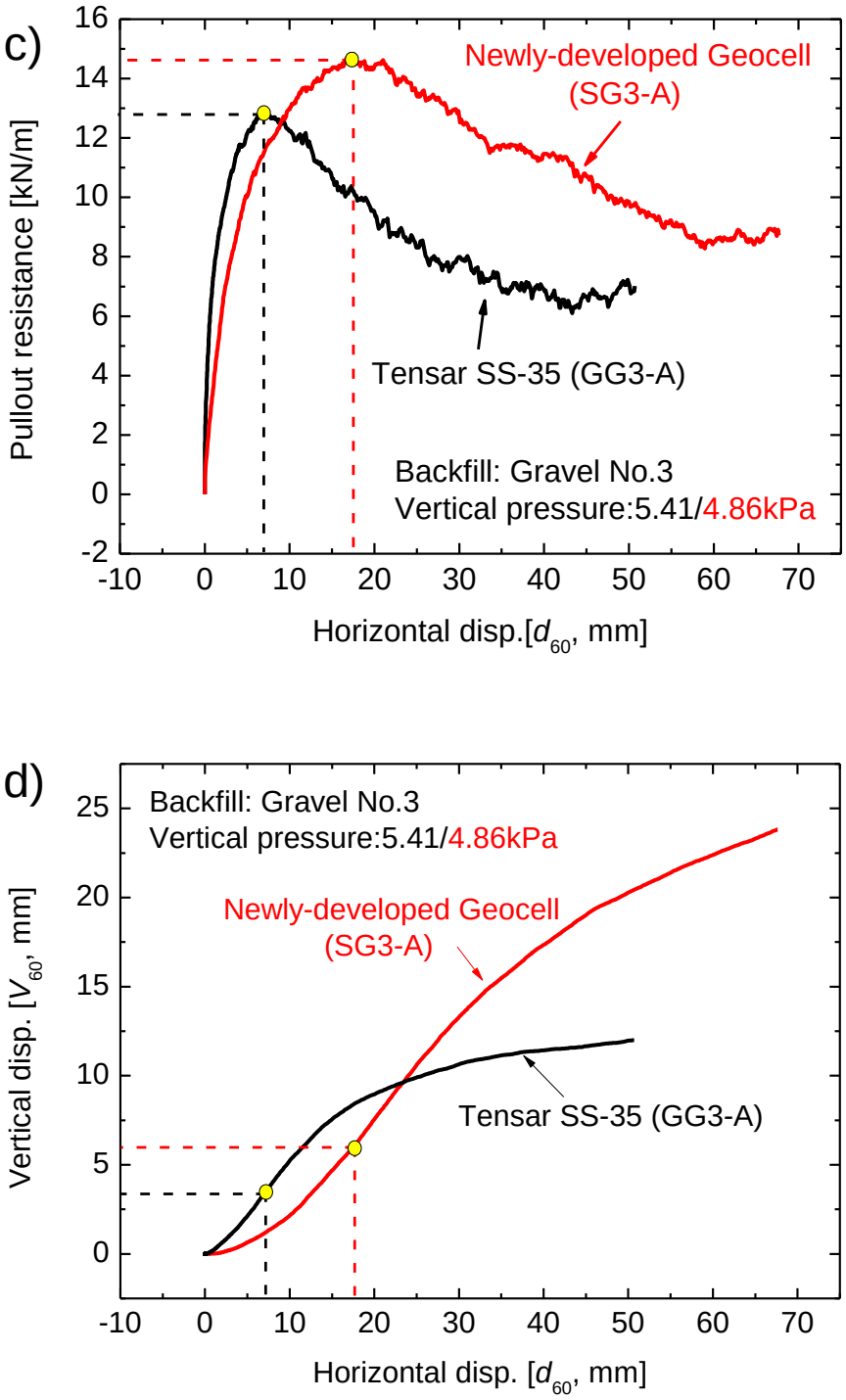

Fig. 4.7 (Continued) Typical pullout behaviors of square-shaped geocell and geogrid: (a) and (c), pullout resistance against horizontal displacements (d_{60}); (b) and (d), relationships between vertical displacement (V_{60}) and horizontal displacement (d_{60})

Figure 4.8 shows the distributions of local horizontal displacement in the axial direction of the square-shaped geocell and the geogrid at different applied pullout force levels. The slope of the respective curves represents the local axial strain. The following two different phases may be seen in the tests of square-shaped geocell (Figs. 4.8a and 4.8b).

Phase 1: pre-peak phase

In the pre-peak phase, i.e. before the peak pullout state reach a value of P= 12.6 kN/m or 14.6 kN/m, the tensile force in the geocell is progressively transferred to the adjacent backfill along the geocell from the front end to the rear end. This behavior is associated with an increase in the local tensile strain with an increase in the pullout force at higher rate closer to the front end. The force is transferred via shear resistance at the interface between the geocell and the adjacent backfill and passive anchorage resistance at the cells. During this force transfer process (Fig. 4.5), a cell deforms relatively largely due to its low stiffness associated with an inevitable slackness of transversal members. Deformation of the cell decreases the pre-peak stiffness and delays the development of peak pullout resistance.

Phase 2: post-peak phase

In the post-peak phase, the local displacement and distance curves at different pullout displacements become parallel to each other, which mean that the entire geocell model is pulled out without changing the tensile strain distribution. It is likely that, in this phase, the pullout resistance is controlled by the shear strength at the interface between the geocell and the adjacent backfill, which decreases from the peak to the residual at faster rates at places closer to the front end.

Phases 1 and 2 were observed also in the tests on the geogrid, (Figs. 4.8c and 4.8d). However, the distribution of tensile strain along the geogrid in Phase 1 is more uniform than in the test on the geocell. This means that, due to higher axial stiffness of the geogrid compared to the geocell, the force transfer from the geogrid to the adjacent backfill is less progressive (i.e. more instantaneous) than in the test on the geocell, resulting in a higher pre-peak stiffness and a smaller pull-out displacement at the peak pullout force.

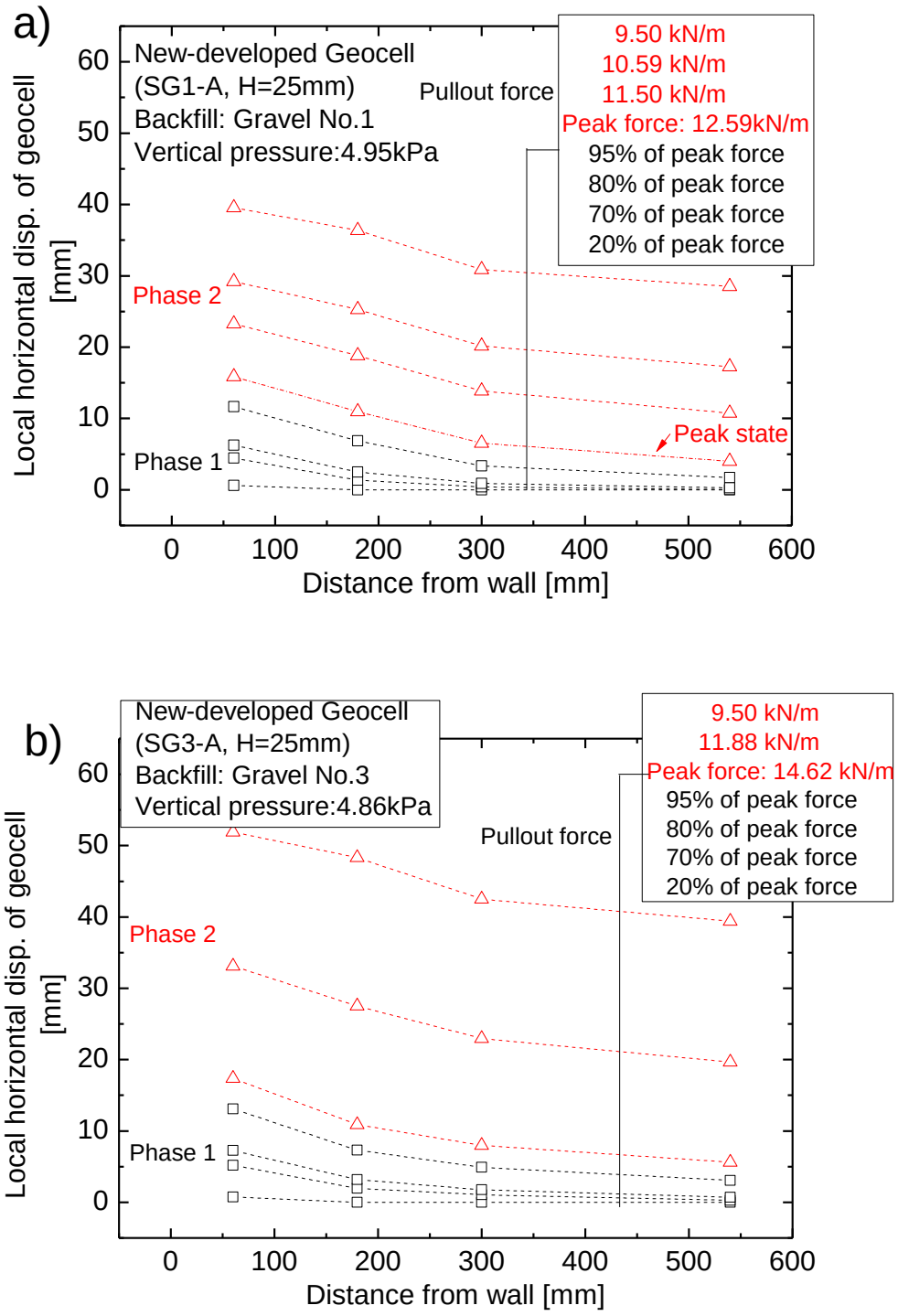

Fig. 4.8 Local horizontal displacements along geocell and geogrid at different pullout force levels: a) square-shaped geocell embedded in Gravel No.1; b) square-shaped geocell embedded in Gravel No.3;

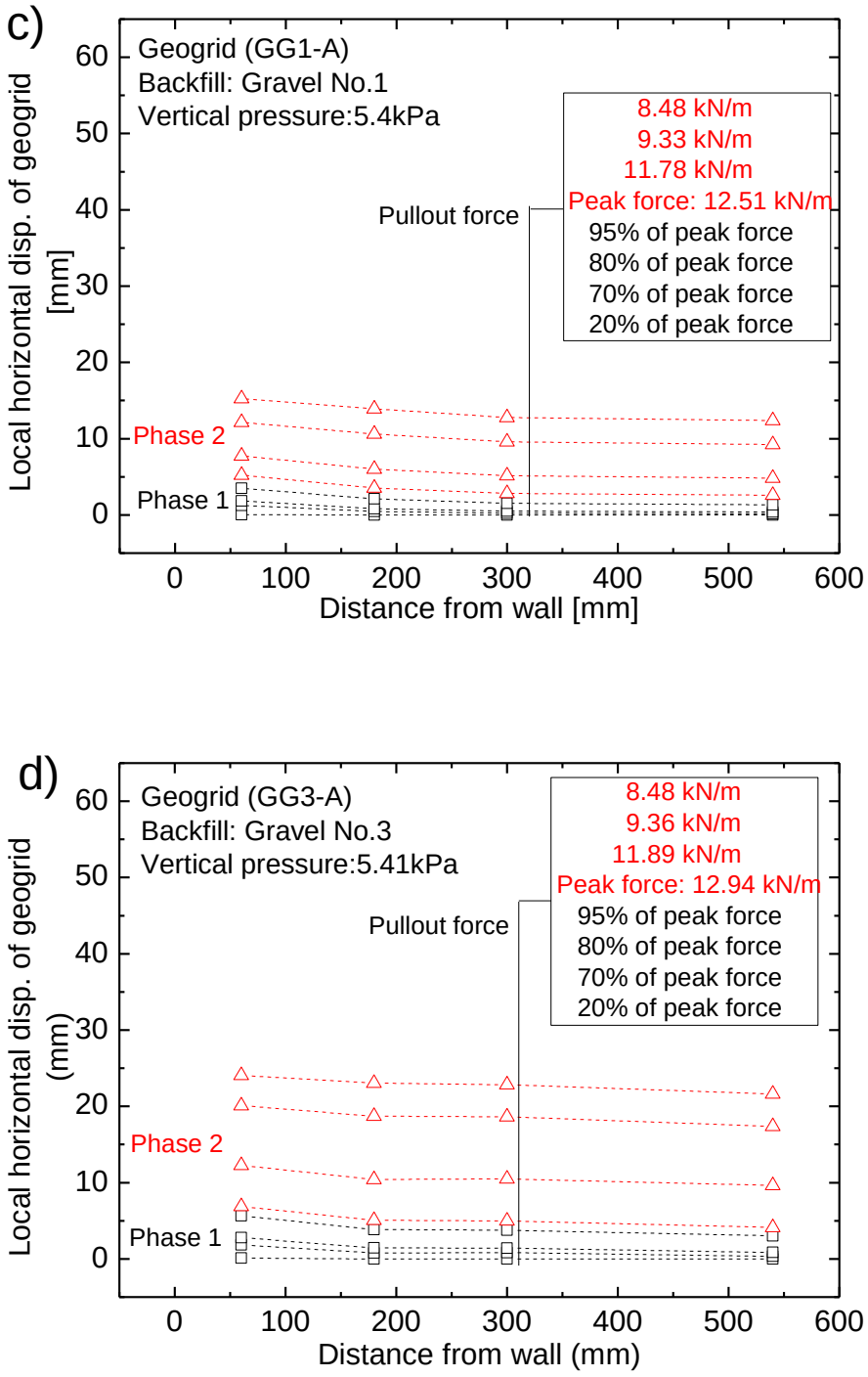

Fig. 4.8 (Continued) Local horizontal displacements along geocell and geogrid at different pullout force levels: c) geogrid embedded in Gravel No.1; d) geogrid embedded in Gravel No.3

4.3.2 Pullout mechanisms between square-shaped geocell and geogrid

Figure 4.9 summarizes the peak and residual pullout resistance (which defined as the pullout resistance when d_{60} reaches 40 mm) of the square-shaped geocell and the geogrid. For the geocell, the peak pullout resistance increases with an increase in the backfill particle size from D_{50} = 3.2 mm (Gravel No.1) to D_{50} = 7.5 mm (Gravel No.3). For the geogrid, this increase is not so significant. This can be attributed to different pullout mechanisms by different structures (i.e. a 3-D structure of the geocell comprising square-shaped cells versus a planar structure of the geogrid, Fig. 3.7a and 3.7c).

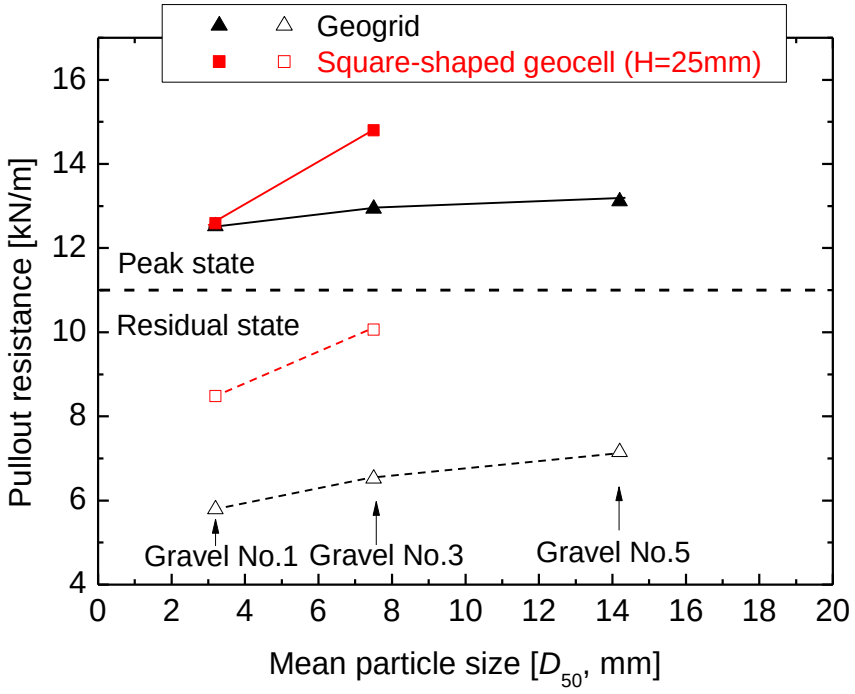

Fig. 4.9 Peak and residual pullout resistances of square-shaped geocell and geogrid in Gravels No.1, 3 and 5.

Pullout mechanism of geogrid reinforcement:

As shown in Figure 4.10b, the pullout resistance of the geogrid is controlled by:

1) Friction between soil particles and the geogrid members;

2) Friction between soil particles interlocked in the grid aperture and adjacent soil particles;

3) Passive soil resistance induced by grid transversal members;

4) The interlocking of soil particles in the aperture of the geogrid has an important influence on the pullout resistance of geogrid reinforcement. An appropriate geogrid aperture size and shape relative to soil particle size and shape, grading, and density, as well as the properties of the geogrid members would induce better interlocking, which would increase the pullout resistance of the geogrid.

In this study, with an increase in the particle size of backfill from 3.2 mm to 14.2 mm, a negligible increase in the pullout resistance means that one or all of these factors does not increase significantly. As the aperture size of the geogrid is 28 mm $\times$ 33 mm, it is likely that the interlocking effect does not increase with this increase in particle size.

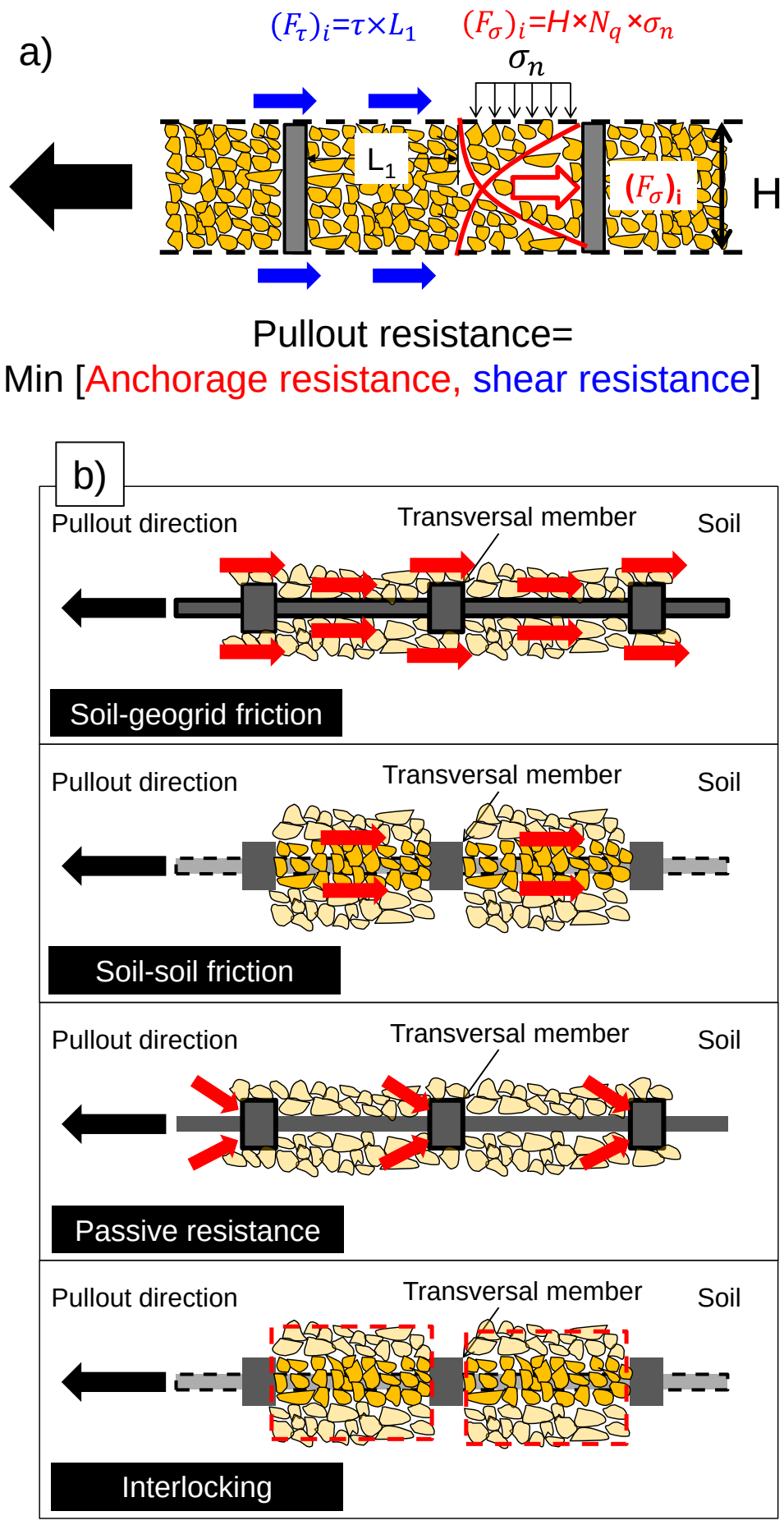

Fig. 4.10 Schematic pullout mechanism of a) square-shaped geocell; b) geogrid

Pullout mechanism of geocell reinforcement:

Unlike the mechanism explained above, as shown in Fig. 4.10a, the pullout resistance of square-shaped geocell can be considered to be the smaller one between: 1) the shear resistance of the shear bands along the upper and bottom boundaries of the geocell; and 2) the anchorage resistance induced by passive pressure developed inside the cells. These two factors have a reciprocal effect, which will be discussed in details in Section 4.5.

Although the peak anchorage resistance is generally larger than the peak resistance of the shear bands, the development of the anchorage resistance is lower. Therefore, the pre-peak pullout stiffness is controlled by the anchorage resistance, which has not yet become larger than the shear resistance of the shear bands. Kiyota et al. (2009) reported that, in tests similar to those reported in this paper, the peak pull-out strength of a geocell does not increase noticeably with an increase in the height of the geocell. As the anchorage resistance increases with the cell height, this test result indicates that the peak and residual pullout strengths are controlled by the shear resistance of the shear bands that have become smaller than the anchorage resistance. The test results shown in Figure 4.9 then indicate that the peak shear resistance of the shear bands increases with an increase in the particle size when the cell height is larger than a certain limit.

Figure 4.11a shows the effects of the ratio of the height (H) of the reinforcement member (i.e. the thickness of the geogrid and the height of the transversal members of the geocell) to the mean particle diameter (D_{50}) on the peak pullout resistance. Fig. 4.11b shows the effects of the ratio of the average width (A) of the aperture to the mean particle diameter (D_{50}) on the peak pullout resistance. For the same value of H/ D_{50} or A/ D_{50}, the pullout resistance of the geocell is noticeably higher than that of the geogrid. This behavior may be due to that large soil particles are confined better by the geocell than the geogrid, which should results in higher anchorage capacity and/or higher shear resistance at the top and bottom interfaces between the geocell and the adjacent backfill than the geogrid.

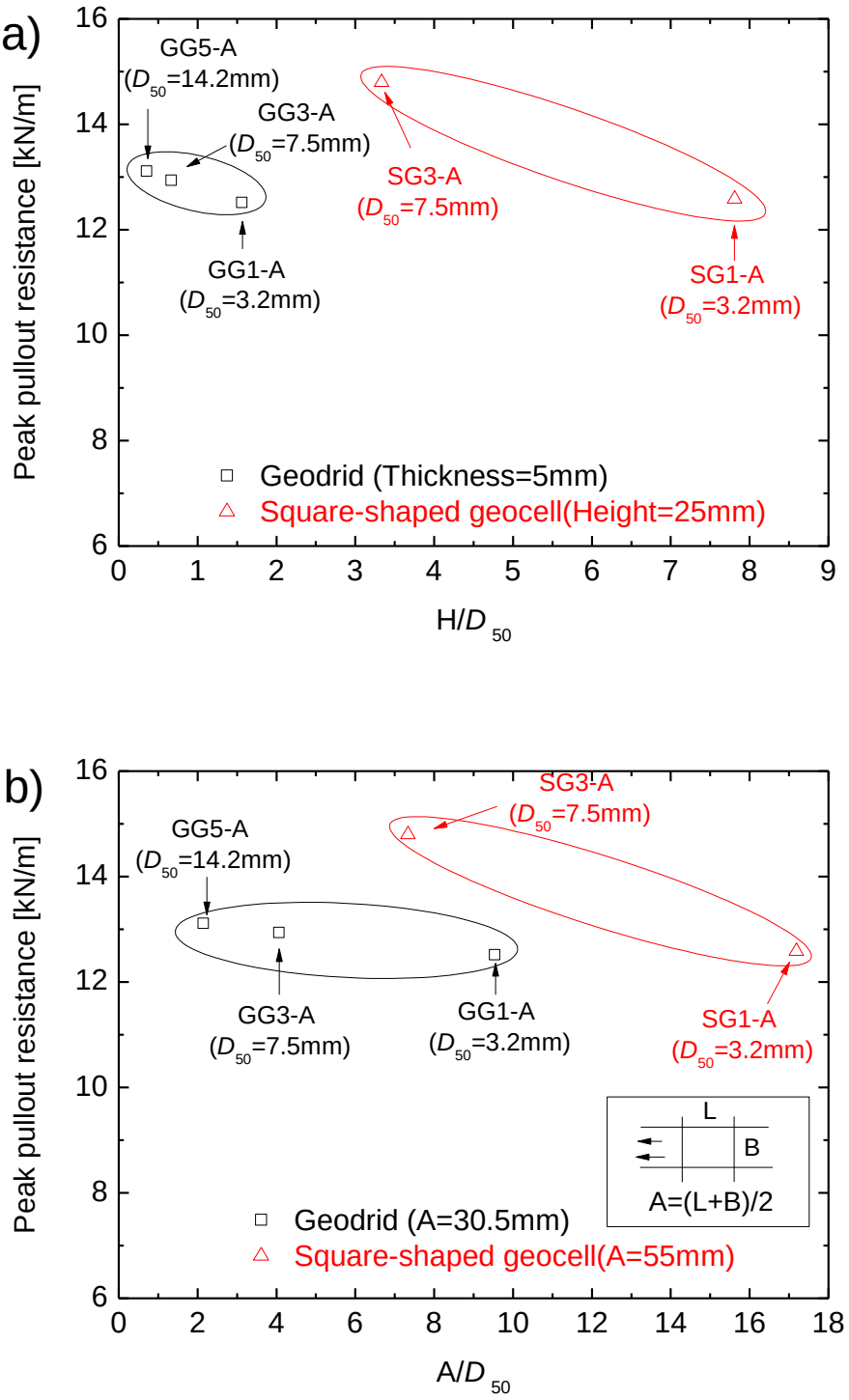

Fig. 4.11 The influence of relative sizes of soil particle (D_{50}) with respect to: (a) height of reinforcement (H); and (b) average size of aperture (A).

4.4 Improvement of newly-developed geocell

For the square-shaped geocell, the pre-peak pullout stiffness in Phase 1 is controlled by the anchorage resistance developed by the transversal members of the geocell. Considering that the pre-peak pullout stiffness increases with an increase in the stiffness of the transversal members and this can be achieved by reducing the slackness of the transversal members (Fig. 4.12b), preloading was applied to the level of the residual pullout strength (Fig. 4.12a). It may be seen that the pre-peak pull-out stiffness during reloading is much higher than the one during primary loading. For Gravel No.1, Fig. 4.13a compares the pullout resistance and the horizontal displacement relationship since the start of reloading with the one observed during primary loading (without preloading). It may be seen that the pre-peak pullout stiffness of the geocell increases significantly by preloading, which can be attributed to a decrease in the slackness of the transversal members that exists initially. For Gravel No.3, the pre-peak pull-out stiffness slightly increases (Fig. 4.13b). On the other hand, the preloading method has little effects on the peak and residual pull-out resistances. This trend is due likely to that preloading provides only a little improvement on the peak shear resistance of the shear bands.

The pre-peak stiffness in this study was defined by the concept of secant modulus, E_{50}, as shown in Fig. 4.14a. Fig. 4.14b summarized the pre-peak pullout stiffness of square-shaped geocell, diamond-shaped geocell and commercial geogrid (Tensar SS-35) tested in Section 4.2, 4.3 and this section. As can be seen clearly, the pre-peak stiffness of square-shaped geocell increased by preloading method, but still lower than that of geogrids (Tensar SS-35). This can be further enhanced by using stiffer longitudinal and transversal members (i.e. HDPE) to reduce the progressive development of tensile forces in the axial direction of the geocell (Fig. 4.5) instead of softer materials (i.e. PET) used in this study.

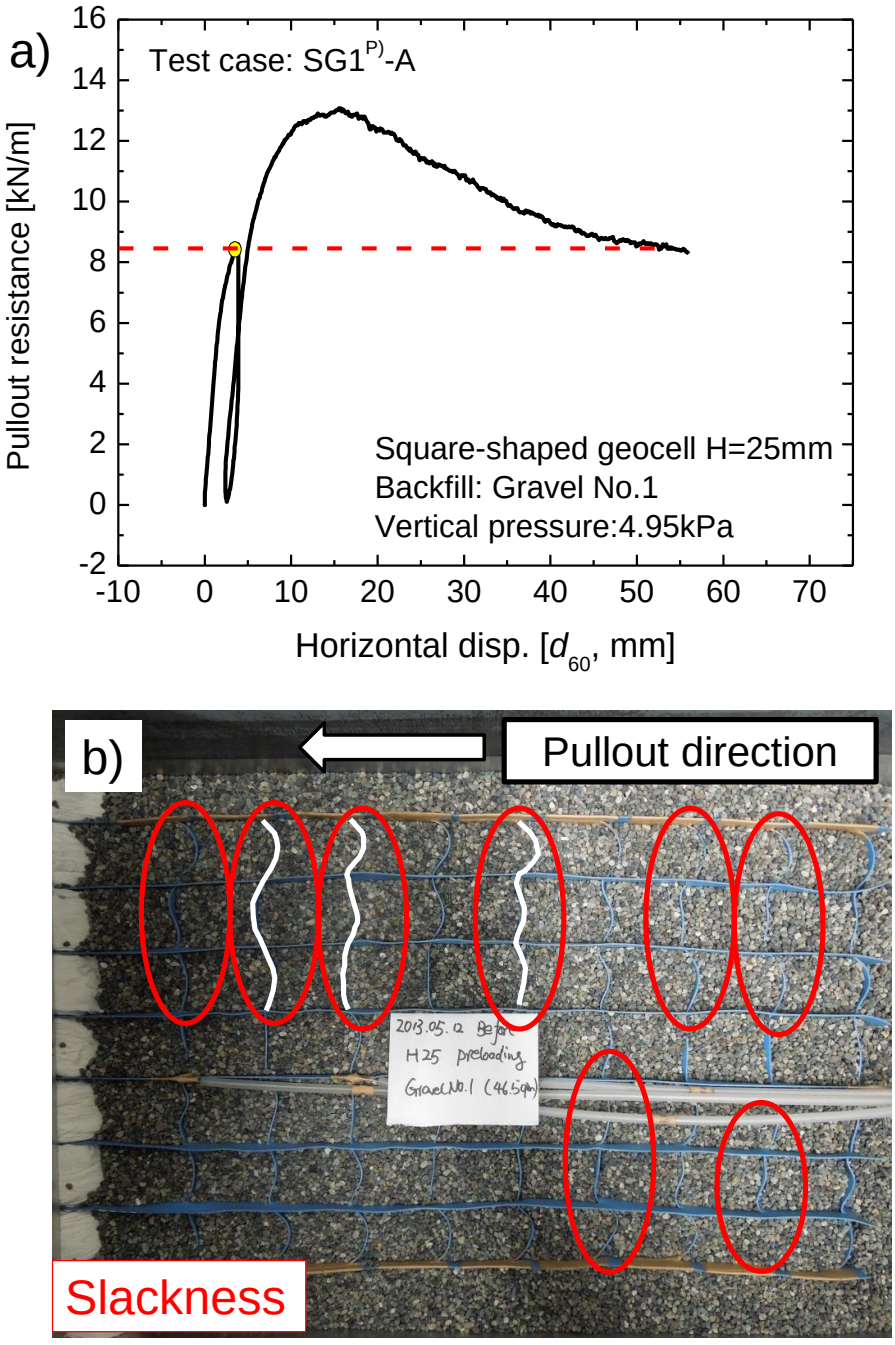

Fig. 4.12 a) Preloading method for square-shaped geocell; b) initial arrangements of transversal cell members before test.

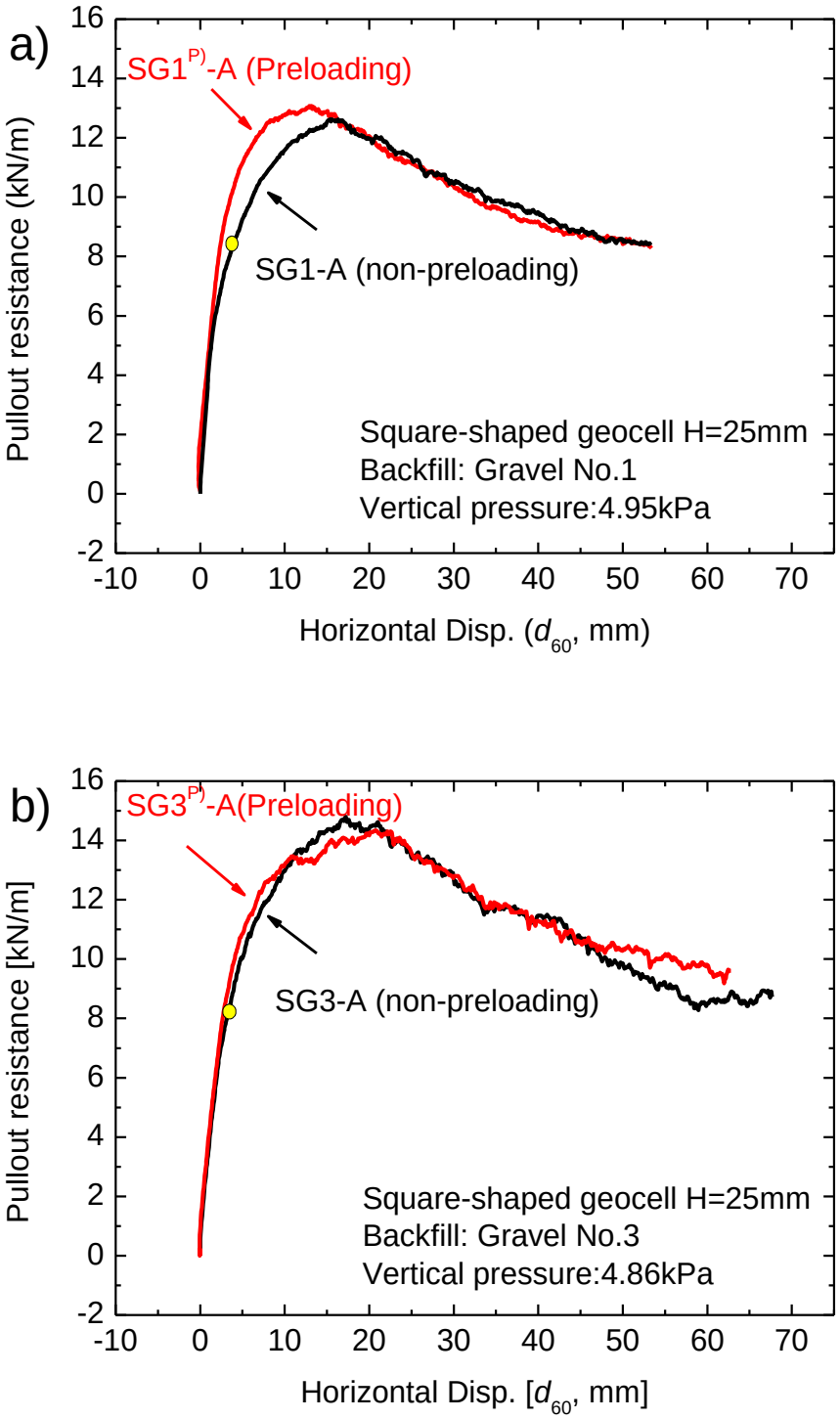

Fig. 4.13 Enhancement of square-shaped geocell by preloading method with the backfill of: a) Gravel No.1; (b) Gravel No.3.

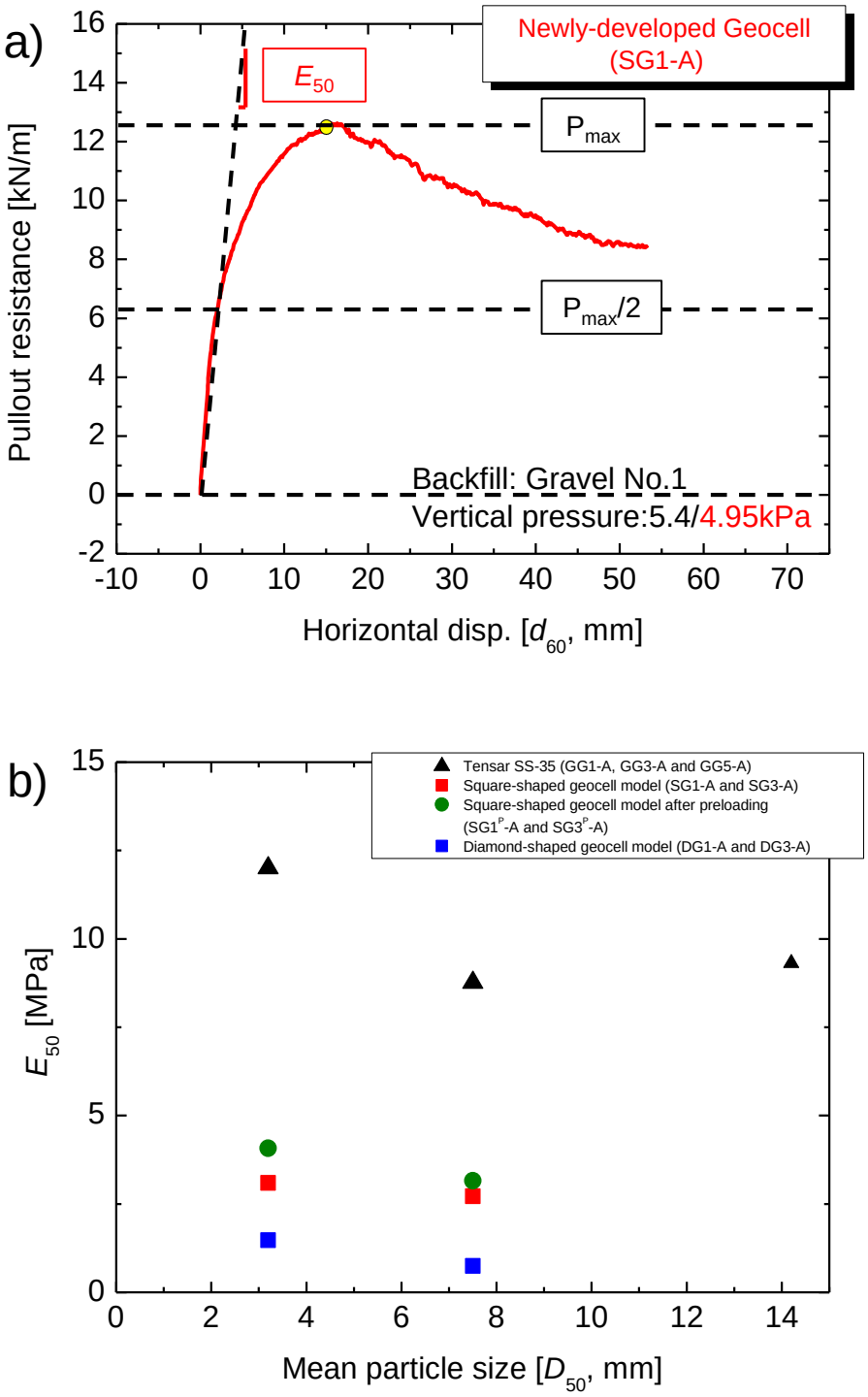

Fig. 4.14 a) Definition of E_{50}; (b) summary of pre-peak pullout stiffness for square-shaped geocell, diamond-shaped geocell and commercial geogrids

4.5 Effect of height of newly-developed geocell related to particle size of backfill soil

Reinforcements with 3-D structure (e.g. square-shaped geocell) have the advantage of providing high pullout bearing resistance by its transversal members (Racana et al., 2003, Khedkar et al., 2009, Horpibulsuk et al., 2010, Suksiripattanapong et al., 2013). Therefore, the effect of particle size relative to height of the geocell was investigated by using square-shaped geocells with different transversal member heights (H) under the same spacing (S = 60 mm) between transverse members conditions arranged in backfill of Gravels No.1 (D_{50} = 3.2 mm), No. 3 (D_{50} = 7.5 mm) and No. 5 (D_{50} = 14.2 mm). The test cases are shown in Table 4.3.

Table 4.3 Test cases for square-shaped geocell having different heights.

Test number	Reinforcement	Reinforcement height (mm)	Cell or grid size (mm)	Backfill materials[A)]	Opening height of front wall (mm)
SG1-12.5B	Square-shaped geocell	12.5	50 × 60	Gravel No.1	100
SG1-25B	Square-shaped geocell	25	50 × 60	Gravel No.1	100
SG1-40B	Square-shaped geocell	40	50 × 60	Gravel No.1	100
SG3-25B	Square-shaped geocell	25	50 × 60	Gravel No.3	100
SG3-40B	Square-shaped geocell	40	50 × 60	Gravel No.3	100
SG3-60B	Square-shaped geocell	60	50 × 60	Gravel No.3	100
SG5-25B	Square-shaped geocell	25	50 × 60	Gravel No.5	100
SG5-40B	Square-shaped geocell	40	50 × 60	Gravel No.5	100
SG5-60B	Square-shaped geocell	60	50 × 60	Gravel No.5	100
SG5-80B	Square-shaped geocell	80	50 × 60	Gravel No.5	100

A) Gravel No.1: D_{50} = 3.2 mm; Gravel No.3: D_{50} = 7.5 mm; Gravel No.5: D_{50} = 14.2 mm (Figs. 3.5 and 3.6);

It may be seen from Figure 4.15 that with an increase in particle size, the peak strength increases while the amount of strain softening decreases (i.e. the residual strength increases with an increase in the particle size to a larger extent than the peak strength). Also, the pullout resistance clearly increases with an increase in the member height from 12.5 mm to 25 mm (Fig. 4.15a), from 25 mm to 40 mm (Fig. 4.15b) and from 25 mm to 60 mm (Fig. 4.15c). However, with further increase in member height, the pullout resistance exhibits only a very small increase.

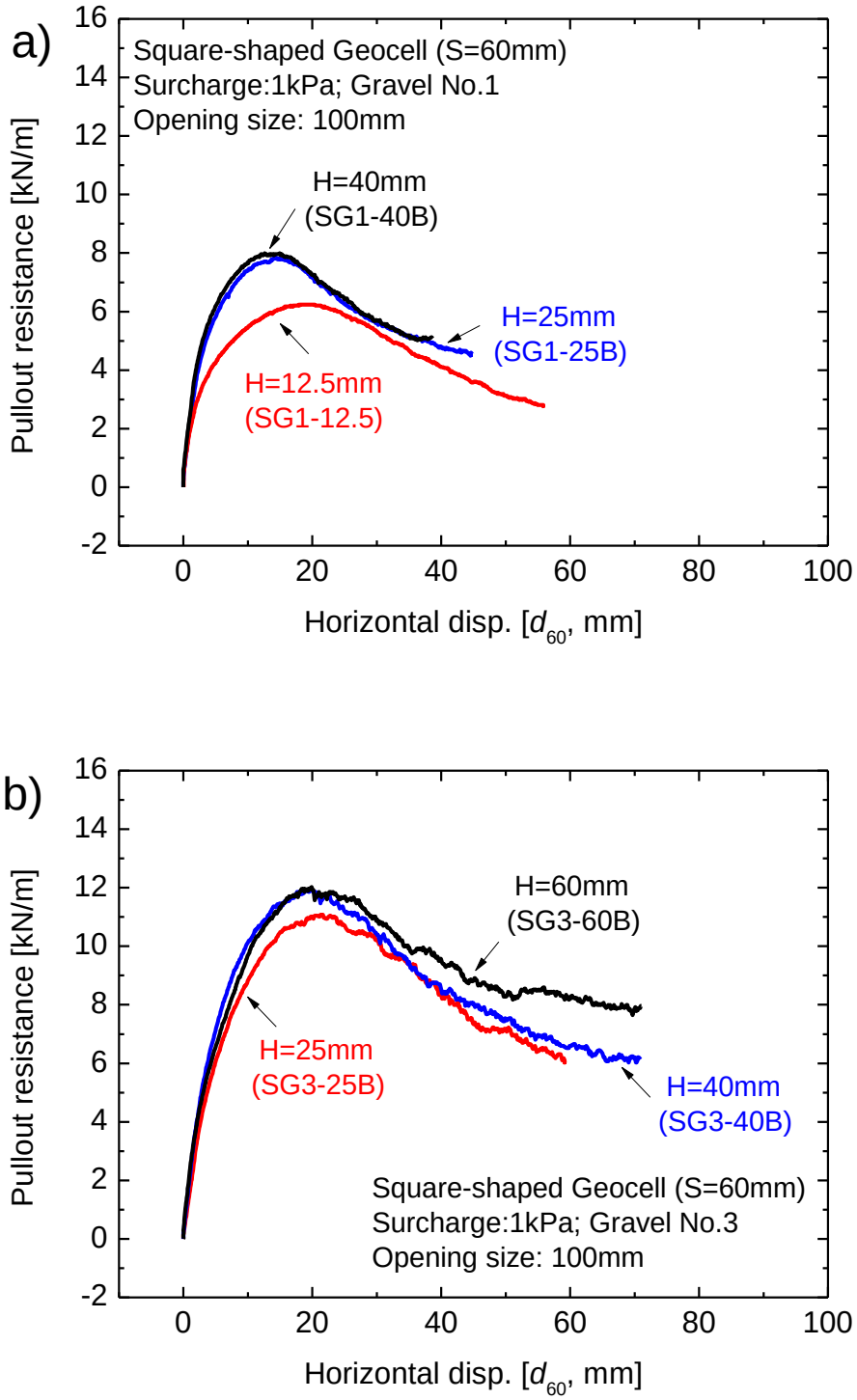

Fig. 4.15 Pullout behaviors of square-shaped geocell with different heights embedded in: a) Gravel No.1; b) Gravel No.3

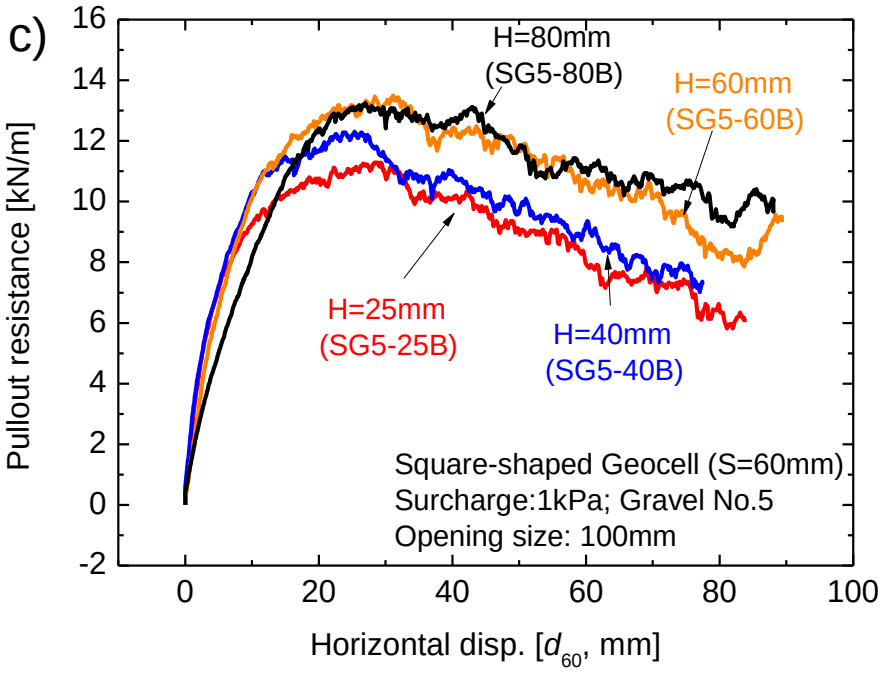

Fig. 4.15 (Continued) Pullout behaviors of square-shaped geocell with different heights embedded in c) Gravel No.5

To analyze this trend, Figure 4.16a summarizes the peak pullout resistance of square-shaped geocells embedded in Gravel No.1, Gravel No.3 and Gravel No.5 (i.e. test cases of SG1-12.5B, SG1-25B, SG1-40B, SG3-25B, SG3-40B, SG3-60B, SG5-25B, SG5-40B, SG5-60B, and SG5-80B). It may be seen that, under the same testing conditions, the pullout resistance increases with an increase in the member height with the square-shaped geocell. However, there exists an upper limit of the pullout resistance that is reached when the height of member becomes a certain value. Both limit height of geocell and limit pullout resistance increase with an increase in the backfill particle size.

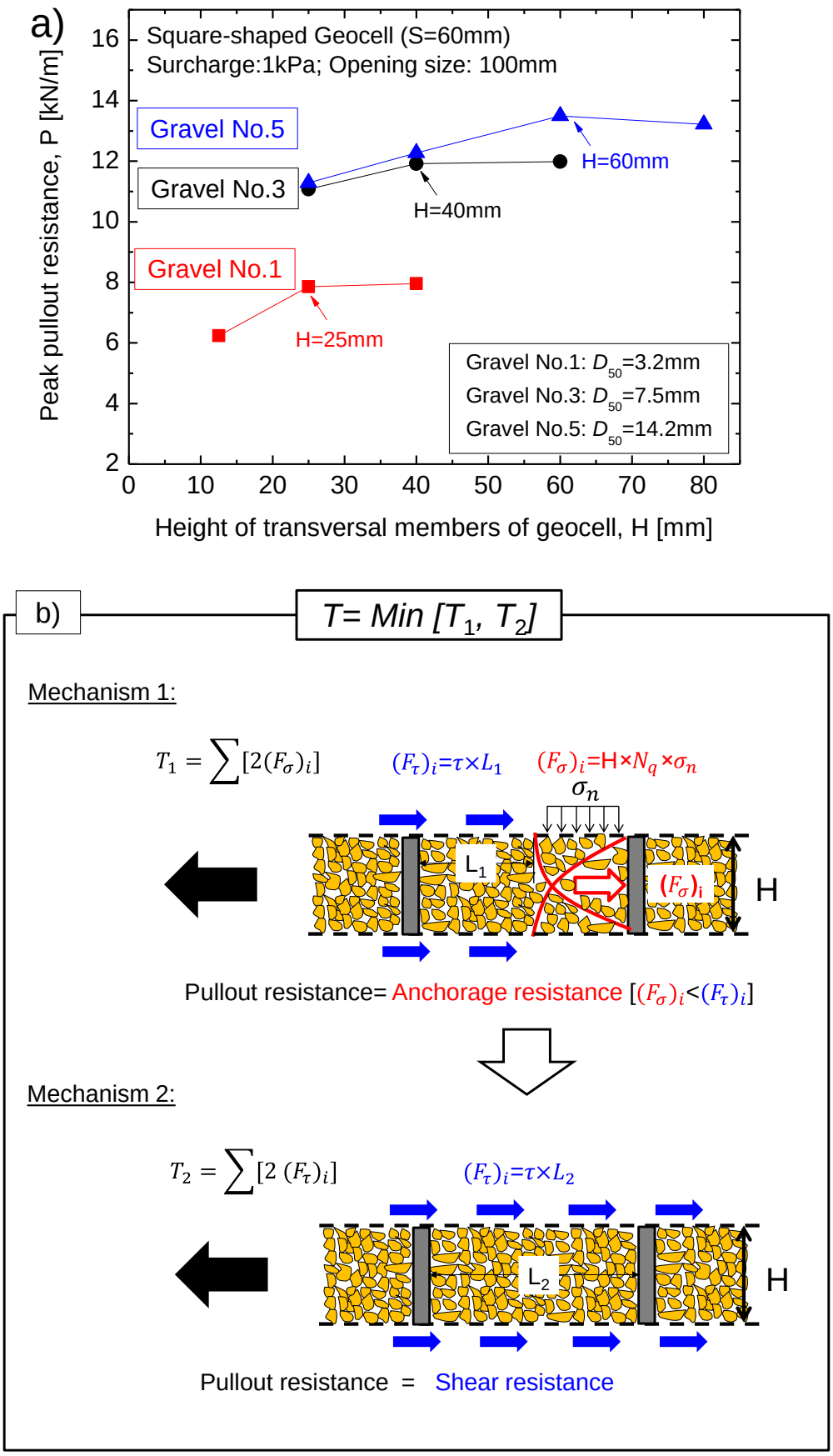

Fig. 4.16 a) Effect of height of geocell relative to particle size of backfill on peak pullout resistance; b) Schematic mechanism of pullout resistance of geocell reinforcements embedded in the backfill with different particle size.

These test results suggest the following fundamental mechanism. As shown in Figure 4.16b, the peak pullout resistance is equal to the smaller between the following two types of resistance: 1) the shear resistance of the shear bands that develops along the upper and bottom faces of a geocell and the backfill, which is independent of the height of transversal member of geocell; and 2) the anchorage resistance induced by passive pressure developing inside the cells, which increases with an increase in the height of transversal member of geocell. Therefore, as the height of geocell increases, the total pullout resistance is first determined by the anchorage resistance which is smaller than the shear resistance and increases with an increase in the height of geocell. When the height of geocell reaches a certain value, the anchorage resistance becomes larger and finally reaches the shear resistance. Then, the pullout resistance is determined by the shear resistance and does not increase with further increase in the height of geocell. Both shear resistance and anchorage resistance increase with an increase in the backfill particle size, therefore the pullout resistance does so too. This behavior becomes stronger at larger pull-out displacements. The test results show that the limit of the height of geocell at which the two types resistance become the same increase with an increase in the backfill particle size.

4.6 Effect of spacing between transversal members of the newly-developed geocell

Section 4.5 showed that the height of the transversal members of geocell (H) is a key influential factor on the interface mechanism between geocell and adjacent backfill soil. The spacing (S) between transversal members is also investigated in this section. A new square-shaped geocell was constructed by increasing the spacing between transversal members from 60 mm to 120 mm, while the height was kept as 25 mm. Two tests (i.e. SG1-25SB and SG3-25SB, Table 4.4) were conducted by using this geocell embedded in Gravel No.1 and Gravel No.3, respectively.

Table 4.4 Test cases for square-shaped geocell having different spacing between transversal members

Test number	Reinforcement	Reinforcement height (mm)	Cell or grid size (mm)	Backfill materials[A)]	Opening height of front wall (mm)
SG1-25SB	Square-shaped geocell	25	50 mm × 120 mm	Gravel No.1	100
SG3-25SB	Square-shaped geocell	25	50 mm × 120 mm	Gravel No.3	100

A) Gravel No.1: D_{50} = 3.2 mm; Gravel No.3: D_{50} = 7.5 mm (Figs. 3.5 and 3.6)

Figure 4.17 compares the pullout behaviors of the square-shaped geocell with transversal spacing of 120 mm and 60 mm. In addition, Fig. 4.18 shows the combined influence of the height and spacing between transversal members. It was found that, in the case of Gravel No.1 (i.e. smaller particles), the geocell with a transversal spacing of 120 mm shows the same peak pullout resistance compared to the geocell with a transversal spacing of 60 mm, because the shear resistance of the shear bands along the upper and bottom boundaries of the geocell controlled the total pullout resistance for the geocell with height of 25 mm in Gravel No.1, which is independent of the height of the geocell as well as the transversal spacing. While in the case of Gravel No.3 (i.e. larger particles), the geocell with a transversal spacing of 120 mm shows slightly lower peak pullout resistance comparing to the geocell with a transversal spacing of 60 mm. This is due to the fact that the anchorage resistance induced by passive pressure developed inside the cells determined the total pullout resistance for the geocell with height of 25 mm in Gravel No.3. As the spacing of transversal members increases (i.e.

decrease in transversal members), the total anchorage resistances decreases, thereby decreasing total pullout resistance.

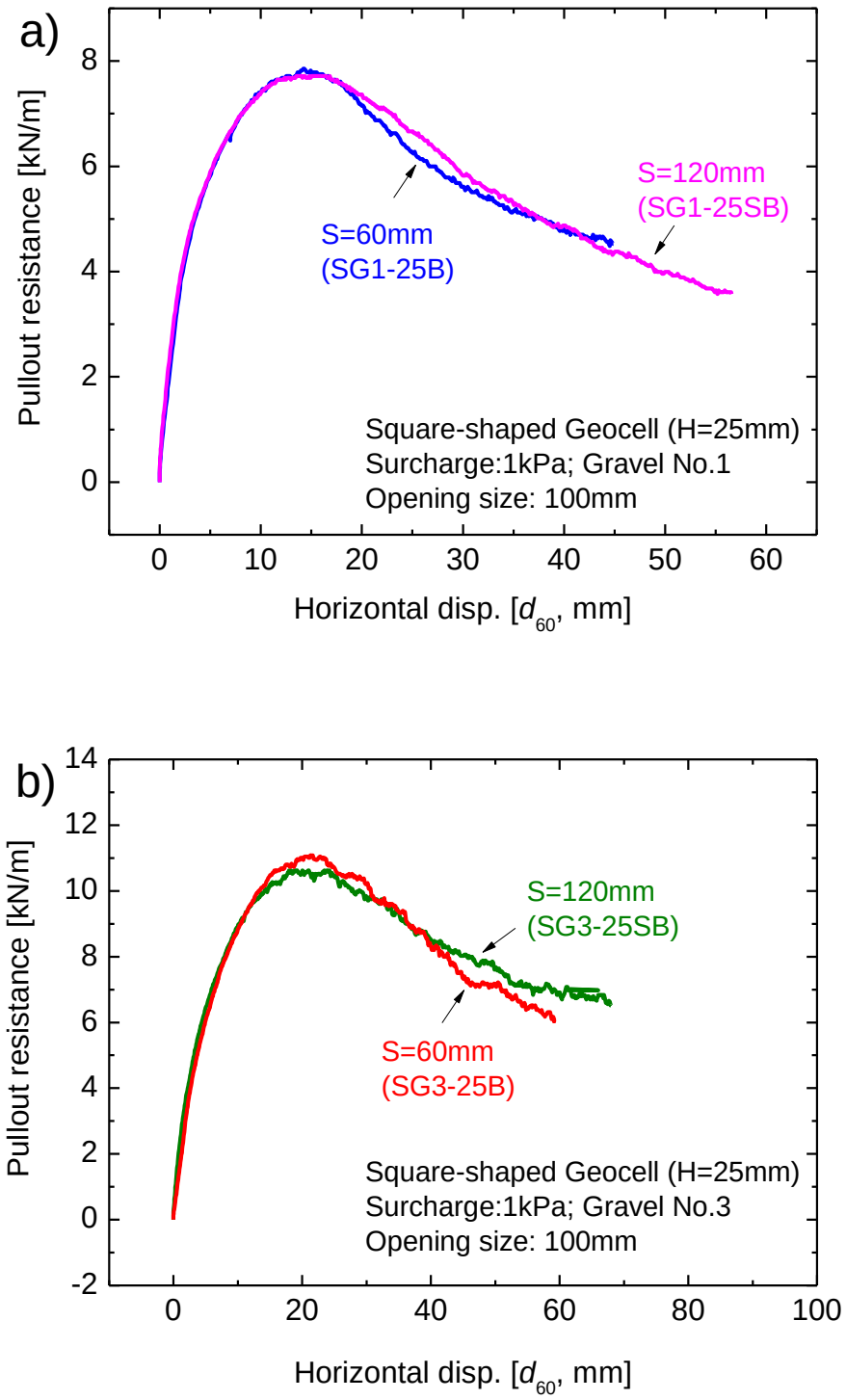

Fig. 4.17 Pullout behaviors of geocell with different spacing between transversal members embedded in: a) Gravel No.1 and b) Gravel No.3.

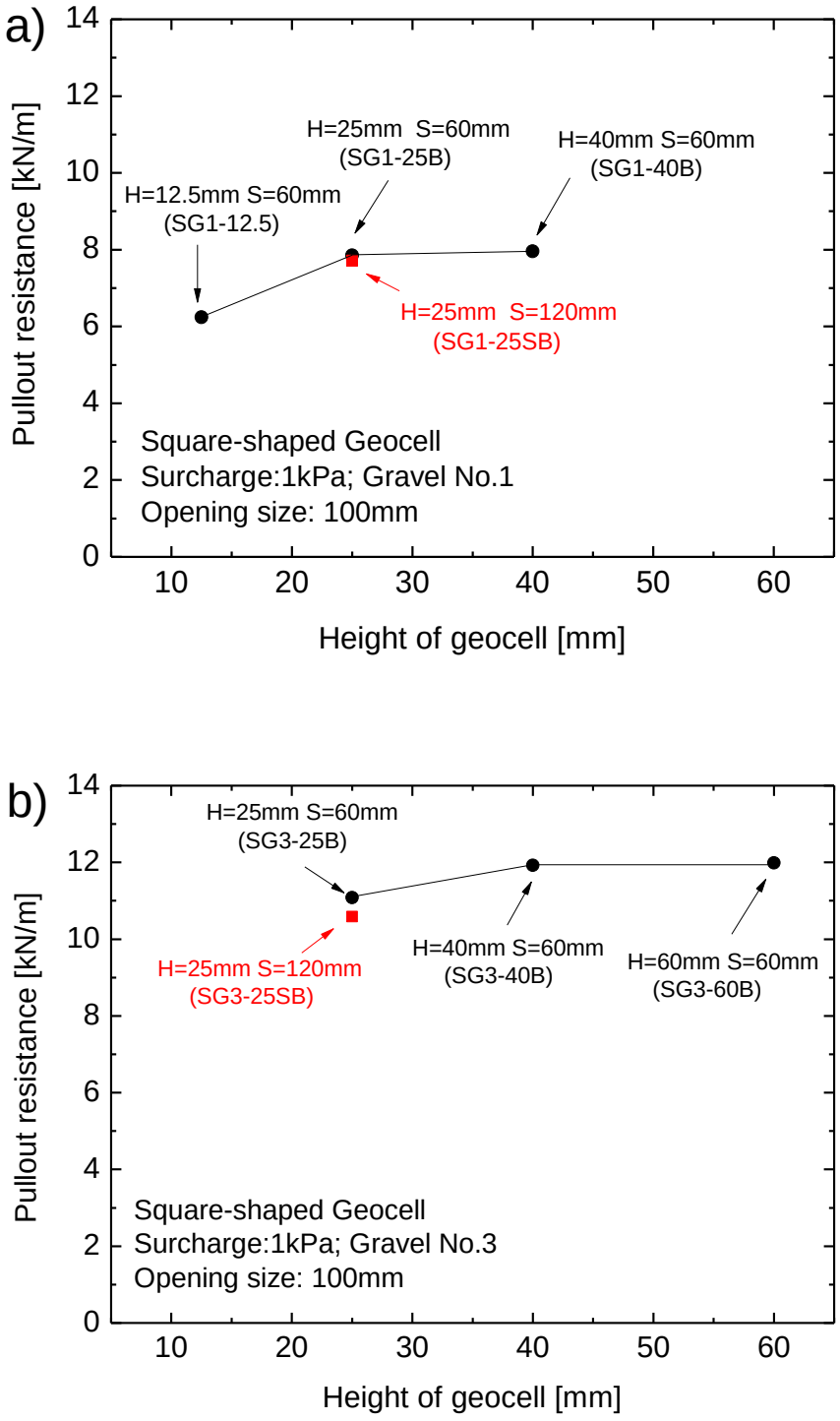

Fig. 4.18 Influence of height of member height and spacing between transversal members on the peak pullout resistance in the backfill of: a) Gravel No.1 and b) Gravel No.3.

4.7 References

1. Horpibulsuk, S. and Niramitkornburee, A. (2010). "Pullout resistance of bearing reinforcement embedded in sand", Soils and Foundations, 50(2), 215-226.
2. Khedkar, M.S. and Mandal, J.N. (2009). "Pullout behaviour of cellular reinforcements", Geotextiles and Geomembranes, 27(4), 262-271.
3. Kiyota, T., Soma, R., Munoz, H., Kuroda, T., Ohta, J., Harata, M. and Tatsuoka, F. (2009). "Pullout behaviour of geocell placed as reinforcement in backfill", Geosynthetics Engineering Journal 24(0), 75-82. (In Japanese).
4. Kongkitkul, W., Hirakawa, D. and Tatsuoka, F. (2007). "Viscous behaviour of geogrids; experiment and simulation", Soils and Foundations, 47(2), 265-283.
5. Racana, N., Grediac, M. and Gourves, R. (2003). "Pull-out response of corrugated geotextile strips". Geotextiles and Geomembranes, 21(5), 265-288.
6. Suksiripattanapong, C., Horpibulsuk, S., Chinkulkijniwat, A. and Chai, J.C. (2013). "Pullout resistance of bearing reinforcement embedded in coarse-grained soils", Geotextiles and Geomembranes, 36, 44-54.

5 SEISMIC PERFORMANCE OF GRS RWS WITH NEWLY-DEVELOPED GEOCELL

5.1 Introduction

In this chapter, to check whether or not the square-shaped geocell reinforced soil retaining wall (geocell-RS RW) has a substantially high seismic stability against a large seismic load, a series of shaking table model tests on geocell-RS RWs backfilled with sandy soil were carried out. For comparison, shaking model tests on a geogrid reinforced soil retaining wall (i.e. geogrid^{M}-RS RW) and traditional non-reinforced RW (i.e. T-shape RW) backfilled with sandy soil were conducted. Additional four shaking table tests on geocell-RS RW, geogrid^{M}-RS RW, geogrid^{C}-RS RW and T-shape RW backfilled with poorly-graded gravel were also conducted to confirm if geocell-RS RW has a higher seismic stability than geogrid-RS RW (i.e. geogrid^{M}-RS RW and geogrid^{C}-RS RW) in backfill with larger particles. The test cases are shown in Table 5.1.

Table 5.1 Shaking table test cases.

Test cases	Model wall type	Reinforcement	Backfill
T-shape RW-S	T-shape RW	-	Sand
Geocell-RS RW-S	GRS RW	Geocell models	Sand
Geogrid^{M}-RS RW-S	GRS RW	Geogrid^{M}	Sand
T-shape RW-G	T-shape RW	-	Gravel
Geocell-RS RW-G	GRS RW	Geocell models	Gravel
Geogrid^{M}-RS RW-G	GRS RW	Geogrid^{M}	Gravel
Geogrid^{C}-RS RW-G	GRS RW	Geogrid^{C}	Gravel

Section 5.2 presents the general test results for each case during shaking including base acceleration of the shaking table as a function of time, response acceleration at the top of wall, deformation of the wall, earth pressure activated on the wall and the settlements of the backfill. The deformation modes of different types of RWs during shaking are revealed through image observation. From this, the basic failure patterns for the RW models are discussed.

In Section 5.3, the seismic performance of geocell-RS RW is evaluated from the following aspects: residual overturning angle of the facing wall, response accelerations of the wall and the backfill soil, settlements of the backfill compared to the seismic performance of geogrid-RS RW and T-shape RW in backfill of sand and gravel, respectively. In addition, a discussion on the critical acceleration for comparing the stability of different types of retaining wall models is also provided.

In Section 5.4, the dynamic stability of geocell-RS RWs is analyzed as a damped single-degree-of-freedom (SDOF) system. Comparison of dynamic stability of different types of RW models backfilled with different soil materials is carried out by evaluating their dynamic strength, dynamic ductility and damping capacity at failure state etc.

5.2 General test results

Case 1: T-shape RW-S

Figure 5.1 presents the deformation mode of the T-shape RW-S with the image sequence taken at completion of shaking stages of 391 gal and 461 gal. Fig. 5.2 shows the input base acceleration (α_b), response acceleration at the top of the wall (α_r), the averaged earth pressure activated on the wall (σ_h), the displacements of the wall at different height (L_s) and the settlement of backfill at different locations (L_v) all as a function of time, which were measured as shown in Fig. 3.22a. Note that α_b (i.e. A7 in Fig. 3.22) was taken as the average base accelerations for 20 cycles at active state (i.e. when the inertial force was in the outward direction) for each shaking stage. Note also that α_r (i.e. A6 in Fig. 3.22) was taken as the acceleration at the 10^{th} cycle for each shaking stage.

Up to shaking stage α_b = 302 gal, only limited L_s and L_v occurred. At shaking stage α_b = 391 gal, L_s started to increase slightly along with an increase in α_r, σ_h and L_v. As can be seen from Fig. 5.1a, slight overturning along with small deformation of the backfill immediately behind the back face of wall occurred. While at shaking stage α_b = 461 gal, a drastic increase in L_s, L_v and α_r as well as a decrease in σ_h, indicated brittle failure behavior of the T-shape RW. As shown in Fig. 5.1b, a single failure plane was formed starting from the heel of the wall, which was associated with larger settlement of the backfill and larger overturning with small sliding of the wall. This failure pattern can be attributed to the loss of bearing capacity of the foundation (Watanabe et al. 2003).

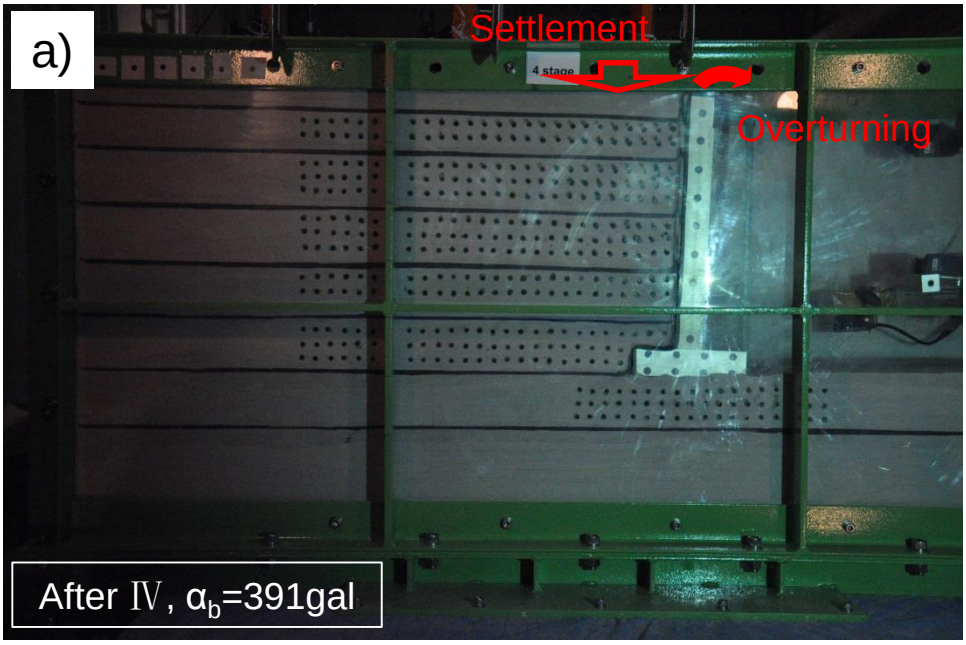

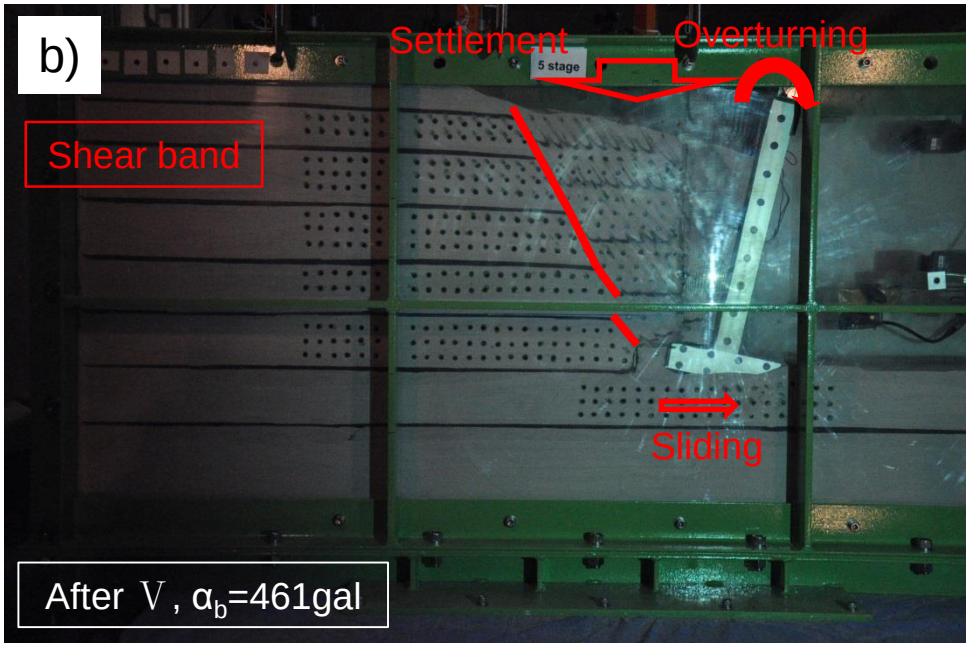

Fig. 5.1 Deformation modes of T-shape RW-S: a) after shaking stage Ⅳ (α_b = 391 gal); b) after shaking stage Ⅴ (α_b = 461 gal)

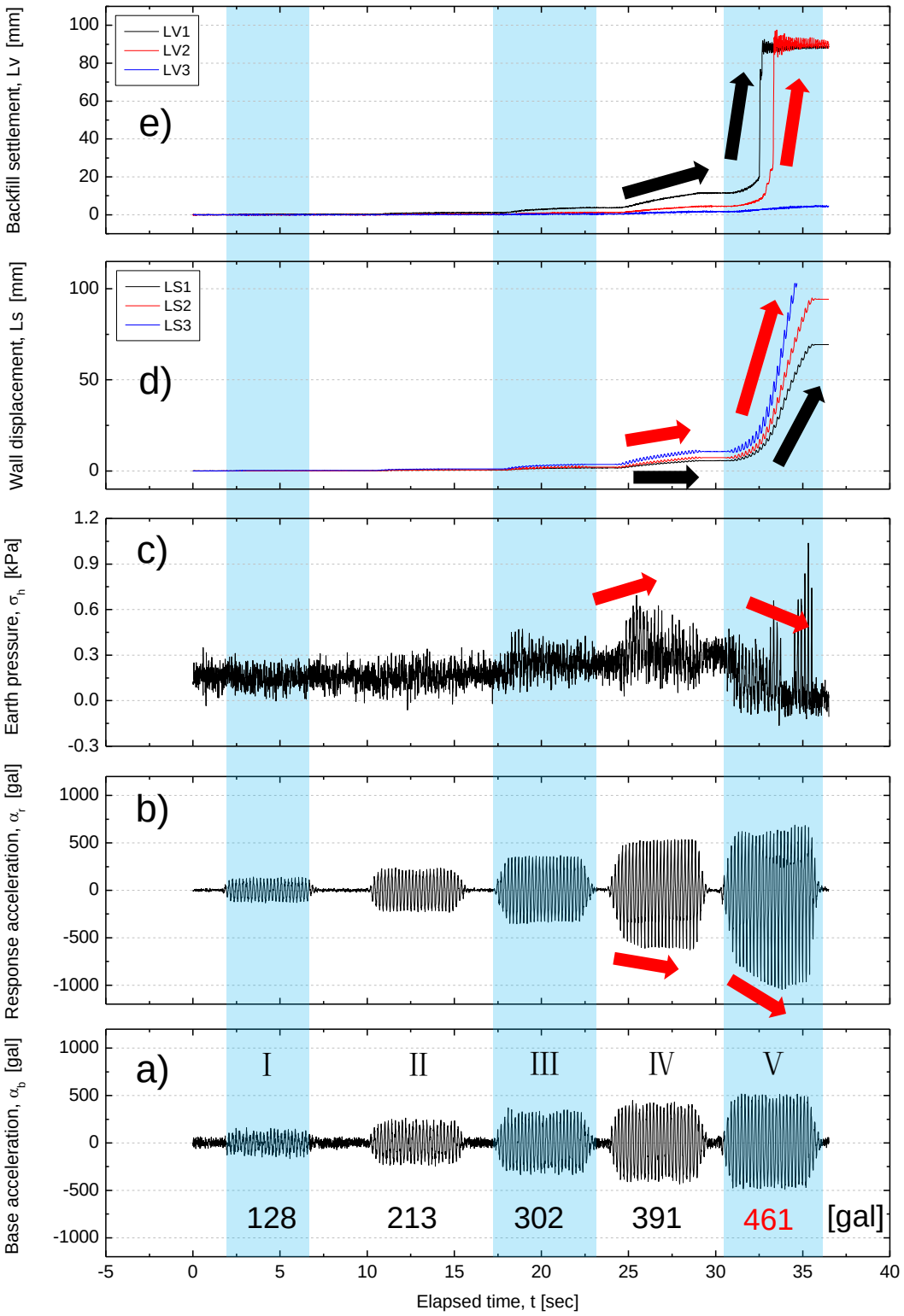

Fig. 5.2 Time history of: a) base acceleration; b) response acceleration at the top of the wall; c) averaged earth pressure; d) facing wall displacements; e) backfill settlements for T-shape RW-S

Case 2: Geogrid^{M}-RS RW-S

Figure 5.3 presents the deformation mode of geogrid^{M}-RS RW-S with the image sequence taken at completion of shaking stages of 531 gal, 613 gal, 695 gal and 772 gal. Fig. 5.4 shows α_b, α_r, σ_h, L_s and L_v as a function of time, which were measured as shown in Fig. 3.22b.

Up to shaking stage α_b = 324 gal, there was no evident deformation of the wall nor the backfill. From shaking stage α_b = 425 gal to α_b = 613 gal, both L_s and L_v started to increase gradually. As shown in Fig. 5.3b, at shaking stage α_b = 613 gal, small deformation of the backfill and settlement of the backfill immediately behind the reinforced backfill zone occurred due to slightly overturning and sliding of the wall induced by the seismic force. In addition, a slightly bulge in the upper part of the reinforced backfill zone can be observed from the black sand layers. From shaking stage α_b = 695 gal to α_b = 772 gal, L_s and L_v increased largely, especially at shaking stage α_b = 772 gal. From Fig. 5.3c, at shaking stage α_b = 695 gal, two obvious shear bands were observed: one was located at the Line A between the reinforced zone and the unreinforced zone around 15 cm; the other was located at the Line B in the unreinforced zone and originated from the end of reinforcement Layer 2 (Figs. 3.22b and 5.3c) around 20 cm. Note that both the shear bands did not reach the ground surface of the backfill. Due to the formation of shear band 1 (i.e. Fig. 5.3c), a relative larger overturning with smaller sliding of the wall and smaller settlement of the backfill occurred. At shaking stage α_b = 772 gal, multiple shear bands were clearly formed. Shear band 1 located at Line A was extended to the position near the end of reinforcement Layer 2 (Figs. 3.22b and 5.3d) along the edge of the reinforced zone. Shear band 1 located at Line B was extended to the surface of the unreinforced backfill zone. Due to full formation of the shear bands, overturning of the wall and settlement of the backfill increased significantly, which can be defined as failure state of the geogrid^{M}-RS RW-S.

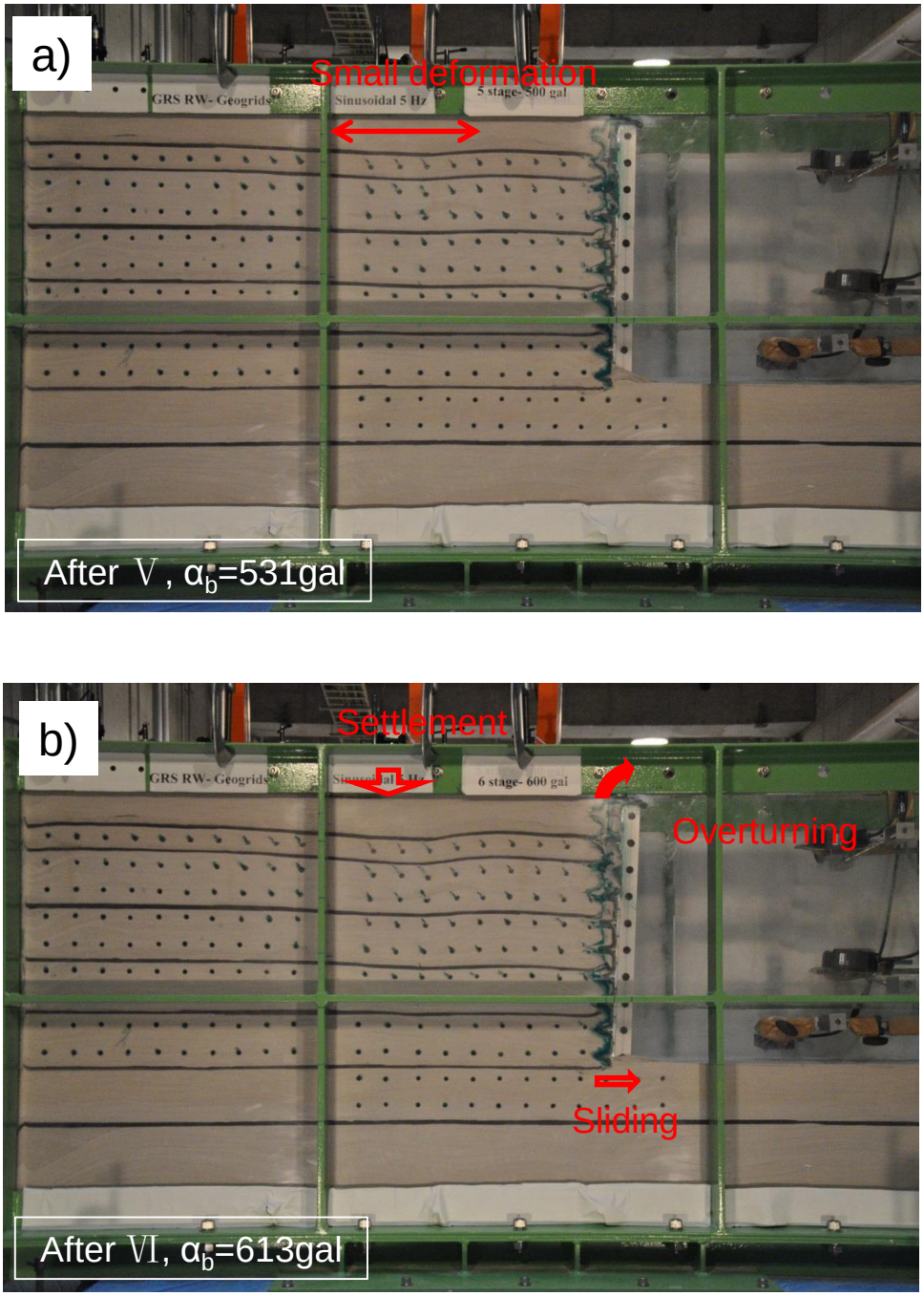

Fig. 5.3 Deformation modes of geogrid^{M}-RS RW-S: a) after shaking stage Ⅴ (α_b=531 gal); b) after shaking stage Ⅵ (α_b=613 gal);

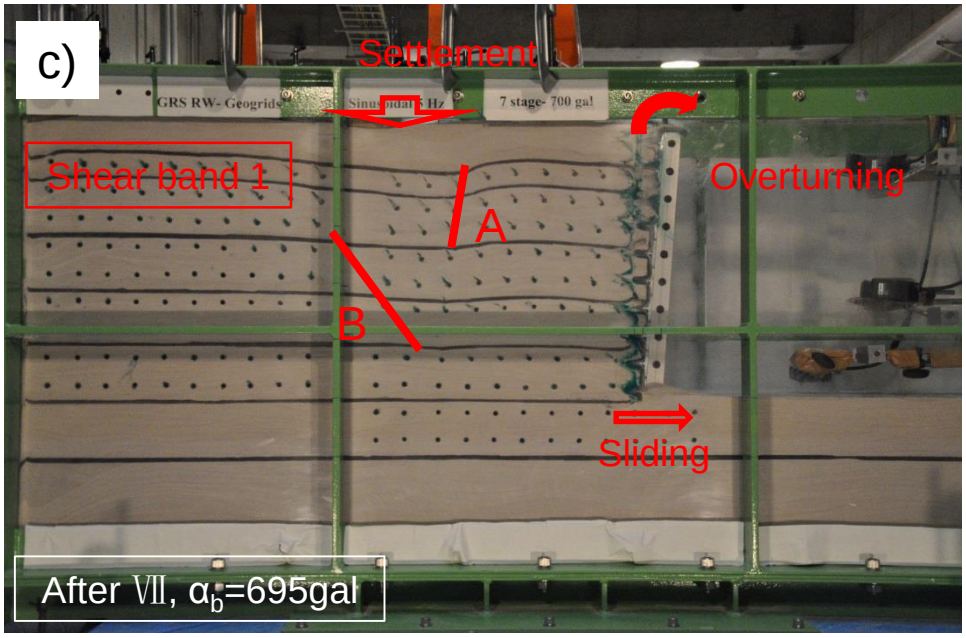

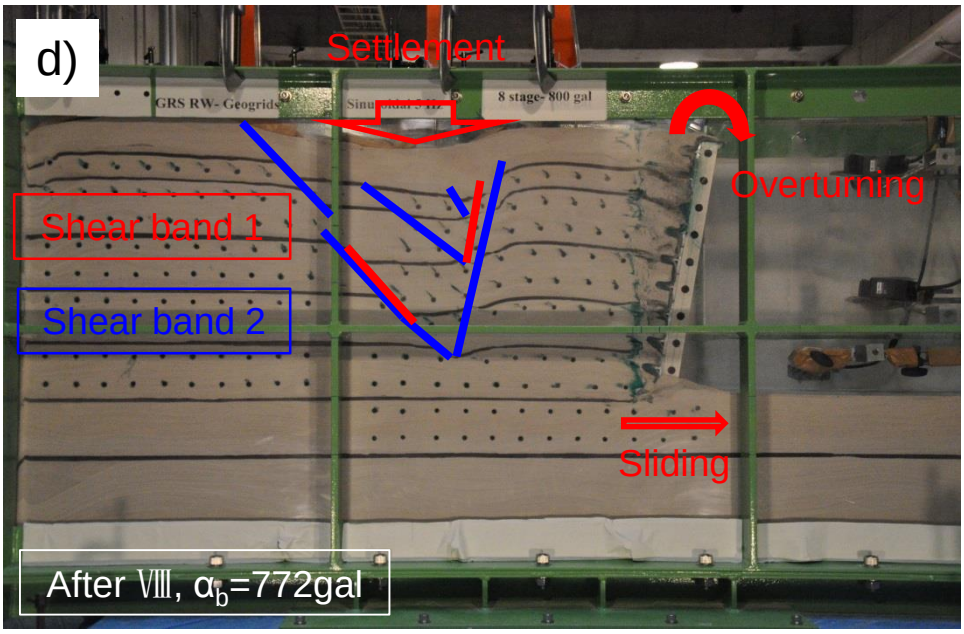

Fig. 5.3 (Continued) Deformation modes of geogrid^{M}-RS RW-S: c) after shaking stage Ⅶ (α_b=695 gal); d) after shaking stage Ⅷ (α_b=772 gal)

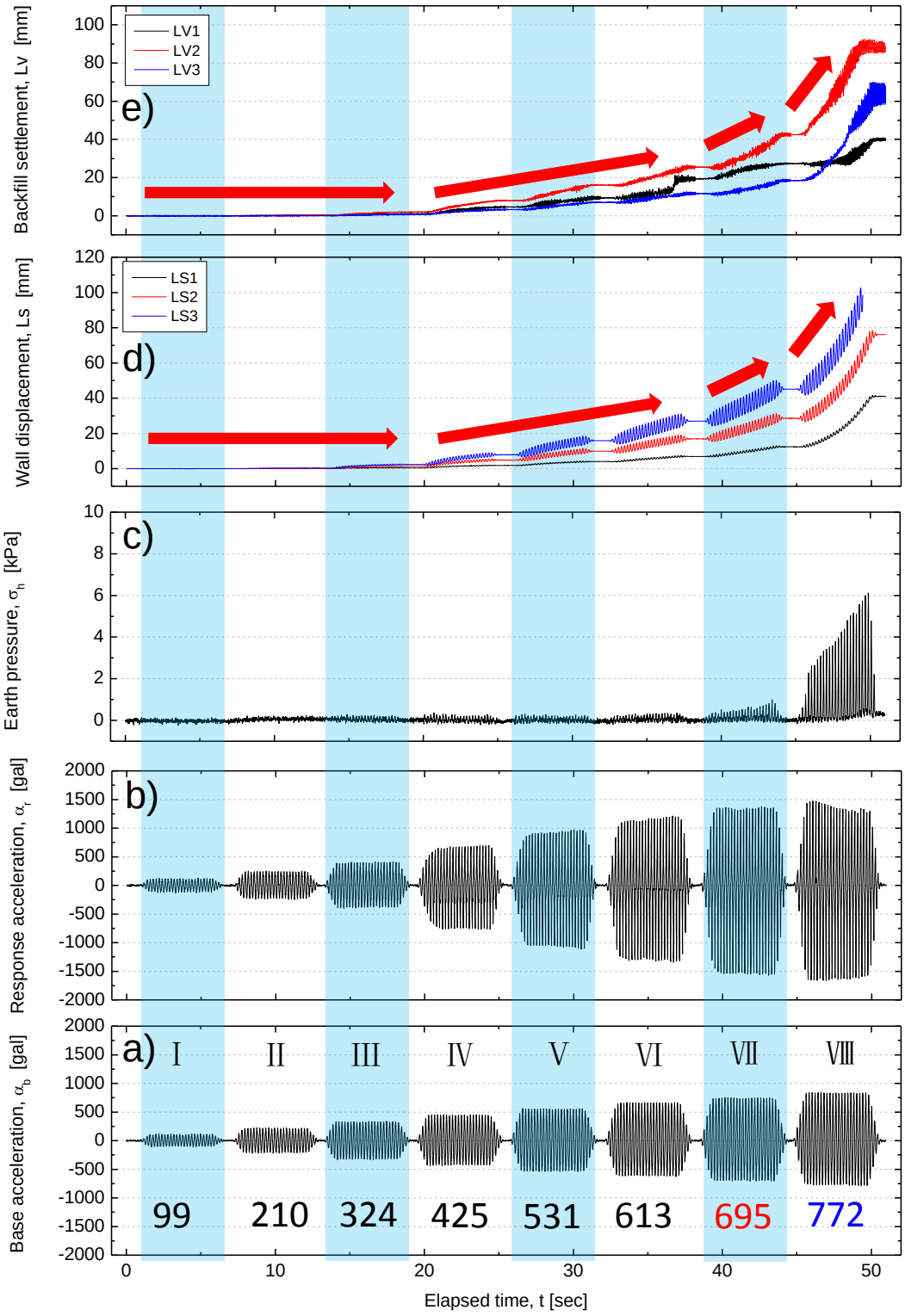

Fig. 5.4 Time history of: a) base acceleration; b) response acceleration at the top of the wall; c) averaged earth pressure; d) facing wall displacements; e) backfill settlements for geogrid^{M}-RS RW-S

Case 3: Geocell-RS RW-S

Figure 5.5 presents the deformation mode of geocell-RS RW-S with the image sequence taken at completion of shaking stages of 550 gal, 631 gal, 756 gal and 865 gal. Fig. 5.6 shows the time history of α_b, α_r, σ_h, L_s and L_v, which were measured as shown in Fig. 3.22b. Similar deformation mode of geocell-RS RW-S was found also for geogrid^M-RS RW-S (i.e. Case 2). Up to shaking stage α_b = 477 gal, there was almost no development of deformation of the wall or the backfill. From shaking stage α_b = 550 gal to α_b = 756 gal, L_s and L_v started to increase gradually. As shown in Fig. 5.5b, at shaking stage α_b = 631 gal, a small shear band in Area A started to form. Due to the decrease in pullout resistance of the geocell reinforcement in the upper part of the backfill (i.e. Layer 10, Layer 9 and Layer 8, as shown in Fig. 3.22b), relatively large overturning but small sliding of the retaining wall can be observed, which was associated with small settlement of the backfill immediately behind the reinforced zone. At shaking stage α_b = 756 gal, more small shear bands formed in Area B along the edge of the reinforced zone (Fig. 5.5c). During this stage, pullout resistances of the geocell reinforcements may continue to decrease gradually from the top to the bottom layer. At the final shaking stage α_b = 865 gal, small shear bands in Area B were linked to each other forming a unified shear band. In addition, multiple shear bands in the unreinforced backfill zone also formed resulting in larger overturning with smaller sliding of the wall and larger settlement of the unreinforced backfill (Fig. 5.5d). Note that both shear bands 1 and 2 did not reach the bottom of the reinforced zone but the end of geogell reinforcement Layer 2 (as shown in Figs. 3.22b and 5.5d), which indicated that the bottom reinforcement layers (i.e. Layer 1 and Layer 2) constrained sliding of the retaining wall effectively.

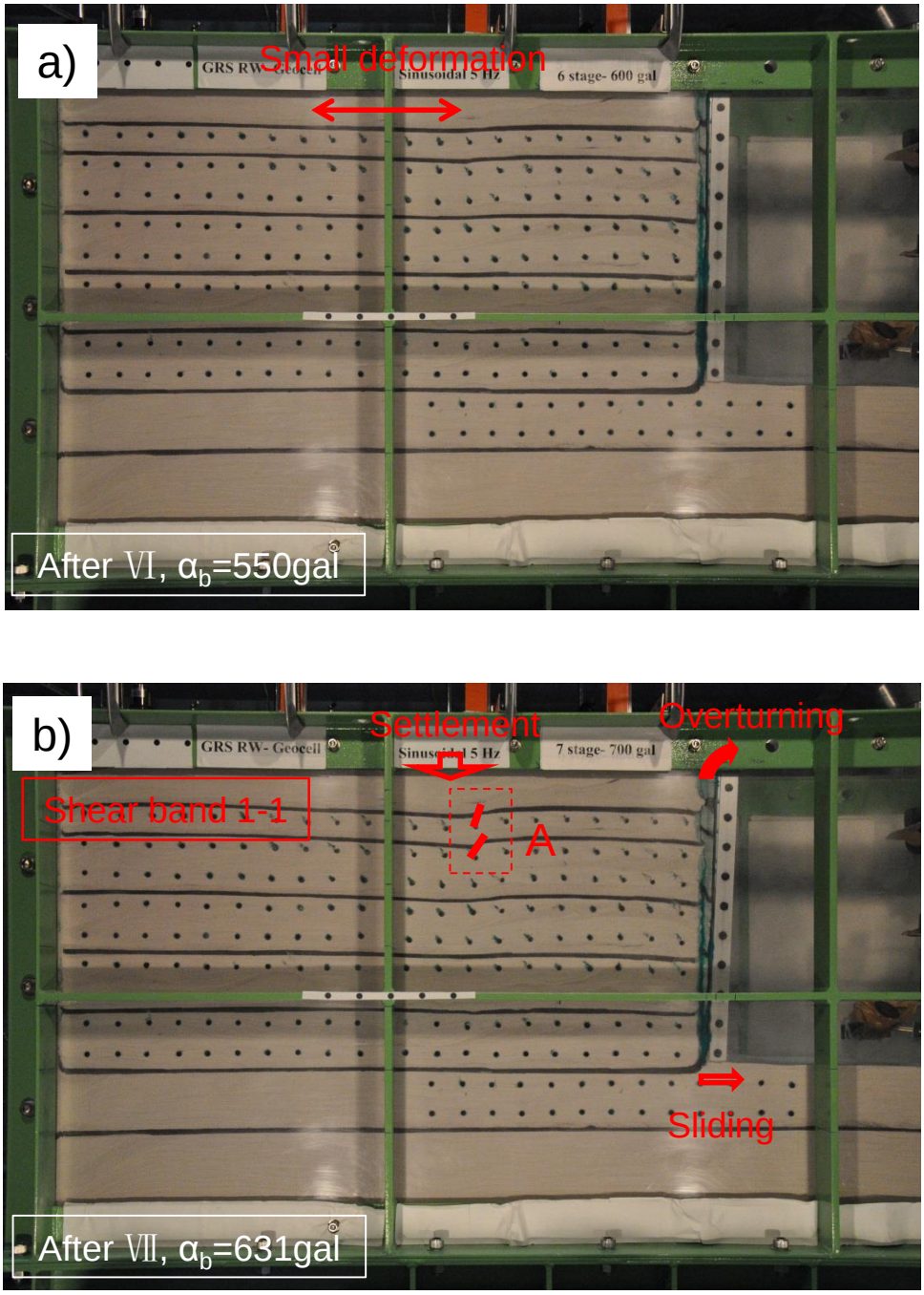

Fig. 5.5 Deformation modes of geocell-RS RW-S: a) after shaking stage Ⅵ (α_b = 550 gal); b) after shaking stage Ⅶ (α_b = 631 gal);

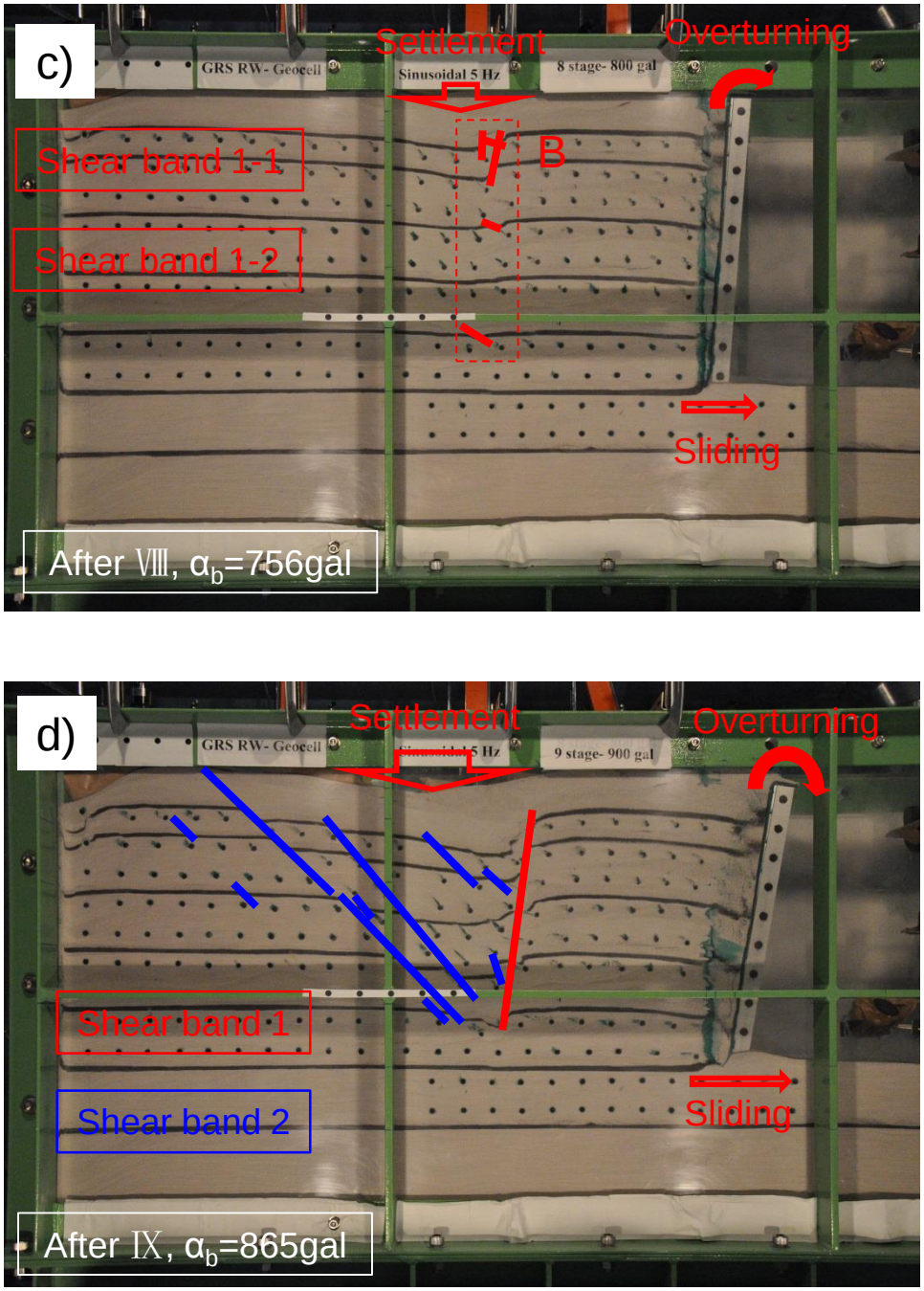

Fig. 5.5 (Continued) Deformation modes of geocell-RS RW-S: c) after shaking stage Ⅷ (α_b = 756 gal); d) after shaking stage Ⅸ (α_b = 865 gal)

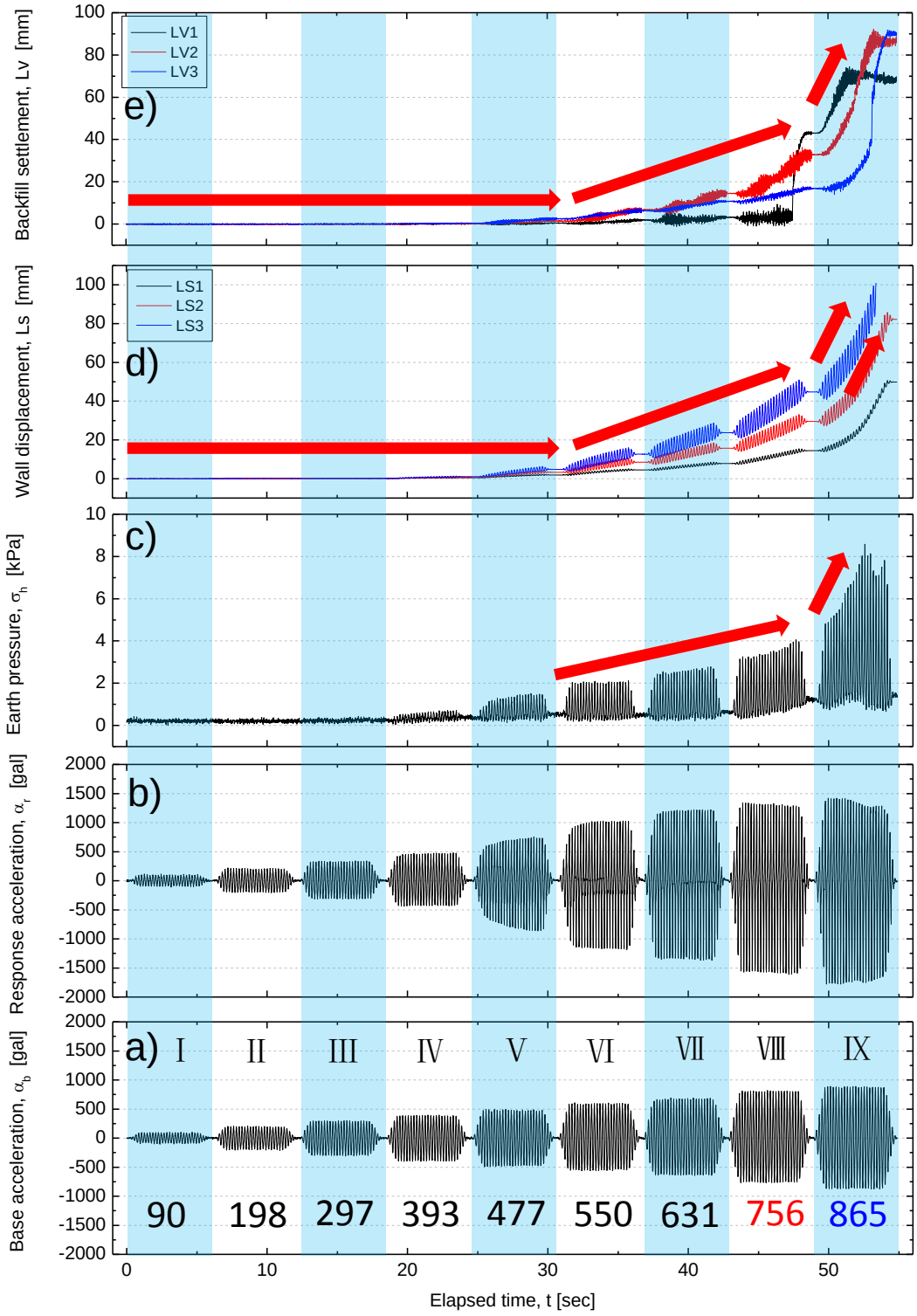

Fig. 5.6 Time history of: a) base acceleration; b) response acceleration at the top of the wall; c) averaged earth pressure; d) facing wall displacements; e) backfill settlements for geocell-RS RW-S

Case 4: T-shape RW-G

The time history of α_b, α_r, L_s and L_v are plotted in Fig. 5.8 as well as the deformation modes during shaking in Fig. 5.7. Up to shaking stage α_b = 319 gal, only limited L_s and L_v occurred. At shaking stage α_b = 417 gal, L_s started to increase abruptly along with a drastic increase in α_r and L_v, indicating brittle failure behavior of the T-shape RW. As shown in Fig. 5.7b, a potential Shear band 1* located in Area A formed starting from the heel of the wall, which was associated with larger settlement of the backfill, larger sliding of the wall and settlement of the wall foundation. The failure mode of T-shape RW-G in Case 4 was predominantly sliding and was associated with a small component of overturning, which was different from that backfilled with sand (i.e. Case 1). This may be due to the fact that the used gravel subsoil with larger particles may increase the bearing capacity of the foundation of the wall (Tatsuoka et al., 1989) compared with sandy soil.

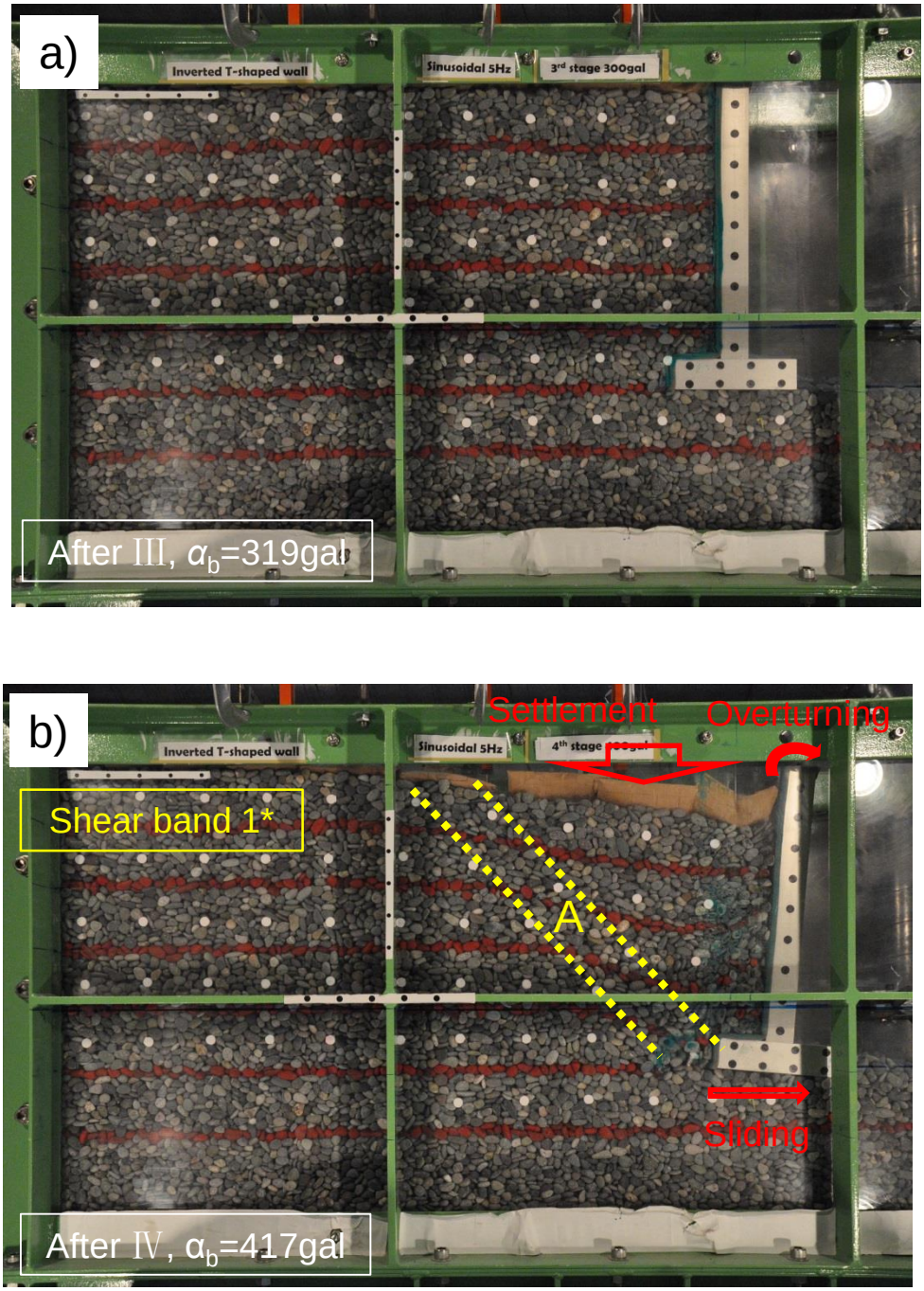

Fig. 5.7 Deformation modes of T-shape RW-G: a) after shaking stage Ⅲ. (α_b = 319 gal); b) after shaking stage Ⅳ (α_b = 417 gal).

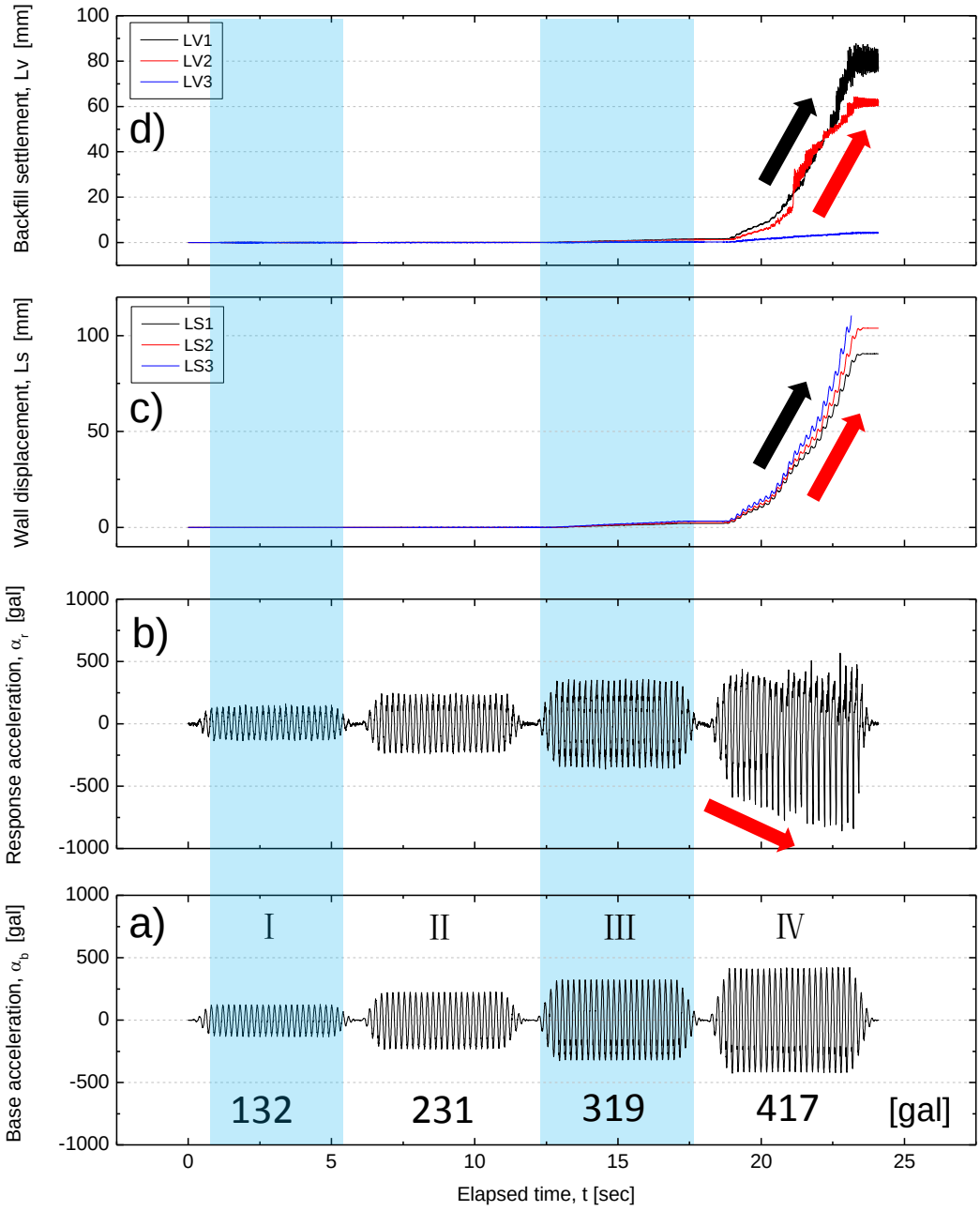

Fig. 5.8 Time history of: a) base acceleration; b) response acceleration at the top of the wall; c) facing wall displacements; d) backfill settlements for T-shape RW-G

Case 5: Geogrid^{M}-RS-G

The time history of α_b, α_r, σ_h, L_s and L_v are plotted in Fig. 5.10 as well as the deformation modes during shaking in Fig. 5.9. Up to shaking stage α_b = 383 gal, there was no marked deformation of the wall as well as the backfill and the wall started to overturn at shaking stage α_b = 465 gal (Fig. 5.10). Following this, the deformation of the wall and settlement of the backfill became larger. As shown in Fig. 5.9b, at shaking stage α_b = 628 gal, a potential shear band 1* located at Line A around 15 cm was formed, indicating that the pullout resistances of the geogrid reinforcement in the upper part of the reinforced zone (i.e. Layer 8, Layer 9 and Layer 10 shown in Figs. 3.22b and 5.9b) firstly started to decrease. At shaking stage α_b = 755 gal (Fig. 5.9c), a probable shear band 2* in the unreinforced zone developed at the end of reinforcement Layer 2 (Figs. 3.22b and 5.9c), but it was not extended to the ground surface of the backfill. Due to the formation of two potential shear bands 1* and 2*, larger overturning associated with a small component of sliding of the wall as well as larger settlement of the backfill occurred.

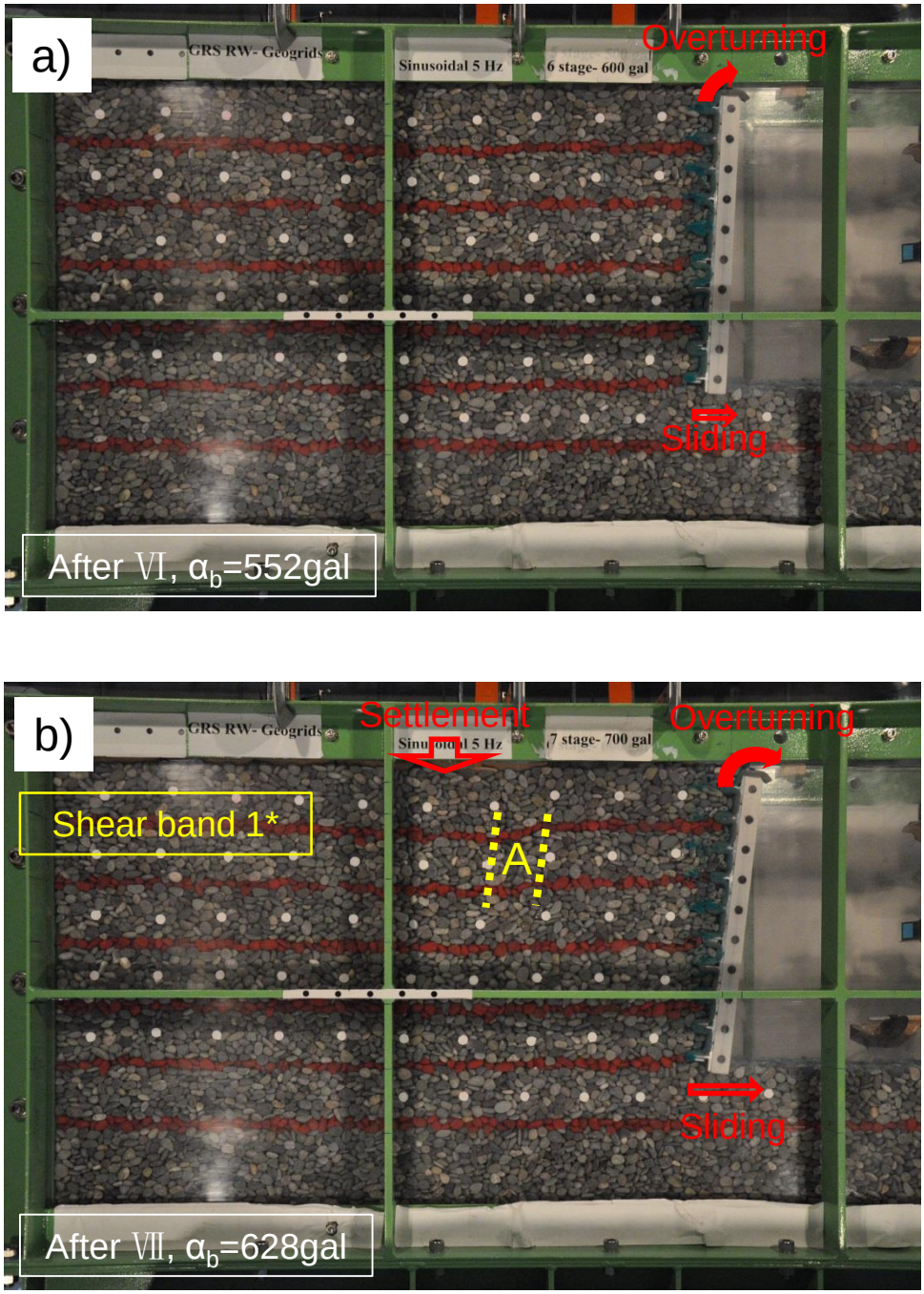

Fig. 5.9 Deformation modes of geogrid^{M}-RS RW-G: a) after shaking stage Ⅵ (α_b = 552 gal); b) after shaking stage Ⅶ (α_b = 628 gal);

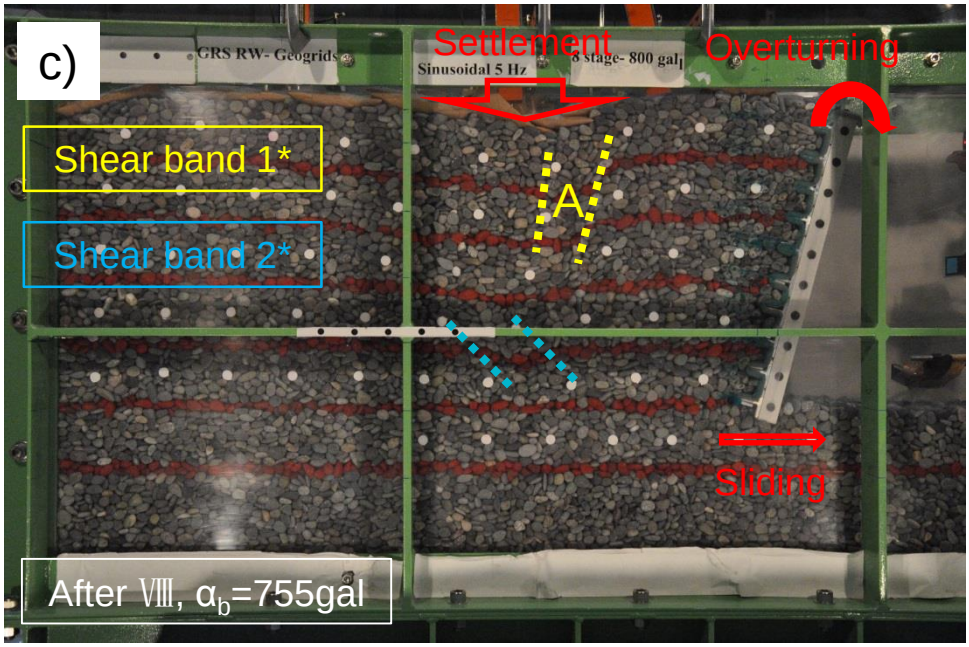

Fig. 5.9 (Continued) Deformation modes of geogrid^{M}-RS RW-G: c) after shaking stage Ⅷ (α_b = 755 gal).

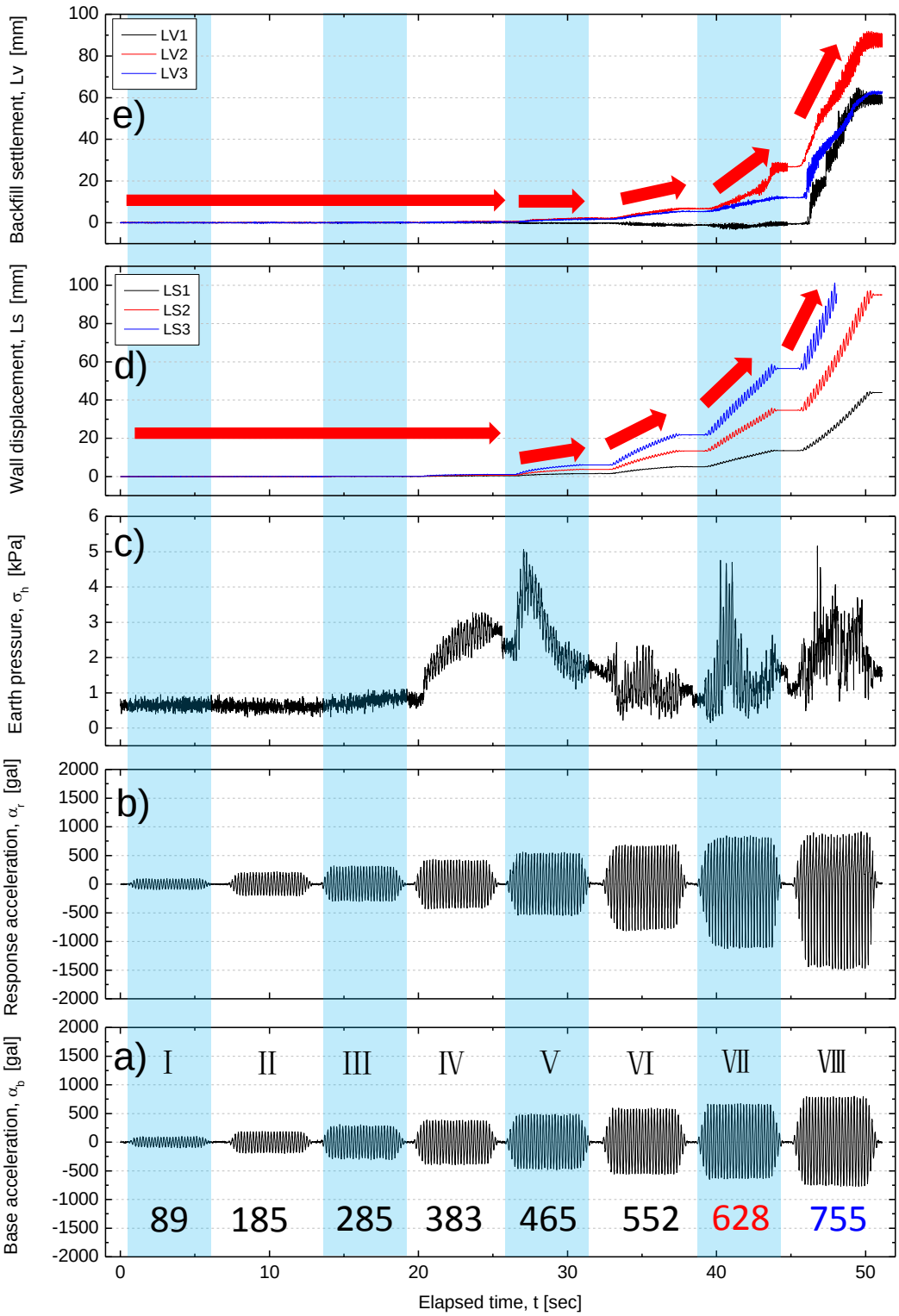

Fig. 5.10 Time history of: a) base acceleration; b) response acceleration at the top of the wall; c) averaged earth pressure; d) facing wall displacements; e) backfill settlements for geogrid^{M}-RS RW-G

Case 6: Geogrid^{C}-RS RW-G

The time history of α_b, α_r, σ_h, L_s and L_v are plotted in Fig. 5.12 as well as the deformation modes during shaking in Fig. 5.11. Similar trend was found as in Case 5. Up to shaking stage α_b = 316 gal, there was no apparent deformation of the wall or the backfill. From shaking stage α_b = 411 gal to α_b = 598 gal, L_s and L_v started to increase gradually. At shaking stage α_b = 690 gal (Fig. 5.11b), due to the formation of potential shear bands 1*, larger overturning associated with a small component of sliding of the wall as well as larger settlement of the backfill occurred. Note that, as shown in Fig. 5.12, at shaking stage α_b = 598 gal, the response acceleration at the top of the wall firstly increased and then dropped gradually to a certain value. Lateral wall displacements accumulated in an obvious non-linear manner, while at shaking stages α_b = 500 gal and α_b = 690 gal, lateral wall displacements accumulated in a linear manner. These unexpected results suggestted that at shaking stage α_b = 598 gal some unexpected testing conditions affected the seismic behavior of geogrid^{C}-RS RW. A possible explanation was that the wall facing may be touching the side wall of the soil container due to the asymmetric overturning of the wall facing during shaking, which restricted the movement of the RW.

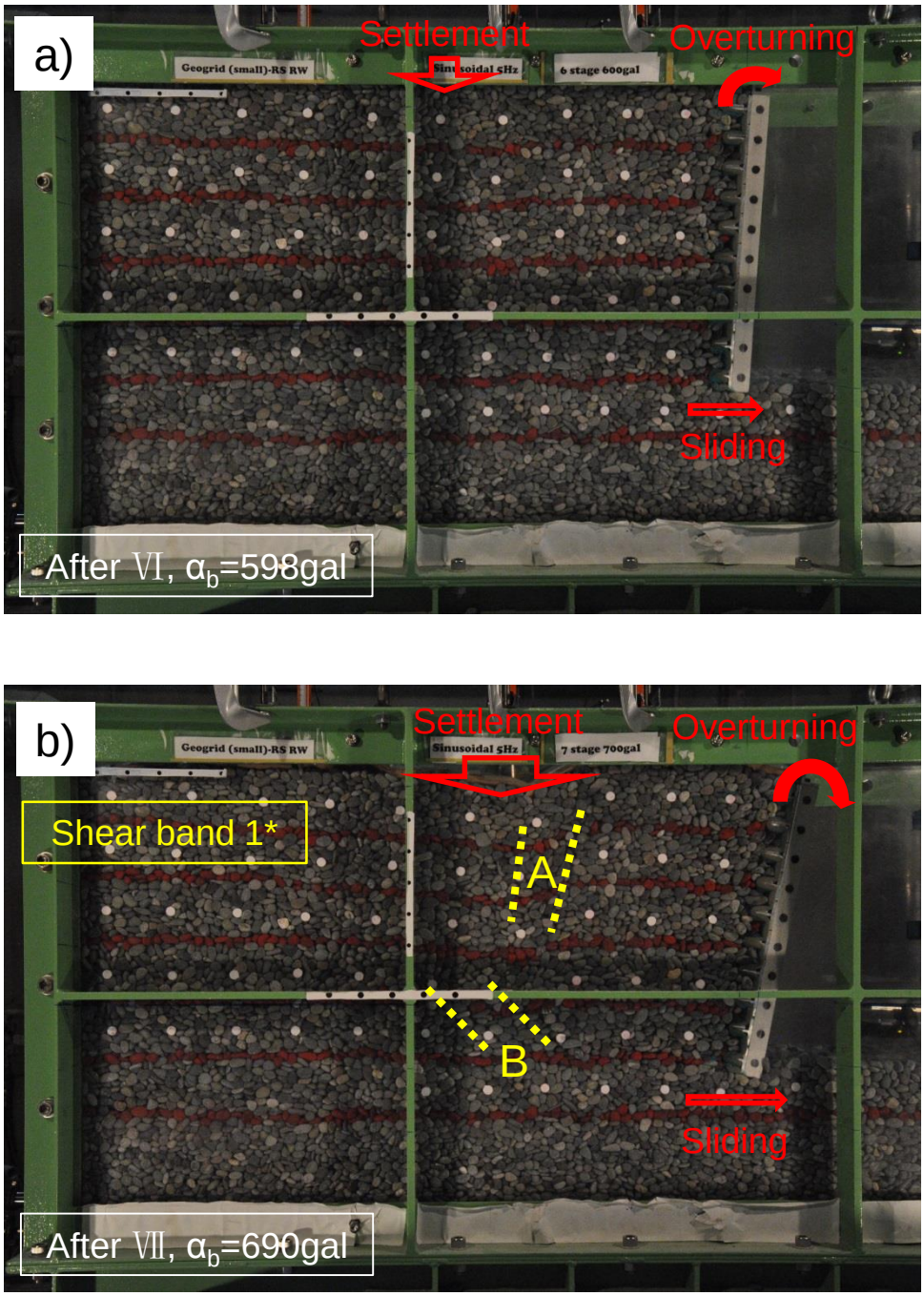

Fig. 5.11 Deformation modes of geogrid^{C}-RS RW-G: a) after shaking stage Ⅵ (α_b = 598 gal); b) after shaking stage Ⅶ (α_b = 690 gal).

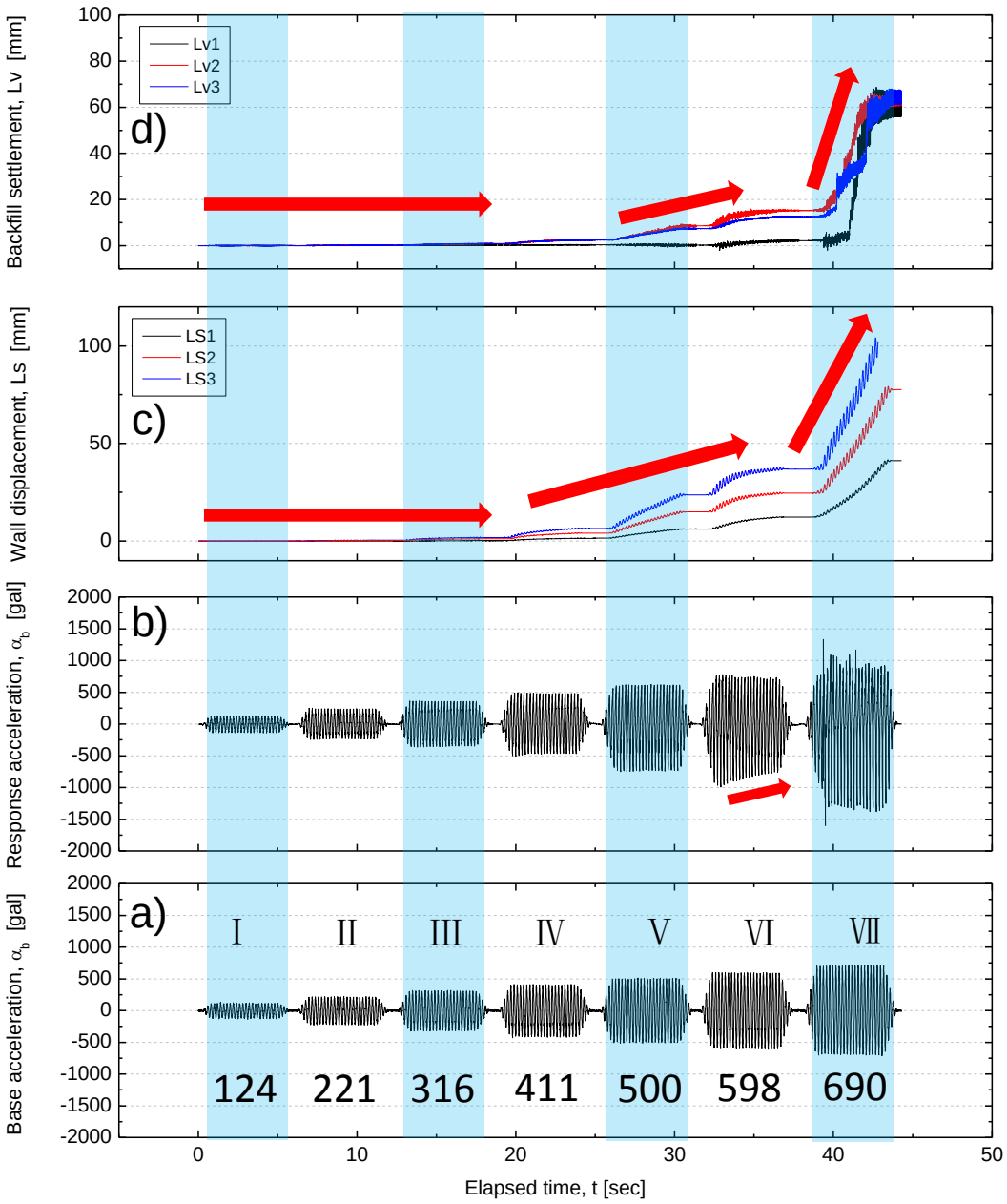

Fig. 5.12 Time history of: a) base acceleration; b) response acceleration at the top of the wall; c) facing wall displacements; d) backfill settlements for geogrid^{C}-RS RW-G

Case 7: Geocell-RS RW-G

Similar to the other cases studied, the time history of α_b, α_r, σ_h, L_s and L_v are plotted in Fig. 5.14 as well as the deformation modes during shaking in Fig. 5.13. Similar trends as in Case 5 and 6 were also found. Up to shaking stage α_b = 468 gal, there was no evident deformation of the wall or the backfill and the wall started to overturn only at shaking stage α_b = 570 gal. Following this, the deformation of the wall and settlement of the backfill became larger. As shown in Fig. 5.13b, at shaking stage α_b = 732 gal, potential shear band 1* located at Line A around 15 cm was formed, indicating that that the pullout resistances of the geogrid reinforcement in the upper part of the reinforced zone (i.e. Layer 8, Layer 9 and Layer 10 shown in Figs. 3.22b and 5.13b) firstly started to decrease. At shaking stage α_b = 843 gal (Fig. 5.13c), potential shear band 2* in the unreinforced zone was developed from the end of reinforcement Layer 2 (Figs. 3.22b and 5.13c), but it did not extend to the ground surface of the backfill. At this stage, larger overturning associated with a small component of sliding of the wall and larger settlement of the backfill immediately behind the reinforced zone were observed. Note, in this study, the measurement of earth pressure was not accurate enough, due to limited capacity of the employed load cell, which will be improved (i.e. by using two-component load cell used by Koseki et al. 1998) in future studies.

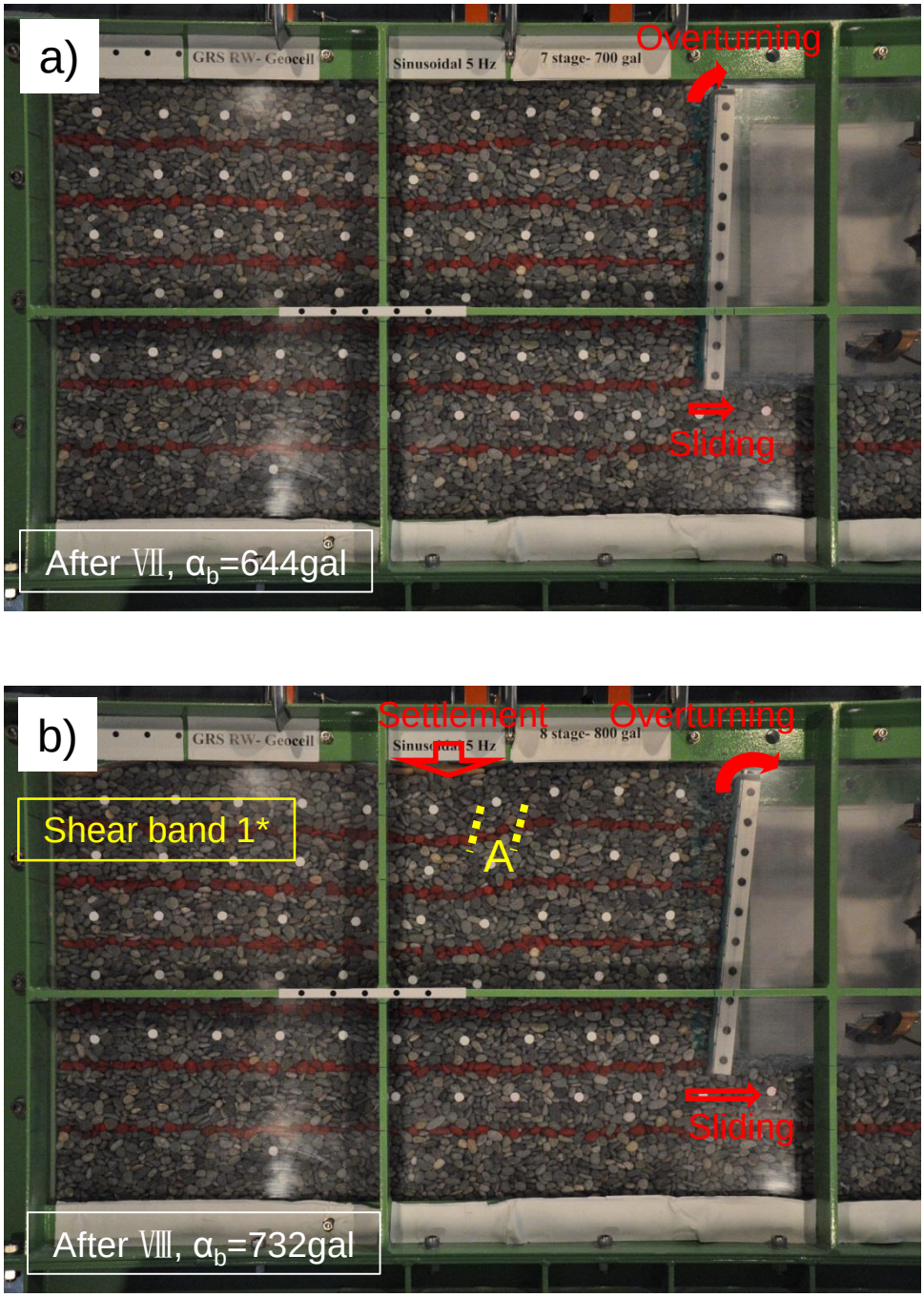

Fig. 5.2-13 Deformation modes of geocell-RS RW-G: a) after shaking stage Ⅶ (α_b = 644 gal); b) after shaking stage Ⅷ (α_b = 732 gal);

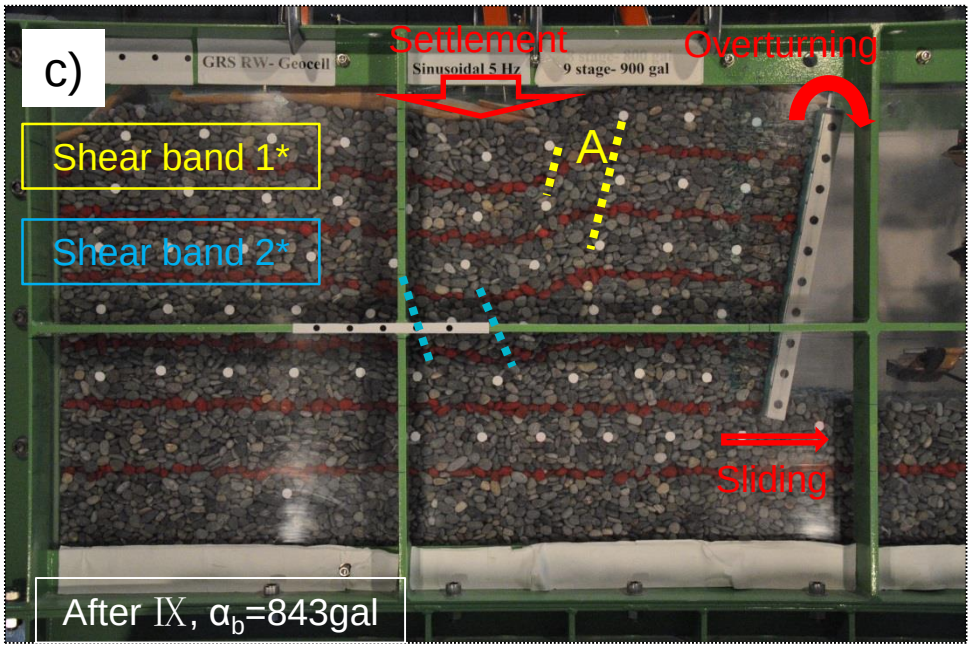

Fig. 5.2-13 (Continued) Deformation modes of geocell-RS RW-G: c) after shaking stage Ⅸ (α_b = 843 gal)

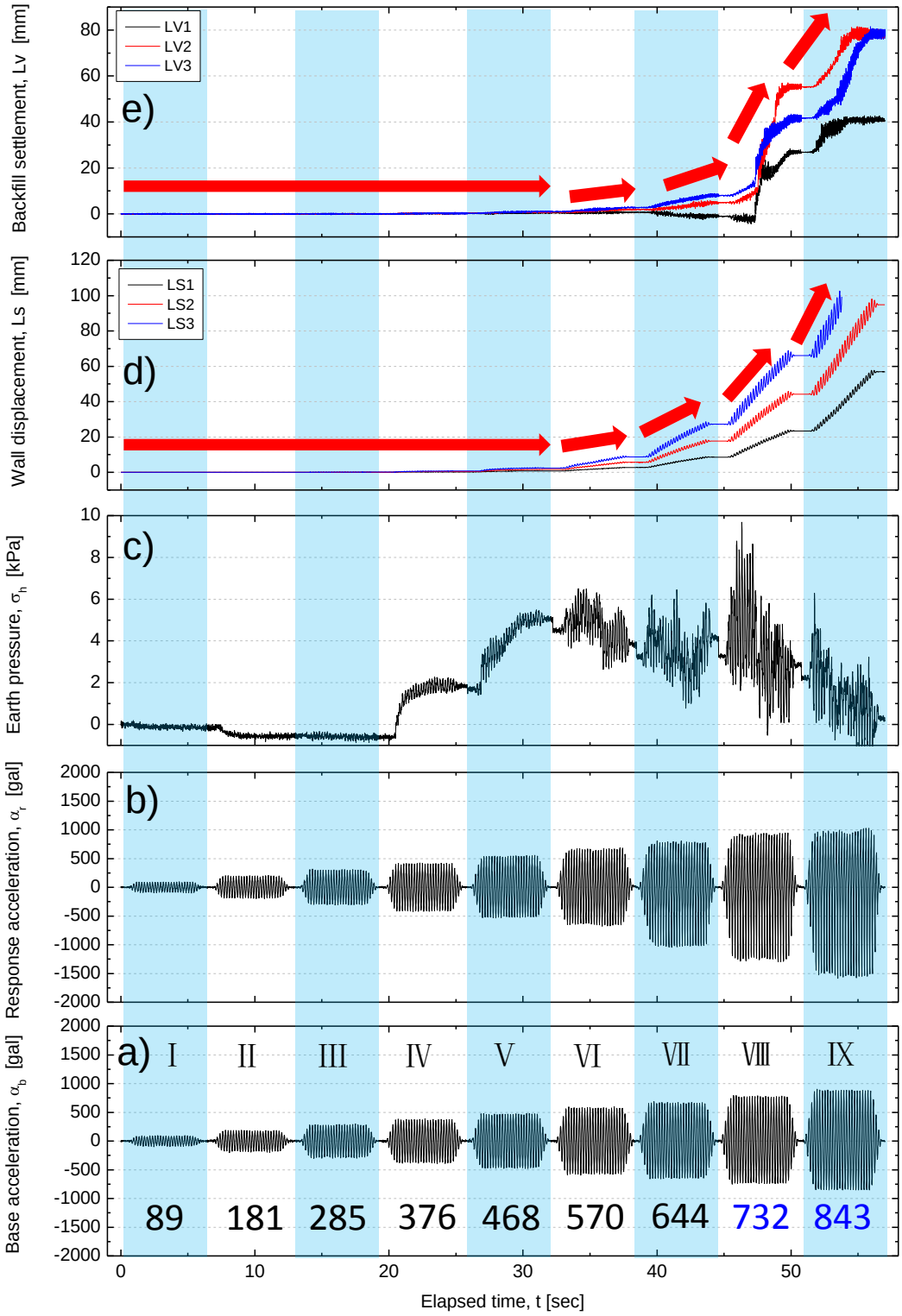

Fig. 5.14 Time history of: a) base acceleration; b) response acceleration at the top of the wall; c) averaged earth pressure; d) facing wall displacements; e) backfill settlements for geocell-RS RW-G

5.3 Analysis of test results

5.3.1 Residual deformation of wall and settlements of backfill

Representative residual displacements of walls in terms of overturning angle (θ), base sliding (d_s) and settlements at the crest of backfill (S_{10} and S_{36}), after each shaking step are plotted in Figs. 5.15, 5.17, 5.18 and 5.19 versus α_b. As shown in Fig. 3.22, L_{s1} (or d_s), is measured at the height of 10 cm or 5 cm from the bottom of the facing, L_{s2}, is measured at the height of 25 cm from the bottom of the facing and L_{s3}, is measured at the height of 45 cm from the bottom of the facing. The overturning angle is measured and calculated from the lateral displacements at the top and the bottom of the facing. The settlements S_{10} and S_{36} are measured at the crest of backfill at 10 cm and 36 cm from the back of facing, respectively.

Residual overturning angle:

As discussed in Section 5.2 (i.e. Figs.5.1b, 5.3d, 5.5d, 5.7b, 5.9c, 5.11b, 5.13c), for the cases of T-shaped RW backfilled with sand, geogrid (or geocell)-RS RWs backfilled with sand and gravel, the predominant deformation mode of the wall facing is overturning associated with small component of sliding. While for T-shaped RW backfilled with gravel (Fig.5.7b), the predominant deformation mode of the wall facing is sliding associated with small component of overturning. In the case of backfill of sand, as can be seen in Fig. 5.15a, up to a base acceleration value of around 320 gal no significant difference could be observed. However, under higher base accelerations (i.e. when the base acceleration is larger than 320 gal), the residual wall overturning accumulates rapidly for the T-shaped RW. In contrast, the geogrid^M-RS RW and the geocell-RS RW exhibit both a more ductile behavior. In particular, the geocell-RS RW shows smaller residual overturning angle for increasing base acceleration indicating a higher resistance against seismic loading. For example, during a base acceleration value of around 500 gal, the geogrid^M-RS RW has a overturning angle around 1.3 degrees, while the geocell-RS RW has only a overturning angle around 0.4 degrees.

Similar trend is also found when the T-shaped RW, geogrid-RS RW (i.e. geogrid^M-RS RW and geogrid^C-RS RW) and geocell-RS RW were embedded in gravel, as shown in Fig. 5.15b. There is no significant difference prior to the base acceleration of around 319 gal, but under higher base acceleration (i.e. when the base acceleration is larger than 319 gal), the residual wall overturning accumulated rapidly for the T-shaped RW. When the base acceleration is larger than 380 gal, geocell-RS RW shows smaller residual overturning angle for increasing

base acceleration than geogrid^{M}-RS RW and geogrid^{C}-RS RW. This indicates that geocell-RS RW shows more ductile behavior than geogrid^{M}-RS RW and geogrid^{C}-RS RW, and this trend becomes stronger in the backfill of gravel comparing to the backfill of sand (Fig. 5.15a). It is also noted that geogrid^{M}-RS RW shows more ductile behavior than geogrid^{C}-RS RW.

The overturning of the facing wall of GRS-RW is mainly controlled by the shear deformation of the reinforced backfill zone (Nakajima et al. 2010) which can be restricted by the pullout behaviors of different reinforcements. Fig. 5.16 shows the pullout behaviors of geocell model, geogrid^{M} and geogrid^{C} used in the shaking table tests. It is found that, as particle size increases, the geocell model provides a larger pullout resistance to a larger extent than geogrid, which restrict the deformation of reinforced backfill to a lager extent in the backfill of gravel, therefore a smaller overturning or more ductile behavior of geocell-RS RW backfilled with gravel comparing to geogrid^{M}-RS RW and geogrid^{C}-RS RW. In particular, geogrid^{M} shows larger peak pullout resistance than geogrid^{C} backfilled with gravel, which result in a more ductile behavior of geogrid^{M}-RS RW. This is due to the fact that the interlocking effect decreases when the aperture size of geogrid^{C} is smaller than the mean particle size of gravel (Fig. 5.16c).

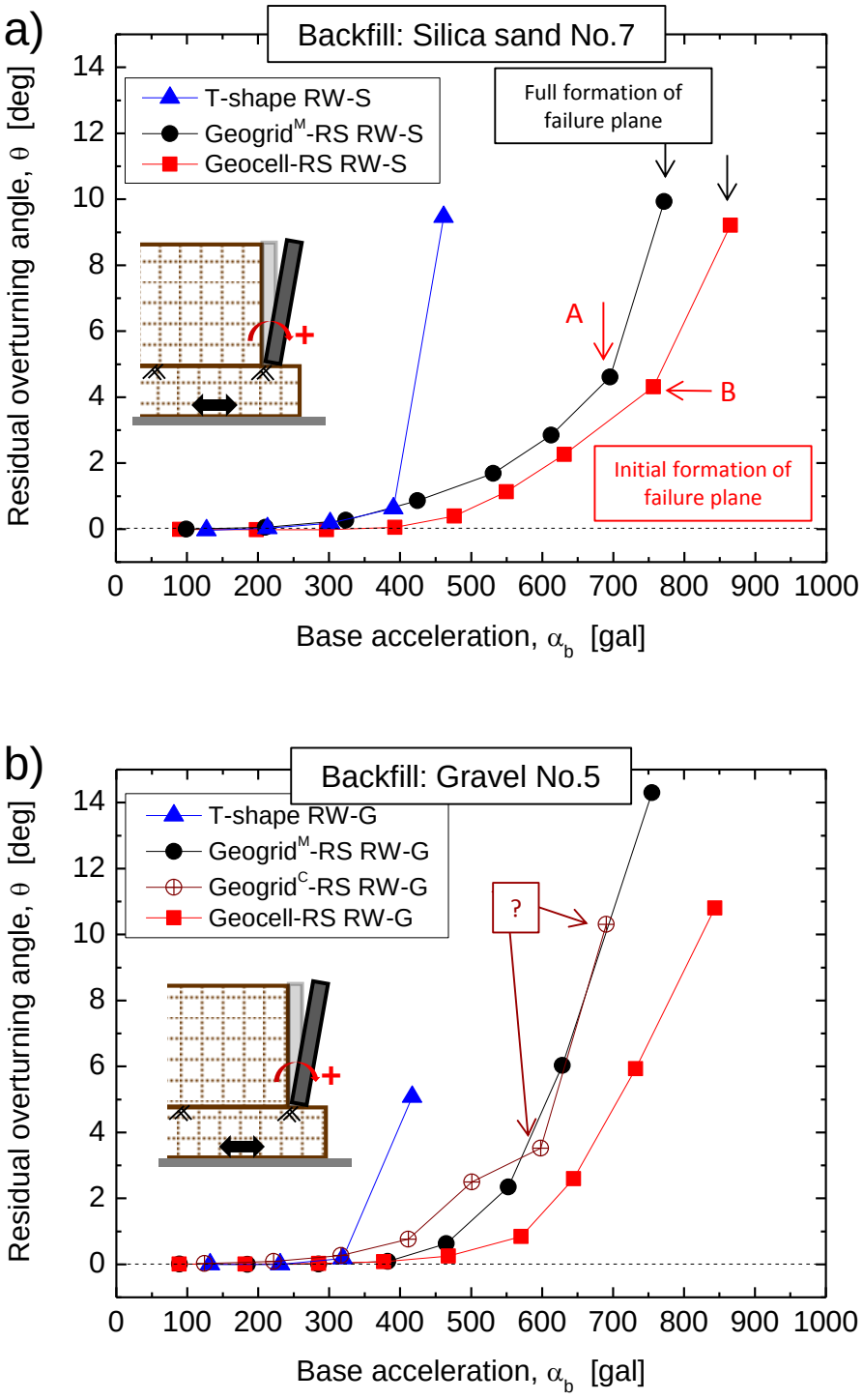

Fig. 5.15 Residual overturning angle of facing wall in the backfill of: a) sand; and b) gravel.

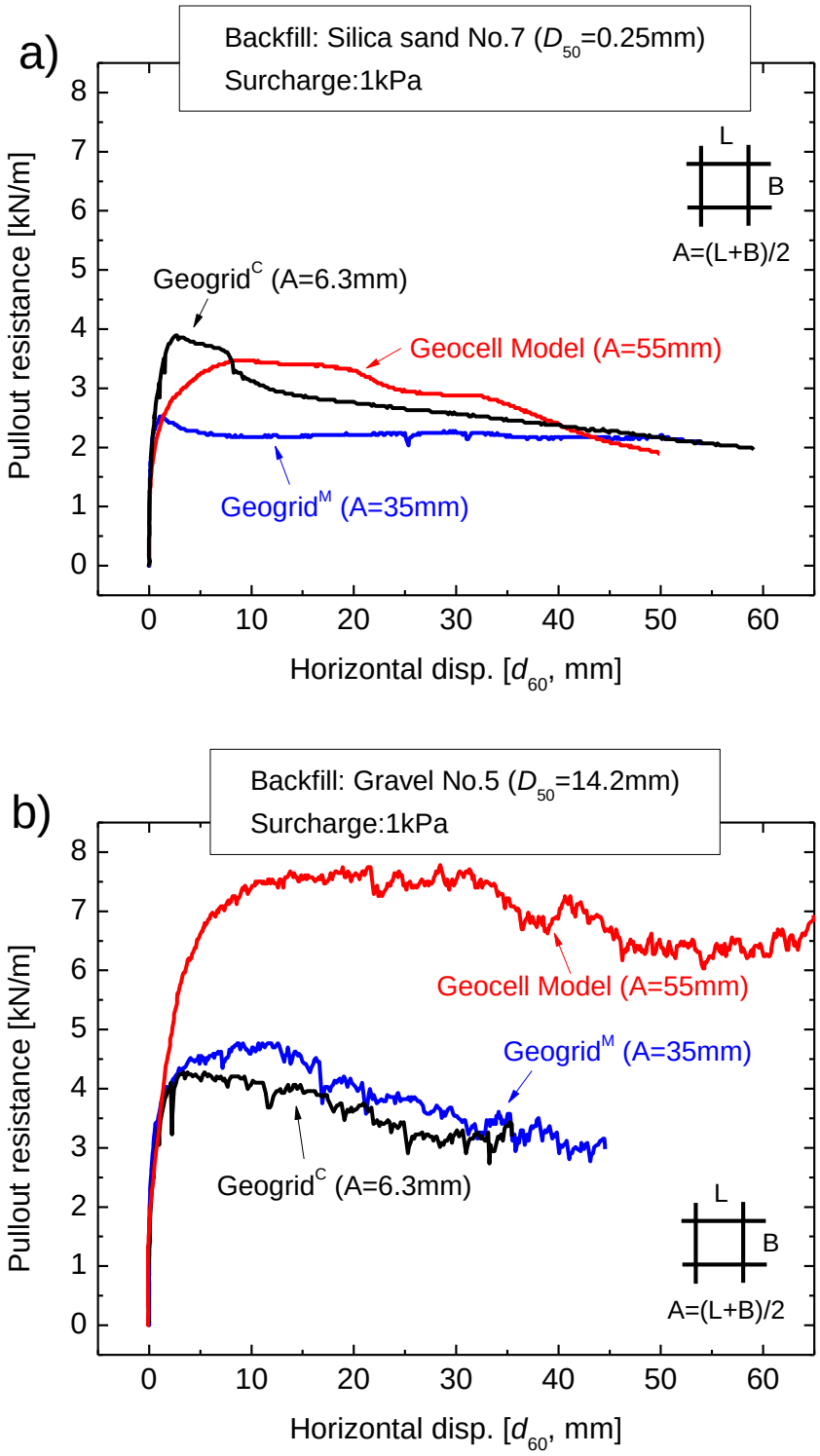

Fig. 5.16 Pullout behaviors of geocell model, geogrid^{M} and geogrid^{C} embedded in: a) Silica sand No.7 and b) Gravel No.5;

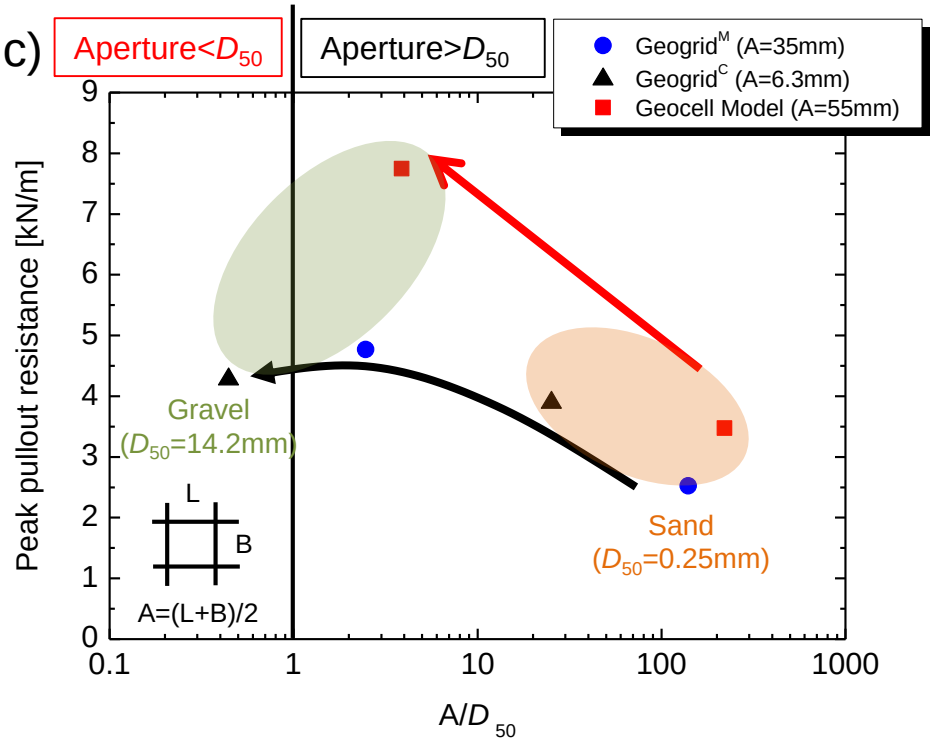

Fig. 5.16 (Continued) c) Peak pullout resistance of geocell model, geogrid^{M} and geogrid^{C} used in shaking table tests.

Residual sliding displacement:

Figure 5.17 presents the residual base sliding of facing wall against base acceleration. In the case of backfill of sand (Fig. 5.17a), the T-shaped RW, the geogrid^{M}-RS RW and the geocell-RS RW show very limited sliding displacements and no significant difference could be observed prior to the base acceleration of around 300 gal. Afterwards, the sliding displacement of the T-shaped RW is larger than that of both the geogrid^{M}-RS RW and the geocell-RS RW. The sliding displacement of wall facing mainly depends on the friction between the face of the bottom of the wall foundation and the subsoil properties. As shown in Figs. 3.12b, and 3.15, the foundation of the T-shaped RW is roughed by sand paper No.5 and has size of 395 mm × 200 mm. However, the foundation of geogrid-RS RW and geocell-RS RW can be regarded as the sum of width of facing wall and the reinforced backfill zone (i.e. 395 mm × 360 mm, Figs. 3.16 and 3.17), which have not only a higher friction angle between reinforced soil and subsoil but also a wider interaction area, thereby inducing a lower sliding displacement comparing to the T-shaped RW. The sliding displacements of the geogrid^{M}-RS RW and the geocell-RS RW are the same until a base acceleration value of around 700 gal, after which a larger sliding displacement of the geogrid^{M}-RS RW occurs. This is due to the fact that the sliding displacement of facing wall of a GRS RW is mainly induced by the shear deformation of the subsoil beneath the reinforced backfill (Nakajima et al. 2010). In this study, the subsoil conditions are the same for the two types of GRS RWs resulting in the same sliding displacement before initial failure planes are formed (points at A and B shown in Fig. 5.17a), after which the bottom layers of reinforcement (i.e. Layer 1 and 2 shown in Figs. 5.3d and 5.5d) may restrict the sliding of the wall to different extents by different reinforcements, which induce different sliding displacements. This phenomenon also demonstrates that the geocell reinforcement in the bottom of reinforced zone provide a larger pullout resistance than the geogrid^{M} reinforcement as shown in Fig.5.16a. Similar trend is also found when the geogrid^{M}-RS RW, the geogrid^{C}-RS RW and the geocell-RS RW were embedded in gravel as shown in Fig. 5.17b. There is no significant difference prior to the base acceleration of around 380 gal, while at higher base acceleration than 380 gal, the geocell-RS RW shows smallest residual sliding displacement for increasing base acceleration, and the geogrid^{C}-RS RW shows largest residual sliding displacement for increasing base acceleration. This is attributed to the fact that the largest pullout resistance is provided by geocell reinforcement to restrict the sliding displacement of the RW comparing to the geogrid^{M} and the geogrid^{C} as shown in Fig. 5.16b.

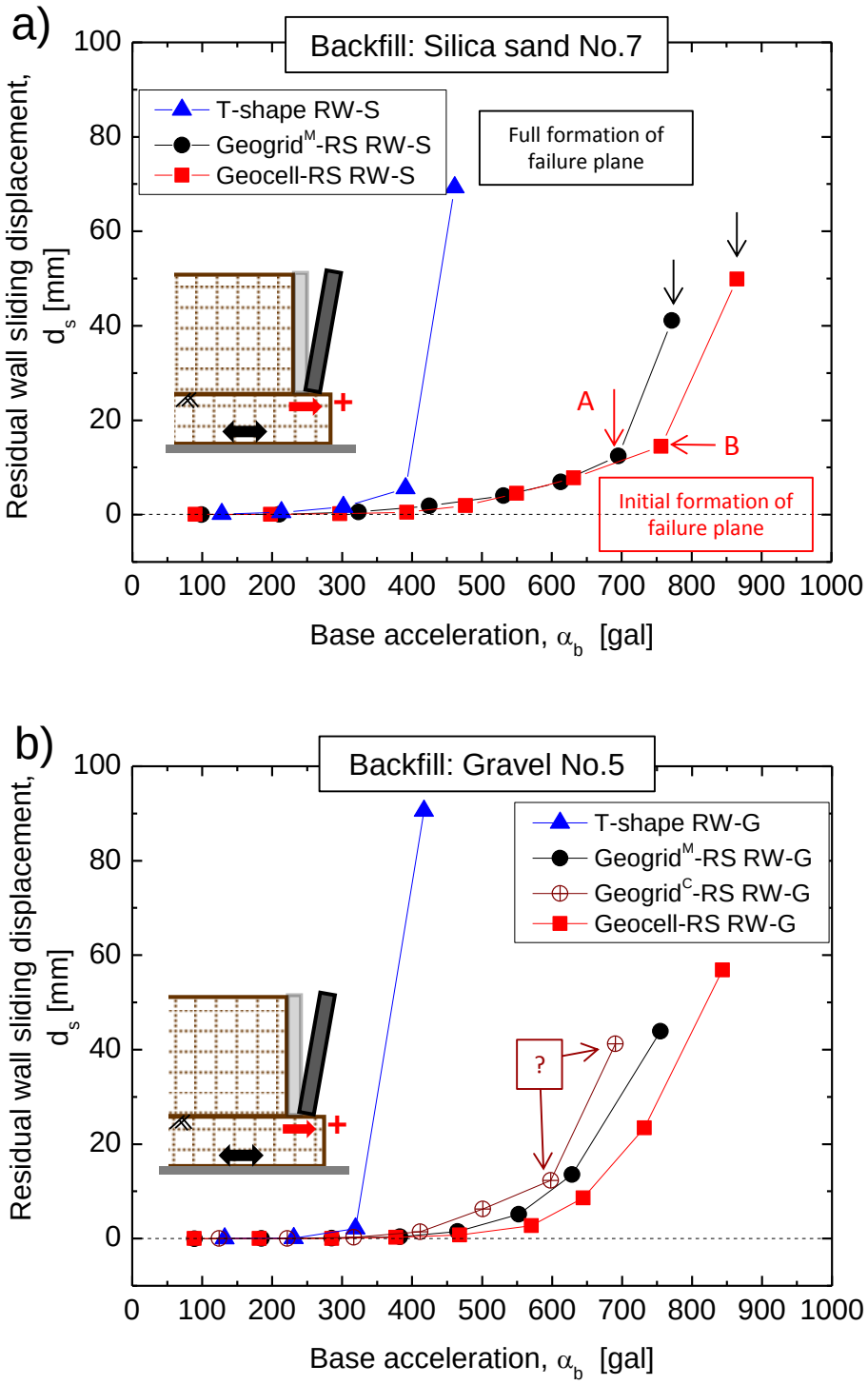

Fig. 5.17 Residual sliding displacement of facing wall in the backfill of: a) sand; and b) gravel

Settlements of the backfill:

In the case of backfill of sand (Fig. 5.18), up to shaking stage of around 320 gal, almost no accumulated settlements, S_{10} and S_{36}, of the geocell-RS RW and the geogrid^{M}-RS RW could be observed, but the settlement S_{10} of T-shape RW starts to accumulate. Afterwards, the accumulated settlements S_{10} and S_{36} of the geocell-RS RW are smaller than that of both the geogrid^{M}-RS RW and the T-shape RW. Note that, S_{10}, of the T-shape RW, is relative larger than S_{36}, during the initial shaking stage of 213 gal and 391 gal. This may be attributed to the dual ratchet mechanism (Tatsuoka et al. 2009) that settlement of the backfill is the summation of the accumulation of active sliding with cyclic loading and the accumulation of passive deformation of the passive zone. In the case of backfill of gravel (Fig. 5.19), the accumulation of settlements of the geocell-RS RW, S_{10} and S_{36}, are the same with that of the geogrid^{M}-RS RW and the geogrid^{C}-RS RW until the base acceleration of around 600 gal (for S_{10}) or 400 gal (for S_{36}), but the geocell-RS RW shows better performance for restricting settlements under higher base acceleration than both the geogrid^{M}-RS RW and the geogrid^{C}-RS RW. Note that, the measurements of settlement of the backfill (i.e. Lv-1, Lv-2 as shown in Figs. 3.22, 5.18 and 5.19) were missing under higher base acceleration. This is due to the facts that, larger lateral deformation of the facing wall occurred associated with the lateral deformation of the backfill under higher base acceleration (i.e. Figs. 5.1b, 5.3d, 5.5d, 5.7b, 5.9c, 5.11b, 5.13c), which leads to the missing of the target plate for the measurement of the LVDT.

In summary, the geocell-RS RW shows better performance for restricting settlements on higher base acceleration.

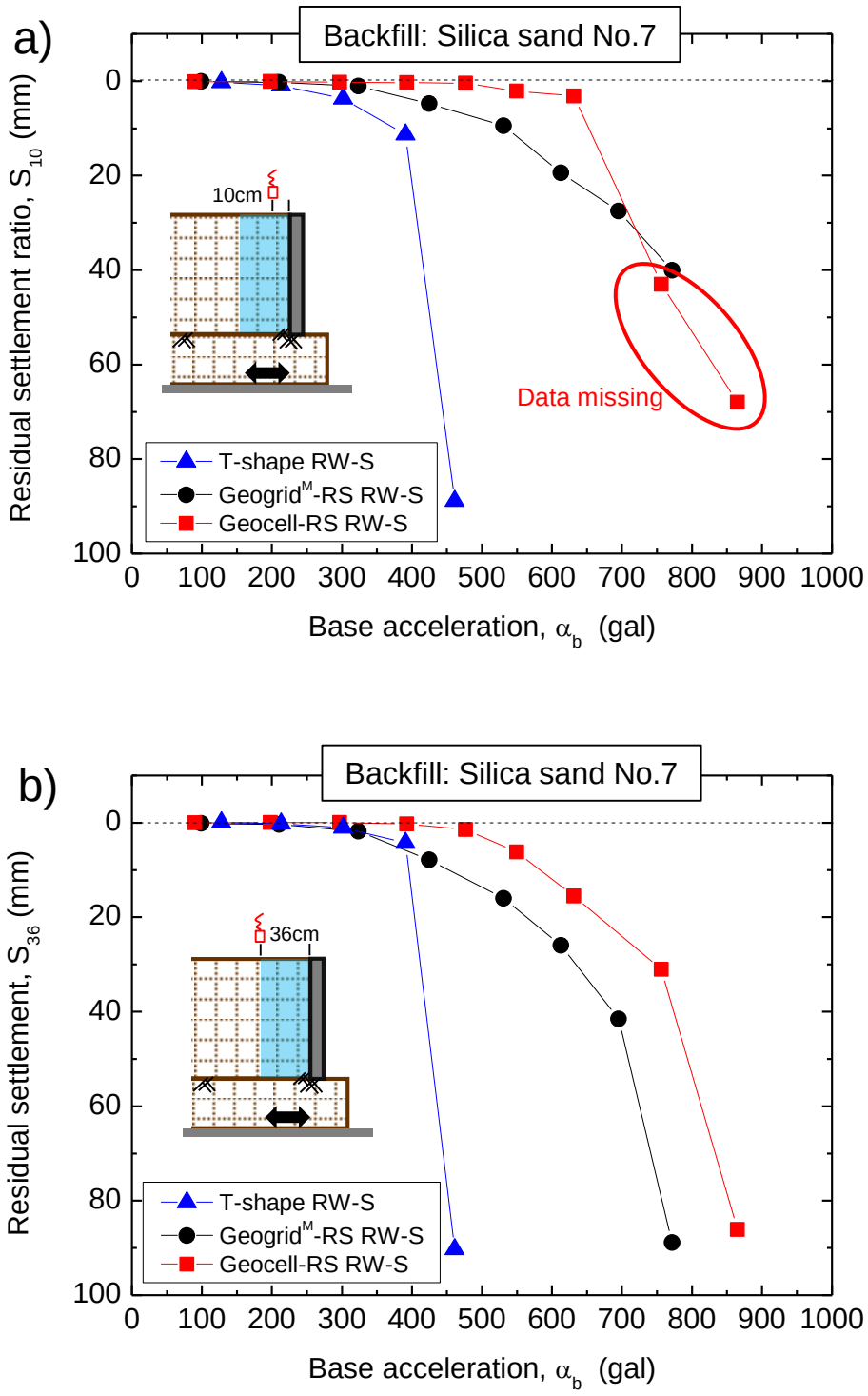

Fig. 5.18 Settlements of the sand backfill at the positions of : a) 10 cm and b) 36 cm away from the back facing of the wall

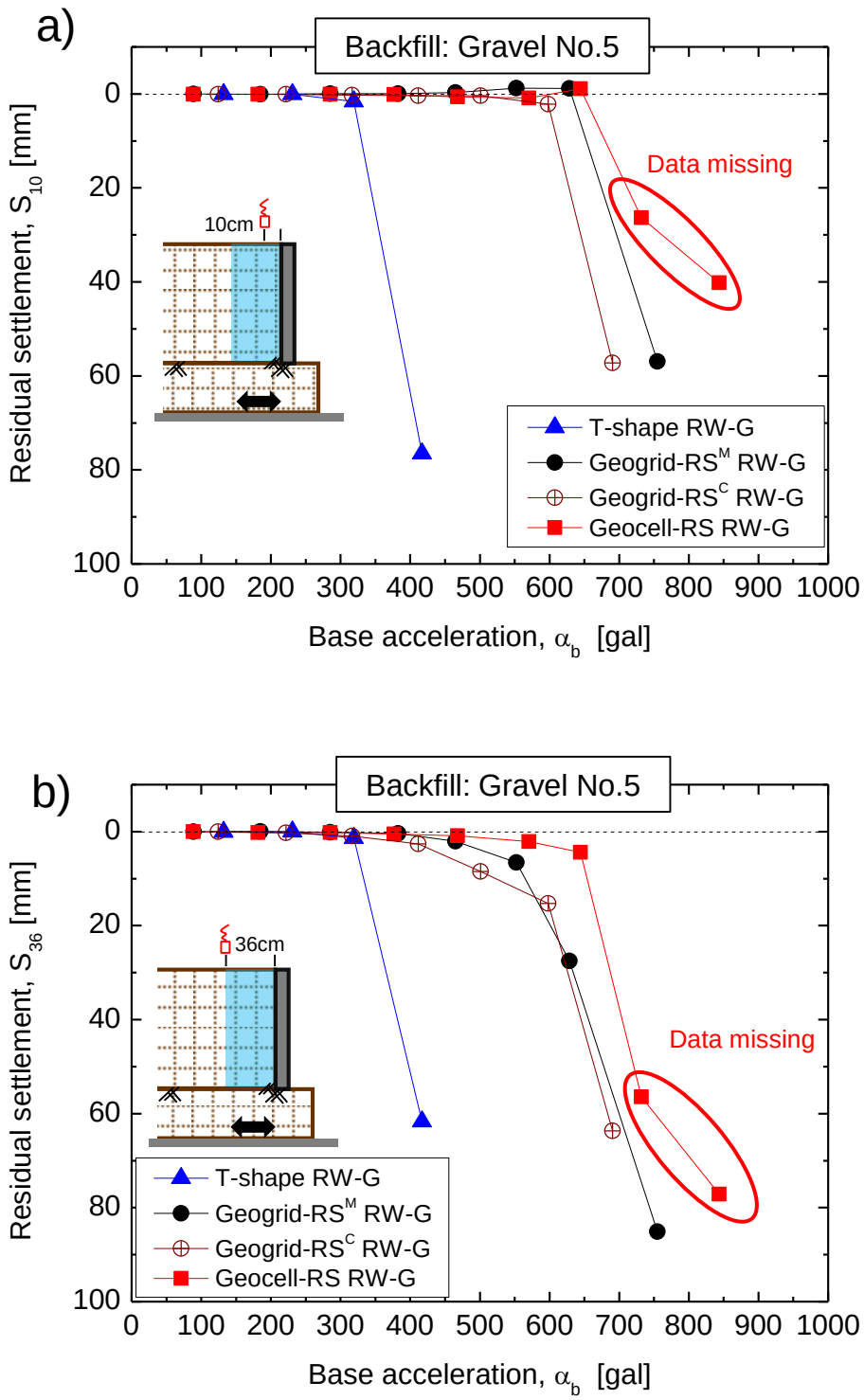

Fig. 5.19 Settlements of the gravel backfill at the positions of : a) 10 cm and b) 36 cm away from the back facing of the wall

5.3.2 Threshold acceleration discussion

Threshold acceleration is important measure of stability. If achieved, the dynamic factor of safety will be less than one and thus permanent displacement will be induced. As shown in Figs. 5.15 and 5.17, for the T-shape RW, the residual facing wall displacement-acceleration curves were clearly bi-linear. That is, taking the T-shape RW-S as example, deformation was small until 391 gal, after which deformation was suddenly increased. Thus the value of 391 gal could be considered the model specific threshold acceleration value. However, the determination of threshold accelerations for the geogrid-RS RW and the geocell-RS RW is not an easy task, since they showed a gradual increase in the facing wall displacements with the increase of base acceleration.

Previous researchers have defined the threshold acceleration observed in model studies with different measurements. Nova-Roessig and Sitar (2006) defined threshold acceleration as the minimum acceleration that caused the slope to deform permanently. El-Emam and Bathurst (2007) compared rotation and sliding failure modes as a means of observing threshold acceleration. The acceleration coefficient that caused a sudden increase in sliding, compared to the rotation, indicated the threshold acceleration value.

In this study, in order to evaluate the seismic stability of different types of GRS RW models, the threshold acceleration is defined as the amplitude of the base acceleration in the active state (i.e. when the inertial force is in the outward direction) when the residual lateral displacement of the facing wall at the position of the top of the wall reaches 5% of the total wall height or $\gamma = 5\%$ (Fig. 5.20), which is recorded and calculated at an elevation of 450 mm for the height of the 500 mm high walls in this experiment, showing the overturning level of retaining wall facing (Koseki et al. 1998, Nakajima et al. 2010).

Fig. 5.21 summarizes the threshold accelerations for each GRS RW models with the backfill of sand and gravel. A high threshold acceleration implies a higher acceleration which is necessary to induce failure, and reduced deformation at low acceleration, which can be an index to evaluate the stability of retaining wall. It is found that at threshold state (i.e. $\gamma = 5\%$), the threshold acceleration of geocell-RS RW is higher than that of the geogrid^{M}-RS RW and the geogrid^{C}-RS RW in both backfills of sand and gravel, indicating that the geocell-RS RW exhibits a higher seismic stability than the geogrid^{M}-RS RW and the geogrid^{C}-RS RW. It is also noted that as the backfill changes from sand to gravel, the threshold acceleration of

geocell-RS RW almost keeps steady, while the threshold acceleration of geogrid^{M}-RS RW decreases slightly.

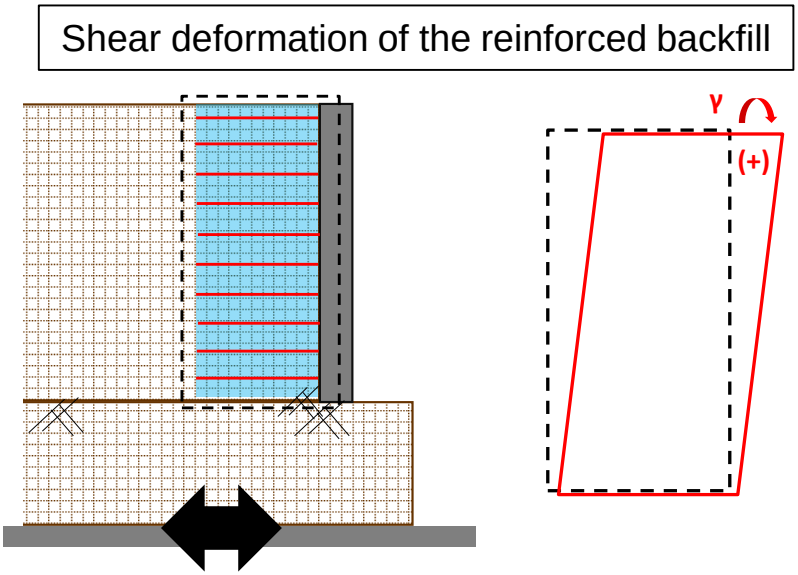

Fig. 5.20 Schematic diagram of the shear deformation of the reinforced backfill

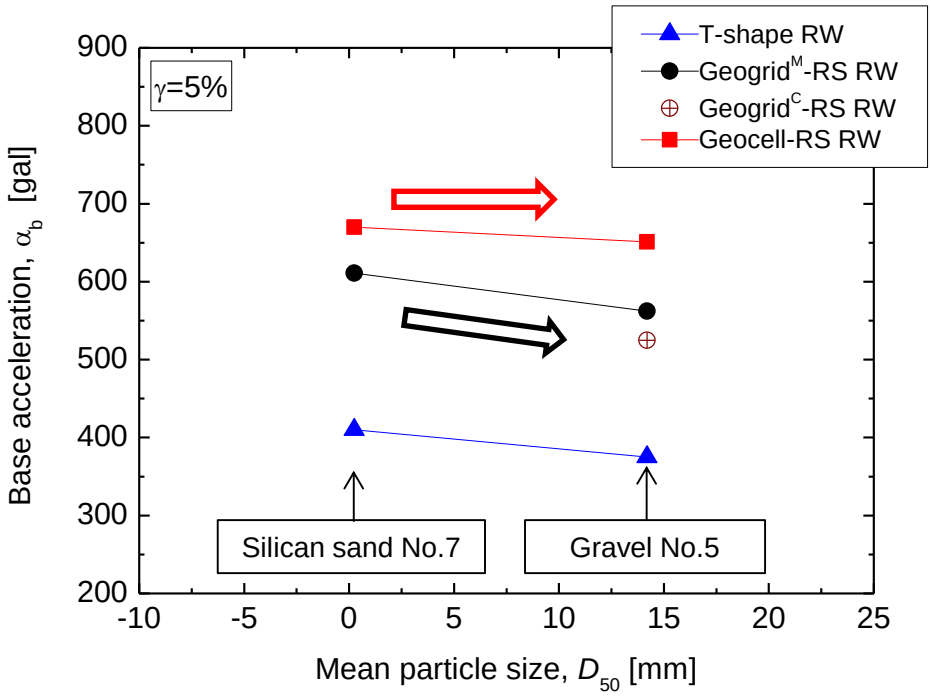

Fig. 5.21 Observed threshold accelerations for all types of retaining wall models with backfill of sand and gravel

5.3.3 Acceleration response of the wall and backfill soil

Typical acceleration responses of the retaining wall system are measured as shown in Fig. 3.22. The acceleration response of the wall (α_r) at the top of the wall, the acceleration responses of the reinforced backfill zone ($\alpha_{r(A2)}$, $\alpha_{r(A3)}$, $\alpha_{r(A5)}$) at different height, the acceleration response of the unreinforced backfill zone ($\alpha_{r(A4)}$) and the acceleration response of subsoil ($\alpha_{r(A1)}$) are recorded and compared with the input base acceleration (α_b). Note that, α_b is taken as the averaged base accelerations (i.e. A7 in Fig. 3.22) for 20 cycles at active state (i.e. when the inertial force is in the outward direction) for each shaking stage. Other acceleration responses are taken as the corresponding accelerations at the 10th cycle for each shaking stage.

Amplification of acceleration is defined as the ratio between α_r/α_b, which is a design concern because it can generate larger accelerations leading to larger destabilizing dynamic earth pressure and wall inertia. Fig. 5.22 shows that the α_r at top of the wall against α_b relationships exhibit a general trend of increasing amplification with increasing base acceleration. In the case of backfill of sand, up to the base acceleration of around 320 gal, the amplification responses for three types of retaining walls (i.e. T-shape RW, geogrid^M-RS RW and geocell-RS RW) are relative small and similar. From base acceleration of 320 gal to 550 gal, the amplification response of T-shape RW increases by 2.17 times until failure at base acceleration of 461 gal, while the amplification responses of geogrid^M-RS RW and geocell-RS RW increase largely by 1.98 times and 2.11 times at the base acceleration of 531 gal and 550 gal, respectively. But the amplification response of geocell-RS RW is only slightly lower than geogrid^M-RS RW and T-shape RW. Afterwards, the amplification responses of geogrid^M-RS RW and geocell-RS RW continues to increase slightly until the maximum value by 2.19 times at base acceleration of 695 gal and 2.13 times at base acceleration of 631 gal, and then a slightly decrease until the failure stage of 772 gal and 865 gal, respectively.

In the case of backfill of gravel, up to the base acceleration of around 319 gal, the amplification responses for all four types of retaining walls (i.e. T-shape RW, geogrid^M-RS RW, geogrid^C-RS RW and geocell-RS RW) are relative small and similar. Afterwards, the amplification response of T-shape RW increases by 1.68 times until failure takes place at a base acceleration of 416 gal. Prior to 468 gal, geogrid^M-RS RW and geocell-RS RW show a similar trend of slightly increasing of amplification response by about 1.11 times. Subsequently, both the geogrid^M-RS RW and the geocell-RS RW exhibit increasing

amplification responses by the maximum value of 1.94 times at the failure state of 755 gal and 1.85 times at the failure state of 844 gal, respectively. Nonetheless, the geocell-RS RW shows a smaller amplification response than that of the geogrid^{M}-RS RW during each shaking stage. In addition, although unexpected results of geogrid^{C}-RS RW are observed at shaking stage of α_b = 598 gal (as explained in Section 5.2), a stronger increasing trend of amplification response for the geogrid^{C}-RS RW comparing to the geogrid^{M}-RS RW and the geocell-RS RW is found.

Smaller amplification response within higher input base acceleration indicates that the geocell-RS RW has a higher seismic stability than the geogrid-RS RW under higher base acceleration especially backfilled with gravels with larger particles. This is because the geocell has an important benefit to confine larger soil particles in their three dimensional cells and respective cells provide large anchorage capacity inducing a higher pullout resistance, while the pullout resistance of geogrid may not increase as particle size increases to a certain level due to the decrease of interlocking effect, as previously discussed in Chapter 4. In this study, as shown in Fig. 5.16, the pullout resistances of the geocell model, the geogrid^{M} and the geogrid^{C} increase with an increase of particle size from silica sand to gravel. Alternatively, geocell model shows a larger pullout resistance to a relative larger extent than geogrid^{M} and geogrid^{C} as particle size increases, therefore decreasing the amplification response of RW.

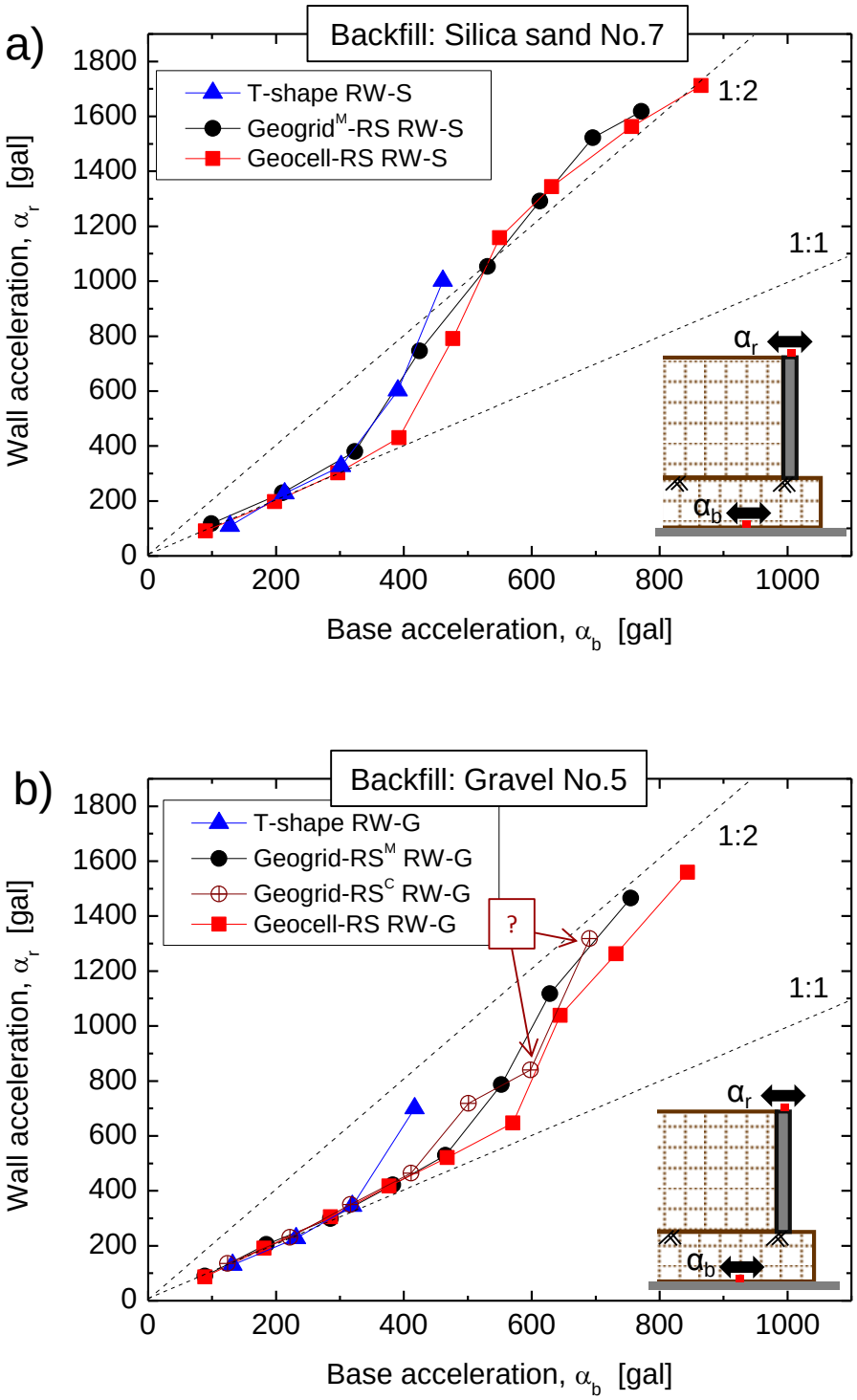

Fig. 5.22 Relationship between response acceleration at the top of wall and base acceleration in the backfill of: a) sand; and b) gravel

Figures 5.23 and 5.24 show the response accelerations in the backfill soil during shaking. It is found that the response acceleration of the subsoil ($\alpha_{r(A1)}$) almost coincides with the input base acceleration (α_b) for all cases. Response accelerations measured in several location along the vertical direction within the reinforced soil zone ($\alpha_{r(A2)}$, $\alpha_{r(A3)}$ and $\alpha_{r(A5}$) show an increase with increasing wall elevation and with base acceleration amplitude when the base acceleration amplitude reaches a certain level. The difference confirms the general believe that the entire wall system does not act as a whole block.

In the case of backfill of sand (Fig. 5.23), the response accelerations of reinforced backfill zone in terms of $\alpha_{r(A3)}$, $\alpha_{r(A5)}$, start to increase at the base acceleration of 324 gal for the geogrid^M-RS RW and 393 gal for the geocell-RS RW and then the response amplification of the reinforced backfill zone is almost the same for both the geogrid^M-RS RW and the geocell-RS RW. In the case of backfill of gravel (Fig. 5.24), the response accelerations of reinforced backfill zone in terms of $\alpha_{r(A3)}$, $\alpha_{r(A5)}$, start to increase largely at the base acceleration of 500 gal for the geogrid^C-RS RW, 552 gal for the geogrid^M-RS RW, and 644 gal for the geocell-RS RW, respectively. Afterwards the response amplification of the reinforced backfill zone for the geocell-RS RW is relative smaller than that of the geogrid^M-RS RW. And also, both the geocell-RS RW and the geogrid^M-RS RW backfilled with gravel show smaller response amplification than those both backfilled with sand.

From the analysis above, it is clear that, the geocell-RS RW shows better seismic stability (i.e. smaller response amplification) under higher base acceleration than both the geogrid^M-RS RW and the geogrid^C-RS RW when they are backfilled with gravel. This can be attributed to the advantage of geocell which can confine larger soil particles and provide larger pullout resistance, as discussed in Chapter 4.

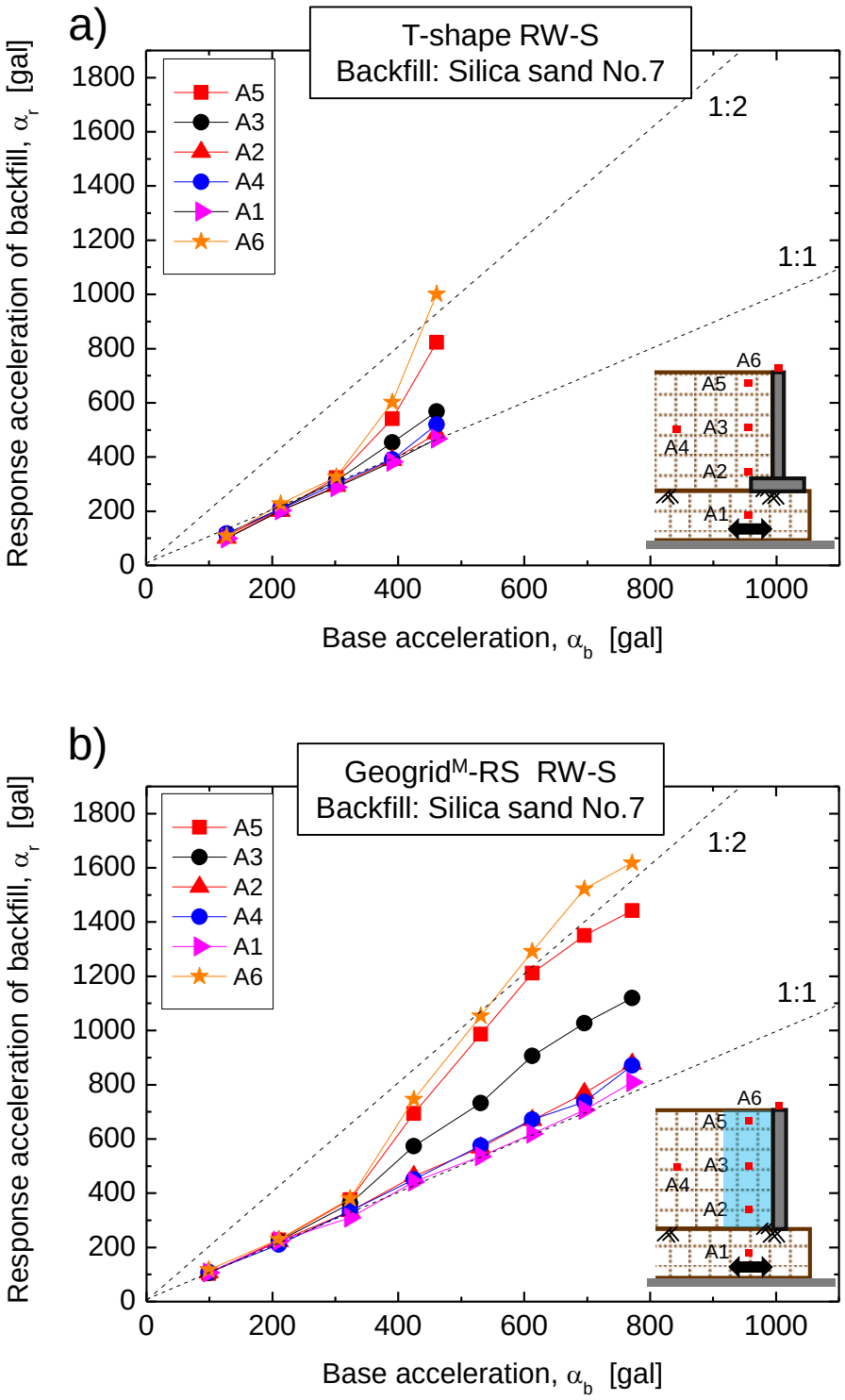

Fig. 5.23 Response acceleration of the sand backfill for: a) T-shape RW; b) geogrid^M-RS RW

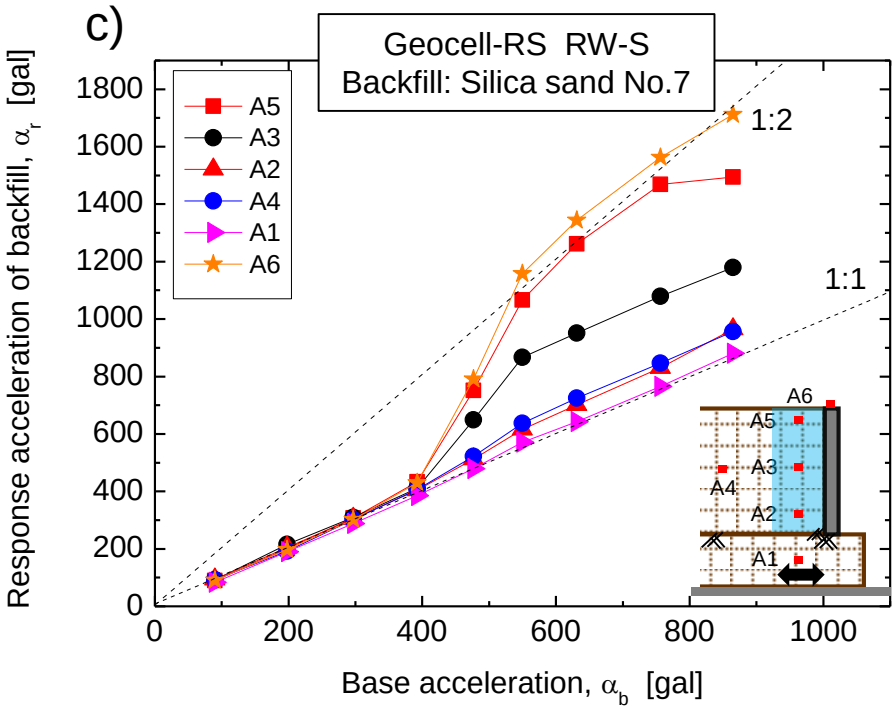

Fig. 5.23 (Continued) Response acceleration of the sand backfill for: c) geocell-RS RW

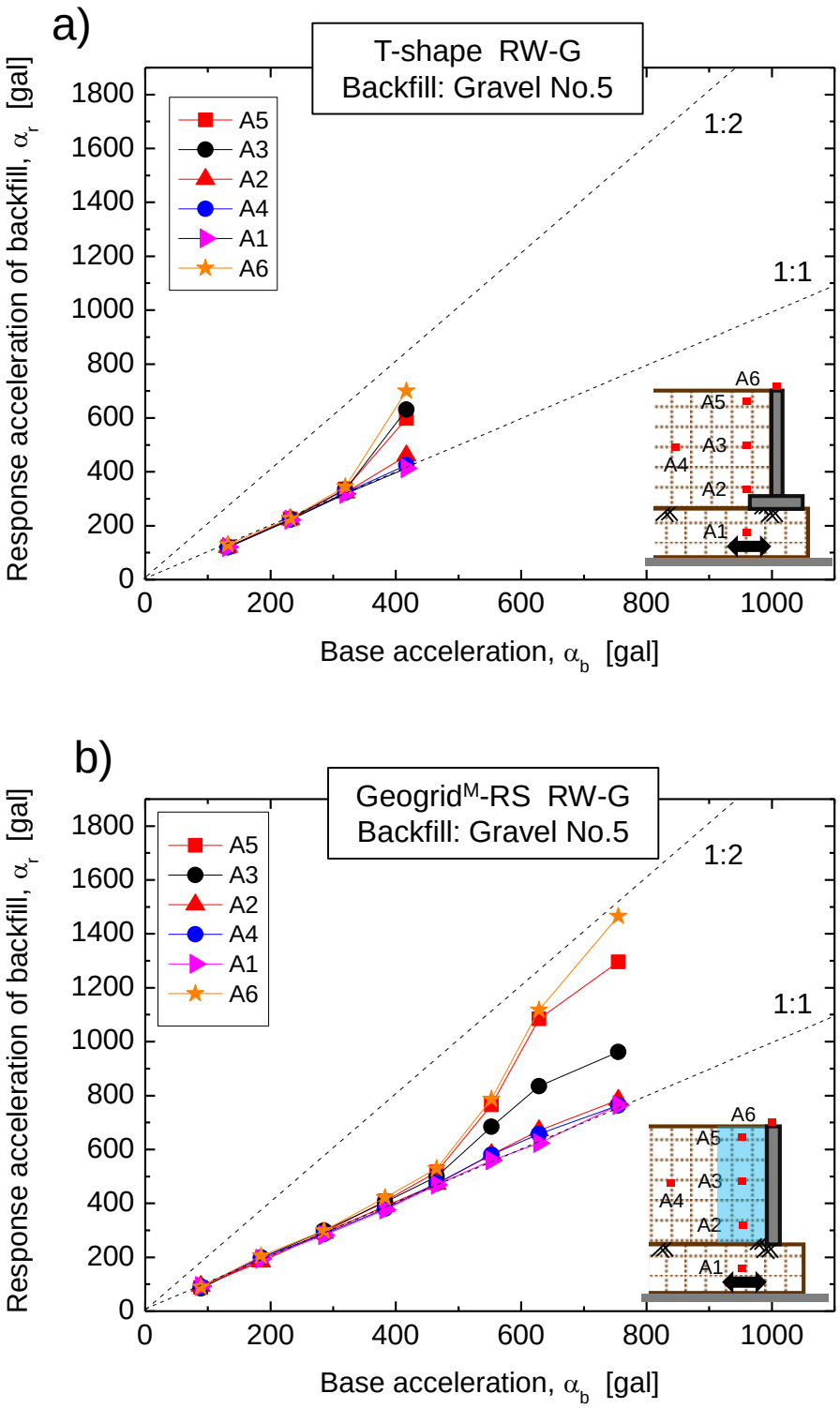

Fig. 5.24 Response acceleration of the gravel backfill for: a) T-shape RW; b) geogrid^M-RS RW

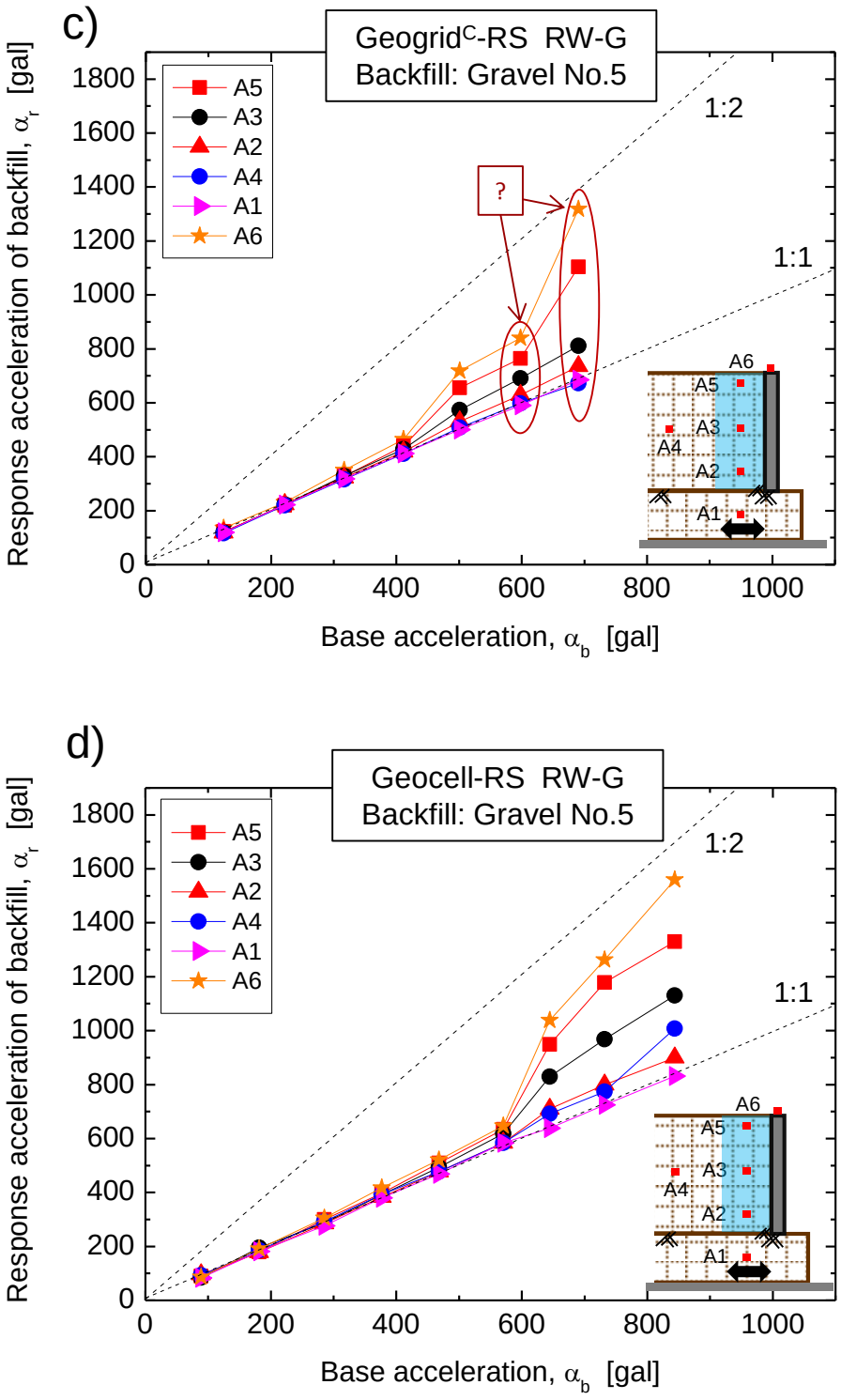

Fig. 5.24 (Continued) Response acceleration of the gravel backfill for: c) geogrid^{C}-RS RW; d) geocell-RS RW

5.4 Simplified analysis of the dynamic response characteristics of GRS RWs

As discussed in the Section 5.3, the response amplification would increase significantly after certain value of base acceleration. A possible explanation is that the larger model wall deformations (i.e. Figs.5.1b, 5.3d, 5.5d, 5.7b, 5.9c, 5.11b, 5.13c), that occur at this limit base acceleration stage may have led to a reduction in the stiffness of the RW system. Theoretically, the amplification response can be analyzed from a SDOF system subjected to base excitation (as shown in Equation 5.1). In addition, the phase difference between response acceleration and base acceleration was observed to increase significantly after a certain value of base acceleration, as shown in Appendix A. The phase difference reflects an oscillatory motion of the wall about the toe, similar to a SDOF oscillator. Therefore, in this section, the evaluation of seismic stability of different types of retaining wall backfilled with different soil materials was conducted in the framework of SDOF theory.

5.4.1 A brief introduction to the damped SDOF theory

The seven types of retaining walls (T-shape RW backfilled with sand, geogrid^{M}-RS RW backfilled with sand, geocell-RS RW backfilled with sand, T-shape RW backfilled with gravel, geogrid^{M}-RS RW backfilled with gravel, geogrid^{C}-RS RW backfilled with gravel and geocell-RS RW backfilled with gravel) were modeled as a damped SDOF system following the method developed by Shinoda et al. (2003) and extended by Muñoz et al. (2012). A detailed introduction of this method has been given by Muñoz (2010) and Kuroda (2012).

Figure 5.25 shows the damped SDOF system subjected to base shaking. From this figure, a brief introduction is given as follows. Equation 5.1 expresses the motion for a damped SDOF system subjected to base acceleration ($\ddot{u}_b$) measured at the shaking table in this study. The total response acceleration at the mass ($\ddot{u}_t$) measured at the top of the wall, is given as the sum of $\ddot{u}_b$ and the acceleration of the mass relative to the base ($\ddot{u}$) as shown by Equation 5.2.

$$m\ddot{u}_t(t) + c\dot{u}_t(t) + ku(t) = 0 \quad (5.1)$$

$$\ddot{u}_t = \ddot{u}_b + \ddot{u} \quad (5.2)$$

where, m, k and c are the mass, the stiffness and the coefficient of viscosity of the system, respectively, and t is the time. In this study, $\ddot{u}_b$ is the input harmonic sinusoidal (Fig. 3.27), described by Equation 5.3.

$$\ddot{u}_b = -\alpha_b \sin(\omega_i t) \quad (5.3)$$

where, α_b is the amplitude of $\ddot{u}_b$. $\ddot{u}_t$ is comprised of the transient response, which is controlled by the initial conditions and decays with time, and the steady-state response (Equation 5.4), which becomes $\ddot{u}_t$ (Equation 5.1) after the transient response dies out.

$$\ddot{u}_t = -\alpha_t \sin(\omega_i t + \varphi) = -\alpha_b M \sin(\omega_i t + \varphi) \quad (5.4)$$

where, α_t is the amplitude of $\ddot{u}_t$, $M = \alpha_t / \alpha_b$ is the magnification ratio of acceleration and φ is the phase difference.

In this study, the transient response is recognized only at the first cycle and ignored in the analysis shown below. For the steady-state response, the values of M and φ can be obtained by:

$$M = \sqrt{\frac{1+4\xi^2\beta^2}{(1-\beta^2)^2+4\xi^2\beta^2}} \quad (5.5)$$

$$\varphi = \arctan\left(\frac{-2\xi\beta^3}{1-(1-4\xi^2)\beta^2}\right) \quad (5.6)$$

where, ξ is the damping ratio of the system and β is the ratio between input frequency of the base acceleration (f_i= 5 Hz) and natural frequency of the RW models (f_0).

The values of M and φ at each cycle are obtained from a single exact sinusoidal wave acceleration recorded at the shaking table (A7) and the top of the wall (A6, Fig. 3.22). From these values for M and φ, the values for β and ξ in each cycle are back-calculated by iteration (i.e. by Newton's method) based on Equations 5.5 and 5.6. These values for β and ξ represent the transient stiffness and the energy dissipation capacity of the respective wall models, which are the two crucial parameters for analysis of the seismic stability of the RWs.

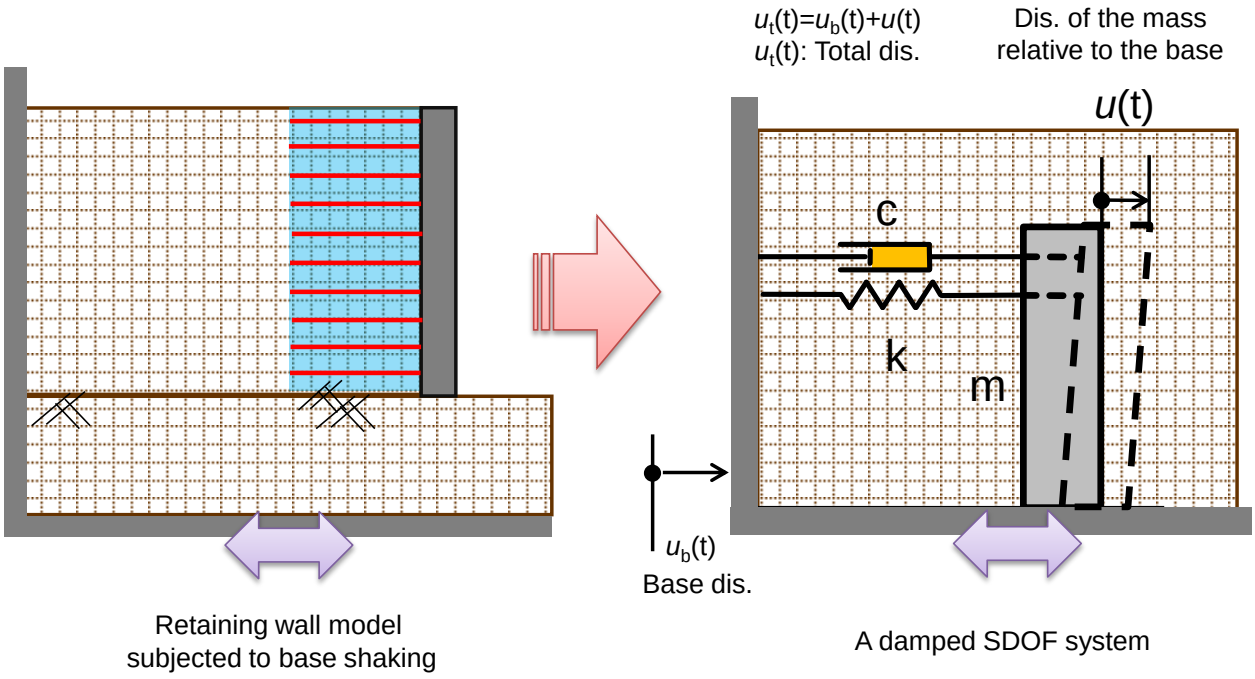

Fig. 5.25 Analysis of retaining wall model as a damped SDOF system.

5.4.2 Data processing

In order to obtain the values of M and φ from a single sinusoidal wave for the SDOF analysis, data processing regarding correction of the base acceleration recorded at the shaking table (A7), namely $\ddot{u}_b$, and the response acceleration at the top of the wall (A6), namely $\ddot{u}_t$, are presented in this section, as well as filtering of these data.

Correction

As discussed in Sections 5.2 and 5.3, the predominant deformation mode of the wall facing is overturning, associated with small sliding except for Case 4 (T-shaped RW backfilled with gravel), which results in the accelerometer at the top of the facing wall (A6) composed of predominantly rotation and small sliding. Therefore, rotation of the accelerometer would induce the errors of measurement due to gravity rotation. Complete raw data recorded at the shaking table (A7) and at the top of the wall (A6) for Case 2 (i.e. Geogrid^{M}-RS RW backfilled with sand) are plotted as a function of time in Fig. 5.26. A negative acceleration value means that the acceleration is directed backwards to the backfill soil (i.e. at active state, when the inertia force is oriented towards the active direction) and a positive acceleration value means that the acceleration is directed forwards to the front wall facing (i.e. at passive state, when the inertia force is oriented towards the passive direction). From Fig. 5.26a, input base acceleration (A7-Time) is symmetric throughout the whole shaking stages and the residual acceleration after each shaking stage can be zero.

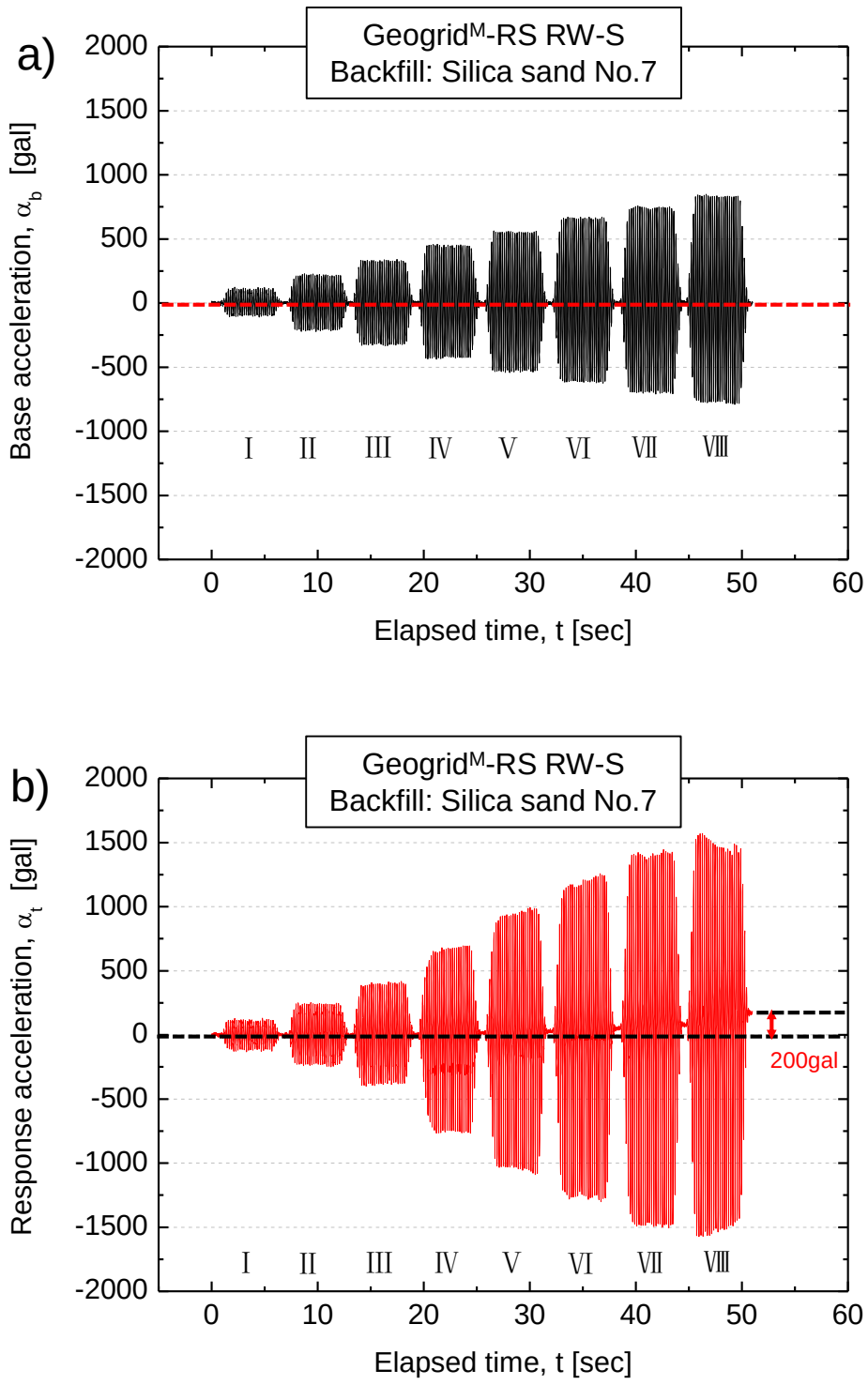

Fig. 5.26 Raw data of: a) the input base acceleration at shaking table; and b) the response acceleration at the top of the wall.

Note that as shown in Fig. 5.26b, from shaking stage Ⅴ (α_b = 531 gal) to Ⅷ (α_b = 772 gal), the residual response acceleration becomes higher than the baseline gradually until around 200 gal after shaking stage Ⅷ (α_b = 772 gal). This is due to the rotation of gravity of the accelerometer induced by overturning of the facing wall, which is necessary for correction (Jackson, P.F., 2010). In this thesis, a similar correction method as described in Jackson (2010) is described hereafter. Firstly, the initial rotation of accelerometer can be corrected stage by stage as shown in Fig. 5.27 and Equation 5.7.

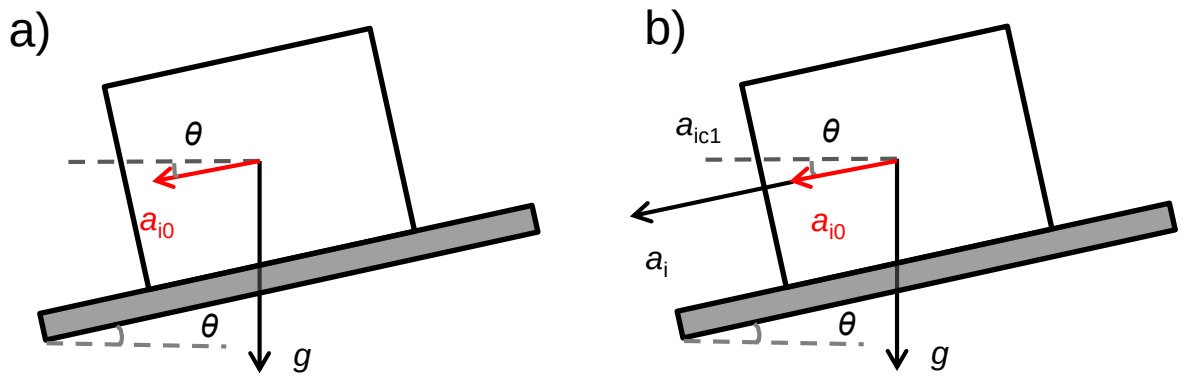

Fig. 5.27 Schematic diagram of correction method

$$a_{ic1} = (a_i - a_{i0}) \times \cos\theta \qquad 5.7$$

where, i is the shaking stage, a_{i0} is the initial acceleration value recorded by accelerometer at the beginning of one shaking stage i, a_i is the acceleration values recorded by accelerometer during the shaking stage i, θ is the rotation angle of the accelerometer with respect to the horizontal plane, which can be obtained directly from Fig. 5.15.

When the rotation angle of the accelerometer is small enough, the influence of rotation of the accelerometer can be ignored where $a_{ic1} = a_i$. In the case of geogrid^M-RS RW backfilled with sand up to shaking stage Ⅳ (α_b = 425 gal), the value of θ is only 0.861°, the value of a_{i0} is around zero, thus $a_{ic1} = a_i$. When the rotation angle of the accelerometer becomes larger, correction is needed using Equation 5.7. In the case of geogrid^M-RS RW backfilled with sand, from shaking stage Ⅴ (α_b = 531 gal) to Ⅷ (α_b = 772 gal), the correction is made based on Equation 5.7.

Furthermore, during one shaking stage, the accelerometer undergoes further rotation, which can be corrected by a linearly increment equation (Equation 5.8).

$$a_{ic2} = a_{ic1} - \Delta a_{ic1} \qquad 5.8$$

where, Δa_{ic1} varies linearly with respect to the time and can be determined by the initial acceleration value and residual acceleration value during one shaking stage.

The result of data correction of response acceleration at the top of the wall for Case 2 (i.e. Geogrid^{M}-RS RW backfilled with sand) is shown in Fig. 5.28. Comparison of Fig. 5.26b and Fig. 5.28 indicates that the residual acceleration of response acceleration at the top of the wall has been recovered to zero after the data correction.

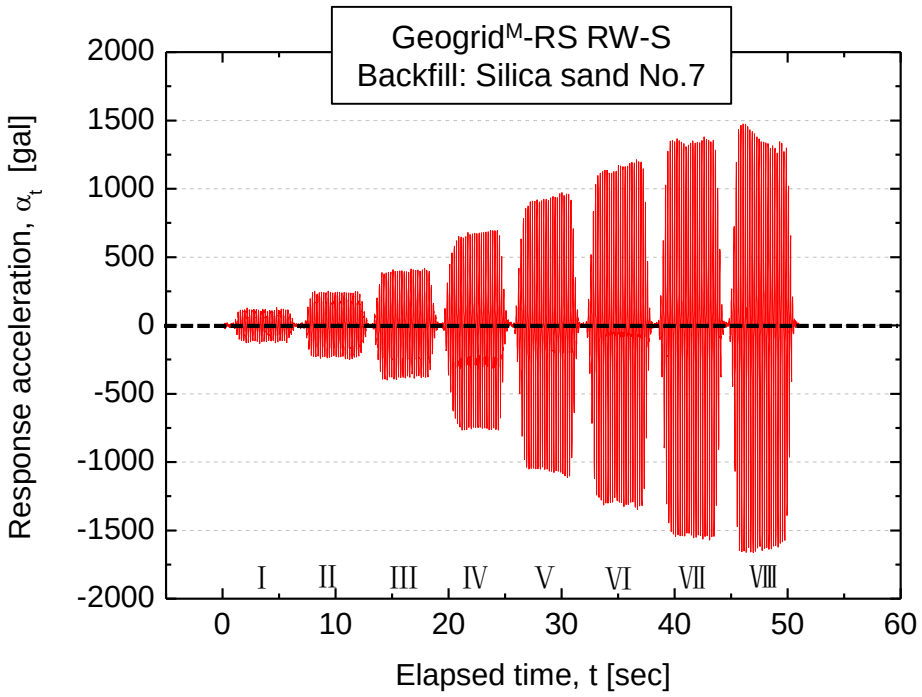

Fig. 5.28 Corrected data of the response acceleration at the top of the wall.

Filter

Filtering (or smoothing) of the output data is necessary to remove undesirable noise recorded by the accelerometers. Fig. 5.29 shows the corrected but un-filtered data of input base acceleration (A7) and response acceleration at the top of the wall (A6) as a function of time for Case 2 (geogrid^{M}-RS RW backfilled with sand). Fig. 5.30 exhibits Fast Fourier Transform (FFT) of the input base acceleration and response acceleration at the top of the wall, showing that a peak acceleration amplitude with respect to the predominant frequency appears, along with several smaller secondary peaks at higher frequencies. For example, the predominant frequency of input base acceleration is 5 Hz, associated with very slightly noise at frequency of 10 Hz, 20 Hz, 25 Hz, 35 Hz, and 45 Hz, while the response acceleration at the top of the wall consists of predominantly of 5 Hz frequency components, and relative larger noise at frequency of 10 Hz, 15 Hz, 20 Hz, 30 Hz, 40 Hz and 45 Hz.

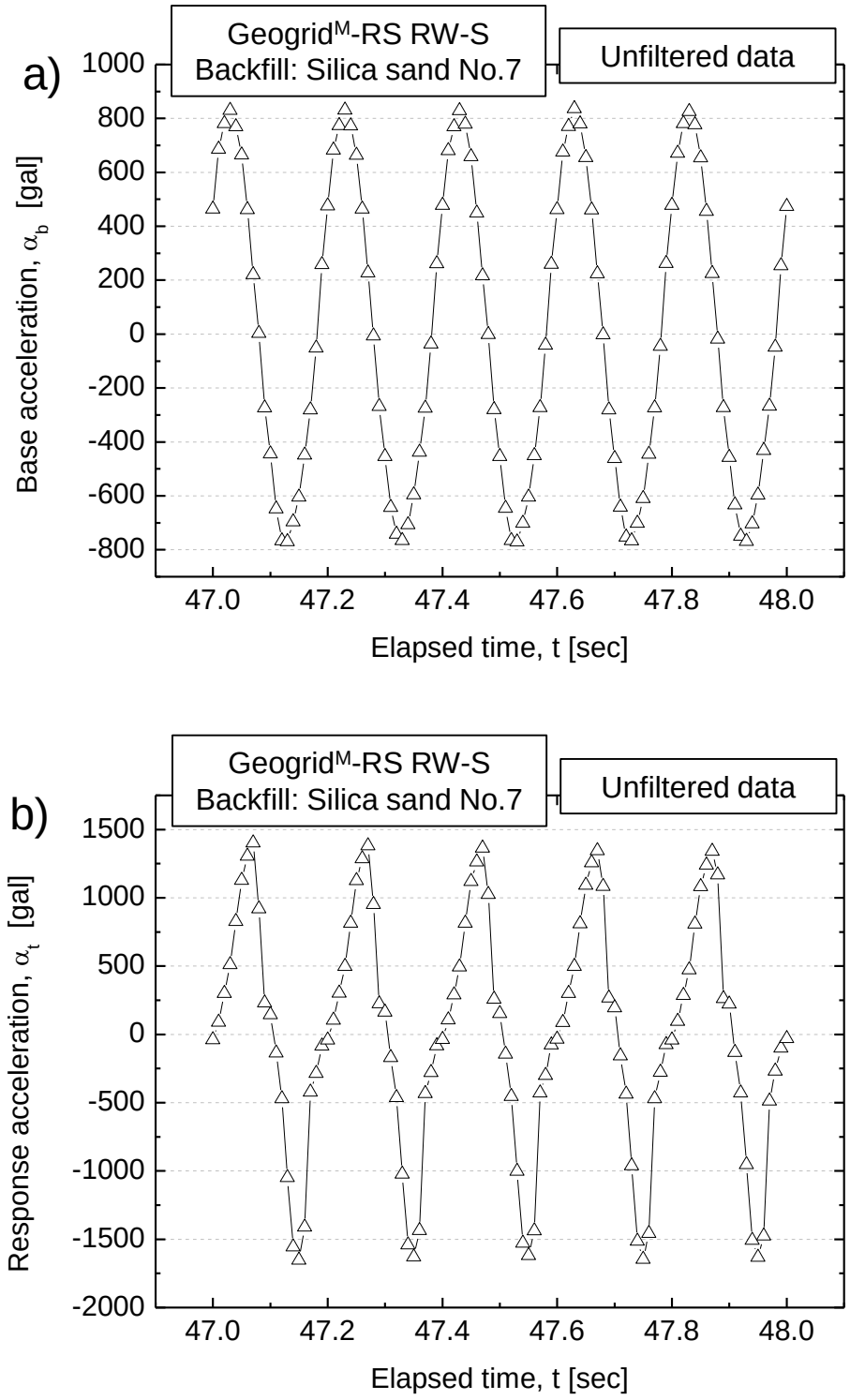

Fig. 5.29 Typical unfiltered data of: a) input base acceleration; and b) response acceleration at the top of the wall.

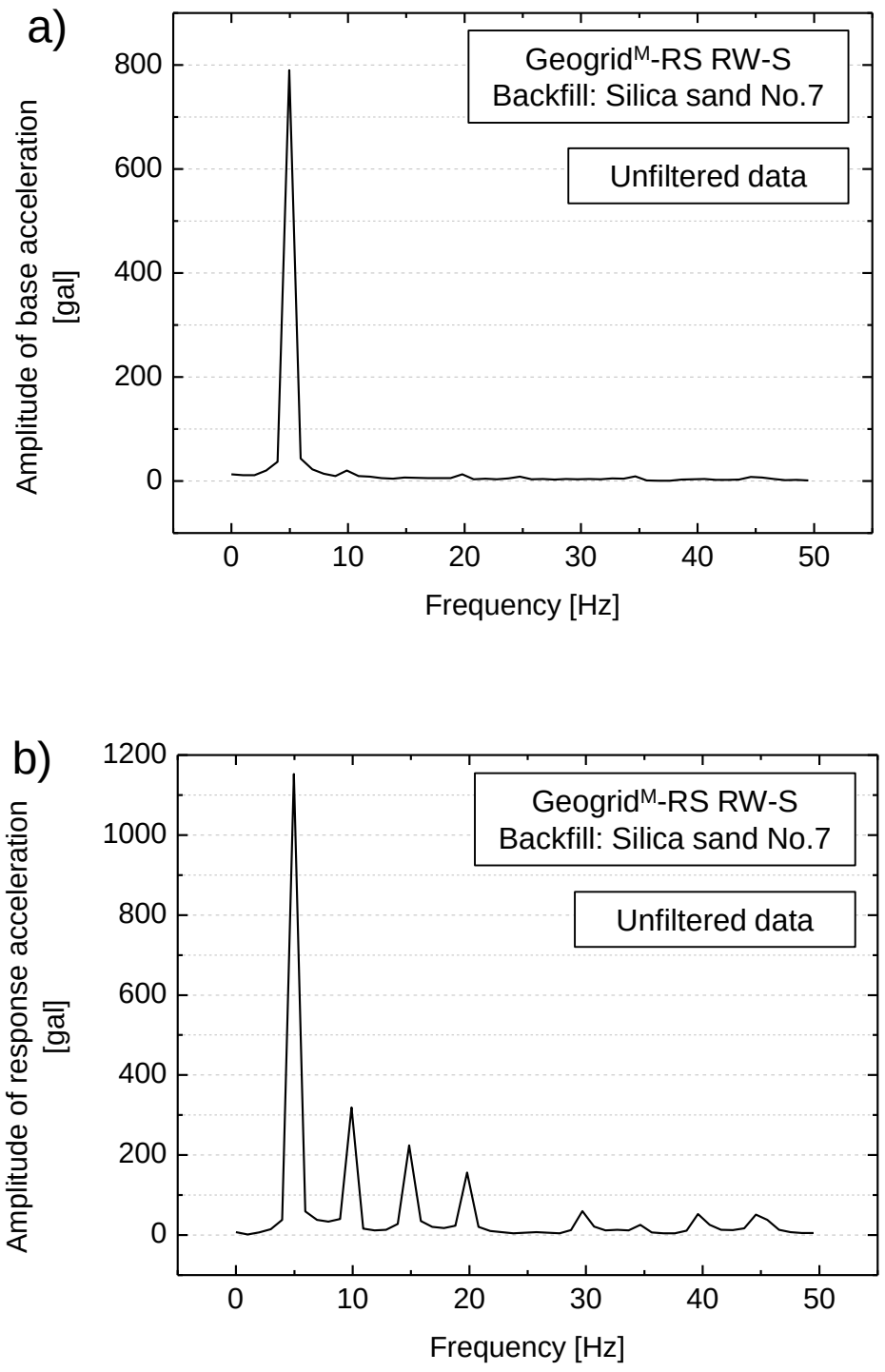

Fig. 5.30 Fast Fourier Transform (FFT) of the unfiltered data of: a) the input base acceleration; and b) response acceleration at the top of the wall.

In this study, a FFT filter is applied to smooth the accelerations A7 and A6 recorded by two accelerometers. This process can be accomplished by removing Fourier components with frequencies higher than 25 Hz from the acceleration record. The unfiltered and filtered data is shown in Fig. 5.31, while Fig. 5.32 shows the FFT of filtered data. A comparison between unfiltered and filtered data indicates that some secondary peaks (or noise) at frequencies higher than 25 Hz were removed from the original data. For the filtered response acceleration at the top of the wall (A6), there still exits some peaks at frequencies of 10 Hz, 15 Hz, and 20 Hz, which are due to the asymmetric response of the RW during shaking. The filtered process leads to a slight decrease in peak acceleration values. Nevertheless, it produces almost a zero phase shift between unfiltered data and filtered data, as shown in Fig. 5.31.

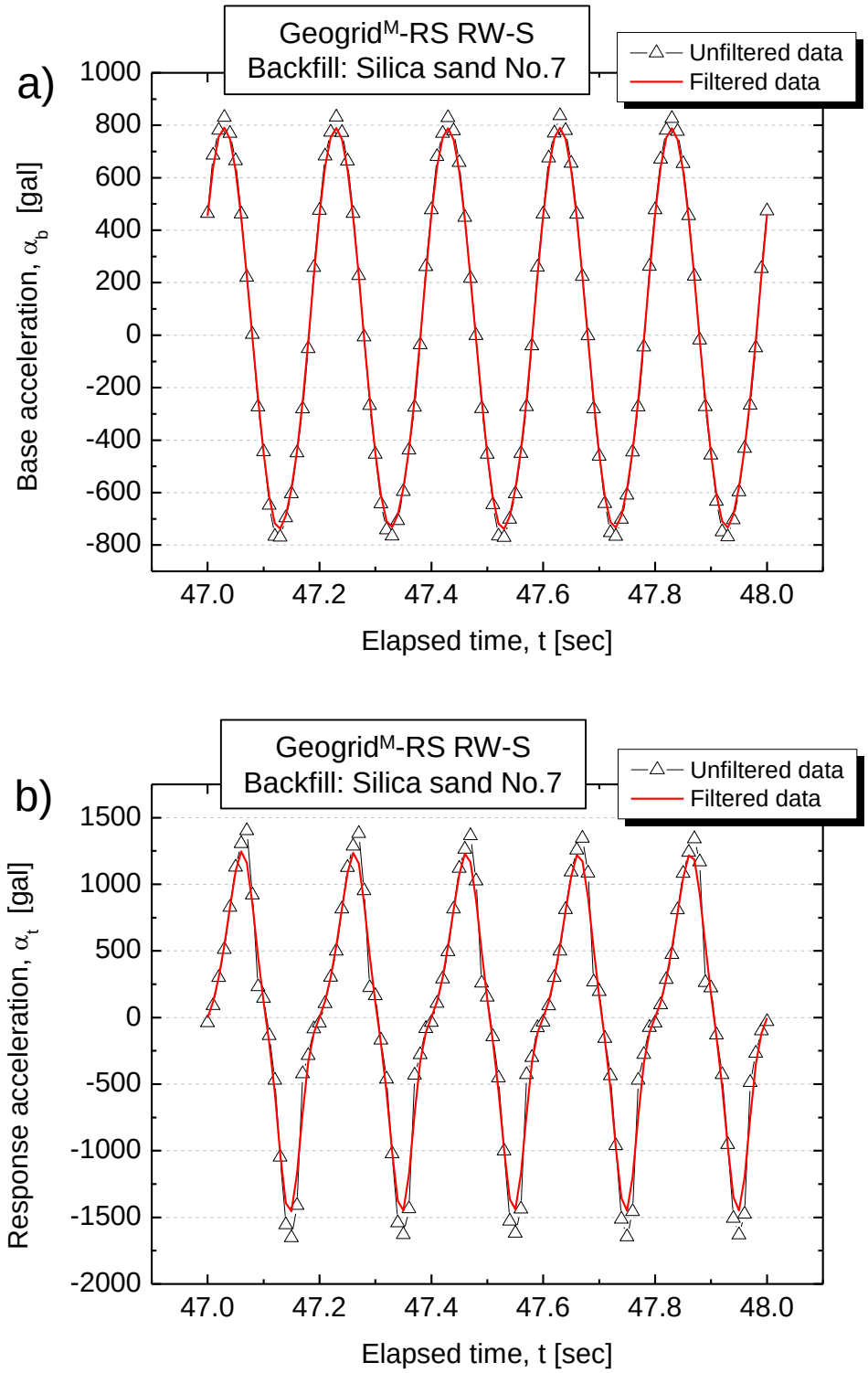

Fig. 5.31 Comparison of typical unfiltered and filtered data of: a) input base acceleration; and b) response acceleration at the top of the wall against one-second time history.

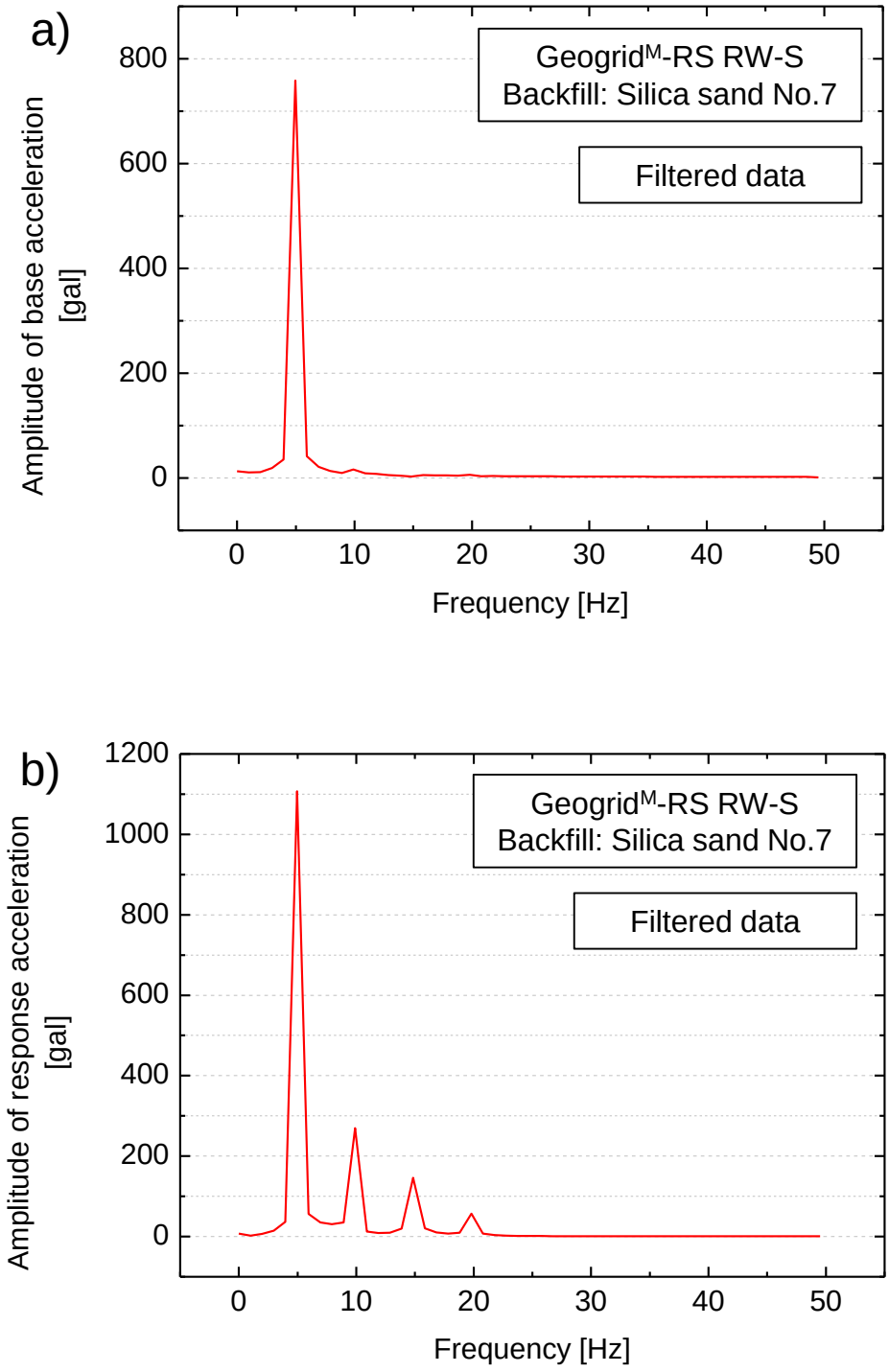

Fig. 5.32 Comparison of Fast Fourier Transform (FFT) of the filtered data of: a) the input base acceleration; and b) response acceleration at the top of the wall.

Fig. 5.33 shows the data after correction for overturn effects and noise filtering. From Fig. 5.33a, input base acceleration (A7-Time) is symmetric throughout all shaking stages. From Fig. 5.33b, response acceleration (A6-Time) is also symmetric under lower base acceleration, but it becomes asymmetric under higher base acceleration. It is shown that the response acceleration amplitude at active state is relative larger than that at passive state under higher input base acceleration (i.e. at the shaking stage Ⅷ, α_b = 772 gal). This is contributed to the fact that larger deformation occurs at this shaking stage resulting in a reduction in the stiffness of the RW system, associated with the formation of shear planes in the backfill soil. Therefore, smaller shear modulus of backfill soil at the active state compared to that at the passive state induces relatively larger response acceleration amplitude at the active state.

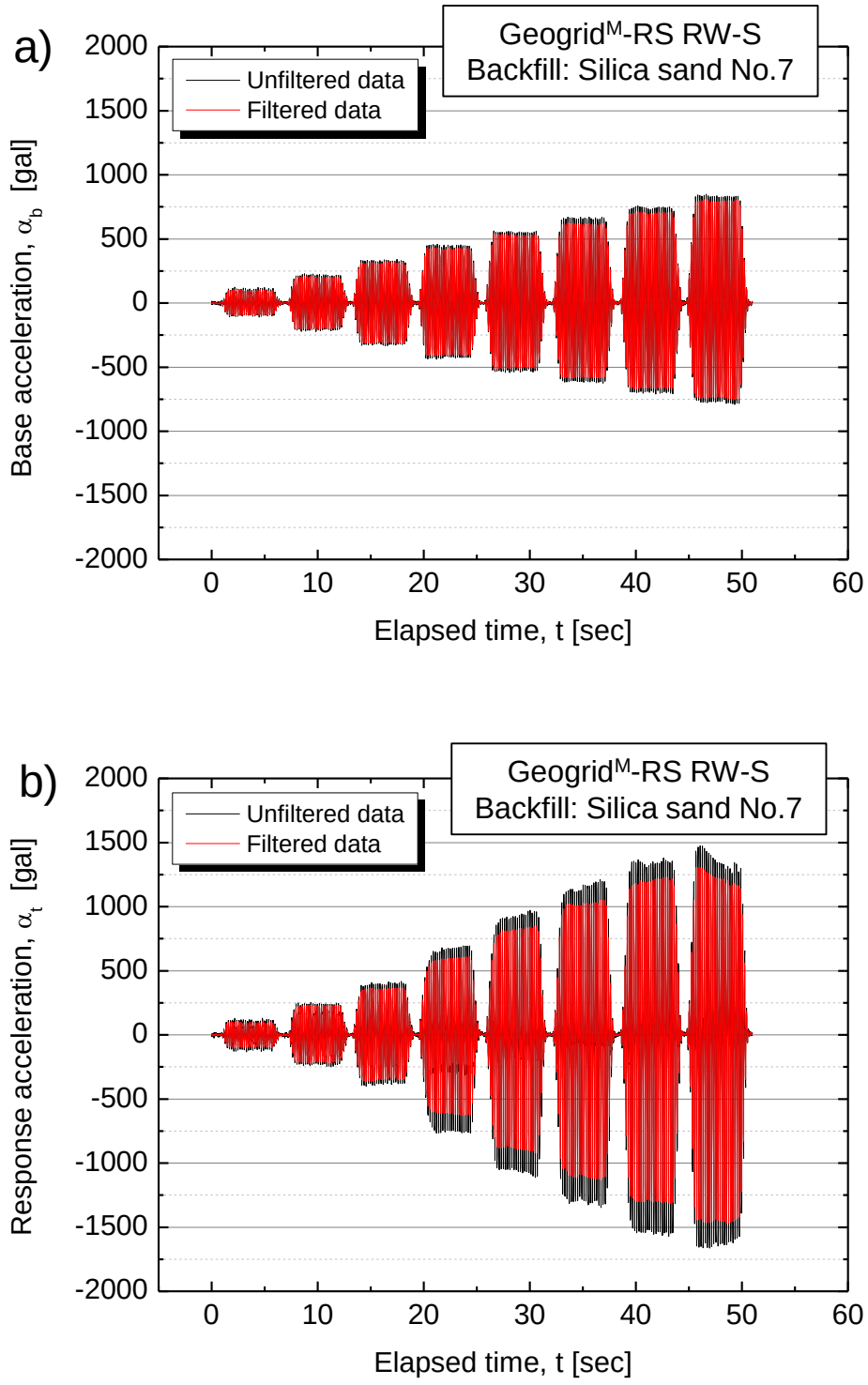

Fig. 5.33 Comparison of unfiltered and filtered data of: a) input base acceleration; and b) response acceleration at the top of the wall.

Acquisition of the values of M and φ

Throughout the shaking table test, the base acceleration recorded at the shaking table (A7), namely $\ddot{u}_b$, for the SDOF analysis as described in Section 5.4.1, and response acceleration at the top of the wall (A6), namely $\ddot{u}_t$, were measured, corrected and filtered. Fig. 5.34 shows the acquisition of the values of M and φ from a single sinusoidal wave after data process. Since the asymmetric response of the retaining wall under higher base acceleration, the values of M and φ are obtained at the active state (i.e. when the inertia force is oriented towards the active direction).

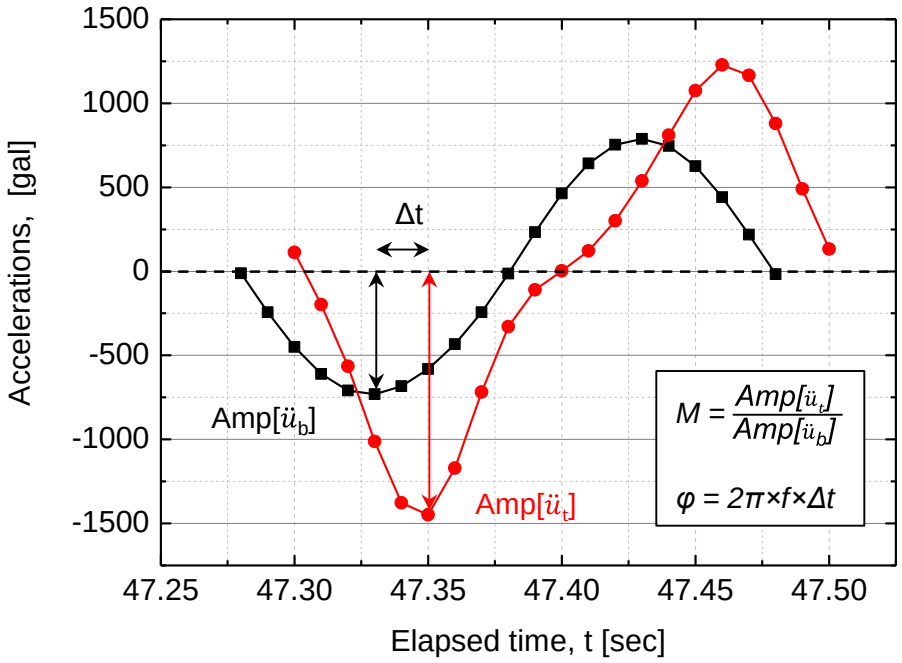

Fig. 5.34 Acquisition of values of M and φ from a single sinusoidal wave after data process to the raw base acceleration and response accelerations

5.4.3 Dynamic stability of various types of retaining wall models

The dynamic performances of all types of retaining wall models are firstly analyzed.

Case1: T-shape RW-S

Figure 5.35a shows the relationship between the back calculated values of M and β at each cycle for T-shape RW backfilled with sand, compared to the theoretical relations for different ξ values. Fig. 5.35b shows the corresponding φ-β relationships. During shaking stage Ⅰ (α_b = 128 gal) - Ⅳ (α_b = 391 gal), the M value increases from 1 to 1.5 and the β value also increases from 0 to 0.58 with an increase in the number of shaking cycles and α_b. The φ value is equal to zero. This suggests that the RW system moves almost rigidly and that the response acceleration is essentially controlled by the stiffness of the reinforced RW system and the wall displacement is in phase with the base acceleration. At shaking stage Ⅴ (α_b = 461 gal), the φ value starts to increase and the M value and β value continue to increase with an increase in the number of cycles until the peak value of M (2.14), where β becomes $\beta_{resonance}$ (0.77), and ξ becomes 0.1686. After passing this state, with an increase in the number of cycles, the M value decreases associated with an increase in the β and ξ value. As shown in Fig. 5.1b, at this shaking stage, the T-shape RW shows the full formation of the shear band, larger overturning of the wall and larger settlement of the backfill. As a result, stiffness of the RW system decreases inducing an increase in ξ, and finally, the failure of T-shape RW occurs.

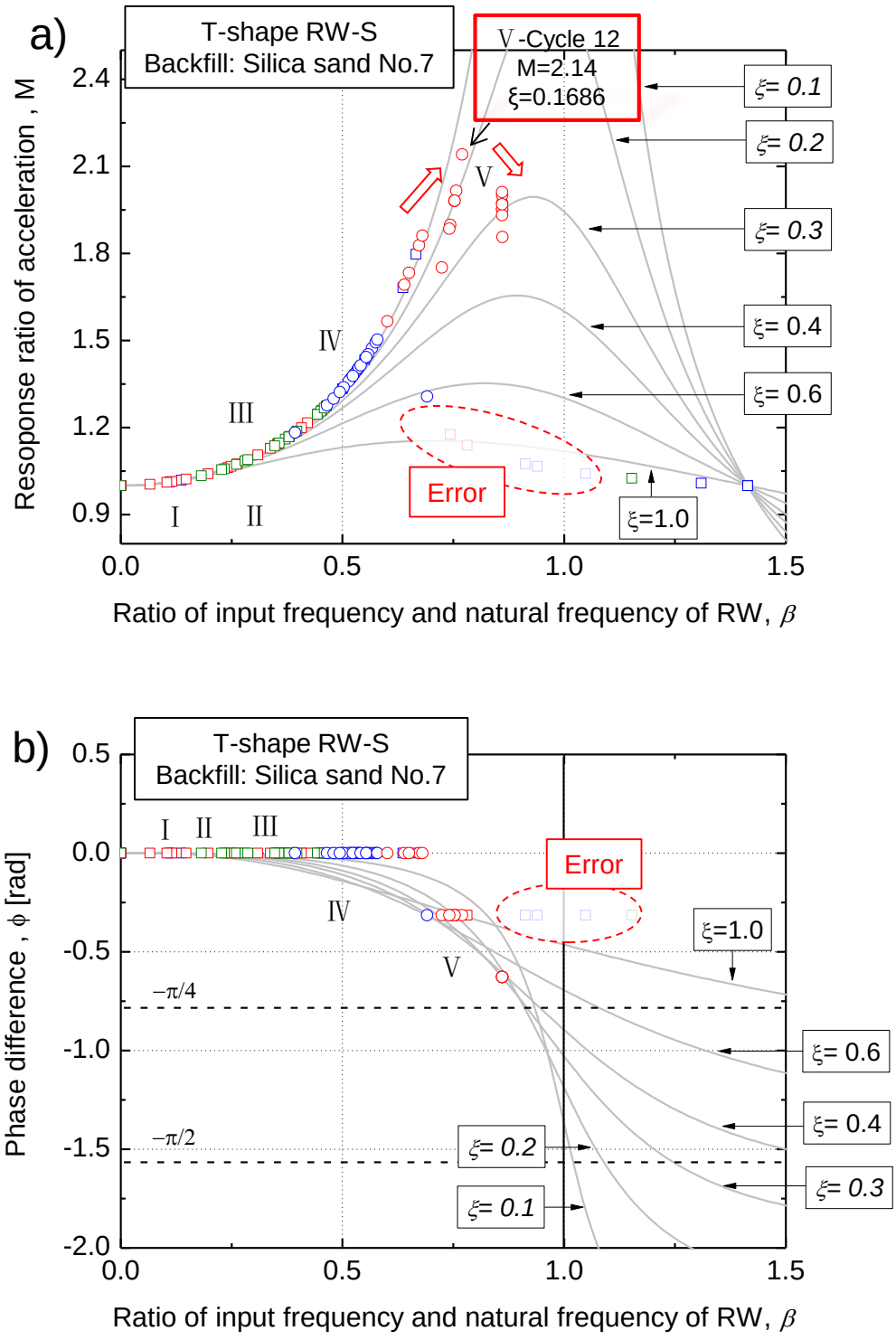

Fig. 5.35 Dynamic performance of T-shape RW model backfilled with sand: a) *M*-β and b) φ-β relationship.

Case2: Geogrid^{M}-RS RW-S

Figure 5.36a shows the relationship between the back calculated values of M and β at each cycle for geogrid^{M}-RS RW backfilled with sand, compared to the theoretical relationship for different ξ values. Fig 5.36b shows the corresponding φ-β relationship. During shaking stage Ⅰ (α_b = 99 gal) - Ⅳ (α_b = 425 gal), the M value increases from 1 to 1.56 and the β value also increases from 0 to 0.6 with an increase in the number of cycles and α_b. The φ value is equal to zero. That suggests that geogrid^{M}-RS RW moves almost rigidly and that the response acceleration is essentially controlled by the stiffness of the RW and the wall displacement is in phase with the base acceleration. From shaking stage Ⅴ (α_b = 531 gal) to Ⅷ (α_b = 772 gal), although there are some oscillations in the values of M and β during stage Ⅵ and Ⅶ, φ starts to increase and M and the β show an increasing trend with an increase in the number of cycles until the peak value of M (2.00) is reached, where β becomes $\beta_{resonance}$ (0.86), ξ becomes 0.2863 at shaking stage Ⅷ (α_b = 772 gal). After passing the peak value of M at shaking stage Ⅷ (α_b = 772 gal) with the same α_b value, M decreases slightly, while β and ξ slightly increase. At this stage, full formation of the shear bands, larger overturning of the wall and larger settlement of the backfill were also observed, suggesting that failure of the geogrid^{M}-RS RW occurs (Fig. 5.3d).

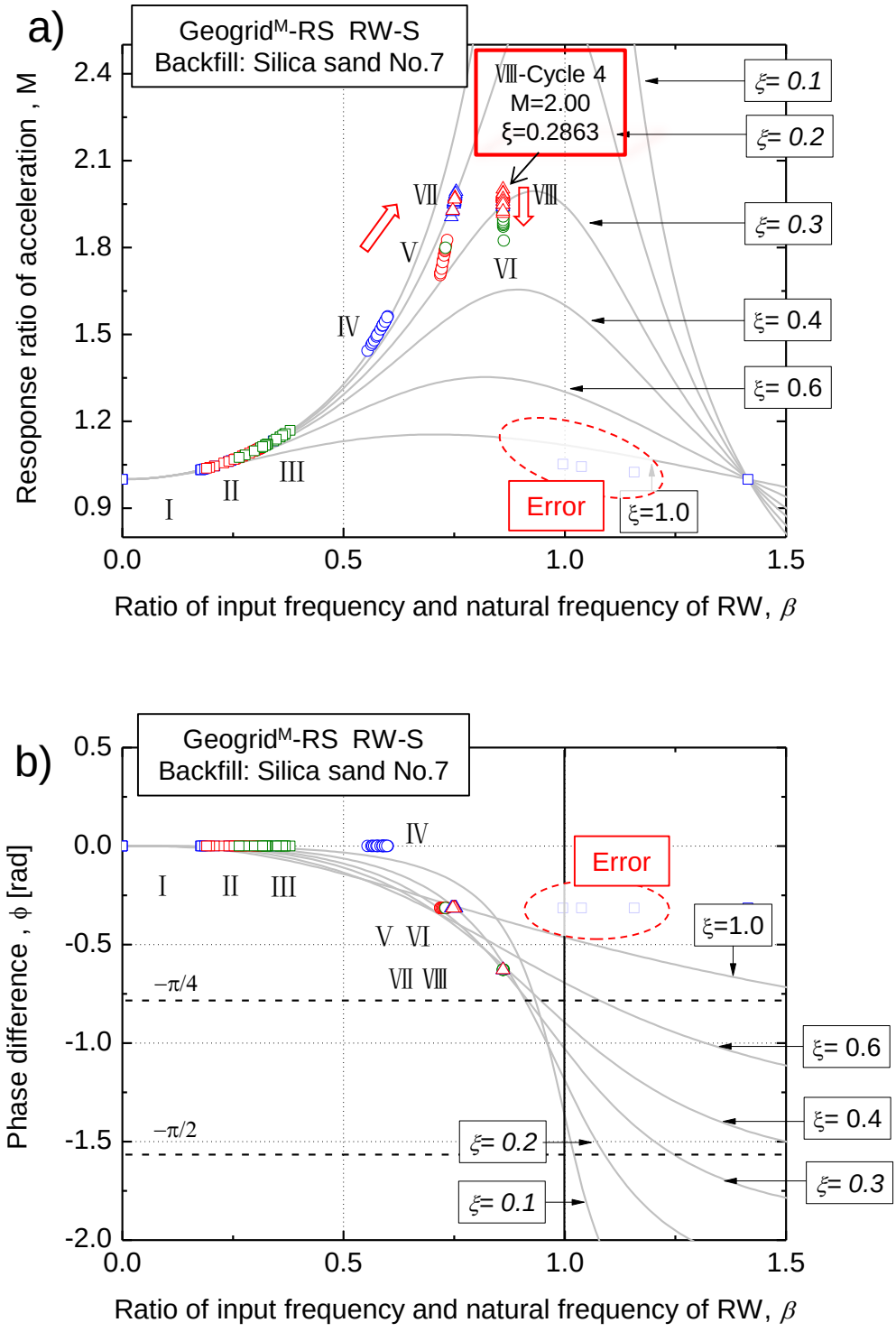

Fig. 5.36 Dynamic performance of geogrid^{M}-RS RW model backfilled with sand: a) *M-β* and b) *φ-β* relationship.

Case3: Geocell-RS RW-S

For the geocell-RS RW backfilled with sand shown in Fig. 5.37, φ is equal to zero, M increases from 1 to 1.46 and β increases from 0 to 0.56 until shaking stage Ⅴ (α_b = 477 gal), indicating that the initial stiffness of the geocell-RS RW may be slightly higher than that of geogrid^M-RS RW (i.e. φ is equal to zero until shaking stage Ⅳ (α_b = 425 gal), at which M = 1.56, β = 0.6) and T-shape RW (i.e. the φ value is equal to zero until shaking stage Ⅳ (α_b = 391 gal), at which M = 1.5, β = 0.58). However, geocell-RS RW reaches the resonance state (M = 2.00, β = 0.86, ξ = 0.2863) only at stage shaking stage Ⅶ (α_b = 631gal, at the 18th cycle), at which only very small shear bands in Area A are formed (Fig. 5.5b), while full formation of shear band occurs at the shaking stage Ⅸ, α_b = 865 gal (Fig. 5.5d).

By comparing the dynamic performances of RW models for T-shape RW, geogrid^M-RS RW and geocell-RS RW backfilled with sand, it was found that: 1) under lower base acceleration, the seismic stability of RW models is mainly controlled by stiffness of the RW system; 2) under higher base acceleration, the seismic stability of the RW models is controlled by both stiffness of the RW system and the damping capacity of the RW system.

In addition, some unstable dynamic performances were observed. For the geogrid^M-RS RW backfilled with sand, there were some oscillations in the values of M and β during shaking stage Ⅵ and Ⅶ. For example, at shaking stage Ⅵ, the value of β is near the value of $\beta_{resonance}$ (0.86) and no clear failure plane was observed (Fig. 5.3b). While at shaking stage Ⅶ, β decreases associated with a slight increase in M. At this stage, the initial failure plane is clearly formed (Fig. 5.3c). For the case of the geocell-RS RW backfilled with sand, the geocell-RS RW reaches the resonance state (M = 2.00, β = 0.86, ξ = 0.2863) only at shaking stage Ⅶ (α_b = 631 gal, at the 18th cycle), at which only very small shear bands in Area A are formed (Fig. 5.5b). However, the full formation of shear band occurs at shaking stage Ⅸ, α_b = 865 gal. These unstable behaviors of the geogrid^M-RS RW and the geocell-RS RW backfilled with sand may be due to the improper similitude rule on the relationship between the weight of the wall and the pullout stiffness of the reinforcements, since a heavy wall model relative to the pullout stiffness of tensile reinforcement (i.e. geogrid^M and geocell model) may result in very unstable oscillations of the facing wall during strong shaking.

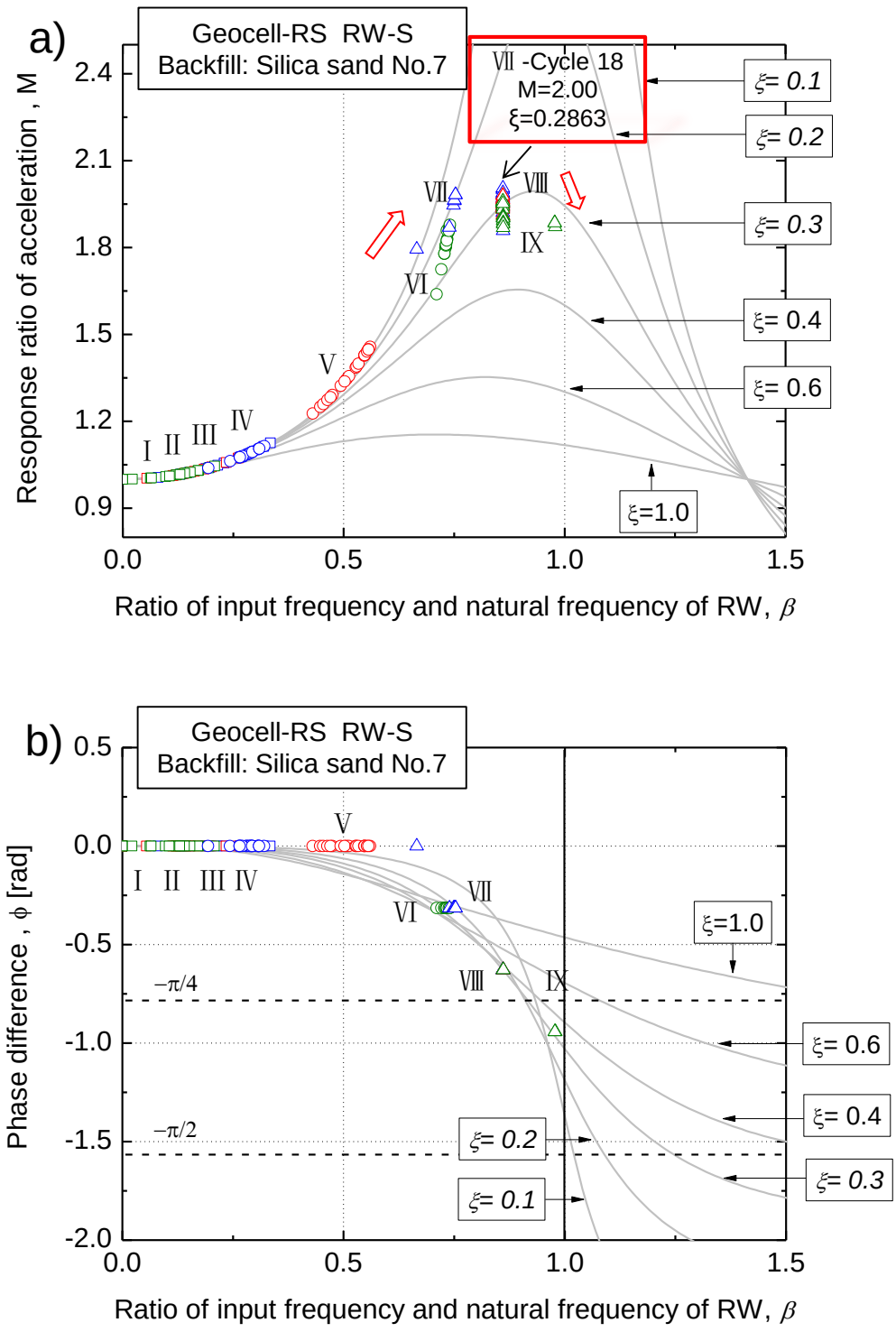

Fig. 5.37 Dynamic performance of geocell-RS RW model backfilled with sand: a) *M-β* and b) *φ-β* relationship.

Case4: T-shape RW -G

For T-shape RW backfilled with gravel (Fig. 5.38), during shaking stage Ⅰ (α_b = 132 gal) - Ⅲ (α_b = 319 gal), M increases from 1 to 1.06 and β increases from 0 to 0.23 with an increase in the number of shaking cycles and α_b. The φ value is equal to zero. This suggests that the RW system moves almost rigidly and the response acceleration is essentially controlled by the stiffness of the RW system and that the wall displacement is in phase with the base acceleration. At shaking stage Ⅳ (α_b = 417 gal), φ starts to increase and M and β values continue to increase with an increase in the number of cycles until the peak value of M (1.80), where β becomes $\beta_{resonance}$ (0.987), and ξ becomes 0.34. At this shaking stage, the T-shape RW shows larger sliding of the facing wall and larger settlement of the backfill. As a result, the stiffness of RW system decreases inducing an increase in ξ and, finally, failure of the T-shape RW occurs (Fig. 5.7b).

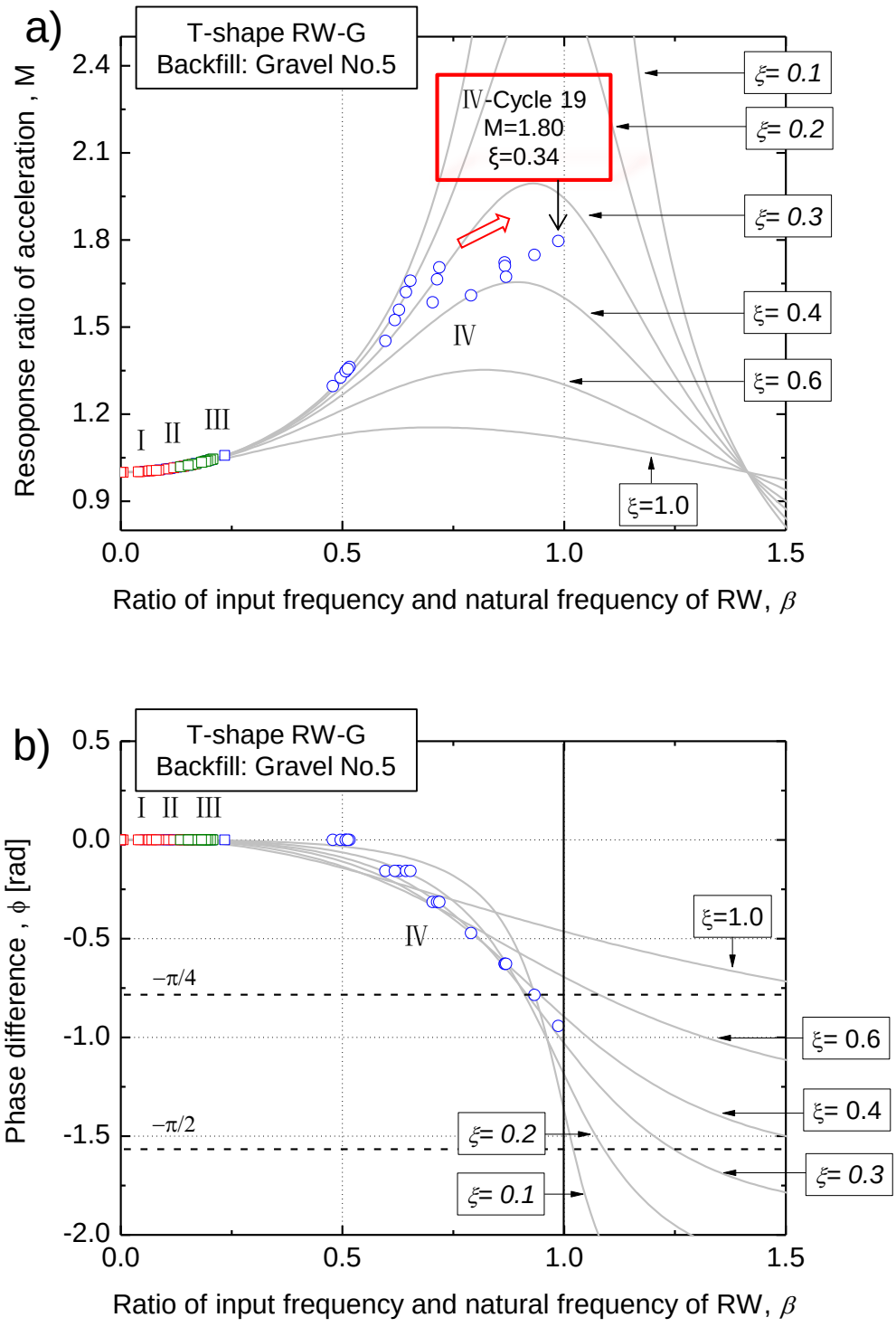

Fig. 5.38 Dynamic performance of T-shape RW model backfilled with gravel: a) *M-β* and b) *φ-β* relationship.

Cases 5 and 6: Geogrid^{M}-RS RW-G and Geogrid^{C}-RS RW-G

Figs. 5.39 and 5.40 show the dynamic performances of the geogrid^{M}-RS RW and the geogrid^{C}-RS RW backfilled with gravel in terms of the M-β and φ-β relationships. For the geogrid^{M}-RS RW backfilled with gravel (Fig. 5.39), φ is equal to zero, M increases from 1 to 1.48 and β increases from 0 to 0.57 until shaking stage Ⅶ(α_b = 628 gal, at the second cycle). While for the geogrid^{C}-RS RW backfilled with gravel (Fig. 5.40), φ is equal to zero, M increases from 1 to 1.13 and β increases from 0 to 0.34 until shaking stage Ⅳ (α_b = 411 gal, at the 20th cycle), indicating that the initial stiffness of the geogrid^{M}-RS RW is higher than that of the geogrid^{C}-RS RW when backfilled with gravel. On the other hand, the geogrid^{M}-RS RW reaches the resonance state (M = 1.83, β = 0.9835, ξ = 0.3317) at shaking stage Ⅷ (α_b = 755gal, at the 4th cycle). At this stage, larger overturning of the wall and larger settlements of the backfill were observed, indicating failure of the geogrid^{M}-RS RW (Fig. 5.9c). While the geogrid^{C}-RS RW reaches the resonance state (M = 1.77, β = 0.9901, ξ = 0.345) at shaking stage Ⅶ (α_b = 690 gal, at the 14th cycle). At this stage, larger overturning of the wall and larger settlement of the backfill were also observed, indicating failure of the geogrid^{C}-RS RW (Fig. 5.11b).

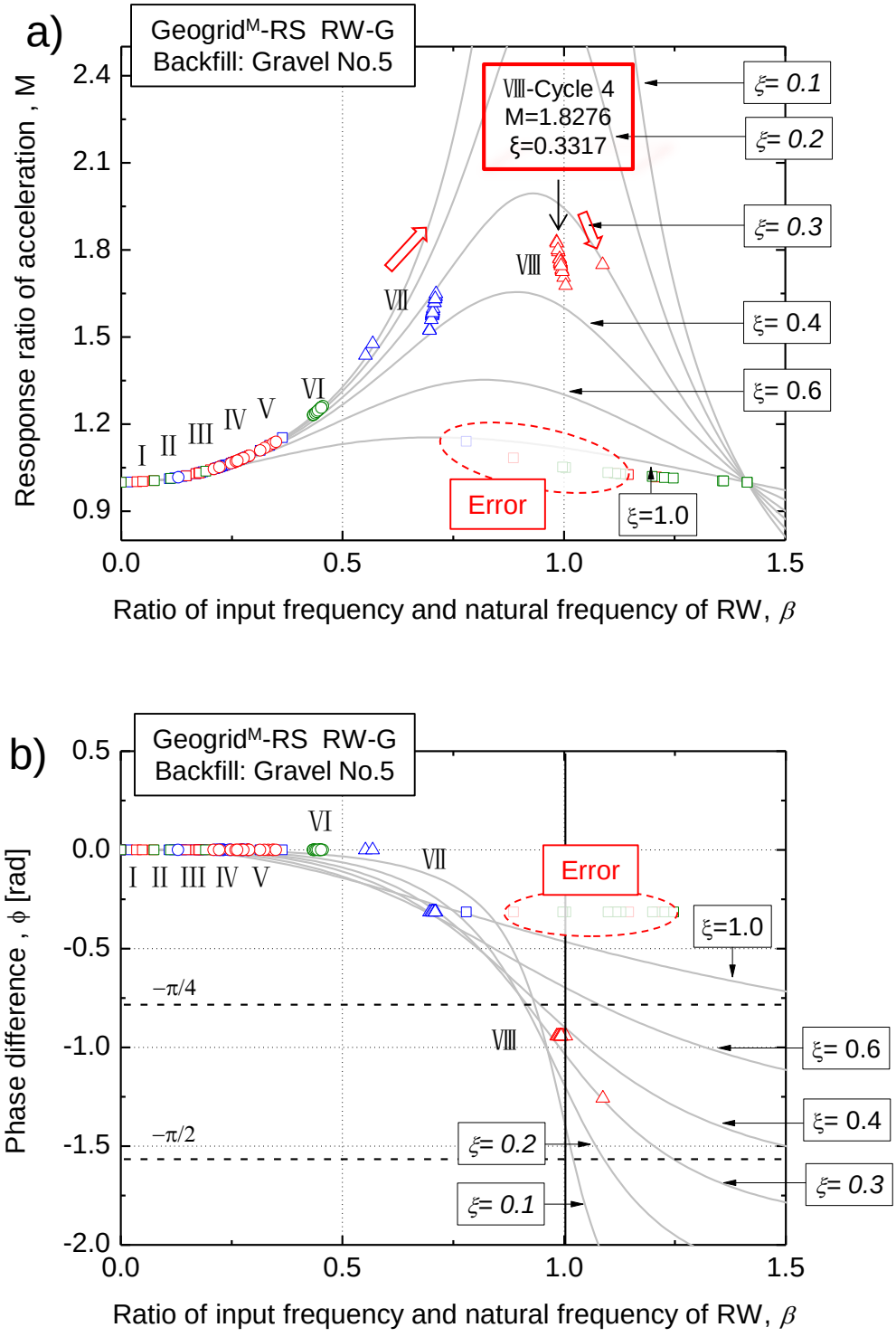

Fig. 5.39 Dynamic performance of the geogrid^{M}-RS RW model backfilled with gravel: a) M-β and b) φ-β relationship.

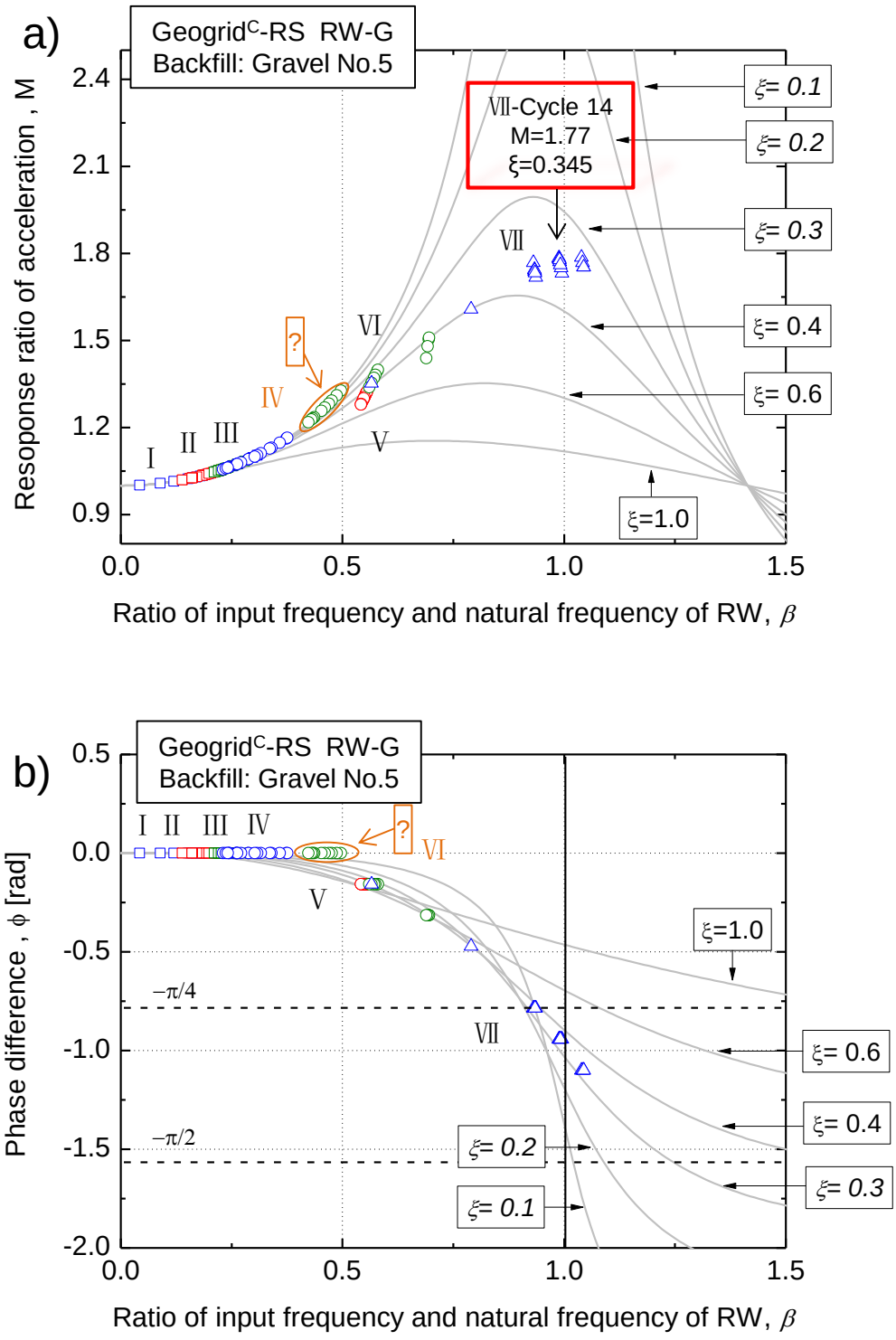

Fig. 5.40 Dynamic performance of the geogrid^{C}-RS RW model backfilled with gravel: a) M-β and b) φ-β relationship.

Cases 7: Geocell-RS RW-G

Figure 5.41 show the dynamic performances of the geocell-RS RW backfilled with gravel in terms of M-β and φ-β relationships. A similar trend was found for Case 5 (geogrid^{M}-RS RW-G) and Case 6 (geogrid^{C}-RS RW-G). During shaking stage Ⅰ (α_b = 89 gal) - Ⅶ (α_b = 644 gal), M increases from 1 to 1.36 and β increases from 0 to 0.52 with an increase in the number of shaking cycles and α_b. The φ value is equal to zero. Comparing Case 7 to Case 5 (geogrid^{M}-RS RW-G) and Case 6 (geogrid^{C}-RS RW-G), this suggests that the initial stiffness of the geocell-RS RW may be slightly higher than that of geogrid-RS RW. From shaking stage Ⅷ (α_b = 732gal) to Ⅸ (α_b = 843 gal), φ starts to increase and M and β continue to increase with an increase in the number of cycles until the peak value of M (1.71), where β becomes $\beta_{resonance}$ (0.9986), and ξ becomes 0.3680. At resonance state during shaking stage Ⅸ (α_b = 843 gal), larger overturning of the wall and larger settlement of the backfill were observed, indicating failure of the geocell-RS RW (Fig. 5.13c).

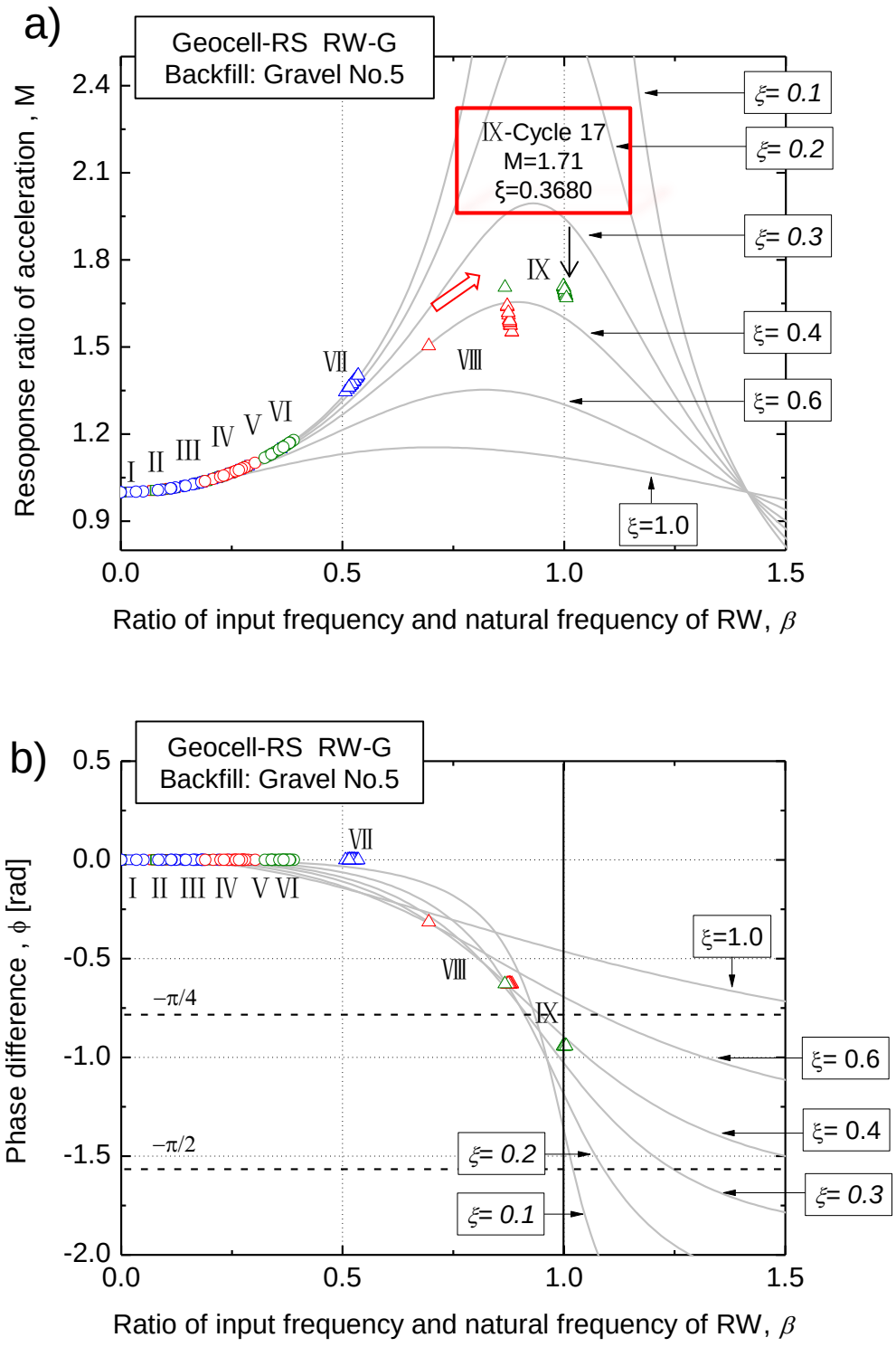

Fig. 5.41 Dynamic performance of the geocell-RS RW model backfilled with gravel: a) *M-β* and b) *φ-β* relationship.

The dynamic stability of the RW models is evaluated from the following aspects: 1) dynamic strength; 2) dynamic ductility (or softening rate); 3) damping capacity at failure state.

Dynamic strength

The failure of full-scale RW structures is usually defined as deformation of the wall (i.e. sliding of the wall or overturning of the wall), settlements or bumps of the backfill, cracking of the concrete walls etc. which exceeds the specified serviceability limit values. In this study, the dynamic strength of a RW model against failure is defined as the value of response acceleration amplitude at the top of the wall (α_t) at resonance state, where the magnification ratio (M) becomes maximum; and the value of β becomes $\beta = \beta_{resonance}$. At this state, the RW model starts to exhibit significant deformation as described case by case previously.

Figure 5.42 shows the relationship between β and α_t. It is clearly shown that, with an increase in β, α_t increases and the largest value of α_t takes place as β approaches unity. With the backfill of sand (Fig. 5.42a), although the geogrid^M-RS RW and the geocell-RS RW show unstable dynamic behavior as described previously, both exhibit obvious higher dynamic strength than the T-shape RW. In particular, the geocell-RS RW shows slightly higher dynamic strength than the geogrid^M-RS RW. With the backfill of gravel, it is also to see that the geocell-RS RW shows slightly higher dynamic strength than the geogrid^M-RS RW but obvious higher dynamic strength than the geogrid^C-RS RW, and all types of GRS RW (i.e. geogrid^M-RS RW, geogrid^C-RS RW and geocell-RS RW) exhibit obvious higher dynamic strength than T-shaped RW.

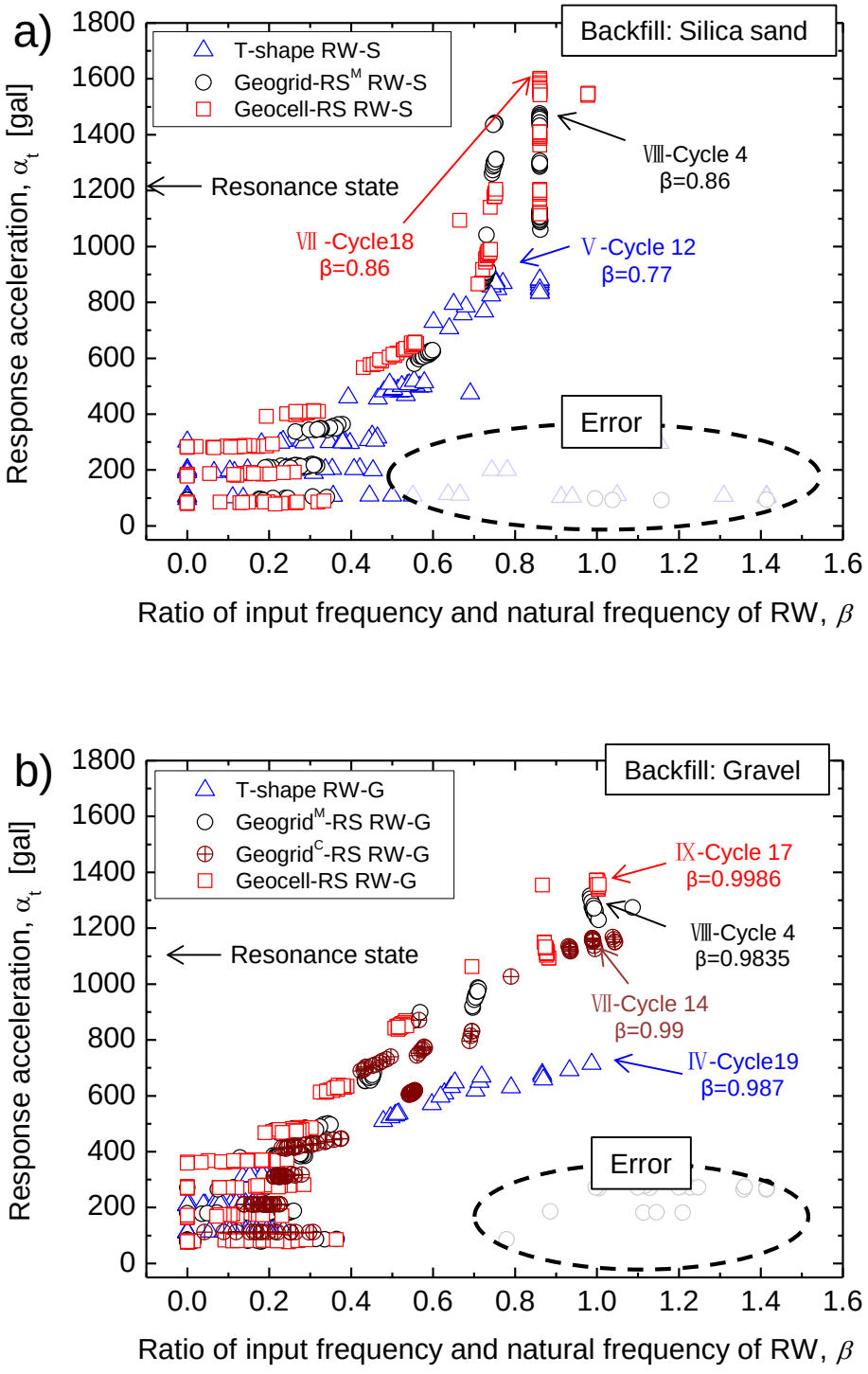

Fig. 5.42 Relationship between β and response acceleration at the top of the wall, α_t for the backfill of: a) sand; and b) gravel.

Dynamic ductility

Previous studies by Tatsuoka et al. (2007, 2012) have demonstrated that a higher dynamic ductility means a lower speed to reach resonance state, at which failure of the structure may occur. Fig. 5.43 shows the α_b-β relationship for the seven testing cases. Smaller increasing rate of β with the input base acceleration level and number of cycles implies a higher dynamic ductility. Therefore, in the backfill of sand, the increasing rates of β, with the input base acceleration level and number of cycles of the geogrid^M-RS RW and the geocell-RS RW are much smaller than that of the T-shape RW, indicating that GRS RWs with geogrid and geocell reinforcements backfilled with sand have higher dynamic ductility than conventional non-reinforced type RW (i.e. T-shape RW).

Although unstable dynamic performances of the geogrid^M-RS RW and the geocell-RS RW were observed, as explained previously, the dynamic ductility of the geogrid^M-RS RW was similar to that of the geocell-RS RW when backfilled with sand. While in the backfill of gravel, the increasing rate of β of the geocell-RS RW becomes smaller than that of the geogrid^M-RS RW when α_b is larger than around 600 gal, and the increasing rate of β of the geocell-RS RW is much smaller than that of the geogrid^C-RS RW when α_b is larger than around 450 gal. This indicates that GRS RW with geocells can effectively decrease the rate approaching to the resonance state, therefore increase dynamic ductility, compared to that of the geogrid reinforcement (i.e. geogrid^M and geogrid^C). All types of GRS RW show obvious higher dynamic ductility than T-shape RW.

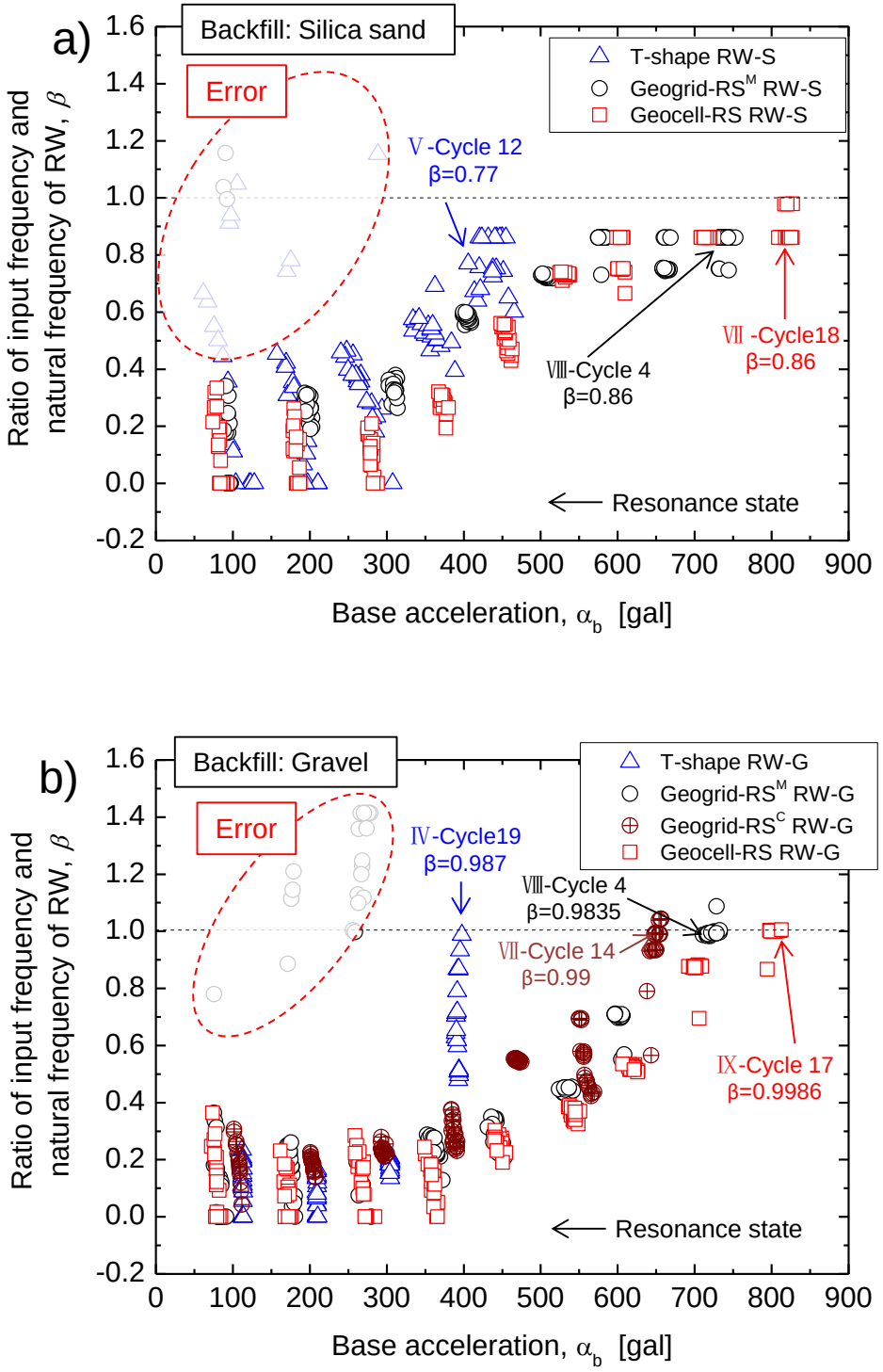

Fig. 5.43 Relationship between base acceleration, α_b, and β, for the backfill of: a) sand; and b) gravel.

Damping capacity

The test results of the geogrid^{M}-RS RW, the geogrid^{C}-RS RW and the geocell-RS RW in the backfill of gravel are analyzed. As shown in Figs. 5.39a, 5.40a and 5.41a, at resonance state, the value of damping ratio of the geocell-RS RW (ξ = 0.368) is relatively larger than that of the geogrid^{M}-RS RW (ξ = 0.3317) and the geogrid-RS RW (ξ = 0.3450), which results in a relatively smaller M value for the geocell-RS RW (M = 1.71) compared with the geogrid^{M}-RS RW (M = 1.83) and the geogrid^{C}-RS RW (M = 1.77), therefore a higher dynamic strength of geocell-RS RW (Fig. 5.42b). In the GRS RW system, ξ is controlled by the following factors: 1) the material damping (i.e. facing wall material, backfill soil and subsoil material and the reinforcement material); 2) the interaction among the components of the GRS RW system (i.e. the connection between the wall and reinforcements, the interaction between the reinforcements and backfill soil). In this case, under the same conditions, factor 2) becomes more significant due to the fact that the geocell reinforcement may provide relatively better confinement of larger backfill soil particles, which makes good contact of the wall facing with the backfill soil, thereby a relative higher damping capacity for geocell-RS RW backfilled with gravel comparing to geogrid-RS RW.

5.5 References

1. El-Emam, M. M. and Bathurst, R. J. (2007). "Influence of reinforcement parameters on the seismic response of reduced-scale reinforced soil retaining walls", Geotextiles and Geomembranes, 25(1), 33-49.
2. Jackson, P.F. (2010). "An investigation into the deformation behaviour of geosynthetic reinforced soil walls under seismic loading", Master Thesis, Department of Civil and Natural Resources Engineering, University of Canterbury.
3. Koseki, J., Munaf, Y., Tatsuoka, F., Tateyama, M., Kojima, K. and Sato, T. (1998). "Shaking and tilt table tests of geosynthetic-reinforced soil and conventional-type retaining walls", Geosynthetics International, 5(1-2), 73-96.
4. Kuroda, T. (2012). "Evaluation of static and seismic stability of bridges with reinforced backfill and integrated structural (new type and rehabilitated type bridges) by model tests", Master Thesis, Department of Civil Engineering, Tokyo University of Science. (In Japanese).
5. Muñoz, H., Tatsuoka, F., Hirakawa, D., Nishikiori, H., Soma, R., Tateyama, M. and Watanabe, K. (2012). "Dynamic stability of geosynthetic-reinforced soil integral bridge", Geosynthetics International 19(1), 11-38.
6. Muñoz, H. (2010). "Dynamic performance of conventional type and reinforced soil bridges", Master Thesis, Department of Civil Engineering, Tokyo University of Science.
7. Nakajima, S., Koseki, J., Watanabe, K. and Tateyama, M. (2010). "Simplified procedure to evaluate earthquake-induced residual displacement of geosynthetic reinforced soil retaining walls", Soils and Foundations, 50(6), 659-678.
8. Nova-Roessig, L. and Sitar, N. (2006). "Centrifuge model studies of the seismic response of reinforced soil slopes", Journal of Geotechnical and Geoenvironmental Engineering, 132(3), 388-400.
9. Shinoda, M., Uchimura, T. and Tatsuoka, F. (2003). "Improving the dynamic performance of preloaded and prestressed mechanically reinforced backfill by using a ratchet connection", Soils and Foundations, 43(2), 33-54.
10. Tatsuoka, F., Tani, K., Okahara, M., Morimoto, T., Tatsua, M., Takagi, M. and Mori H. (1989). "Discussion of Influence of the foundation width on the bearing capacity factor by Hettler y Gudehus (1988)", Soils and Foundations, 29(4), 146-154.
11. Tatsuoka, F., Hirakawa, D., Nojiri, M., Aizawa, H., Nishikiori, H., Soma, R., Tateyama, M. and Watanabe, K. (2009). "A new type of integral bridge comprising geosynthetic-reinforced soil walls", Geosynthetics International, 16(4), 301-326.
12. Tatsuoka F., Tateyama, M., Mohri, Y. and Matsushima K. (2007). "Remedial treatment of soil structures using geosynthetic-reinforcing technology", Geotextiles and Geomembranes, 25(4-5), 204-220.
13. Tatsuoka F., Tateyama M. and Koseki J. (2012). "GRS structures recently developed and constructed for railways and roads in japan", Proc. of 2nd International Conference on Transportation Geotechnics (ICTG), Hokkaido, Japan, pp 63-85.
14. Watanabe, K., Munaf, Y., Koseki, J., Tateyama, M. and Kojima, K. (2003). "Behaviors of several types of model retaining walls subjected to irregular excitation", Soils and Foundations, 43(5), 13-27.

6 CONCLUSIONS AND RECOMMENDATIONS

6.1 Conclusions

6.1.1 Introduction

In this study, a new type of tensile reinforcement, which can confine larger on-site soil particles and provide larger pullout resistance, thereby increasing the seismic stability of GRS RW structures (i.e. GRW integral bridge, etc.) was developed. It consists of a new type of geocell, named square-shaped geocell, comprised of square-shaped cells constituted by straight longitudinal members with transversal walls at separated locations.

In this thesis, detailed specifications of the newly-developed square-shaped geocell are firstly introduced as well as its potential advantages as tensile-reinforcement for the backfill of RWs. The tensile function of the newly-developed square-shaped geocell is evaluated by pullout tests and compared to that of traditional diamond-shaped geocell and traditional planar tensile reinforcement (i.e. commercial geogrid) for GRS RWs embedded in gravelly soils with different particles. Furthermore, the seismic performance of GRS RWs with square-shaped geocell reinforcement is also investigated by shaking table model tests and compared to that of GRS RWs with geogrid reinforcement and traditional type non-reinforced RWs (i.e. T-shape RWs) embedded in different backfill soils. The following conclusions can be drawn from the experimental investigations carried out in this current study.

6.1.2 Pullout test

By comparing the pullout behaviors of the square-shaped geocell model and the diamond-shaped geocell model, the square-shaped geocell shows much less pronounced progressive deformation exhibiting not only higher peak pullout resistance but also higher pre-peak stiffness than diamond-shaped geocell in both backfills of Gravel No.1 (D_{50}=3.2mm) and Gravel No.3 (D_{50}=7.5mm). This can be attributed to differences in the mobilization mechanism of strength in the backfill that are caused by different geometries of geocell. Different stress-deformation mechanisms of the geocells during the pullout process show one advantage of the square-shaped geocell: the straight longitudinal members reduce the progressive deformation of the cells when subjected to a tensile force, compared to the diamond-shaped geocell, which enhances both the pullout pre-peak stiffness and pullout resistance.

By comparing the pullout behaviors of the square-shaped geocell model and commercial geogrids embedded in different gravelly soils (i.e. Gravel No.1 (D_{50}=3.2mm) and Gravel No.3 (D_{50}=7.5mm)), both peak and the residual pullout resistances of the square-shaped geocell increase and become higher than those of the geogrids with an increase in backfill soil particle size. This behavior confirms the advantageous properties of the square-shaped geocell over the geogrids due to efficient confinement of larger soil particles in the cells resulting in a larger anchorage capacity of the cells.

Based on the test results, different pullout mechanisms between the geogrid (with a planar structure) and square-shaped geocell (with a 3-D structure) can be identified. Pullout resistance of the geogrid is controlled by the following factors: 1) Friction between the soil particles and geogrid members; 2) Friction between the soil particles interlocked in grid aperture and adjacent soil particles; 3) Passive soil resistance induced by the grid transversal members. In addition, appropriate geogrid aperture size relative to soil particle size would induce better interlocking, which would increase the pullout resistance of the geogrid. From this study, with an increase in the particle size of the backfill from 3.2 mm to 14.2 mm, a negligible increase in the pullout resistance of the geogrid means that one or all of these factors does not increase significantly. As the aperture size of the geogrid was 28 mm × 33 mm, it is likely that the interlocking effect does not increase with an increase in particle size.

Unlike the mechanism explained above, the pullout resistance of square-shaped geocell can be considered to be the smaller one between: 1) the shear resistance of the shear bands along the upper and bottom boundaries of the geocell; and 2) the anchorage resistance induced by passive pressure developing inside the cells. These two factors have a reciprocal effect. From this study, with an increase in the particle size of the backfill from 3.2 mm to 7.5 mm, a significant increase in the pullout resistance of the geocell means that large soil particles are confined better by the geocell than the geogrid, which results in higher anchorage capacity and/or higher shear resistance at the top and bottom interfaces between the geocell and the adjacent backfill than in the geogrid.

The pullout interaction mechanism between the geocell and adjacent backfill soil was investigated by considering the significant effect of geocell height relative to backfill soil particle size. It was found that the pullout resistance increases with an increase in member height with the square-shaped geocell. However, there exists an upper limit with the pullout resistance that is reached when the height of the member becomes a certain value that increases with an increase in the backfill particle size. A conceptualized pullout interaction mechanism was proposed based on the test results. The pullout resistance is equal to the smaller value between: 1) the shear resistance of the shear bands along the upper and bottom faces of the geocell, which is independent of the height of the geocell; and 2) the anchorage resistance induced by passive pressure developed inside the cells, which increases with an increase in the geocell height. Therefore, as the height of the geocell increases, the total pullout resistance is equal to the anchorage resistance and increases with an increase in geocell height. When the height of the geocell reaches a certain value, the pullout resistance becomes the same as the shear resistance and does not increase with further increase in height. Both shear and anchorage resistance, thereby the pullout resistance, increase with an increase in backfill particle size.

The effect of spacing between transversal members on pullout resistance of the geocell was also investigated. It was shown that when the pullout resistance of the geocell is mainly determined by shear resistance of the shear bands along the upper and bottom faces of the geocell, the spacing between transversal members has only a small influence on the pullout resistance, which means reducing the number of transversal members is possible for cost effectiveness.

Some suggestions for construction work have also been proposed based on related research. For example, although the pre-peak pullout stiffness of the geocell model is lower than the geogrid, this drawback can be alleviated partly by preloading to reduce the slackness of the transversal members. The pre-peak stiffness may increase not only by good initial preparations to reduce the initial slackness of the transversal members, but also by using stiffer longitudinal and transversal members mainly to reduce the progressive development of tensile forces in the axial direction of the geocell.

6.1.3 Shaking table model test

The seismic performance of square-shaped geocell-reinforced GRS RWs (geocell-RS RWs) backfilled with sand was evaluated and compared to that of conventional type non-reinforced RWs (i.e. T-shape RW) and geogrid-RS RWs (with geogrid^{M} reinforcements) by shaking table model tests. In addition, other shaking table tests on T-shape RW, geocell-RS RW and geogrid-RS RW (with geogrid^{M} reinforcements having larger aperture size and geogrid^{C} reinforcements having smaller aperture size) backfilled with gravel were also conducted to check if geocell-RS RW has a higher seismic stability than geogrid-RS RWs in backfill with larger particles.

Based on results of image analysis on the displacement of the facing wall, deformation of the backfill, response acceleration of the wall etc. for different types of RWs during shaking, the deformation and failure modes of geogrid-RS RW are found to be consistent with previous research (Koseki et al. 1998). In addition, the geocell-RS RW shows similar deformation and failure patterns with the geogrid-RS RW.

From the evaluation of residual overturning angle of the facing wall, the geocell-RS RW shows more ductile behavior than that of the geogrid-RS RW and T-shape RW when backfilled with sand. This trend becomes stronger when backfilled with gravel under higher base acceleration. This is due to the fact that as particle size increases, the geocell model provides a larger extent of pullout resistance than the geogrid, which increases the overall stability of the reinforced backfill to a larger extent in the backfill of gravel, therefore a smaller overturning or more ductile behavior of the geocell-RS RW with gravel backfill compared to the geogrid-RS RW.

From the evaluation of residual sliding of the facing wall under low base acceleration (i.e. before initial failure planes are formed in the backfill of sand), geocell-RS RW and geogrid-RS RW exhibit similar residual sliding displacement because of the same subsoil condition. While under high base acceleration (i.e. soil wedges have been clearly observed, Figs. 5.3 and 5.5), the residual sliding displacement of geocell-RS RW is smaller than that of geogrid-RS RW. This may be due to the fact that the geocell reinforcement in the bottom of the reinforced zone provides larger pullout resistance than geogrid reinforcement against higher base acceleration.

From the evaluation of settlement of the backfill soil, geocell-RS RW shows better performance than geogrid-RS RW and T-shape RW for restricting settlements under higher base acceleration.

From the evaluation of response acceleration of the wall and the backfill soil, in the case of sand backfill, the response amplification of geocell-RW is similar to that of geogrid-RS RW. While in the case of gravel backfill, geocell-RS RW shows a smaller amplification response than geogrid-RS RW under higher base acceleration. This indicates that geocell-RS RW has a higher seismic stability than geogrid-RS RW under higher base acceleration (i.e. from 468 gal to 844 gal) especially if embedded in gravels with larger particles.

A critical acceleration is defined as the amplitude of the base acceleration in the active state when the residual displacement at the top of the wall reaches 5% of the total wall height. A high critical acceleration implies a higher acceleration necessary to induce failure, and reduced deformation at low acceleration, which can be an index to evaluate the stability of RWs. Based on this approach, it was found that at critical state the critical acceleration of geocell-RS RW is higher than that of geogrid-RS RW in both backfill of sand and gravel, indicating that geocell-RS RW exhibits a higher seismic stability than geogrid-RS RW.

The dynamic behavior of geocell-RS RW was analyzed as a damped single-degree-of-freedom system. Based on the concepts of dynamic strength, dynamic ductility, and damping capacity at failure state, it was shown that when backfilled with sand, although geogrid-RS RW and geocell-RS RW show some unstable dynamic behaviors, both exhibit obvious higher dynamic strength, dynamic ductility, and damping capacity at failure than T-shape RW. While when backfilled with gravel, it was clearly observed that geocell-RS RW shows higher dynamic strength, dynamic ductility and damping capacity at failure than geogrid-RS RW.

6.2 Recommendations for future research

With reference to results of this study, the following issues for future research were identified.

6.2.1 Pullout test

Boundary condition of soil container

Relative ideal boundary conditions are necessary to keep the accuracy of results for the future numerical simulation and evaluation of the seismic performance of GRS RWs. Therefore in the future, reduction in friction of the front and side walls is required by gluing low friction materials (i.e. rubber membrane) to these walls. In order to reduce the influence of opening of the front wall, reinforcement is suggested to be put away from the wall facing. In particular, better technology for pulling the geocell through the opening of the front wall should be developed, since it has a 3-D structure.

Normal pressure

Current pullout tests were carried out under a surcharge of 1 kPa. It is recommended to conduct the pullout tests under higher surcharge (i.e. 30 kPa, 60 kPa etc.), since the normal pressure has a great influence on the pullout resistance, development of stress at the soil-reinforcement interface and the tensile failure of the reinforcement.

Geocell reinforcement

The influence of material stiffness on the pullout resistance of the geocell should be investigated. The current geocell model was prepared with relatively weak material (i.e. PET) inducing a relatively lower pullout pre-peak stiffness. Therefore, a relatively stiffer material (i.e. HDPE) can be used to enhance the pullout resistance or pre-peak stiffness of the geocell. In addition, the optimum size of the cells on the pullout resistance should also be determined for cost-effective design.

Soil materials

Present research demonstrates that a geocell exhibits better performance than a geogrid when embedded in uniform soils with larger particles, which makes the use of low-quality local soils possible. In the future, the influence of grading, relative density (or degree of compaction considering the same energy of compaction) of soil materials should also be investigated.

Influence of interval spacing between geocell reinforcement layers

The interval spacing between geogrid reinforcement layers was set to 30 cm in the current design of the GRS RWs. Due to different in-plane structure of the geocell and different interaction mechanism with adjacent soil, the interval spacing between geocell reinforcement layers is recommended to study for practical applications.

Other influential factors

The influences of pullout rate and cyclic loading are also of interest in the future.

Pullout mechanism of geocell

The pullout mechanism can be further investigated by using Discrete Element Method (DEM) simulations or small-scale pullout tests combined with Particle Image Vecolocity (PIV) analysis.

6.2.2 Shaking table model test

Earth pressure

Current research fails to measure the earth pressure. Therefore, new load cell (i.e. two-component load cell) for exact measurement of earth pressure is necessary.

Similitude rule

From the SDOF analysis, unstable dynamic performances of geogrid-RS RW and geocell-RS RW are obtained, which made evaluation difficult. This may be due to the improper similitude rule on the relationship between the weight of the wall and the pullout stiffness of the reinforcements, since a heavy wall model relative to the pullout stiffness of tensile reinforcement (i.e. geogrid model and geocell model) may result in very unstable oscillations of the facing wall during strong shaking. Therefore, proper similitude on the relationship between the weight of the wall and the pullout stiffness of the reinforcements should be considered in the future.

Data acquisition and processing

In the SDOF analysis, some errors occur: a higher tuning ratio (i.e. β =0.9 or 1) appears under very low base acceleration, which is unreasonable. This can be attributed to the fact that the directly obtained values of peak response acceleration and phase difference from a single exact sinusoidal wave acceleration recorded at the shaking table and the top of the wall is not so accurate due to the noise of the response shaking waves and the asymmetry of the response of the retaining wall. This may suggest the use of appropriate data filter technology, better fitting technology as well as increasing sampling time (current scanning rate is only 100 Hz) to capture output data in the experiments.

Influence of the interval spacing between geocell reinforcement layers

Similar with Section 6.2.1, interval spacing between geocell reinforcement layers can also be investigated by shaking table test to provide guidance for the design of GRS RWs with geocells.

Image analysis

The general deformation and failure modes of the geocell-RS RW and geogrid-RS RW were captured by high-speed camera and digital camera. Subsequent image analyses are also

necessary to determine more in-depth deformation characteristics of the backfill region based on the strain field.

Performance-based design

Critical acceleration is a very important parameter in the predication of residual displacements of RWs. Due to time constraints, discussion on the critical acceleration is very limited in this current study. In the future, further investigation is required to confirm the accuracy of the obtained critical acceleration values, and also a performance-based design procedure for geocell-RS RWs should be developed.

7 APPENDIXES

7.1 Appendix A

For all test cases, time histories of base acceleration at the shaking table and response acceleration at the top of the wall for the tenth cycle of every shaking stage after data correction and filter are shown in Appendix A.

From these figures and as discussed in Chapter 5, the response amplification and the phase difference between base acceleration at the shaking table and the response acceleration at the top of the wall can be observed to increase gradually with an increase of input base acceleration. This indicates that the dynamic stability of different types of retaining walls backfilled with different soil materials can be evaluated in the framework of single-degree-of-freedom (SDOF) theory.

As shown in Appendix A, the values of the response amplification, M, and the phase difference, φ, from a single sinusoidal wave can be obtained directly at the active state, (i.e. negative acceleration value where the inertia force is oriented towards the active direction).

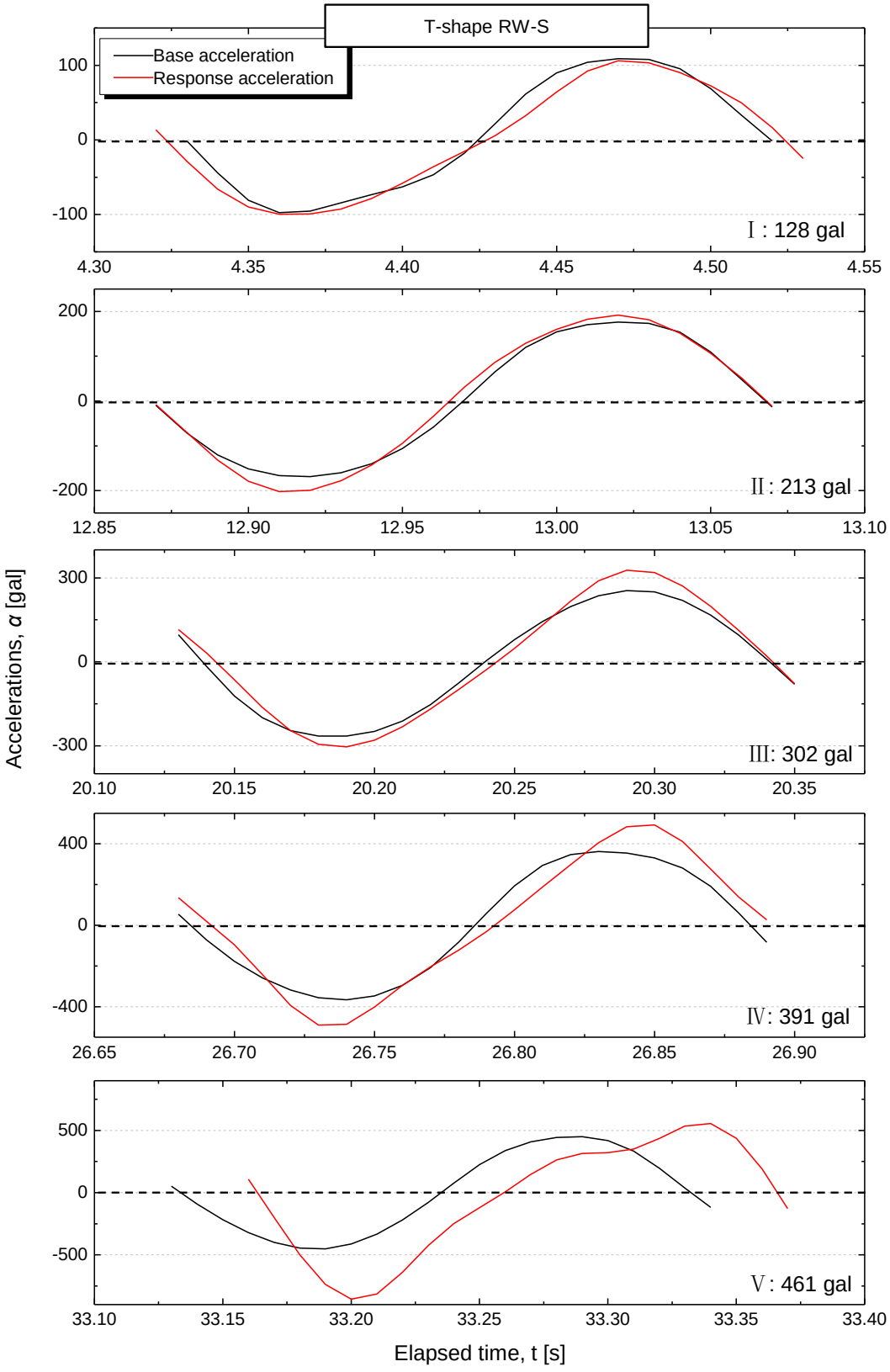

Fig. A.1 One cycle time history of base acceleration and response acceleration for every shaking stage of T-shape RW-S

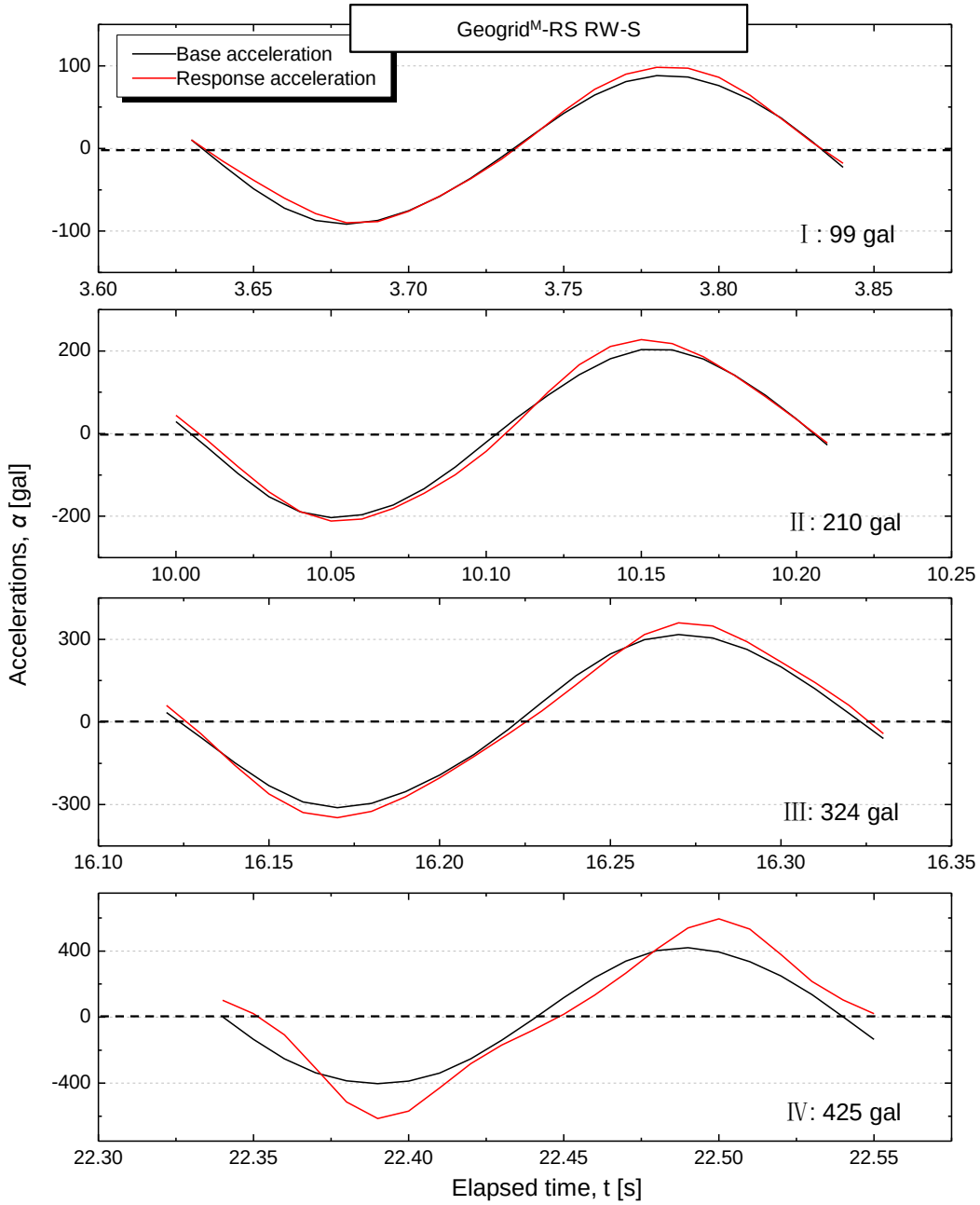

Fig. A.2 One cycle time history of base acceleration and response acceleration for shaking stage Ⅰ~Ⅳ of Geogrid^{M}-RS RW-S

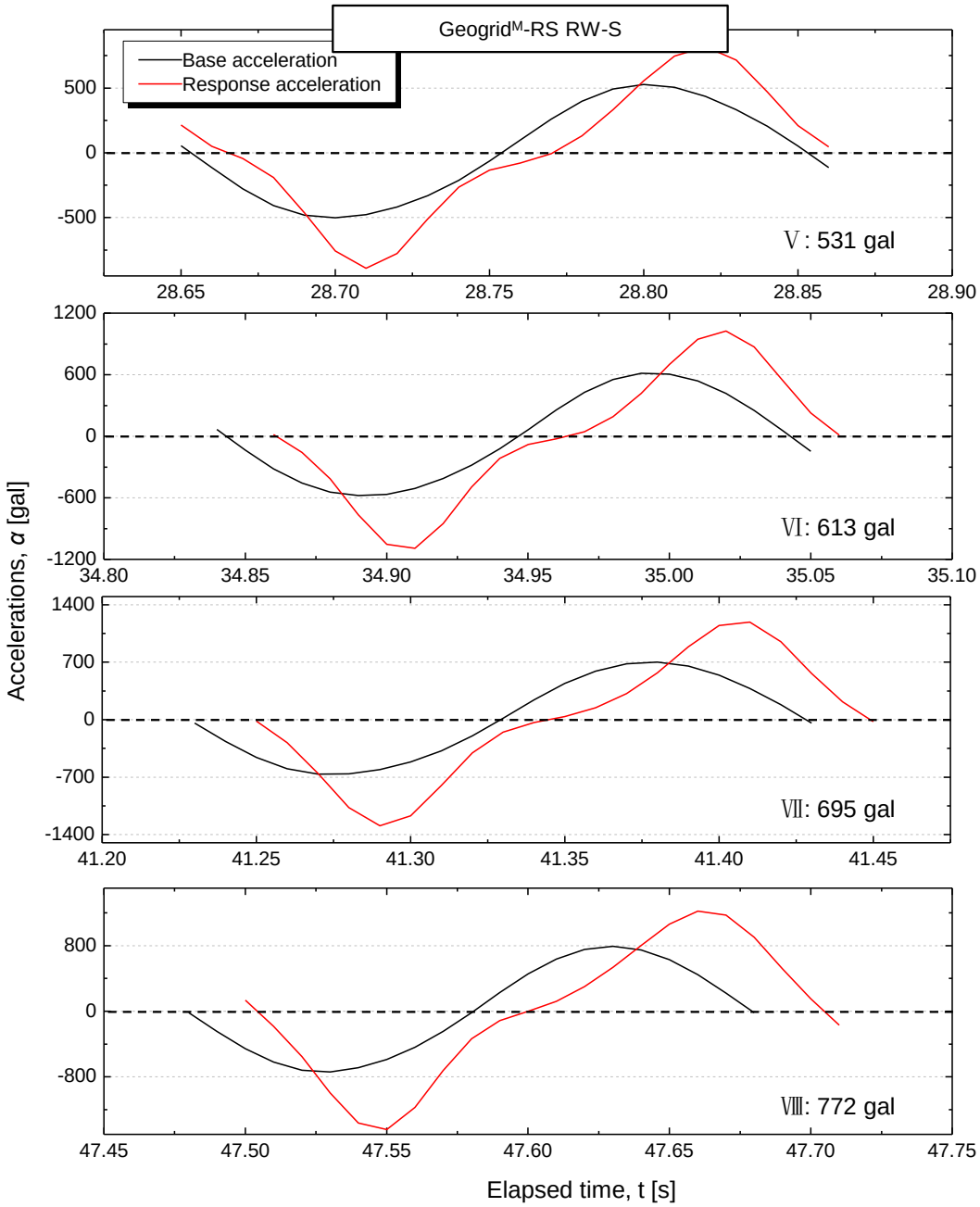

Fig. A.2 (Continued) One cycle time history of base acceleration and response acceleration for shaking stage Ⅴ~Ⅷ of Geogrid^{M}-RS RW-S

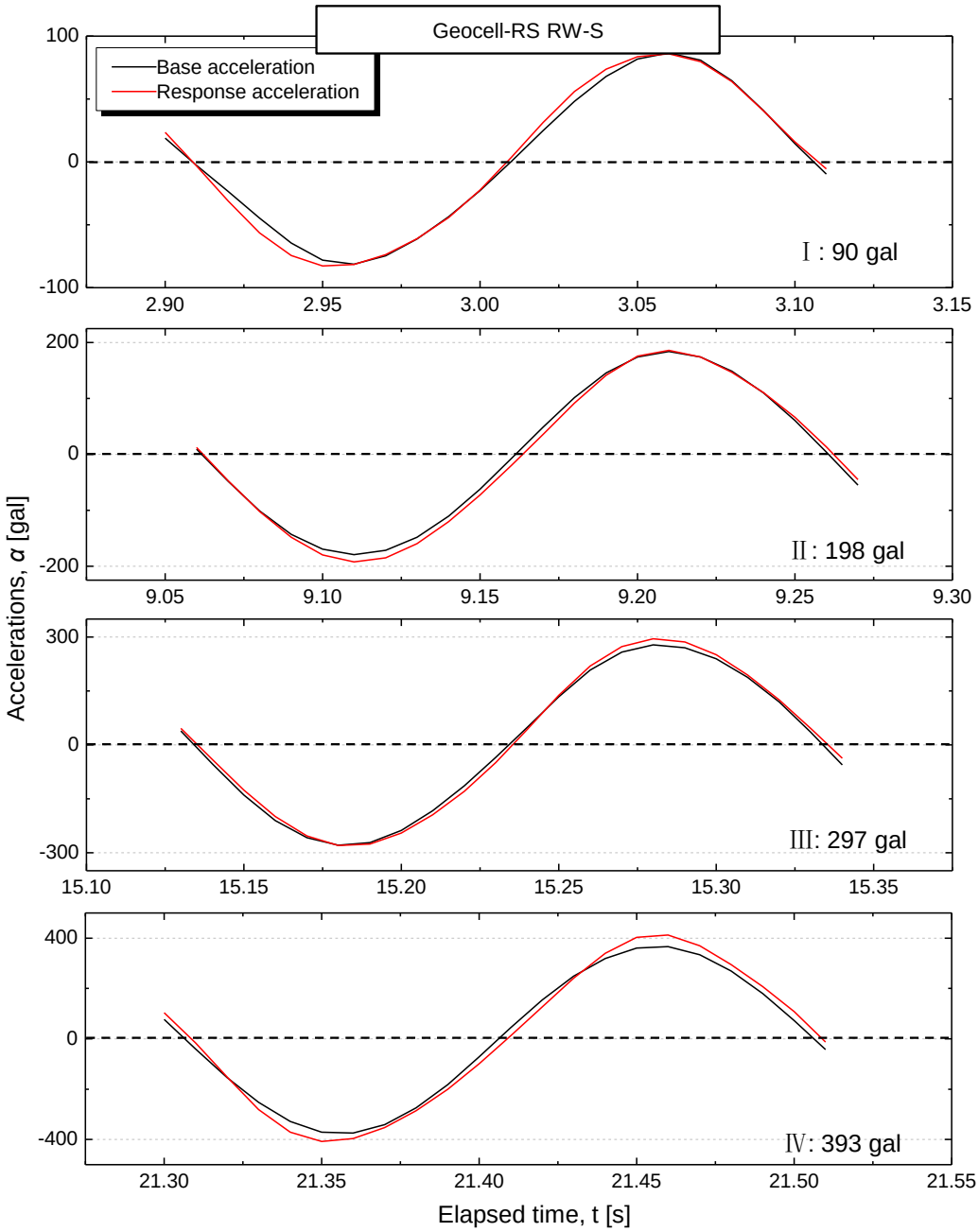

Fig. A.3 One cycle time history of base acceleration and response acceleration for shaking stage Ⅰ~Ⅳ of Geocell-RS RW-S

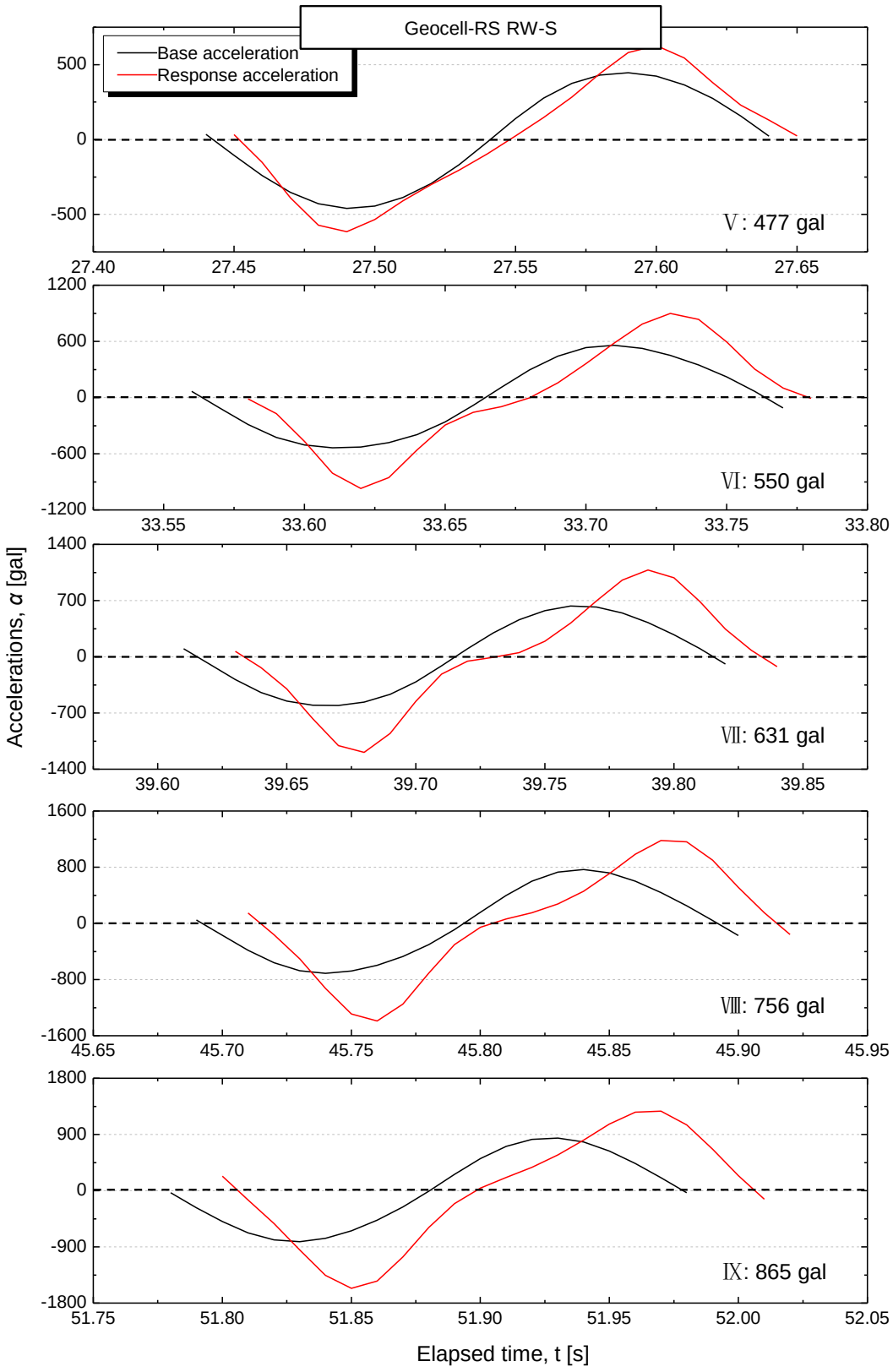

Fig. A.3 (Continued) One cycle time history of base acceleration and response acceleration for shaking stage Ⅴ~Ⅸ of Geocell-RS RW-S

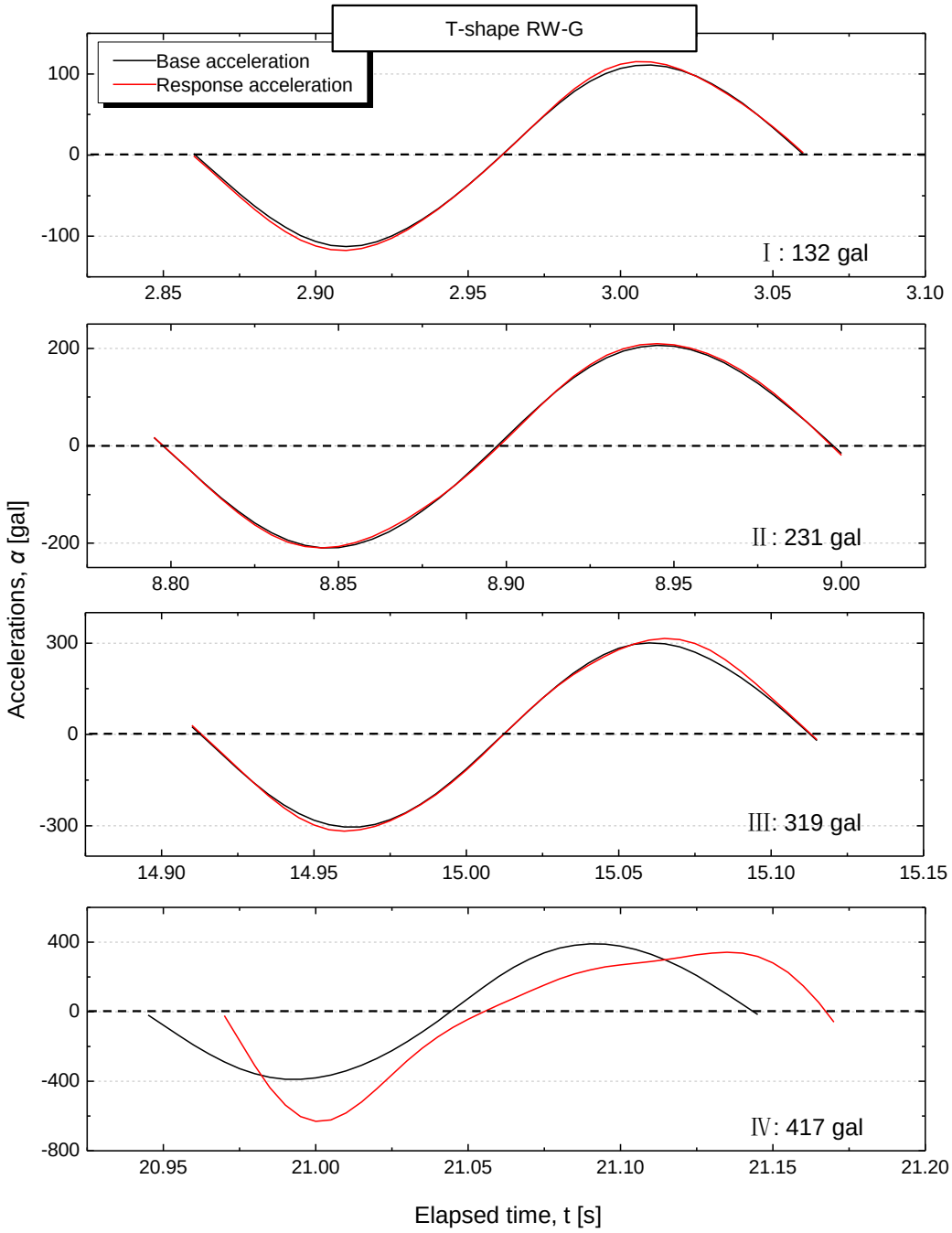

Fig. A.4 One cycle time history of base acceleration and response acceleration for every shaking stage of T-shape RW-G

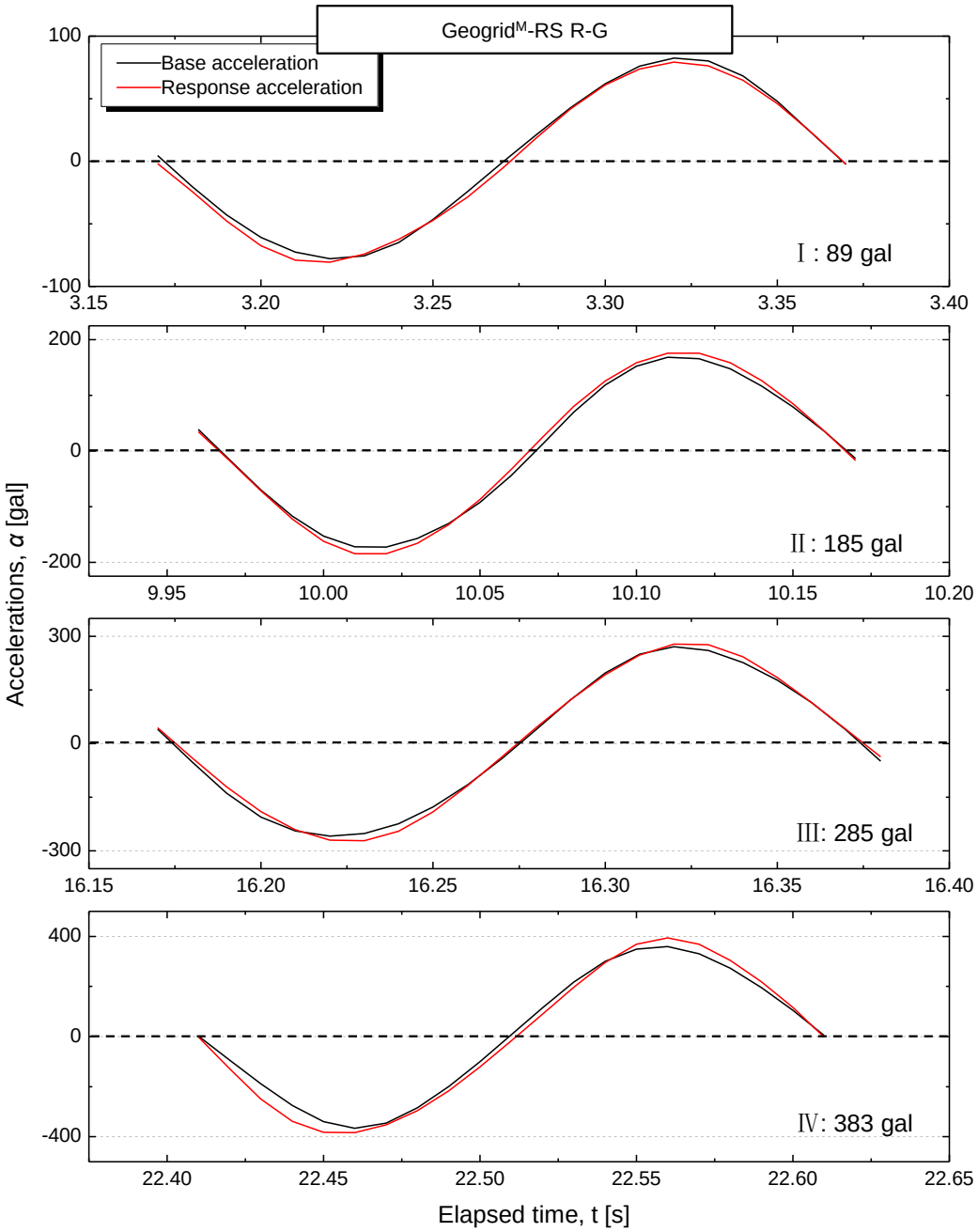

Fig. A.5 One cycle time history of base acceleration and response acceleration for shaking stage Ⅰ~Ⅳ of Geogrid^{M}-RS RW-G

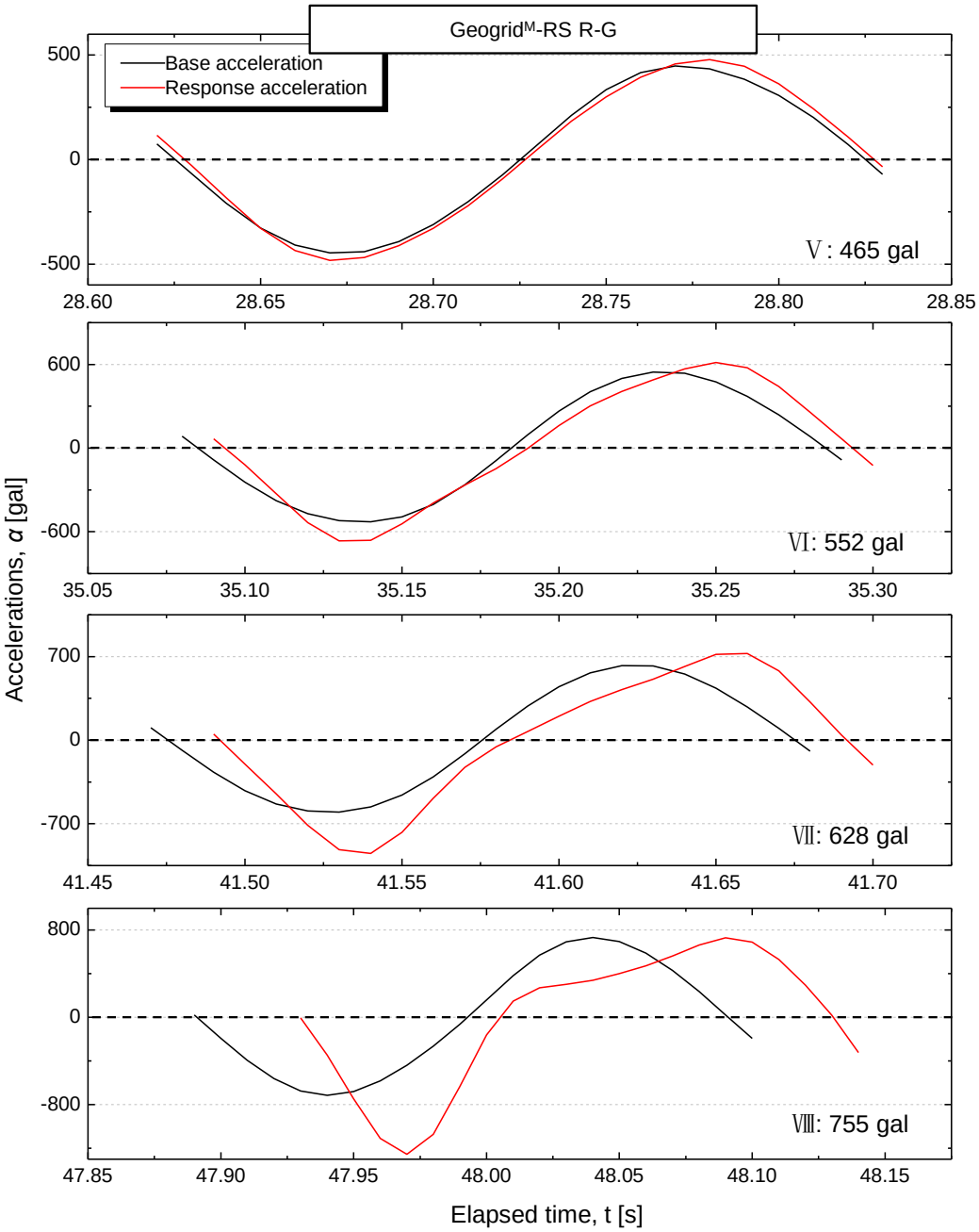

Fig. A.5 (Continued) One cycle time history of base acceleration and response acceleration for shaking stage Ⅴ~Ⅷ of Geogrid^{M}-RS RW-G

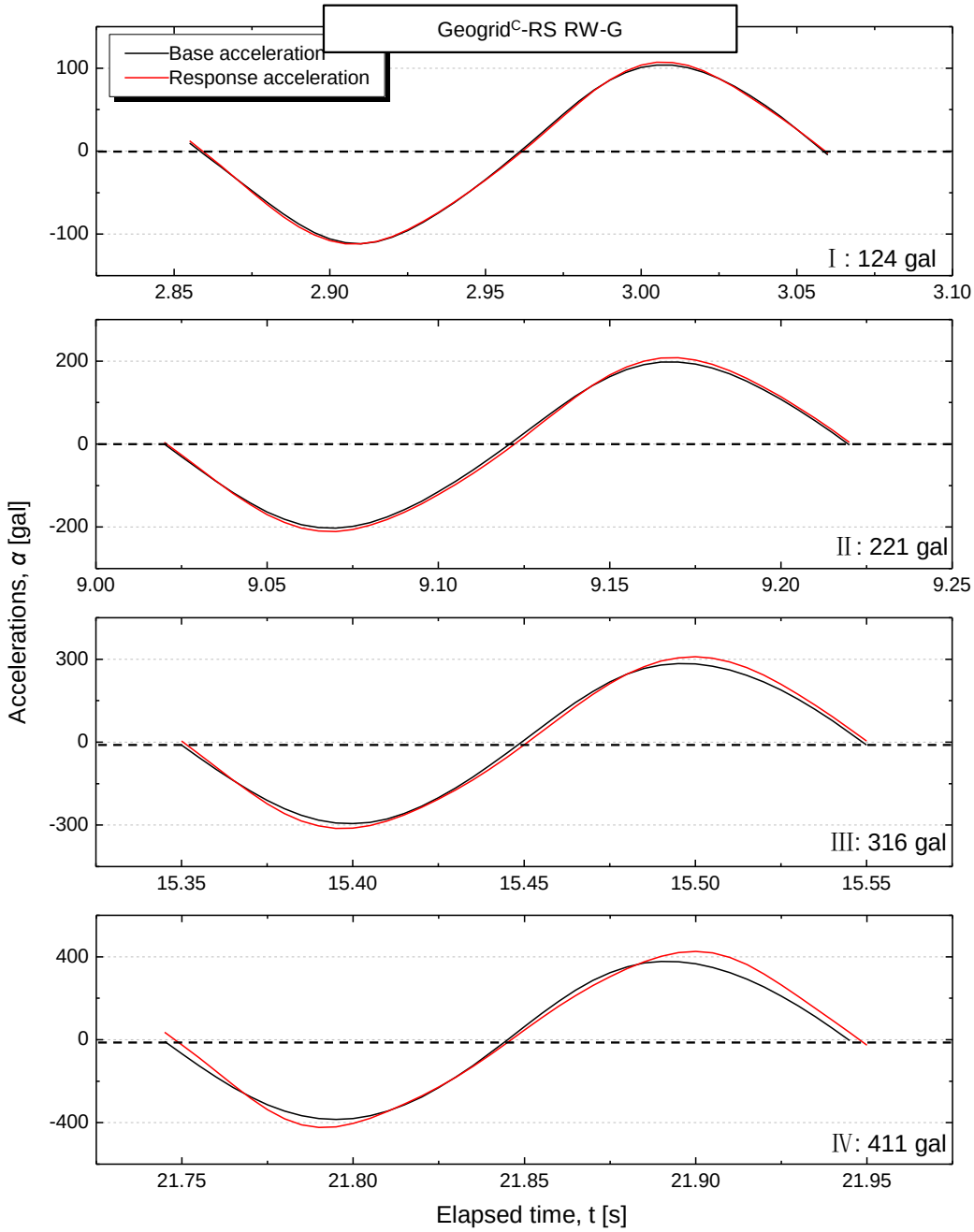

Fig. A.6 One cycle time history of base acceleration and response acceleration for shaking stage Ⅰ~Ⅳ of Geogrid^{C}-RS RW-G

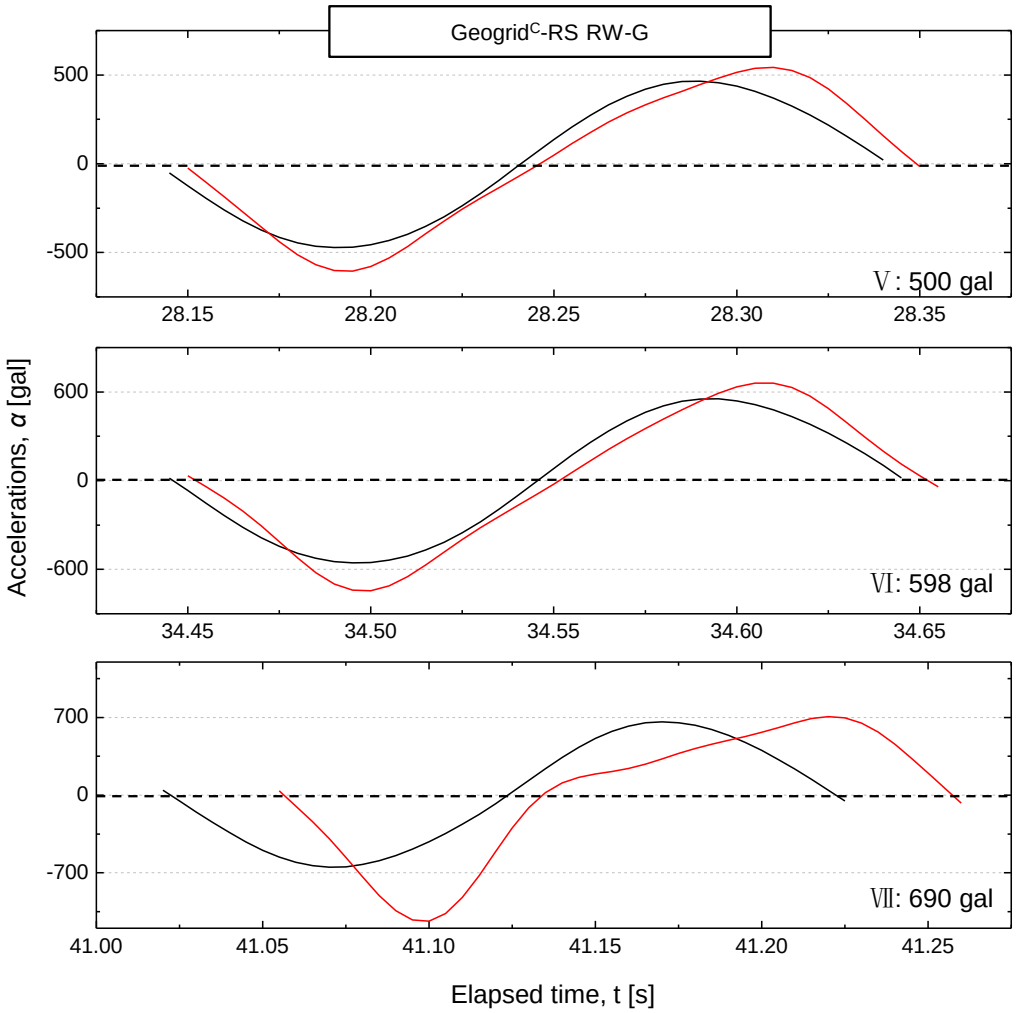

Fig. A.6 (Continued) One cycle time history of base acceleration and response acceleration for shaking stage Ⅴ~Ⅶ of Geogrid^{C}-RS RW-G

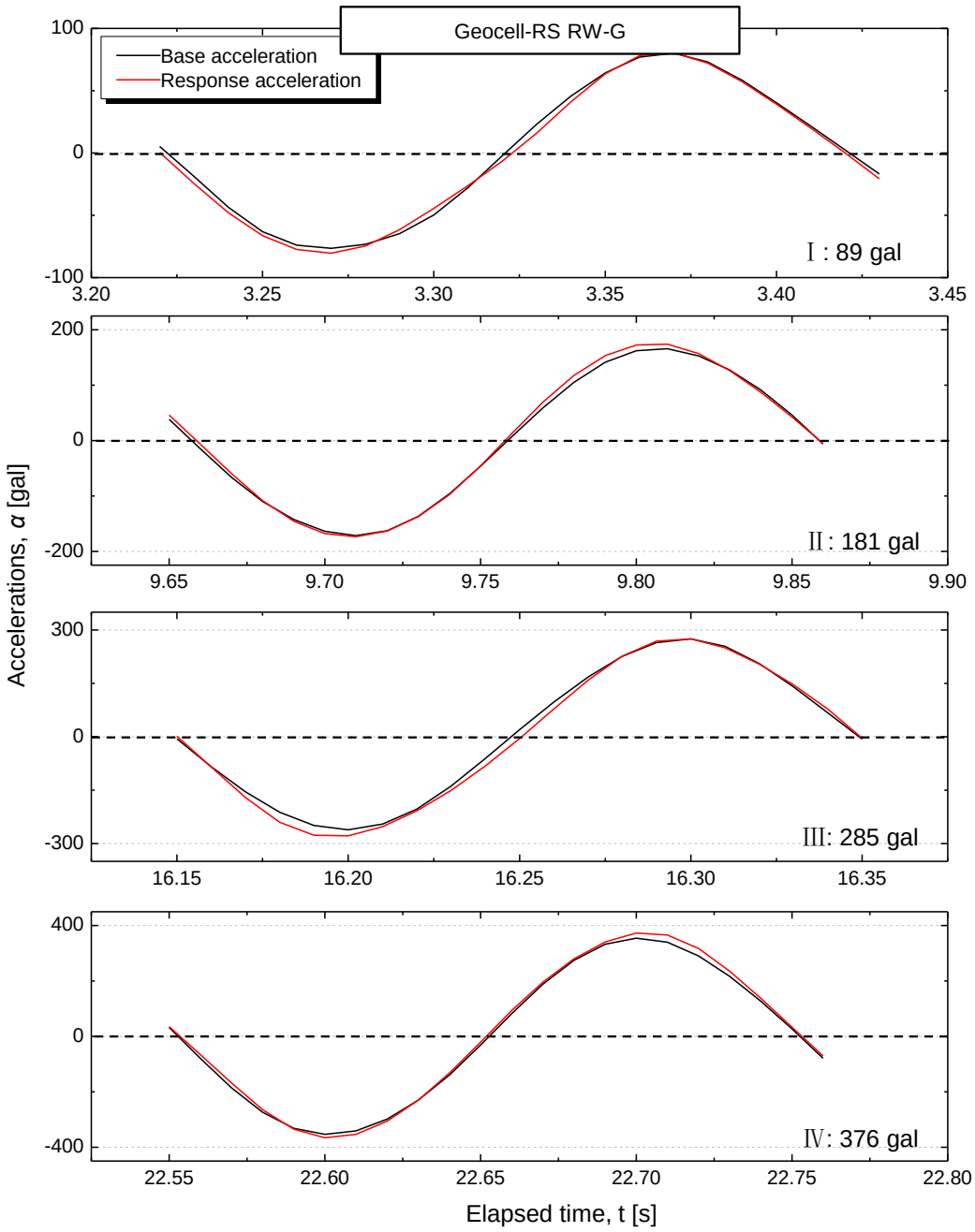

Fig. A.7 One cycle time history of base acceleration and response acceleration for shaking stage Ⅰ~Ⅳ of Geocell-RS RW-G

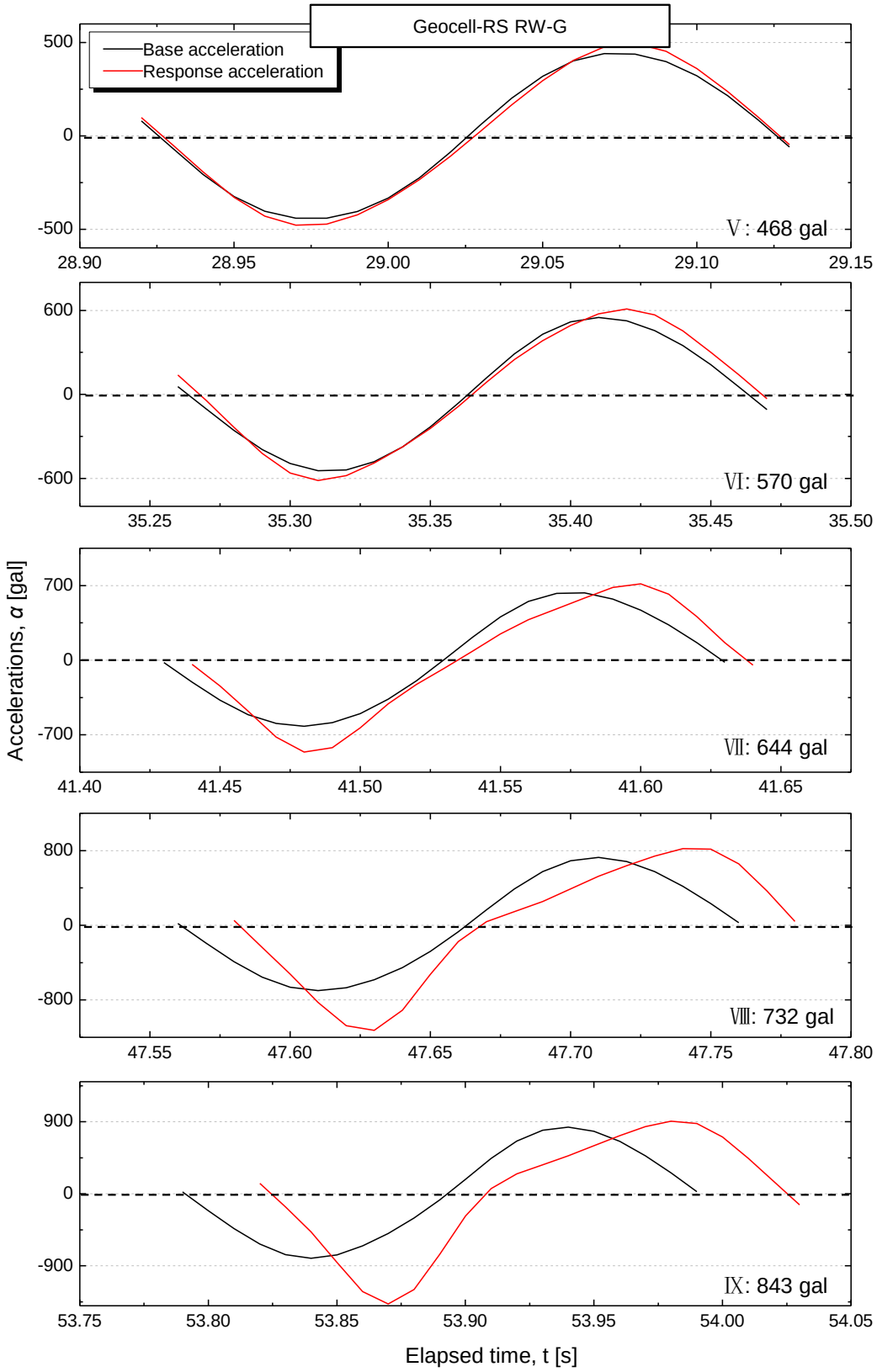

Fig. A.7 (Continued) One cycle time history of base acceleration and response acceleration for shaking stage Ⅴ~Ⅸ of Geocell-RS RW-G